THÈSE

Pour obtenir le grade de

DOCTEUR DE L'UNIVERSITÉ GRENOBLE ALPES

École doctorale : PHYS - Physique
Spécialité : Physique appliquée
Unité de recherche : CEA LETI - Laboratoire d'électronique et de technologie de l'information

Etude et développement d'implants intracérébraux radioluminescents pour le traitement des maladies neurodégénératives

Study and development of radioluminescent brain implants for the treatment of neurodegenerative diseases

Présentée par :

Irene MUÑOZ VELASCO

Direction de thèse :

Pierre BLEUET DIRECTEUR DE RECHERCHE, CEA CENTRE DE GRENOBLE	Directeur de thèse
Grégory PIETERS INGENIEUR HDR, CEA CENTRE DE PARIS-SACLAY	Co-directeur de thèse

Rapporteurs :

GEORGES WAGNIERES
MAITRE DE CONFERENCES, ECOLE POLYTECHNIQUE FEDERALE DE LAUSANNE
AUDREY POTDEVIN
MAITRESSE DE CONFERENCES HDR, CLERMONT AUVERGNE INP

Thèse soutenue publiquement le **26 novembre 2025**, devant le jury composé de :

FREDERIC LEROUGE, PROFESSEUR DES UNIVERSITES, ENS DE LYON	Président
GEORGES WAGNIERES, MAITRE DE CONFERENCES, ECOLE POLYTECHNIQUE FEDERALE DE LAUSANNE	Rapporteur
AUDREY POTDEVIN, MAITRESSE DE CONFERENCES HDR, CLERMONT AUVERGNE INP	Rapporteure
STEPHAN CHABARDES, PROFESSEUR DES UNIVERSITES - PRATICIEN HOSPITALIER, UNIVERSITE GRENOBLE ALPES	Examinateur

To my family and friends,
for all their support throughout
these three years of work.

Acknowledgements

First of all, I want to thank each and every member of the jury for accepting the challenge of evaluating this highly multidisciplinary work. To the reporters, Georges Wagnières and Audrey Potdevin, and the examiners, Stéphan Chabardès and Frédéric Lerouge, being the last, the president of the jury. Thank you for all those fascinating discussions that made my PhD defense such an enriching experience.

Obviously, I want to express my deepest gratitude to my thesis director, Pierre Bleuet, and my co-director, Grégory Pieters. This project simply would not have been possible without you both — without Pierre, the mastermind behind this seemingly crazy idea of developing a radioluminiscent implantable brain device, and without Grégory, the one who said "yes, let's make it happen" and collaborated to bring it to life. I owe you my guidance, your absolute trust, and constant support throughout these three years of work. Pierre, thank you for being there every single day, for your explanations, advice, and above all, your good humor that made everything more manageable even during the toughest moments in the last months. Grégory, thank you for your kindness during each and every one of my visits to your laboratory over these three years.

This has been a truly multidisciplinary project, involving different CEA departments: first, CEA-LETI with the Clinatec team and Pierre as project lead; then CEA-LITEN with the invaluable help and always kindly treatment from Sonia de Sousa Nobre and Olivier Renard, who have trained me in the aerogel synthesis; CEA-IRIG with Céline Rivaux and Peter Reiss for those famous quantum dots — all of them at the Grenoble center — as well as the wonderful CEA-JOLIOT team at Paris-Saclay led by Grégory: Sébastien Garcia-Argote, Pierre Colonna, Sophie Feuillastre, and Maxime Jay, where we carried out the radioactive experiments. I also cannot forget Névine Rochat for training me in cathodoluminescence; Florence Ricoul and Sébastien Jacquinot for the porosity measurements; and the radioprotection team — Christophe Brouard, Arnaud Guiot, and Arnaud Gaudu. I not only thank all the scientists who trained me, gave me advice, and accompanied me throughout this time, but also each and every lab manager for allowing

them to participate in this project when it was not their priority.

I am deeply grateful for all the affection I have received from the entire Clinatec team over these years. Thank you all so much for everything we have shared together. I would like to give a special thanks to my office mate — the one Pierre told me at the beginning I would have to work in synergy with, and with whom I hoped I would get along. Well, I barely spent a second apart from him during these three years, and I could not have laughed more, both inside and outside the office: Marvin Brun-Cosme-Bruny, with whom I truly hope to keep this wonderful friendship for a long time. It will be hard to find such a great work companion — you have set the bar very high — but I hope we will continue sharing new adventures and trips together. A warm hug as well to my colleagues Violaine Juillard and Serpil Karakas, with whom I have spent countless hours gossiping (always accompanied by Marvin). And of course, my colleague and friend Elodie Faure, whom I leave in charge of caring for my plants; and my little Latin community, Andrés Carvallo and Napoleón Torres, for all the laughs we have shared.

Greetings also to the FLS and CEA cybersecurity teams for the little stories that emerged over these three years, which were not funny at the time but will remain as amusing anecdotes in memory.

Finally, I would like to thank my entire family, who despite the distance has been there supporting me through the good times and the not-so-good ones. Especially my parents, Charo and Miguel, and my brother, Víctor, who even came all the way to Grenoble to accompany me on such a special day as my PhD defense. Thank you to my friend Raquel, whom I only see every three or four months, but every time we are together it is like we were never apart. Thank you for listening to me every time I complained about something and for your wise advice. Last but not least, thank you to Kévin, who has accompanied me through these three wonderful years, making me feel at home in a city that was completely unknown to me; who had the patience to teach me to ski for the first time in my life; and who dared to take me camping despite my very urban nature. Thank you for all your support, especially during these last few months, which have been the most difficult ones, when I have been more irritable, insufferable, and in a worse mood than usual. Thank you for always believing in me, even when I did not believe in myself — you have made everything so much easier.

Every single person I have met throughout these three years has added a grain of sand, their personal touch, to an experience in which I have grown not only professionally but, more importantly, personally. It is an experience I will never forget, one I will always remember with great affection, and for which I could not feel more grateful.

Willpower is the crown jewel of conduct.
A person with willpower goes further than an intelligent person.
— Enrique Rojas

Contents

General Introduction **1**

Introduction Générale **3**

1 Neurodegenerative Disorders and Parkinson's Disease: Current Treatments and Emerging Therapies **5**

1.1 Neurodegenerative Diseases 5

1.2 Parkinson's Disease (PD) 8

1.3 Current Symptomatic Treatments 10

1.3.1 Pharmacological 10

1.3.2 Deep Brain Stimulation (DBS) 11

1.3.3 Lesioning Procedures 13

1.4 Exploratory Therapeutic Treatments 13

1.4.1 Cell Therapy 14

1.4.2 Gene Therapy 18

1.4.2.1 For Modulating Mutations 18

1.4.2.2 For Neuroprotection 20

1.4.3 Non-Drug Approaches 21

1.4.4 Drug Approaches 25

1.4.5 Photobiomodulation (PBM) for Parkinson's Disease (PD) 27

1.4.5.1 Transcranial Photobiomodulation (tPBM) 33

1.4.5.2 Intracranial Photobiomodulation (iPBM) 37

1.4.5.2.1 Ongoing Clinical Trial at Clinatec 39

1.5 Fundamentals of Light Propagation and Interaction in Biological Tissue . 41

1.6 Conclusion 43

2 Radioluminescence and Strategies for the Development of Radioluminescent Light Sources for Photobiomodulation 45

2.1 History of Radioactivity 45
2.2 Ideal Radioisotope Characteristics 50
2.3 Selection of the Best Radioisotope Candidate 53
2.4 Safety Considerations for the Proposed Radioluminescent Device 54
2.5 Approaches for Tritium-Based Radioluminescent Device Development . . 56
2.5.1 Gaseous Tritium Light Sources (GTLS) 56
2.5.2 Liquid Tritium Light Sources 59
2.5.3 Solid-state Tritium Light Sources 61
2.5.3.1 Pure Organic Formulations 62
2.5.3.1.1 Tritiated DEB Matrix Containing Organic Phosphors 62
2.5.3.2 Hybrid Formulations 64
2.5.3.2.1 Tritiated Rare Earth-Exchanged Dried Zeolites 64
2.5.3.2.2 Tritiated Siloxane Matrix and Inorganic Phosphors 66
2.5.3.3 Inorganic Formulations 68
2.5.3.3.1 Tritiated Titanium with Inorganic Phosphor Coating 68
2.5.3.3.2 Inorganic Phosphors Embedded in Tritiated Silica Aerogels 69
2.6 Conclusion 73

3 Design and Fabrication of a Radioluminescent Device 75

3.1 Device Specifications 75
3.2 Choice of Materials 77
3.3 Synthesis and Formulation of Materials 81
3.3.1 Luminescent Materials 81
3.3.1.1 YVO_4:Eu^{3+} Nanophosphors 81
3.3.1.2 $AgInS_2$/ZnS Quantum Dots (QDs) 82

3.3.1.3 $CuInS_2$/ZnS Quantum Dots (QDs) 84
3.3.2 Synthesis of Luminescent Aerogels 86
3.3.2.1 Cellulose Aerogels 86
3.3.2.2 Silica Aerogels 90
3.4 Tritium Production and Exposure to Tritium Gas 95
3.4.1 Home-Built System for Radioluminescence (RL) Measurements under Tritium Atmosphere 99
3.4.2 Fundamentals of Radiometry 104
3.5 Characterization Techniques 105
3.5.1 Prior to Tritium Exposure 105
3.5.1.1 Spectral Characterization by Photoluminescence (PL) . 105
3.5.1.1.1 Instrumentation 106
3.5.1.1.2 Sample Preparation 107
3.5.1.2 Two-Dimensional Morphological and Spectral Characterization by Cathodoluminescence (CL) 108
3.5.1.2.1 Instrumentation 111
3.5.1.3 Three-Dimensional Morphological Characterization by Gas Adsorption/Desorption Measurements 112
3.5.1.3.1 Physical Principles of Adsorption and Desorption 112
3.5.1.3.2 Measurements 113
3.5.1.3.3 Instrumentation 118
3.5.1.3.4 Sample Preparation 119
3.5.1.4 Three-Dimensional Morphological Characterization by X-Ray Tomography 121
3.5.1.4.1 European Synchrotron Radiation Facility (ESRF) 122
3.5.1.4.2 ID16A Beamline 124
3.5.1.4.3 Sample Preparation 128
3.5.1.4.4 Data Treatment 130
3.5.1.5 Optical Efficiency Characterization via Quantum Yield Measurements 132
3.5.1.5.1 Instrumentation 133

3.5.2 After Tritium Exposure . . . 135
3.5.2.1 Liquid Scintillation Counting (LSC) . . . 135
3.5.2.2 Thermodesorption Measurements . . . 136
3.6 Conclusion . . . 136

4 Characterization of Luminescent Materials 141
4.1 Spectral Characterization by Photoluminescence (PL) . . . 141
4.2 Spectral Characterization by Cathodoluminescence (CL) . . . 143
4.3 Three-Dimensional Morphological Characterization via Gas Adsorption and Desorption Measurements . . . 146
4.4 Optical Efficiency Characterization via Quantum Yield Measurements . . . 149
4.5 Conclusion . . . 150

5 Tritium Exposure Results 153
5.1 Dependence of Radiance on Tritium Activity . . . 153
5.2 Influence of Sample Size on Radiance . . . 158
5.3 Radiance Evolution Over Time . . . 159
5.4 Encapsulation . . . 161
5.5 Aging Effects . . . 163
5.6 Maximum Tritium Dose . . . 165
5.7 Comparison with Radiance Values Reported in the Literature . . . 165
5.8 Conclusion . . . 166

6 Characterization Techniques and Supporting Analyses 169
6.1 Characterization of Luminescent Aerogels Before Tritium Exposure . . . 169
6.1.1 Spectral Characterization by Photoluminescence . . . 169
6.1.2 Two-Dimensional Morphological and Spectral Characterization by Cathodoluminescence . . . 172
6.1.2.1 Surface Imaging with Secondary Electrons . . . 173
6.1.2.2 Emission Spectra at 5.7 keV . . . 176
6.1.2.3 Local Homogeneity of Emission . . . 178
6.1.2.4 Energy Dependence of Emission Spectra . . . 181
6.1.2.5 Rapid Aging Effects under Electron Beam Exposure . . . 184

6.1.3 Three-Dimensional Characterization via Gas Adsorption and Desorption Measurements . . . 196
6.1.3.1 Adsorption/Desorption Isotherms . . . 196
6.1.3.2 BET Surface Area Determination . . . 200
6.1.3.3 Pore Volume Distribution . . . 204
6.1.4 Three-Dimensional Characterization by X-Ray Tomography . . . 206
6.1.4.1 Laboratory X-Ray Tomography . . . 207
6.1.4.2 Synchrotron Radiation Tomography . . . 207
6.1.4.2.1 Y_2O_3:Eu^{3+} Embedded in CMC . . . 207
6.1.4.2.2 YVO_4:Eu^{3+} Embedded in CMC . . . 213
6.1.4.2.3 $AgInS_2$ Embedded in CMC . . . 215
6.1.4.2.4 $CuInS_2$ Embedded in CMC . . . 216
6.2 Characterization of Radioluminescent Aerogels After Tritium Exposure . 221
6.2.1 Spectral Properties of Radioluminescence . . . 221
6.2.1.1 Comparison of Spectral Properties under Different Excitation Mechanisms . . . 222
6.2.2 Optical Efficiency Characterization via Quantum Yield Measurements . . . 223
6.2.2.1 Photoluminescence (PL) Quantum Yield Measured Using a Commercial System . . . 223
6.2.2.2 Radioluminescence (RL) Quantum Yield . . . 225
6.2.2.3 Determination of Cathodoluminescence (CL) Quantum Yield . . . 226
6.2.3 Radiochemical Characterization via Tritium Quantification . . . 228
6.2.3.1 Liquid Scintillation Counting (LSC) . . . 228
6.2.3.2 Thermodesorption Measurements . . . 230
6.3 Radioluminescent Implant vs. Electroluminescent Implant . . . 232
6.4 Conclusion . . . 233

General Conclusion & Perspectives **235**

Perspectives . . . 236

Conclusion Générale et Perspectives **239**

Perspectives 240

Bibliography **245**

Acronyms

α-syn α-synuclein.

6-OHDA 6-hydroxydopamine.

A-MSCs Adipose-derived Mesenchymal Stem Cells.

AADC aromatic L-amino acid decarboxylase.

AD Alzheimer's Disease.

AE Auger Electrons.

AFM Atomic Force Microscopy.

AIE Aggregation-Induced Emission.

ALS Amyotrophic Lateral Sclerosis.

ANR Agence Nationale de la Recherche.

ATP adenosine triphosphate.

BBB Blood-Brain Barrier.

BET Brunauer–Emmett–Teller.

BJH Barret-Joyner-Halenda.

BSE Backscattered Electrons.

CANDU Canadian Deuterium Uranium.

CB Conduction Band.

CCD Charge-Coupled Device.

CcO cytochrome c oxidase.

CEA Commissariat à l'Energie Atomique et aux Energies Alternatives.

CL Cathodoluminescence.

CMC sodium carboxymethyl cellulose.

CNS Central Nervous System.

COMT catechol-O-methyltransferase.

CPMAS cross-polarization MAS.

CSF CerebroSpinal Fluid.

DBS Deep Brain Stimulation.

DEB 1,4-bis(phenylethynyl)benzene.

DES Direction des Energies.

DLS Dynamic Light Scattering.

DNA deoxyribonucleic acid.

DPA dipicolinic acid.

DRF Direction de la Recherche Fondamentale.

DRT Direction de la Recherche Technologique.

DTIS Département des Technologies pour l'Innovation en Santé.

EDX Characteristic X-ray.

ENS École Normale Supérieure.

ESC-DAPs Embryonic Stem Cells-derived Dopamine Progenitor cells.

ESCs Embryonic Stem Cells.

ESRF European Synchrotron Radiation Facility.

ET Essential Tremor.

FDA Food and Drug Administration.

FEG Field Emission Gun.

FMT Fecal Microbiota Transplantation.

FoV Reference Field of View.

FTIR Fourier Transform Infrared spectroscopy.

FUS Focused Ultrasound.

FWHM Full Width at Half Maximum.

GCase glucocerebrosidase.

GCH guanosine triphosphate cyclohydrolase.

GLP-1 glucagon-like peptide-1.

GLP-1R glucagon-like peptide-1 receptor.

GM Gray Matter.

GPi Globus Pallidus pars interna.

GSH glutathione.

GTLS Gaseous Tritium Light Sources.

HD Huntington's Disease.

HIE Hydrogen Isotope Exchange.

HUC-MSCs Human Umbilical Cord-derived Mesenchymal Stem Cells.

ICP-AES Inductively Coupled Plasma Atomic Emission Spectroscopy.

iPBM intracranial Photobiomodulation.

iPSC-DAPs induced Pluripotent Stem Cells-derived Dopamine Progenitor cells.

iPSCs induced Pluripotent Stem Cells.

IRIG Institut de Recherche Interdisciplinaire de Grenoble.

IUPAC International Union of Pure and Applied Chemistry.

IWL Interfacial Water Layers.

JOLIOT Institut des Sciences du Vivant Frédéric Joliot.

K-B Kirkpatrick-Baez.

LED Light Emitting Diode.

LETI Laboratoire d'Electronique et de Technologie de l'Information.

Linac Linear Accelerator.

LITEN Laboratoire d'Innovation pour les Technologies des Energies Nouvelles et les Nanomatériaux.

LLLT Low-Level Laser Therapy.

LPS lipopolysaccharide.

LS Lesioning Surgeries.

LSC Liquid Scintillation Counting.

MAO-B monoamine oxidase B.

MAS Magic Angle Spinning.

MC methylcellulose.

MIP Mercury Intrusion Porosimetry.

MPTP 1-methyl-4-phenyl-1,2,3,6-tetrahydropyridine.

MR Magnetic Resonance.

MRgFUS MR-guided FUS.

MRI Magnetic Resonance Imaging.

MSCs Mesenchymal Stem Cells.

NASA National Aeronautics and Space Administration.

NIR Near-Infrared.

NMR Nuclear Magnetic Resonance.

NPCs Neural Progenitor Cells.

NSCs Neural Stem Cells.

OBT Organic Bound Tritium.

OECD Organisation for Economic Co-operation and Development.

PBM Photobiomodulation.

PD Parkinson's Disease.

PDMS polydimethylsiloxane.

PE-PTC Programmes Exploratoire et Transversaux de Compétences.

PET Positron Emission Tomography.

PL Photoluminescence.

PMT Photomultiplier Tube.

PTFE polytetrafluoroethylene.

QDs Quantum Dots.

R-NIR Red-to-Near-Infrared.

RF Radiofrequency.

RFoV Reference Field of View.

RL Radioluminescence.

ROI Region of Interest.

ROS Reactive Oxygen Species.

rTMS repetitive Transcranial Magnetic Stimulation.

SE Secondary Electrons.

SEM Scanning Electron Microscope.

SN Substantia Nigra.

SNpc Substantia Nigra pars compacta.

SRLS Solid-state Radioluminescent Light Sources.

SRS Stereotactic Radiosurgery.

STN Subthalamic Nucleus.

TBI Traumatic Brain Injury.

TBS Theta Burst Stimulation.

tDCS transcranial Direct Current Stimulation.

TEM Transmission Electron Microscopy.

TEOS tetraethyl orthosilicate.

TH tyrosine hydroxylase.

TMS Transcranial Magnetic Stimulation.

tPBM transcranial Photobiomodulation.

TRF Tritium Removal Facility.

UCBL1 Université Claude Bernard Lyon 1.

VB Valence Band.

Vim Ventral intermediate nucleus of the thalamus.

VM Fetal Ventral Mesencephalon tissue.

WHO World Health Organization.

WM White Matter.

General Introduction

Cancer has long been a major health challenge worldwide, demanding intense research and clinical efforts. In recent years, however, neurodegenerative diseases have gained increasing importance as their diagnosis rates rise alongside aging populations. Despite advances in medical science, the brain remains one of the least understood organs, presenting significant challenges to developing effective treatments.

Among neurodegenerative diseases, Parkinson's Disease (PD) stands out as a growing concern, being the second most common after Alzheimer's Disease (AD). This disease is characterized by the loss of dopaminergic neurons located in a deep brain region called the Substantia Nigra pars compacta (SNpc). Currently, patients affected by this neurological disorder only have access to treatments that alleviate symptoms, such as pharmaceutical therapies or the Deep Brain Stimulation (DBS), which delivers electrical impulses to a specific brain region. However, no existing treatment addresses the disease at its origin by slowing the cellular death of dopaminergic neurons.

Given the complexity and mystery surrounding the brain, novel approaches aim to interact directly with brain tissue using emerging technologies. One promising method is photobiomodulation, which utilizes light to stimulate specific brain regions depending on the neurodegenerative disease, potentially offering new therapeutic avenues beyond conventional treatments. This approach is being studied clinically in what is considered the world's first clinical trial of PBM for PD, conducted by the Clinatec group at the Commissariat à l'Energie Atomique et aux Energies Alternatives (CEA) center in Grenoble.

This clinical trial involves seven patients implanted with a battery under the clavicle, connected via a cable to a laser diode housed in the skull. The laser diode is coupled to an optical fiber inserted into the brain, extending down to the third ventricle, to deliver red light at 670 nm to the brain region affected by the disease.

More than two years of study have been completed with the first three patients, and preliminary results of the clinical trial have been reported in January 2025. These results

are very promising, prompting investigations into the next generation of implants, as the current device has certain limitations.

The first limitation is that its installation requires two surgical procedures: one to implant the battery beneath the clavicle and another for inserting the laser diode and optical fiber. Contrary to intuition, the first surgery is more invasive, as the second part of the procedure is similar to that performed in DBS and is thus well known. Moreover, the catheter used to insert the optical fiber follows natural brain pathways, making it less invasive than battery implantation. The second limitation is the need to recharge the implant's battery up to twice per week via induction. The third, and equally important, limitation arises from simulations of light propagation emitted by the device in the brain that estimate photon losses of between four and five orders of magnitude from the fiber optic output to absorption in the SNpc. Additionally, the current medical device is a point-like, directional light source, which poses challenges if it were to be used for the treatment of other neurodegenerative diseases like AD. In these cases, broader brain regions such as the cortex and hippocampus, which are much larger than the SNpc, would require a diffuse light source, rendering the current device unsuitable.

These challenges motivate the search for new, more compact medical devices that lack electronics or batteries and emit diffuse light. This naturally leads to considering radioluminescent devices. Although studying radioluminescent devices dates back to the 1950s and is not a new concept, many current medical treatments, such as brachytherapy for cancer, already employ radiation. Thus, developing a radioluminescent device for PD treatment via PBM is a plausible approach.

Therefore, this doctoral thesis addresses the entire technological development, spanning several scientific fields such as nuclear physics, optics, and chemistry (both organic and inorganic), with strong emphasis on biomedical engineering and translational neuroscience. The main goal is to find the best approach to develop this device while ensuring essential safety concerns due to the radioactive nature of the device, prioritizing patient benefit. Equally important is identifying the optimal materials that maximize light output, as the therapeutic light dose for treating PD is still not well established. This area remains under active research, influenced by multiple factors including disease progression and patient brain anatomy.

This interdisciplinary work requires collaboration with various teams across CEA centers in Grenoble and Paris Saclay, coordinating each team's expertise in their respective fields.

Introduction Générale

Le cancer a longtemps représenté un défi majeur pour la santé mondiale. Ces dernières années, cependant, les maladies neurodégénératives ont pris une importance croissante à mesure que leurs taux de diagnostic augmentent avec le vieillissement des populations.

Parmi les maladies neurodégénératives, la maladie de Parkinson (PD) se distingue comme une préoccupation grandissante, étant la deuxième la plus fréquente après la maladie d'Alzheimer (AD). Cette maladie se caractérise par la perte des neurones dopaminergiques situés dans une région profonde du cerveau appelée la substance noire pars compacte (SNpc). Actuellement, les patients affectés par ce trouble neurologique disposent uniquement de traitements symptomatiques tels que les thérapies médicamenteuses ou la stimulation cérébrale profonde (DBS), qui délivre des impulsions électriques à une région cérébrale spécifique. Cependant, aucun traitement existant n'agit à l'origine de la maladie en ralentissant la mort cellulaire de ces neurones dopaminergiques.

Compte tenu de la complexité et du mystère entourant le cerveau, de nouvelles approches visent à interagir directement avec le tissu cérébral à l'aide de technologies émergentes. Une méthode prometteuse est la photobiomodulation (PBM), qui utilise la lumière pour stimuler des régions cérébrales spécifiques en fonction de la maladie neurodégénérative, offrant potentiellement de nouvelles voies thérapeutiques au-delà des traitements conventionnels. Cette approche est actuellement étudiée en clinique lors de ce qui est considéré comme le premier essai clinique mondial de PBM pour la PD, conduit par le groupe Clinatec au centre CEA de Grenoble.

Cet essai clinique implique sept patients implantés d'une batterie sous la clavicule, reliée par un câble à une diode laser logée dans la boîte crânienne. La diode laser est couplée à une fibre optique insérée dans le cerveau, allant jusqu'au troisième ventricule, afin de délivrer de la lumière rouge à 670 nm à la région cérébrale affectée par la maladie.

Plus de deux années d'étude ont été menées avec les trois premiers patients, et les résultats préliminaires de l'essai clinique ont été rapportés en janvier 2025. Ces résultats sont très prometteurs, encouragent la recherche pour la prochaine génération d'implants, car le

dispositif actuel présente certaines limitations.

La première limitation est que son installation requiert deux interventions chirurgicales: une pour implanter la batterie sous la clavicule et une autre pour insérer la diode laser et la fibre optique. Contrairement à l'intuition, la première chirurgie est plus invasive; la seconde, semblable à celle effectuée en DBS, est donc bien connue. De plus, le cathéter utilisé pour insérer la fibre suit des voies naturelles du cerveau, la rendant moins invasive que l'implantation de la batterie. La deuxième limitation est la nécessité de recharger la batterie de l'implant jusqu'à deux fois par semaine par induction. La troisième limitation, tout aussi importante, provient des simulations de propagation de la lumière émise par le dispositif dans le cerveau, estimant des pertes de photons de l'ordre de quatre à cinq décades entre la sortie de la fibre optique et l'absorption dans la SNpc. Par ailleurs, le dispositif médical actuel est une source lumineuse directionnelle ponctuelle, posant des défis s'il devait être utilisé pour traiter d'autres maladies neurodégénératives telles que la AD. Dans ces cas, des régions cérébrales plus larges comme le cortex et l'hippocampe, beaucoup plus vastes que la SNpc, nécessiteraient une source lumineuse diffuse, rendant le dispositif actuel inadapté.

Ces enjeux motivent la recherche de dispositifs médicaux nouveaux, plus compacts, dépourvus d'électronique ou de batteries, émettant une lumière diffuse. Cela conduit naturellement à considérer les dispositifs radioluminescents. Bien que l'étude des dispositifs radioluminescents remonte aux années 1950 et ne soit pas un concept nouveau, de nombreux traitements médicaux actuels, tels que la curiethérapie anticancéreuse, utilisent déjà la radiation. Ainsi, développer un dispositif radioluminescent pour le traitement de la PD par PBM est une approche plausible.

Par conséquent, cette thèse doctorale couvre l'ensemble du développement technologique, couvrant plusieurs domaines scientifiques tels que la physique nucléaire, l'optique, la chimie (organique et inorganique), avec une forte emphase sur le génie biomédical et les neurosciences translationnelles. L'objectif principal est de trouver la meilleure approche pour développer ce dispositif tout en assurant les impératifs de sécurité essentiels liés à la nature radioactive du dispositif, avec la priorité donnée au bénéfice patient. Il est également crucial d'identifier les matériaux optimaux maximisant la sortie lumineuse, car la dose thérapeutique de lumière pour traiter la PD n'est pas encore bien établie. Ce domaine reste en cours de recherche active, influencé par plusieurs facteurs incluant la progression de la maladie et l'anatomie cérébrale du patient.

Ce travail interdisciplinaire requiert la collaboration de diverses équipes réparties dans plusieurs centres du CEA à Grenoble et Paris Saclay, coordonnant l'expertise propre à chaque équipe dans leur domaine respectif.

Chapter 1

Neurodegenerative Disorders and Parkinson's Disease: Current Treatments and Emerging Therapies

In the first chapter of this thesis, different neurodegenerative diseases are presented, with particular emphasis on Parkinson's Disease (PD). The next section reviews the treatments currently offered to patients with PD, which only inhibits symptoms while the disease continues to progress. For this reason, the chapter introduces current exploratory therapeutic approaches that aim to be curative, with special attention given to Photobiomodulation (PBM).

1.1 Neurodegenerative Diseases

Neurodegenerative diseases are a group of chronic conditions characterized by the progressive loss of neurons, a process known as neurodegeneration, which impairs the structure and function of the Central Nervous System (CNS). Among these, four major diseases stand out due to their prevalence and impact: Alzheimer's Disease (AD), Parkinson's Disease (PD), Amyotrophic Lateral Sclerosis (ALS) and Huntington's Disease (HD).

AD is the most common neurodegenerative disorder worldwide, affecting approximately 33 to 39 million people in 2021 according to the World Health Organization (WHO) [1]. It begins with the gradual degeneration of neurons in the hippocampus, a crucial structure for memory, before spreading to other areas of the brain, including the cortex [2]. The

early symptoms include short-term memory loss, followed by impairments in executive functions such as planning and task execution. Patients may forget how to use familiar objects, lose their sense of time and place, and experience language deficits, movement disorders, mood disturbances (anxiety, depression, irritability) and sleep disorders. As the disease progresses, cognitive abilities and autonomy deteriorate significantly. Age is the primary risk factor, with incidence increasing after 65 and surging after 80. Additionally, AD is about twice as prevalent in women as in men.

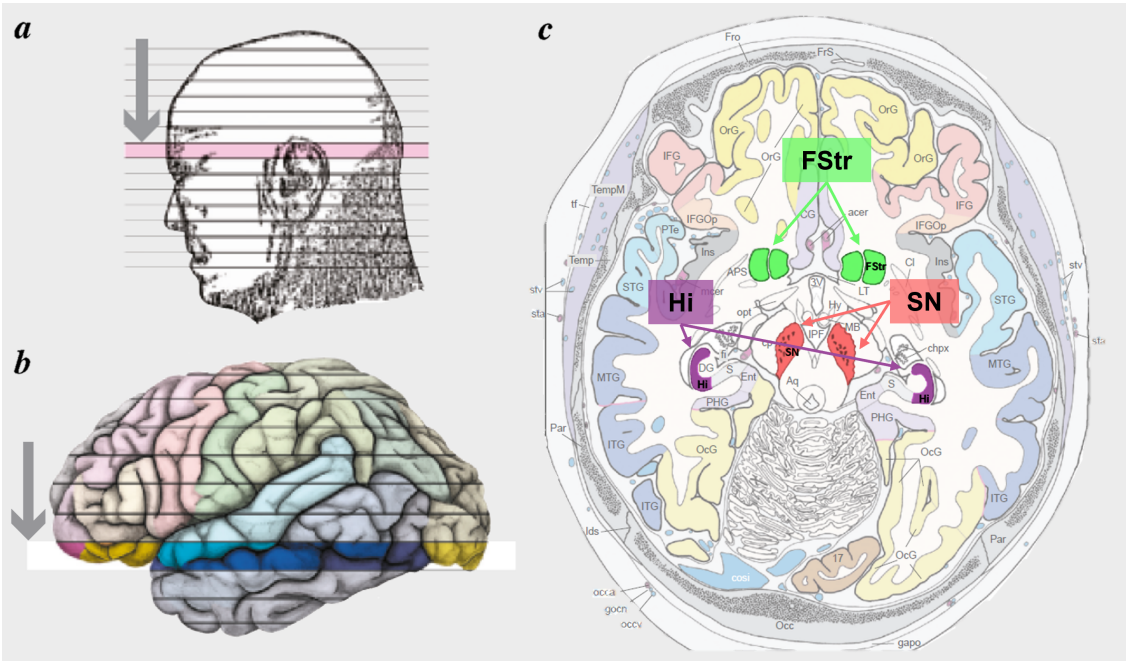

Figure 1.1: ***a***) Schematic representation of the axial brain slice on a sagittal view of the head. ***b***) Lateral view of the brain showing the approximate level of the axial section. ***c***) Axial section of the brain highlighting the hippocampus (annotated as Hi, and colored in purple), the striatum (annotated as FStr, and colored in green) and the Substantia Nigra (annotated as SN, and colored in red). Adapted from [3].

PD is the second most common neurodegenerative disorder after AD, affecting around 10 million people globally in 2025 [4]. It is a chronic and progressive disease characterized by the loss of neurons that produce dopamine in the Substantia Nigra (SN) [5]. The early stage of the disease, where neuronal damage occurs without noticeable symptoms, may last for years. During this period, the brain compensates for dopamine loss through plasticity mechanisms. Symptoms emerge only after 50–70% of dopamine-producing neurons have been lost. The hallmark motor symptoms include akinesia (difficulty initiating movement), bradykinesia (slowness of movement), limb rigidity, and tremors. Additionally, patients may experience non-motor symptoms such as cognitive decline, depression, gastrointestinal

and genitourinary dysfunctions, and sleep disturbances. The exact causes of neuronal degeneration remain unclear but are likely multifactorial, involving aging, genetics, and environmental factors. The disease primarily affects individuals over 60 years, and its prevalence has doubled in the last 25 years due to the aging population. Men are 1.5 times more likely to develop PD than women.

ALS, also known as Charcot's disease, is the third most common neurodegenerative disease worldwide, affecting between 160 000 and 240 000 people globally in 2023 [6]. It is a severe neurodegenerative disorder causing progressive paralysis of voluntary muscles [7]. ALS results from the gradual death of motor neurons in the spinal cord, which control muscle contraction. The disease also affects speech and swallowing. The onset typically occurs between 50 and 70 years, with earlier cases often linked to genetic factors. Men are 1.5 times more likely to develop ALS than women but the gender differences decreases with age, meaning that in older populations, men and women are affected more equally.

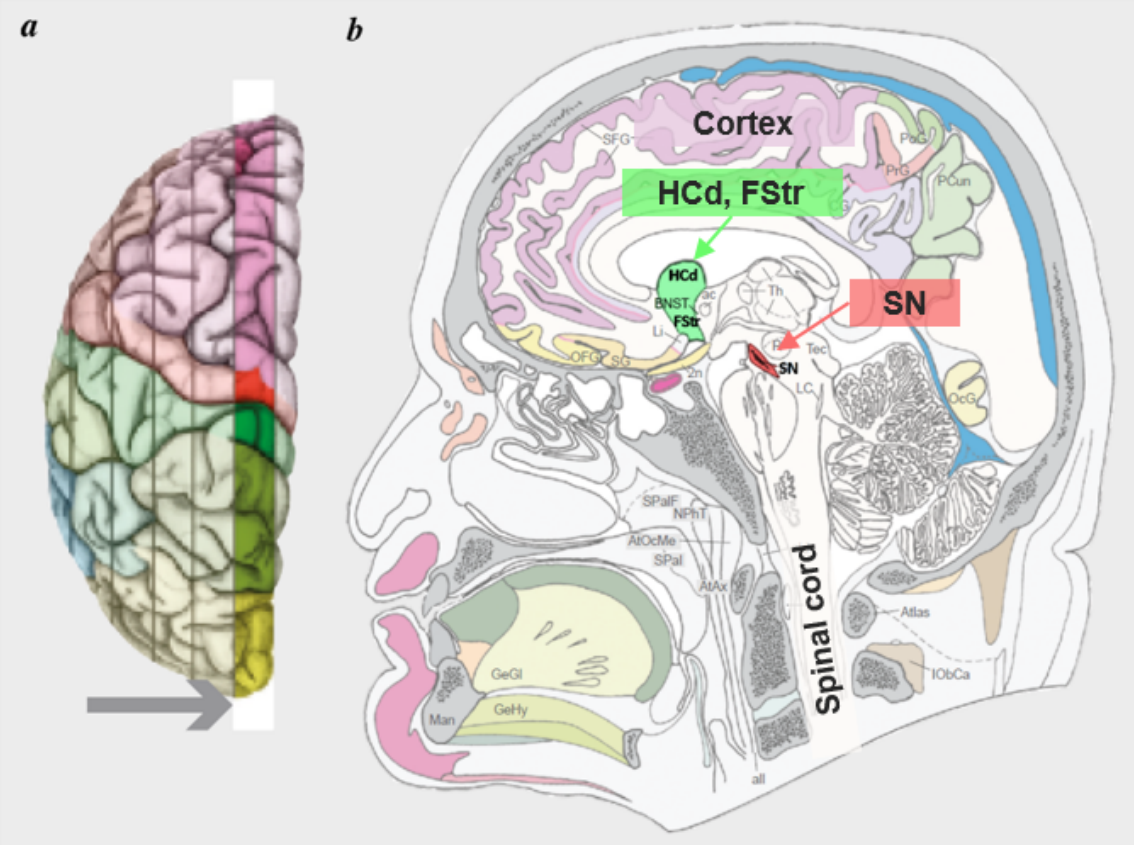

Figure 1.2: ***a***) Lateral view of the brain showing the approximate level of the sagittal section. ***b***) Sagittal section of the brain highlighting the cortex (colored in violet), the striatum (annotated as FStr and HCd, and colored in green), the Substantia Nigra (annotated as SN, and colored in red), and the spinal cord (colored in white). Adapted from [3].

HD is a rare and hereditary neurodegenerative condition, with an estimated prevalence at 5 to 10 cases per 100 000 people in Europe in 2022 [8]. It affects neurons in the striatum and it manifests through motor impairments (characterized by involuntary and unpredictable movements), abnormal postures, muscle rigidity, and bradykinesia. Additionally, it leads to cognitive decline (dementia) and psychiatric symptoms, including depression, anxiety, apathy, and irritability. Over time, symptoms worsen, leading to complete physical and intellectual deterioration. Onset typically occurs between the ages of 30 and 50, and both men and women are equally affected.

The different brain regions affected by these neurodegenerative diseases are illustrated in Figures 1.1 and 1.2.

To date, there is no cure for all these neurodegenerative diseases and patients are offered just symptomatic-only treatments, which help manage symptoms but do not slow down neurodegeneration.

Although AD remains the most common neurodegenerative disorder, PD is the fastest-growing in prevalence. The following sections will explore its pathophysiology, clinical manifestations, and current therapeutic approaches.

1.2 Parkinson's Disease (PD)

As previously mentioned, PD affects approximately 10 million individuals worldwide, and this number is expected to rise substantially due to population aging. Moreover, environmental factors, such as exposure to neurotoxic products like pesticides, may also contribute to the increasing disease burden [9].

The history of PD dates back over 200 years, with the first clinical description published in 1817 by British physician James Parkinson in *An Essay on the Shaking Palsy* [10], where he identified the classic motor symptoms already mentioned including akinesia, bradykinesia, limb stiffness, and tremors as defining features. In the late 19th century, Jean-Martin Charcot was the first to name the condition "Parkinson's disease", rejecting the previous term "paralysis agitans" because not all patients experienced tremors [11, 12].

A crucial breakthrough came in 1893 when Paul Blocq and Georges Marinesco discovered a brain tumor in the SN of a patient with Parkinsonian tremor. This led Edouard Brissaud, a student of Jean-Martin Charcot, to hypothesize in 1895 [13] that the Substantia Nigra pars compacta (SNpc), one of the two divisions into which the SN is divided, was the primary pathological site of PD, an idea later confirmed by Constantin Trétiakoff in 1919 [14].

Nowadays, PD is recognized to be characterized by the cell death of the dopamine-producing neurons, called dopaminergic neurons, located in the SNpc of the midbrain, which is a small region located at the basis of the mesencephalon. This brain region appears darker than neighboring areas due to high levels of neuromelanin produced by these dopaminergic neurons, as shown in Figure 1.3a. However, in the case of a parkinsonian patient (Figure 1.3b), the loss of dopaminergic neurons leads to a loss of neuromelanin so that the SNpc loses its characteristic dark color.

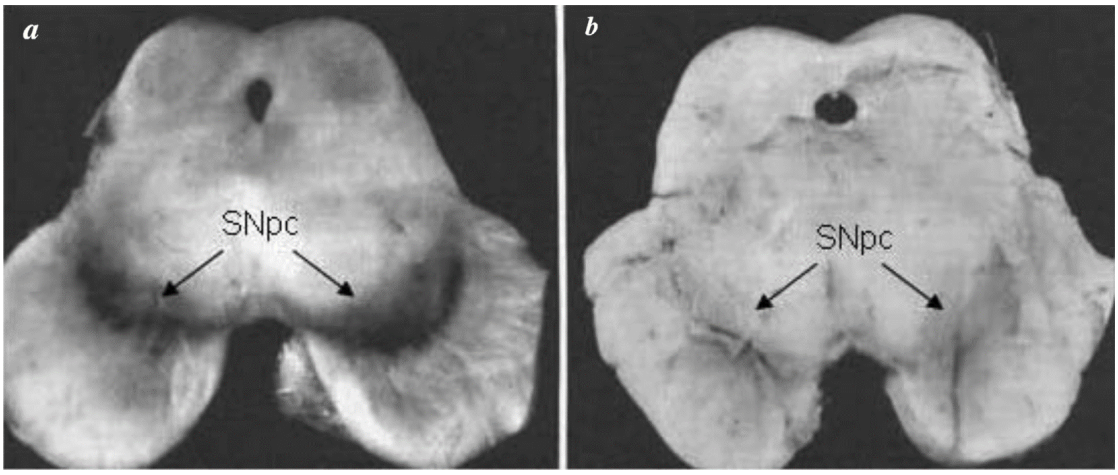

Figure 1.3: Human postmortem midbrain of ***a***) normal and ***b***) Parkinsonian subjects, respectively. Figure reproduced from [15].

As dopaminergic neurons have high energy demands and the mitochondrion has a particularly important role as the cellular "powerhouse", evidence indicates that mitochondria play a crucial role in their degeneration.

In addition to neuronal loss, PD is marked by the abnormal aggregation, or clumping, of an intracellular protein called α-synuclein (α-syn) [16] in the cytoplasm of certain neurons in several different brain regions (not only in the SNpc), forming what are now known as "Lewy bodies". This was first observed in 1912 by Frederic Lewy [17] and later confirmed in 1938.

While most cases of PD are sporadic, approximately 10 to 15% report a family history [18]. An individual's risk of PD is partially the product of as-yet poorly defined polygenic risk factors.

A link between PD and viral influenza infection gained attention following the 1918 influenza pandemic. In the years that followed, a new form of PD known as "postencephalitic Parkinsonism" emerged. Neurologist Constantin von Economo documented alarming numbers of cases presenting with PD symptoms [19], suggesting a connection between viral

infections and neurodegeneration. Decades later, researchers David Poskanzer and Robert Schwab revisited this hypothesis, proposing that PD was triggered by influenza infections and predicting its eventual disappearance [20]. While their prediction did not materialize, the idea that viral infections may contribute to PD remains an area of active research today.

Another major discovery in the history of PD came in the 1980s with the unexpected identification of 1-methyl-4-phenyl-1,2,3,6-tetrahydropyridine (MPTP) as a neurotoxic compound selectively targeting the SNpc. This discovery arose from a tragic case involving seven young adults that developed severe and irreversible PD shortly after they injected themselves with a new synthetic heroin. Investigators traced the cause to MPTP [21], a chemical byproduct that selectively destroys dopaminergic neurons, offering a crucial experimental model for understanding the disease and developing neuroprotective strategies.

While PD was initially thought to be purely a motor disorder, further research has revealed a range of non-motor symptoms, including cognitive decline, depression, gastrointestinal and genitourinary disturbances, as well as sleep abnormalities. Despite extensive research, there is currently no cure for PD and patients are offered just symptomatic-only treatments, aimed at managing the disease's effects rather than stopping its progression.

While our understanding of the disease has come a long way, the pursuit of effective treatments and preventive strategies remains an urgent scientific challenge.

1.3 Current Symptomatic Treatments

1.3.1 Pharmacological

After the discovery that PD was characterized by the cell death of dopaminergic neurons, Arvid Carlsson identified in 1957 that dopamine (at that time referred to as 3-hydroxytyramine) itself acted as an independent neurotransmitter, playing a crucial role in neurotransmission [22]. It led to the knowledge that dopamine is not only produced by dopaminergic neurons but also released to communicate with other neurons through synapses. Dopamine plays then an important role in motor control, motivation, reward and cognition.

Carlsson performed some experiments on reserpine, a naturally occurring substance that depletes dopamine, and induced a loss of movement control similar to the clinical PD symptoms. However, dopamine itself cannot cross the Blood-Brain Barrier (BBB), making it ineffective as a direct treatment.

Nevertheless, Carlsson demonstrated that levodopa (L-DOPA), a precursor of dopamine, crosses the BBB and is then converted into dopamine in the brain, effectively treating these symptoms [23]. For this groundbreaking work, Carlsson was awarded the Nobel Prize in 2000 [24].

The first large-scale clinical trials with L-DOPA, notably by Cotzias and colleagues in 1967-1968 [25], demonstrated dramatic symptom improvement in PD patients through oral administration of L-DOPA, which replaces dopamine levels depleted in the striatum. Although effective, prolonged L-DOPA treatment may cause motor complications, including dyskinesias (uncontrolled and involuntary movements) and severe "on/off" motor fluctuations. A difficult balance must be found between optimizing the control of the motor symptoms, while minimizing the adverse effects.

Dopaminergic agonists are also used to compensate for dopamine deficits by mimicking its action. They stimulate dopamine receptors on post-synaptic neurons, with a more moderate effect on motor function compared to dopamine itself. Agonists have a slightly broader action than L-DOPA and may have an effect on certain non-motor symptoms, such as depression.

There are as many dopaminergic agonists as dopamine receptors, each with its specific benefits. They are generally prescribed as a first-line treatment, especially if the patient is under 65 years old. Medication treatment for PD almost always combines L-DOPA and dopaminergic agonists. Dopaminergic agonists cause fewer dyskinesias than L-DOPA. However, they can lead to other side effects, particularly behavioral changes.

In patients that have previously responded well to L-DOPA, but have developed problematic dyskinesias (affecting around 85% after 10–15 years of treatment), Deep Brain Stimulation (DBS) may be considered, which may allow for the control of motor symptoms on a reduced dose of L-DOPA.

1.3.2 Deep Brain Stimulation (DBS)

DBS is a neurosurgical treatment and its procedure involves placing electrodes on a specific brain region to stimulate it electrically. This technique has been applied to three different targets: the Ventral intermediate nucleus of the thalamus (Vim), the Globus Pallidus pars interna (GPi) and the Subthalamic Nucleus (STN) [26].

In 1987, Benabid and colleagues [27] reported reversible suppression of tremor when electrical stimulation was firstly applied to the Vim. This led to the DBS being approved by the Food and Drug Administration (FDA) for controlling PD tremor and Essential Tremor

(ET). Howewer, this stimulation was ineffective on treating bradykinesia.

Thus, in 1990s the surgical target of interest moved to the STN and GPi. Electrical stimulation in these regions alleviated effectively parkinsonian tremor and, in addition, improved all other motor features of PD. The magnitude of the motor improvement seemed more constant when stimulating the STN than the GPi so STN DBS therapy for PD was approved by the FDA in 2003. Figure 1.4 shows the surgical implantation of stimulation electrodes into the STN.

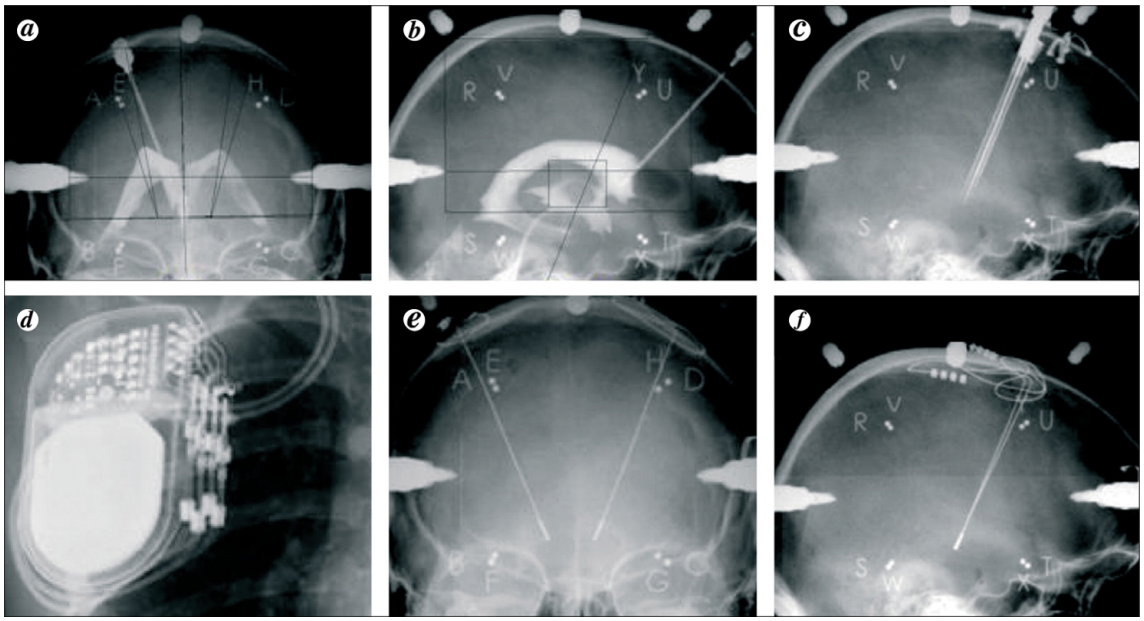

Figure 1.4: Surgical implantation of stimulation electrodes into the STN in advanced PD. ***a, b***) Pretargeting of the STN by stereotactic contrast ventriculography. ***c***) Pretargeting with stereotactic ventriculography and MRI, by use of a microdrive with five parallel microelectrodes, providing the ultimate functional signature of the STN target. ***d***) The implantable programmable generator, located in the right subclavicular area. ***e, f***) Post-operative imaging of the permanent electrodes, showing that they are mainly symmetrical. Figure reproduced from [28].

DBS is a reversible and adjustable method, since the electrical parameters are adjusted as the patient's disease progresses. In contrast, patient eligibility for DBS is substantially lower (around 1.6–4.5% of patients) than for pharmacological treatment with L-DOPA. DBS is reserved exclusively for those who have initially responded well to L-DOPA but subsequently developed motor complications, while also meeting additional stringent criteria such as age under 70 years and absence of dementia or psychiatric disorders.

1.3.3 Lesioning Procedures

Lesioning Surgeries (LS) involve selective destruction of a targeted brain tissue volume in order to interrupt maladaptive neural networks [29]. Although LS have been performed for several decades in selected patients with PD, their use decreased in the 1960s after the introduction of L-DOPA and then again in the 1990s because of DBS.

The field of LS has since grown and currently available techniques include thermoablation based on Radiofrequency (RF) and Focused Ultrasound (FUS), and Stereotactic Radiosurgery (SRS), all of them being used to treat motor symptoms without affecting disease progression.

Similar to DBS, RF thermoablation includes neuroimaging, a stereotactic headframe and placement of an electrode intracranially coupled to an RF generator [29]. The procedure is performed while the patient is awake, allowing for test simulation to confirm the target. Once verified, alternating current is applied to the electrode's tip creating a thermally induced lesion. After the lesioning is complete, the electrode is retracted. This technique produces well-defined lesion boundaries with immediate results, allowing real-time assessment of symptom improvement during surgery. Temporal adverse effects such as visual field deficits, muscular weakness and neuropsychological deficits may occur. The surgical risk associated also includes hemorrhage and infection.

FUS performs thermal ablation utilizing high-intensity focused ultrasound beams targeted to an intracranial region (for tremor, it is the thalamus and for other motor symptoms and dyskinesia, it is the GPi). Accurate and real-time monitoring of the lesion are currently possible with MR-guided FUS (MRgFUS), using MRI-guidance and MR-thermography [30]. However, the effectiveness of the lesion depends on the skull thickness.

SRS lesioning involves delivering a single high dose of ionizing radiation noninvasively to a confined intracranial target volume using computerized dosimetry planning and image-guided stereotaxy [29]. Drawbacks of SRS include the absence of intraoperative feedback, variability in lesion size, poorly defined lesion borders, exposure to ionizing radiation and a delayed therapeutic effect.

1.4 Exploratory Therapeutic Treatments

All the techniques explained in the previous section address only the symptoms of the disease but do not slow its progression. To find a possible cure for PD, various techniques are being investigated. This section will describe each of them.

1.4.1 Cell Therapy

A variety of cell-based exploratory treatments are emerging as promising strategies aiming to inject new dopamine cells into the brain to replace those that are lost or dying [31].

Among them, Embryonic Stem Cells (ESCs) are studied, which are harvested from the early stages of embryonic development. They can differentiate into any type of cell, even the dopaminergic neurons giving rise to Embryonic Stem Cells-derived Dopamine Progenitor cells (ESC-DAPs), which are so important in the PD progression. Studies have shown that the loss of neurons and motor function could be recovered with the transplantation of ESCs. However, there are significant risks of tumor formation after ESCs transplantation and the immune system of the organism may reject them because they would be recognized as foreign intruders.

Fetal Ventral Mesencephalon tissue (VM) is a rich source of dopaminergic neurons derived from fetuses, which is also being studied. Without going through the difficult differentiation steps required for other cell types, this direct neuronal transplantation immediately replaces dopamine.

These two cell-based therapies raises ethical issues due to the use of embryonic cells, that is why researchers are still looking for other cell-based therapies.

A possible option would be the Neural Stem Cells (NSCs) and Neural Progenitor Cells (NPCs) which exist in both embryonic and adult states, potentially alleviating ethical concerns. NSCs are more primitive and undifferentiated, enabling them to generate all cell types existing in the brain, whereas NPCs are more committed to a cell lineage and therefore have a more restrictive potential.

Another type of cell capable of differentiating into dopaminergic neurons are the induced Pluripotent Stem Cells (iPSCs), giving rise to induced Pluripotent Stem Cells-derived Dopamine Progenitor cells (iPSC-DAPs). Although they are emerging as a promising cell-therapy for PD, possible contamination of implanted cells by undifferentiated cells, along with genetic abnormalities inherited from the donor tissue or acquired during *in-vitro* proliferation remain important concerns. iPSCs can be donated by someone other than the patient, called *allogeneic* transplant, but they may also come from patient, *autologous* transplant, thereby reducing the risk of immune rejection. Thus, the treatment could be based on the parkinsonian patient's own cells.

There is particular attention to the Mesenchymal Stem Cells (MSCs) which can also be reprogrammed into dopaminergic neurons. Beyond its therapeutic potential, they can be extracted from a diversity of tissues: from neonatal tissues including human umbilical

cordon (HUC-MSCs) but also from adult tissues such as adipose tissue (A-MSCs), dental pulp, bone marrow (bm-MSCs) and olfactory mucosa, among others.

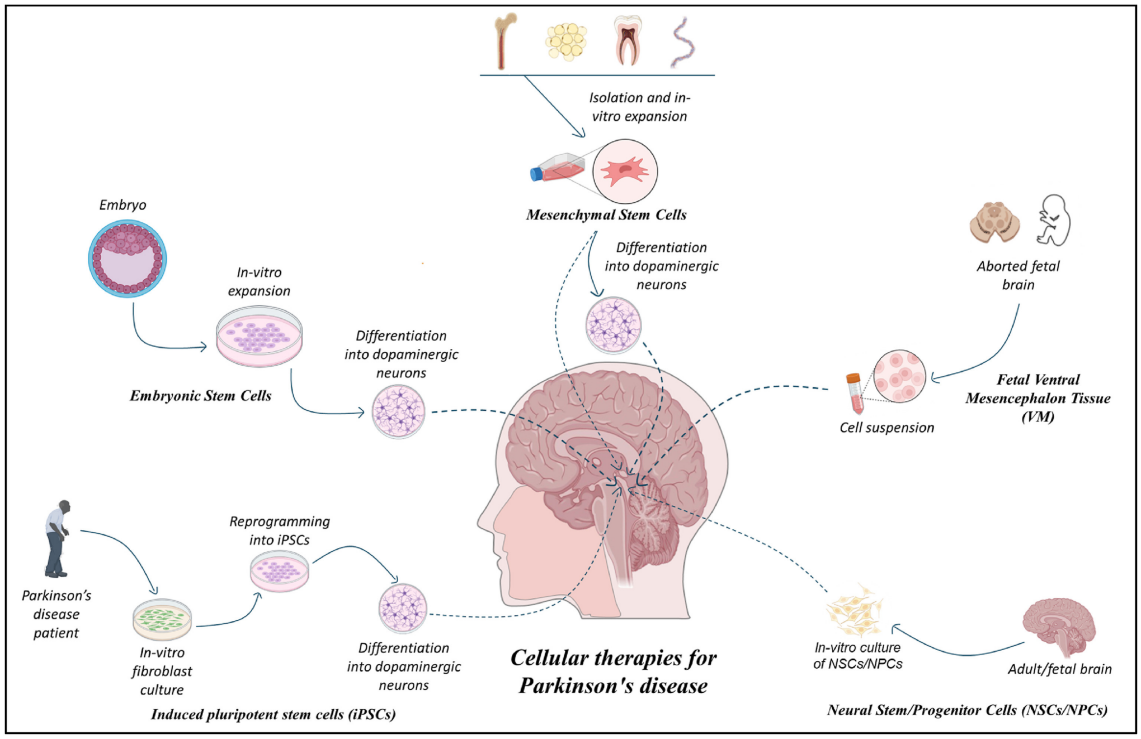

Figure 1.5: Exploratory cell-based therapies for PD. Figure reproduced from [31].

All these cells, illustrated in Figure 1.5, may be directly implanted into the brain. However, some particular cells including MSCs show a strong ability to migrate to sites of injured tissue and inflammation. This migratory competence may allow its administration through many routes, for example intracerebral, intravenous and intranasal.

The ongoing clinical trials based on cell therapies are shown in Table 1.1.

Cell Type	Route of Administration	Collaborators	Patients	Duration	ID
ESC-DAPs Allogeneic	Intracerebral implantation	S.Biomedics Co., Ltd. and Severance Hospital	12	Sep 2023 / Jun 2029	NCT06477744
iPSC-DAPs Autologous	Intracerebral implantation	Shanghai East Hospital	3	Nov 2023 / Dec 2025	NCT06145711
		Aspen Neuroscience and California Institute for Regenerative Medicine (CIRM)	9	Jan 2024 / Apr 2030	NCT06344026
		McLean Hospital, National Institute of Neurological Disorders and Stroke (NINDS) and Oryon Cell Therapies	6	Aug 2024 / Dec 2027	NCT06422208
		Massachusetts General Hospital	8	Dec 2024 / Dec 2028	NCT06687837
		Shanghai UniXell Biotechnology Co., Ltd and Ruijin Hospital	12	Feb 2025 / Dec 2027	NCT06778265

		iCamuno Biotherapeutics Ltd. and The Second Affiliated Hospital Zhejiang University School of Medicine	12	May 2025 / Sept 2026	NCT06821529
iPSC-DAPs Allogeneic	Intracerebral implantation	University of California, Sumitomo Pharma America, Inc., Kyoto University, Sumitomo Pharma Co., Ltd. and CiRA Foundation	7	June 2024 / May 2028	NCT06482268
		iRegene Therapeutics Co., Ltd.	6	Aug 2024 / Mar 2027	NCT06608355
		Anhui Provincial Hospital	12	Oct 2024 / Oct 2028	NCT06583291
		Sumitomo Pharma America, Inc.	23	Dec 2024 / Mar 2029	NCT06753331
HUC-MSCs Allogeneic	Nasal drops	Xuanwu Hospital	100	Nov 2024 / Aug 2028	NCT06607900

A-MSCs Allogeneic	Intravenous injections	ClusterXStem-Costa Rica, Universidad de Costa Rica and University of California	40	Jun 2023 / Nov 2024	NCT06141317

Table 1.1: Clinical trials using cell-based therapies for the treatment of PD.

1.4.2 Gene Therapy

Gene therapy aims to replace "bad deoxyribonucleic acid (DNA) with good DNA" via viral vectors, which are vehicles used to deliver therapeutic genetic material (DNA in that case) into cells [32]. Viral vectors are derived from viruses since they are capable of getting into cells. The viral genes have been previously removed, so only the therapeutic genes are delivered.

Gene therapy approaches broadly fall into two categories: those aimed at modulating or correcting specific genetic mutations associated with PD, and those designed to induce expression of neuroprotective factors to support and preserve dopaminergic neurons.

1.4.2.1 For Modulating Mutations

PD has been linked to mutations in various genes, collectively named "PARK" genes in the order of their discovery. To date, 23 PARK genes have been associated with the disorder [32, 33]. These genes exhibit either dominant or recessive inheritance patterns. Autosomal dominant genes require only one mutated copy (from either parent) to cause this neurological disorder, with a 50% chance of transmission to offspring. In contrast, autosomal recessive genes require two mutated copies (one from each parent) for the disease to manifest, with parents typically being asymptomatic carriers and offspring having a 25% chance of developing PD if both parents are carriers.

One of the first identified PD-related genes was *SNCA* (PARK1/PARK4), responsible for autosomal dominant PD. This gene encodes the α-syn protein, which can misfold and form fibrillar aggregates, leading to the formation of Lewy bodies, as mentioned in section 1.2, and associated with PD. High concentrations of wild-type α-syn are lethal to neurons.

Mutations in another gene known as the *LRRK2* gene (PARK8) also cause autosomal

dominant PD. The protein encoded by *LRRK2* regulates multiple intracellular signaling pathways, including those related to mitochondrial function. Mutant *LRRK2* proteins often promote pathological changes such as neuroinflammation, impaired autophagy (a natural cellular process in which a cell degrades and recycles its own damaged, dysfunctional, or unnecessary components), and neuronal death. *LRRK2* also influences the accumulation of α-syn and microglial cell (the brain's resident immune cells that sustain neural health, defend against pathogens, and help repair damage) activation, contributing to disease progression.

Mutations in the PARK2 gene, which encodes the Parkin protein, are the most common cause of autosomal recessive PD. Parkin protein is essential for mitochondrial quality control. It functions by tagging damaged mitochondria, helping to remove dysfunctional mitochondria, protecting neurons from damage and maintaining cellular health.

Another recessive gene linked to PD is *PINK1* (PARK6), which encodes a protein that acts as a sensor for mitochondrial damage. When mitochondria become dysfunctional, PINK1 accumulates on their surface and recruits Parkin to initiate mitophagy (autophagy, the cellular "self-eating" process, but specialized for mitochondria). Mutations in PINK1 impair this damage-sensing and signaling mechanism, leading to the accumulation of defective mitochondria. This failure promotes apoptosis (programmed cell death) instead of controlled mitochondrial clearance, contributing to neuron loss in PD.

A rarer recessive mutation associated with PD is found in *DJ1* (PARK7). Its encoded protein functions as an antioxidant within mitochondria, especially in the SN. Mutations impair this protective role, leading to increased neuronal susceptibility to oxidative stress and damage.

Mutations in *GBA1* gene are also recognized as an important risk factor for PD, but it does not necessarily follow a strict inherited pattern. These mutations reduce glucocerebrosidase (GCase) activity, leading to the toxic accumulation of α-syn aggregates in the CNS. Because α-syn pathology may be reversible in early stages, therapies that enhance GCase function may have potential as disease-modifying treatments.

Table 1.2 summarizes the different genes involved in PD development.

Gene	Inheritance Pattern	Role
SNCA (PARK1/PARK4)	Dominant	Encodes α-syn protein, leading to the formation of Lewy bodies.
LRRK2 (PARK8)	Dominant	Encodes a protein involved in intracellular signaling; mutations promote neuroinflammation and impaired autophagy.
PARK2	Recessive	Encodes Parkin protein, critical for marking damaged mitochondria for clearance.
PINK1 (PARK6)	Recessive	Encodes a mitochondrial protein that senses mitochondrial damage and recruits Parkin for mitophagy.
DJ1 (PARK7)	Recessive	Encodes an antioxidant protein protecting neurons from oxidative stress.
GBA1	/	Encodes GCase; mutations cause toxic α-syn accumulation.

Table 1.2: Summary of genes implicated in the development of PD.

1.4.2.2 For Neuroprotection

Neurotrophic factors are a group of proteins or peptides that support the growth, survival, maintenance, and differentiation of neurons during development and throughout adulthood. In particular, *GDNF* and *NRTN* promote the survival and regeneration of dopaminergic neurons [34]. Therapeutic approaches aim to deliver *GDNF* or *NRTN* directly into the brain, often using viral vectors or implantable drug delivery systems, because they cannot cross the BBB efficiently.

Table 1.3 summarises current clinical trials evaluating gene-based therapies targeting mutation modulation and neuroprotection.

Gene target	Route of Administration	Collaborators	Patients	Duration	ID
LRRK2	Orally	Neuron23 Inc.	150	Jan 2025 / Sep 2027	NCT06680830

GDNF	Intracerebral implantation	North Bristol NHS Trust	42	Oct. 2012 / Apr. 2016	NCT03652363
		National Institute of Neurological Disorders and Stroke (NINDS)	25	Mar. 2013 / Feb. 2022	NCT01621581
		Brain Neurotherapy Bio, Inc., AskBio Inc. and California Institute for Regenerative Medicine (CIRM)	11	Apr. 2020 / June 2027	NCT04167540
		AskBio Inc. and Bayer	87	June 2024 / Nov. 2027	NCT06285643
NRTN	Intracerebral implantation	Sangamo Therapeutics	57	Oct. 2009 / Sep. 2014	NCT00985517

Table 1.3: Clinical trials using gene therapies for the treatment of PD.

1.4.3 Non-Drug Approaches

The BBB is a highly selective, semi-permeable membrane that protects the brain from harmful substances while allowing essential nutrients to pass through. When neuroprotective drugs are orally taken, they cannot efficiently reach the brain because of this barrier. A promising non-invasive approach to overcoming the BBB is FUS combined with microbubbles [35].

Microbubbles are filled with a high molecular weight gas and coated with a thin film, which are then injected peripherally into the bloodstream. Low-intensity focused ultrasound waves are applied to a specific brain region, which has been previously identified via MRI, using a helmet-like system.

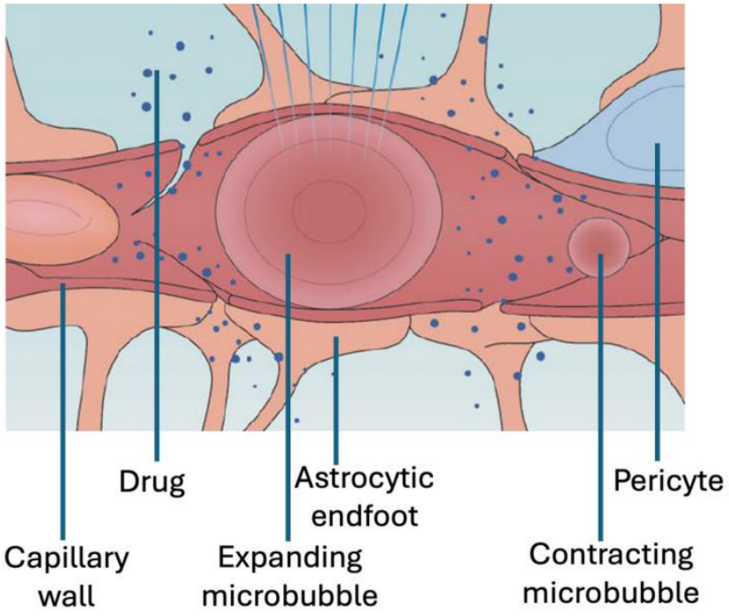

Figure 1.6: Principle of the mechanism of FUS combined with microbubbles for opening the BBB. Figure reproduced from [35].

These waves cause the microbubbles to oscillate through a process called acoustic cavitation, producing mechanical forces that temporarily disrupt the tight junctions of the BBB, as illustrated in Figure 1.6. This transient opening allows therapeutic molecules to enter the CNS. This method is gaining traction not only in exploratory studies for the treatment of PD but also AD and brain tumors.

It is a reversible technique since the BBB re-seals itself within a few hours to a day, reducing the risk of unwanted substances entering the brain.

Other non-invasive techniques currently explored for the treatment of PD are transcranial Direct Current Stimulation (tDCS), repetitive Transcranial Magnetic Stimulation (rTMS) and Theta Burst Stimulation (TBS), which are gaining interest as potential neuromodulatory methods [36]. Like FUS these methods do not require surgical intervention and can modulate brain activity in a targeted manner.

tDCS works by applying low-amplitude direct currents via scalp electrodes, which penetrate the skull. Although part of the current is diverted through the scalp, computational models have demonstrated that a sufficient current reaches the brain, modifying the cortical excitability (the ease with which neurons in the cerebral cortex can be activated), also beyond the stimulation period. In contrast, rTMS utilizes electromagnetic induction to generate currents in the brain. While single-pulse TMS can transiently depolarize neurons, rTMS (where pulses are delivered repetitively) can modulate cortical excitability, either

increasing or decreasing it based on the stimulation parameters. Theta Burst Stimulation (TBS) is emerging as a new form of patterned rTMS treatment mimicking natural brain communication, that is less time-consuming and more effective than traditional rTMS.

These techniques are being investigated for their ability to alleviate motor and cognitive dysfunctions associated with PD by directly targeting cortical circuits, as PD is also characterized by widespread cortical dysfunction.

Emerging research suggests a strong connection between the gut and the brain in PD, reinforcing the gut-brain hypothesis. Studies have shown that many patients experience gastrointestinal symptoms, such as constipation, years before motor symptoms appear. This has led researchers to explore whether disruptions in the gut microbiome contribute to PD pathophysiology and it has been observed that α-syn aggregates are present in the gastrointestinal system during the prodromal phase of the disease. α-syn can then propagate from the intestines to the brain via the vagus nerve. This pathway supports the idea that PD may originate, at least in part, in the gut before affecting the CNS.

Given the growing evidence of gut involvement in PD, Fecal Microbiota Transplantation (FMT) has emerged as a potential therapeutic strategy [37]. FMT involves transferring gut microbiota from a healthy donor to a patient, aiming to restore a balanced microbial ecosystem. Preliminary studies suggest that FMT may improve gastrointestinal function, reduce neuroinflammation and potentially slow disease progression by modulating the gut microbiome. Although still in experimental stages, this approach offers a promising avenue for addressing both the gastrointestinal and neurological aspects of PD, highlighting the importance of the microbiome in neurodegenerative diseases.

The exploratory clinical trials currently being conducted using these techniques are listed in Table 1.4.

Non-Drug Approach	Collaborators	Patients	Duration	ID
FUS	InSightec	7	Sep. 2014 / Dec. 2013	NCT02246374
	InSightec	20	Apr. 2015 / Jul. 2019	NCT02263885
	InSightec	10	Nov. 2018 / Dec. 2021	NCT03608553
	InSightec	10	May 2019 / Jul. 2022	NCT04744493

	Xinhua Hospital, Shanghai Jiao Tong University School of Medicine	20	Oct. 2024 / Oct. 2025	NCT06639945
	Spaulding Rehabilitation Hospital	14	Dec. 2024 / Oct. 2026	NCT06676995
	Assiut University	68	Feb. 2025 / Mar. 2026	NCT06701318
	Ali Rezai	15	Dec. 2025 / Mar. 2028	NCT06763692
tDCS + rTMS	Samsung Medical Center	32	Sep. 2013 / Nov. 2015	NCT02850159
	Amsterdam UMC	20	May 2024 / May 2026	NCT06399731
TBS	Ruijin Hospital	60	Sep. 2023 / Jun. 2025	NCT06193278
FMT	Soroka University Medical Center	10	Aug. 2015 / Jun. 2020	NCT03876327
	Univeristy Ghent, University Hospital Ghent, the Flanders Institute for Biotechnology Research Foundation Flanders, Vlaamse Parkinson Liga and Parkili	49	Dec. 2020 / Dec. 2022	NCT03808389
	Helsinki University Central Hospital	51	Apr. 2021 / Jun. 2023	NCT04854291
	Guangzhou First People's Hospital	30	May 2021 / Dec. 2025	NCT04837313
	Medical University of Warsaw and Human Biome Institute S.A.	60	Nov. 2021 / Dec. 2024	NCT05204641

	Shanghai Zhongshan Hospital	76	Jun. 2024 / May 2026	NCT06388863
	ProgenaBiome	20	Oct. 2024 / Dec. 2026	NCT06647277

Table 1.4: Summary of clinical trials based on non-drug approaches for the treatment of PD.

1.4.4 Drug Approaches

Several innovative drug treatments are currently being evaluated for PD, complementing traditional approaches.

One such treatment under investigation is lixisenatide, a drug originally developed for type 2 diabetes. It belongs to a class of medications known as glucagon-like peptide-1 receptor (GLP-1R) agonists, which mimic the action of a natural intestinal hormone released during meals. While GLP-1R agonists are clinically approved for diabetes treatment, GLP-1 receptors are also present in the brain. Their exact role in neurological function remains unclear, but they are believed to be involved in mechanisms affecting neuronal survival and degeneration. Notably, epidemiological studies suggest a link between type 2 diabetes and PD, with diabetic patients having a higher risk of developing this neurological disorder and experiencing a faster progression of symptoms. Interestingly, individuals treated with GLP-1R agonists show a lower risk of developing PD compared to those receiving other antidiabetic medications. Additionally, post-mortem studies have revealed molecular abnormalities related to insulin resistance in the neurons of PD patients [38].

Another promising candidate is ambroxol, a metabolite of bromhexine that has been used for over 30 years as a mucolytic, with an excellent safety profile and minimal side effects. Ambroxol is of particular interest in Parkinson's research due to its potential to enhance the activity of glucocerebrosidase (GCase), a lysosomal enzyme encoded by the *GBA1* gene (already mentioned in section 1.4.2.1). *GBA1* mutations reduce the enzymatic function of GCase, ultimately promoting the toxic accumulation of α-syn fibrils throughout the CNS. The toxic conversion of physiological α-syn conformers should be reversible at a stage prior to incorporation into fibrils. Therefore, the use of agents able to enhance GCase activity might hold a therapeutic potential. The investigators hypothesize that the greatest impact of ambroxol as a disease-modifying agent will be on cognitive performance [39].

A more direct approach under investigation involves the intracerebroventricular administration of anaerobic dopamine (A-dopamine), a form of dopamine prepared and administered under oxygen-free conditions to prevent oxidation. Since dopamine cannot cross the BBB

and is rapidly oxidized, conventional treatments struggle to replenish dopamine levels in the brain efficiently. This new strategy, illustrated in Figure 1.7, involves delivering A-dopamine directly into the brain via an abdominal pump connected to a subcutaneous catheter implanted in the third ventricle, near the striatum. This method aims to bypass systemic limitations and provide a continuous, localized supply of dopamine to the affected brain regions, potentially offering a more effective way to manage motor symptoms in PD [40].

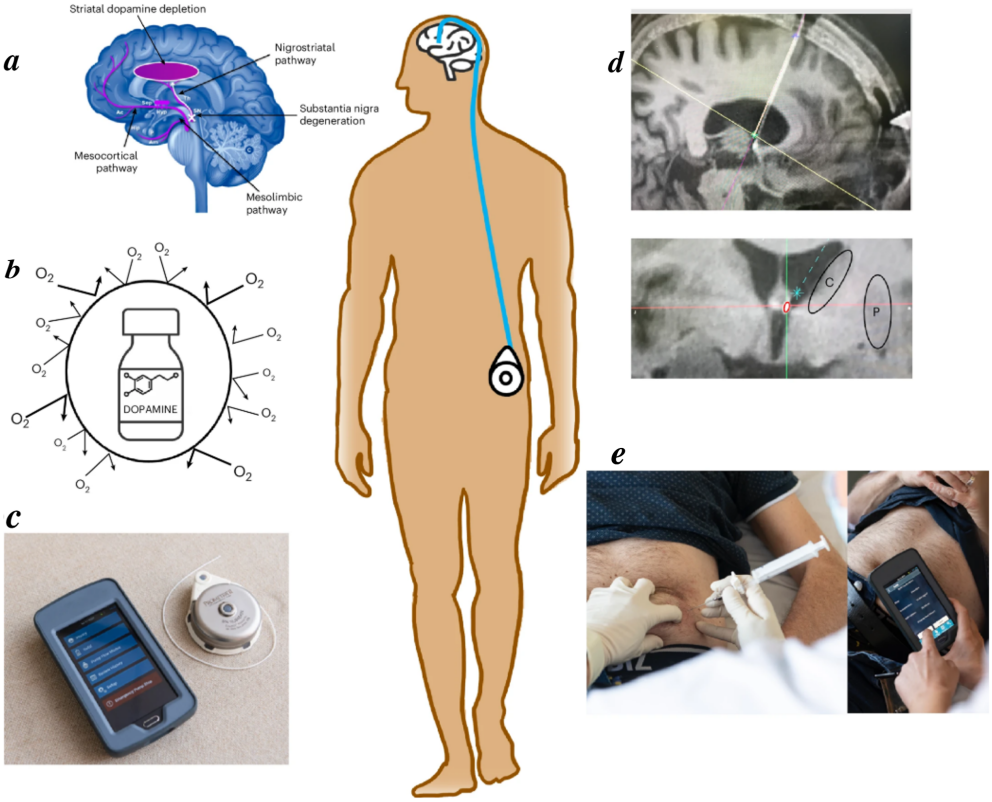

Figure 1.7: ***a***) The degeneration of dopaminergic neurons in the SNpc leads to dopamine depletion in the striatum. ***b***) The preparation, storage and delivery of dopamine occurs under anaerobic conditions to avoid rapid dopamine oxidation. ***c***) Delivery takes place via a commercially available pump (Prometra Flowonix). ***d***) Neurosurgical targeting (red oval) allowing the perfusion of A-dopamine right next to the striatum (C, caudate nucleus; P, putamen). ***e***) Transcutaneous filling of the abdominal pump every 7–15 days under local anesthesia and then adjustment by telemetry of hourly and circadian doses (day and night). Figures reproduced from [40].

These new strategies are being studied in the clinical trials listed in Table 1.5.

Drug Approach	Collaborators	Patients	Duration	ID
Lixisenatide	University Hospital of Toulouse, Cure Parkinson's, Réseau NS-Park, EUCLID Clinical Trial Platform and Sanofi	156	June 2018 / Apr. 2021	NCT03439943
Ambroxol	Fondazione IRCCS Istituto Neurologico Carlo Besta, IRCCS National Neurological Institute "C. Mondino" Foundation and University of Campania Luigi Vanvitelli	65	Feb. 2022 / Dec. 2024	NCT05287503
A-dopamine	University Hospital of Lille and InBrain Pharma	12	Sep. 2020 / May 2024	NCT04332276

Table 1.5: Summary of clinical trials based on non-drug approaches for the treatment of PD.

1.4.5 Photobiomodulation (PBM) for Parkinson's Disease (PD)

The use of light for medical applications dates back centuries. Firstly, in 1895, Niels Ryberg Finsen pioneered the use of ultraviolet light to treat lupus vulgaris (a form of tuberculosis that attacks the skin) [41], an innovative approach that earned him the Nobel Prize in 1903. Decades later, in 1968, Endre Mester performed experiments on shaved mice with malignant tumors, exposing them to red laser light (694 nm) [42]. The aim was to reproduce the experiments previously described by Paul E. McGuff [43]. Unfortunately, or perhaps fortunately, Mester's laser had less power so he was unable to cure any tumors. Instead, he observed accelerated hair growth in the treated mice compared to the controls. Further studies by Mester's team, published in 1971, demonstrated enhanced wound healing using HeNe lasers (633 nm) [44]. Subsequent in vitro experiments confirmed that

Red-to-Near-Infrared (R-NIR) light could stimulate cell proliferation. By the 1990s, CO_2 lasers emitting infrared light became a well-established method of skin photorejuvenation, a technique emerged with Thomas L. Roberts [45].

All of the above cases fall under Low-Level Laser Therapy (LLLT), since the light sources used are lasers. However, this term is now outdated as Light Emitting Diodes (LEDs) are emerging as effective alternatives. In the early 1990s, National Aeronautics and Space Administration (NASA) developed near-monochromatic LEDs for plant growth experiments in space. These LEDs, emitting red (680 nm, 730 nm) and NIR (880 nm) light, were later found to enhance cellular proliferation and improve wound healing in astronauts [46]. This discovery underscored the versatility and therapeutic potential of LEDs in light-based therapies.

The current term that encompasses all forms of light therapy, inducing beneficial cellular responses through non-ablative R-NIR, is Photobiomodulation (PBM).These wavelengths penetrate tissues and are absorbed by specific photoacceptor molecules, called chromophores.

The most studied photoacceptor is cytochrome c oxidase (CcO), a key enzyme in the mitochondrial respiratory chain, playing a crucial role in cellular energy production by reducing oxygen to water using the electrons generated from glucose metabolism. CcO contains two heme centers (heme-*a*, heme-*a3*), components of hemoglobin and other proteins that serve as oxygen-binding sites; and two copper centers (Cu_A, Cu_B), which assist in electron transfer. The absorbance spectrum of CcO, in both oxydized and reduced states, is shown in Figure 1.8.

The aim of studying oxidized and reduced CcO is to understand how the enzyme functions in cellular respiration, as CcO continuously cycles between oxidized and reduced states during this process.

The following features are observed:

- In the visible region, the oxidized enzyme has main absorption peaks at 423 and 598 nm, whereas the reduced enzyme peaks shift to 443 and 603 nm (Figure 1.8a). These absorption peaks correspond primarily to the heme centers.
- In the NIR region, the oxidized enzyme has a broad peak centered at 835 nm (Figure 1.8c), which is attributed to the CuA copper center.
- The oxidized enzyme also exhibits a distinct band at 655 nm (Figure 1.8b), asssigned to the ferric/cupric binuclear heme-*a3*-Cu_B center. This band is diminished upon reduction.

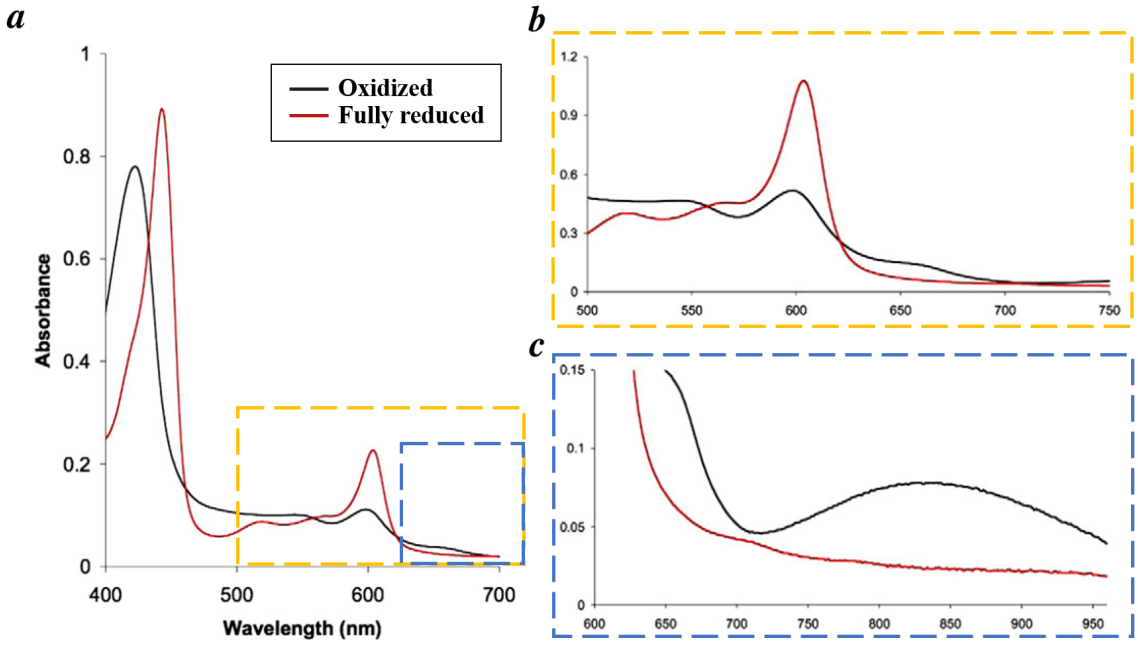

Figure 1.8: Absorbance spectra of oxidized (black) and fully reduced (red) CcO: ***a***) in the 400–700 nm range, ***b***) in the 500–750 nm range, and ***c***) in the 600–950 nm range. Figure adapted from [47].

Under certain physiological conditions, nitric oxide (NO) can bind to the heme and copper centers of CcO. This binding inhibits the enzyme's function, preventing oxygen from binding and reducing adenosine triphosphate (ATP) production. When R-NIR light is absorbed by CcO, photons excite electrons in the heme and copper sites, causing photochemical changes that dissociate NO. This enables oxygen to bind again, allowing the respiratory chain to function properly. It leads to increased ATP production and Reactive Oxygen Species (ROS) modulation [48, 49, 50]. Both ATP and ROS are by-products of mitochondrial respiration, but they serve very different roles. ATP is the main energy source for cells, whereas ROS molecules can have both beneficial and harmful effects: low to moderate ROS levels act as signaling molecules, regulating processes like cell proliferation, inflammation and repair, whereas excessive ROS levels cause oxidative stress, leading to cell death. Nevertheless, it should be noted that in a recent study using mouse and human cell lines lacking CcO, PBM increased ATP levels, indicating that there must be other photoacceptor(s) within the neurons [51].

Water within the mitochondria has been suggested to be one such "other" photoacceptor, specifically in the form of nanoscopic Interfacial Water Layers (IWL) found within the folded mitochondrial membranes. These layers, consisting of 2–3 monolayers of water molecules, tend to become viscous, which can impede ATP synthase (the enzyme that makes ATP) and ultimately lead to neuronal distress. Observational evidence suggests that

R-NIR photons, such as those at 670 nm (a wavelength for which bulk water is practically transparent), interact with these bound water layers. This interaction leads to a reduction in IWL viscosity and volume expansion, improving ATP synthase activity, increasing ATP production, and lowering ROS levels [52].

There is also evidence that chlorophyll metabolites may act as photoacceptors. The ability to convert sunlight into biological energy in the form of ATP is thought to be limited to photosynthetic organisms. However, the same potential to convert light into energy exists in mammals, as chlorophyll metabolites accumulate in mice, rats and swine when fed a chlorophyll-rich diet. The chlorophyll metabolites, when treated with PBM, can catalyze the reduction of coenzyme Q, leading subsequently to CcO activation and an increase in mitochondrial activity and ATP production [53].

The efficacy of PBM is influenced by wavelength, spatial coherence, polarity (the geometric orientation of the light wave with respect to the direction of travel), pulse structure, fluence (total energy), irradiance (energy density) and exposure frequency. And all of these factors contribute to the current debate about which light source is more efficient for PBM, lasers or LEDs, a topic extensively reviewed by Heiskanen and Hamblin [54]. Therefore, this huge variety of parameters have rendered PBM challenging to study through clinical trials.

The therapeutic window typically lies within the red to NIR spectrum (600 – 1000 nm) since:

- UV light (< 400 nm): can cause DNA damage and lead to cell death.
- Blue and green light (400 – 600 nm): are mostly absorbed by melanin and hemoglobin [55], limiting their ability to penetrate deep into tissues.
- Red (600 – 700 nm) and NIR (700 – 1000 nm) light: are absorbed by CcO, as shown in the absorbance spectra from Figure 1.8.
- Mid-infrared and far-infrared (> 1000 nm) light: are strongly absorbed by water molecules in tissues. This causes heat generation rather than photochemical effects, making it more useful for thermal treatments (e.g., CO_2 lasers for surgery) but not for PBM.

Notably, PBM follows a biphasic dose-response curve (Arndt-Schulz Law), where insufficient optical power has limited effects whereas excessive may result in bioinhibition [56]. For example, this phenomenon has been observed in wound healing studies (Figure 1.9), demonstrating that lower doses of PBM enhance tissue repair, whereas higher doses may reduce or even worsen the outcome. However, for PD, there are currently insufficient

preclinical or clinical trials to establish a definitive dose-response curve. Moreover, because the therapeutic goals differ, promoting tissue repair versus modulating neurodegenerative processes, the effective PBM doses may vary significantly between these applications.

In any case, discussing light dosage requires several radiometric concepts: optical power, the energy emitted per unit time (W); fluence, the energy density per unit surface area (J/cm^2); emittance (also called radiant exitance), the optical power density per unit surface area (W/cm^2); and radiance, the emittance per unit solid angle (W/(sr $\cdot$ cm^2)).

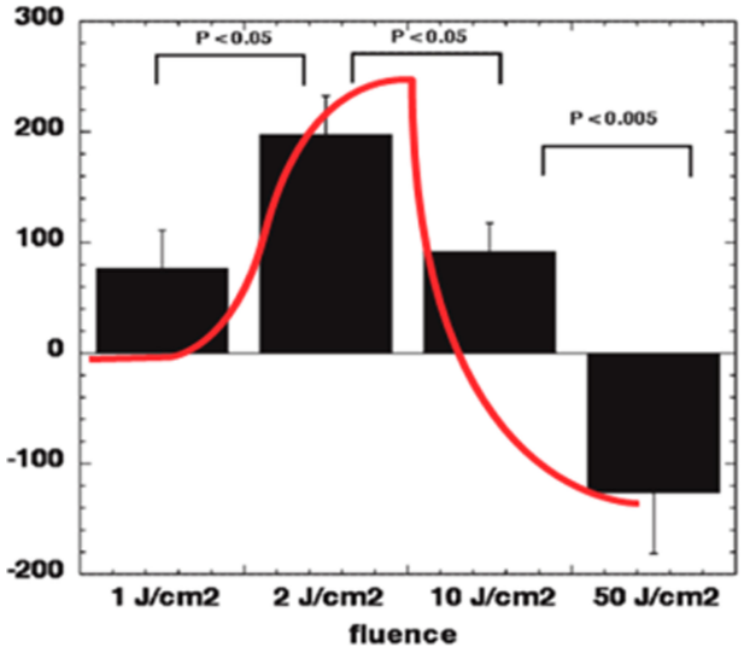

Figure 1.9: Biphasic dose response on wound healing. Figure reproduced from [57].

Since the early 2000s, research on PBM has been growing exponentially, and the range of potential health benefits is being compiled in this database [58]. However, this section will be focused on the application of PBM as a potential treatment for PD. The mechanism of action of PBM for PD remains unclear but it is related to the mitochondrial dysfunction, due to the CcO enzyme and the IWL, which have been previously described.

Over the past fifteen years, various animal models have been developed to study the neuroprotective effects of PBM in the treatment of PD [59]. Among the animal models studied are the *Drosophila* (fruit fly) with a mutation in the PINK1 gene, the transgenic mouse with a K369I (K3) mutation, the mouse injected with MPTP, the rat injected with another neurotoxin known as 6-hydroxydopamine (6-OHDA), the rat injected with lipopolysaccharide (LPS) (a component of a distinct group of bacterial cell walls which replicate neuroinflammation), the mouse overexpressing α-syn, and the non-human primate

injected with MPTP. Several studies have reported that PBM has no neurotoxic effects and that it provides neuroprotection by increasing the survival of dopaminergic neurons in the SNpc.

There are several ways to deliver light to the SNpc, as illustrated in Figure 1.10:

- Transcranially, where light is applied externally through the skull.
- Intracranially, where the light source is directly implanted inside the brain, near the SNpc.
- Intranasally, as the nasal cavity has a thin epithelial barrier and a rich vascular network, allowing light to penetrate into the brain.
- Via oral cavity, as the oral mucosa and soft tissues (such as the floor of the mouth) enable light to reach deeper brain regions.

However, intranasal illumination has limited penetration to midbrain structures, such as the SNpc, and illumination via oral cavity is also less efficient. Thus, for PD treatment based on PBM, preclinical and clinical trials will focus on transcranial and intracranial illumination.

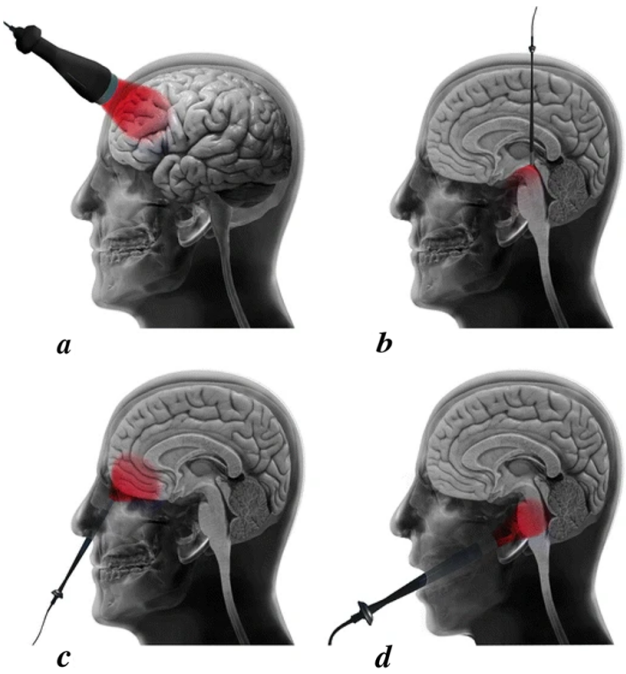

Figure 1.10: Different approaches for light delivery to achieve brain PBM therapy. ***a***) Transcranially, ***b***) intracranially, ***c***) intranasally and ***d***) via oral cavity. Figure reproduced from [60].

1.4.5.1 Transcranial Photobiomodulation (tPBM)

The preclinical trials conducted up to now investigating tPBM for PD are summarized in Table 1.6.

PD Model	**Study**	**Light Source**	**Treatment**
Drosophila PINK1 mutation	Vos et al., (2013) [61]	Laser, 808 nm	One single session of 100 s
MPTP mouse	Shaw et al., (2010) [62]	LED, 670 nm	4 sessions of 90 s over 30 h
	Peoples et al., (2012) [63]		2 groups: 4 sessions of 90 s over 30 h and 10 sessions of 90 s over 5 weeks
	Moro et al., (2013) [64]		4 sessions of 90s over 30 hours
	Johnstone et al., (2014) [65]		4 sessions of 90 s over 30 hours, repeated for 6 days
	Reinhart et al., (2016) [66]		2 sessions of 90 s per day, over 2, 4 or 6 days (3 groups)
	El Massri et al., (2016) [67]		1 session of 90 s per day, over 2, 4 or 8 days (3 groups)
	San Miguel et al., (2019) [68]		1 session of 3 min per day, over 7 days
	Reinhart et al., (2015) [69]	LED, 810 nm	4 sessions of 90 s over 30 h
	Reinhart et al., (2017) [70]	LED, 670 nm + 810 nm	2 sessions of 90 s per day, over 2 days
α-syn rat	Oueslati et al., (2015) [71]	Laser, 808 nm	1 session of 100 s per day, over 8 or 2 weeks (2 groups)

6-OHDA rat	Salgado et al., (2016) [72]	LED, 627 nm / Laser, 630 nm	1 session of 57 s per day for 7 days / 1 session of 88 s per day, for 7 days
LPS rat	O'Brien et al., (2019) [73]	LED, 675 nm	13 sessions of 88 s over 6 days
Transgenic K3 mouse	Purushothuman et al., (2013) [74]	LED, 670 nm	20 sessions of 90s over 4 weeks

Table 1.6: Summary of studies on the effects of tPBM in animal models of PD.

All preclinical trials have shown improvements in various motor symptoms induced by the different neurotoxins and gene mutations that attempt to simulate parkinsonian symptoms, as well as increased survival of dopaminergic neurons. Notably, all preclinical trials using tPBM have been conducted exclusively in rodents, with no reported studies in non-human primates.

Concerning clinical trials on tPBM, the use of helmets delivering light to broader brain regions or other devices providing more focalized illumination has been explored. These clinical studies are shown in Table 1.7.

ID	Collaborators	Patients	Duration	Light Source	Treatment
ACTRN12618000038291	Cromwell Property Group Foundation and San Hospital Group Sydney	12	Nov. 2017 / Sept. 2023	Vielight Neuro Gamma (LED, 810 nm) + Irradia MID 2.5 / MIDCARE (Laser, 810 nm)	tPBM, intranasal, neck and abdominal PBM, sessions of 20 min. 3 sessions/week during weeks 1-4 + 2 sessions/week during weeks 5-8 + 1 session/week during weeks 9-12 and 3 sessions/week for 40 or 25 weeks (2 groups)

NCT03811613	University of Oviedo	35	Jan. 2018 / Mar. 2018	WARP 10, Quantum Devices (LED, 670 nm)	2 sessions of 9 min per week, over 9 weeks
NCT06688357	University of Florida, Parkinson's Disease Foundation and The Parkinson's Institute	23	Jun. 2019 / Aug. 2022	MedX 1116, MCT50252 (LED, 870 nm)	6 sessions of 40 min over 2 weeks
NCT03551392	University of Florida, McKnight Brain Research Foundation and University of Arizona	24	Jun. 2019 / Apr. 2026	Medx Console System + Vielight 810 (LED, 810 nm)	16 sessions of 1.5 h with Medx Console System over 12 weeks + 4 sessions of 25 min intranasal PBM per week
ACTRN12621001722886	SYMBYX Biome and San Foundation	40	Nov. 2021 / Oct. 2023	SYMBYX Neuro (LED, 635 nm + 810 nm)	6 sessions of (12 min 635 nm0 + 810 nm) per week, for 12 weeks

NCT06036433	Gaitway Neurophysio	60	Jan. 2023 / May 2024	PDNeuro v2.0 (Laser, 635 nm + 810 nm) and PDCare (Laser, 904 nm)	3 sessions of (12 min 635 nm + 12 min 810 nm + 20 min 904 nm abdominal PBM) per day, over 8 weeks
NCT05959772	University of Sao Paulo and University of Maryland	82	Jun. 2023 / Jun. 2025	Light-Aid, Bright Photo-medicine (LED, 850 nm)	Sessions of 4-9 mins over 5 weeks
NCT06729125	Al-Zaytoonah University of Jordan	50	Dec. 2024 / Mar. 2025	CG-5000 Laser, Cell Gen Therapeutics LLC (Laser, 1 064 nm)	Single session
NCT05845216	University Hospital of Grenoble	64	Sept. 2023 / May 2026	LUCIOLE Cap (LED, 670 nm + 810 nm)	Single session of 24 min

Table 1.7: Summary of clinical trials focused on tPBM for the treatment of PD.

Nevertheless, most of these clinical studies report positive effects of tPBM therapy in conditions such as Traumatic Brain Injury (TBI), stroke, and depression, where the target areas are within the cerebral cortex of the brain (the first layer below the skull). However, PD pathogenesis is associated with abnormalities in the SNpc, a deep brain region located 80-100 mm below the coronal suture (located on the surface of the skull).

Currently, it is difficult to study the light propagation within brain tissues *in vivo*. A recent study based on numerical simulations for red and NIR light, indicates that 65.1% of the delivered irradiance is absorbed by the scalp, 33.9% by the skull, and 0.01% by the CSF.

As a result, less than a 0.01% of the irradiance reaches the cortex, also called Gray Matter (GM), and the White Matter (WM). Figure 1.11 shows the results of these simulations [75].

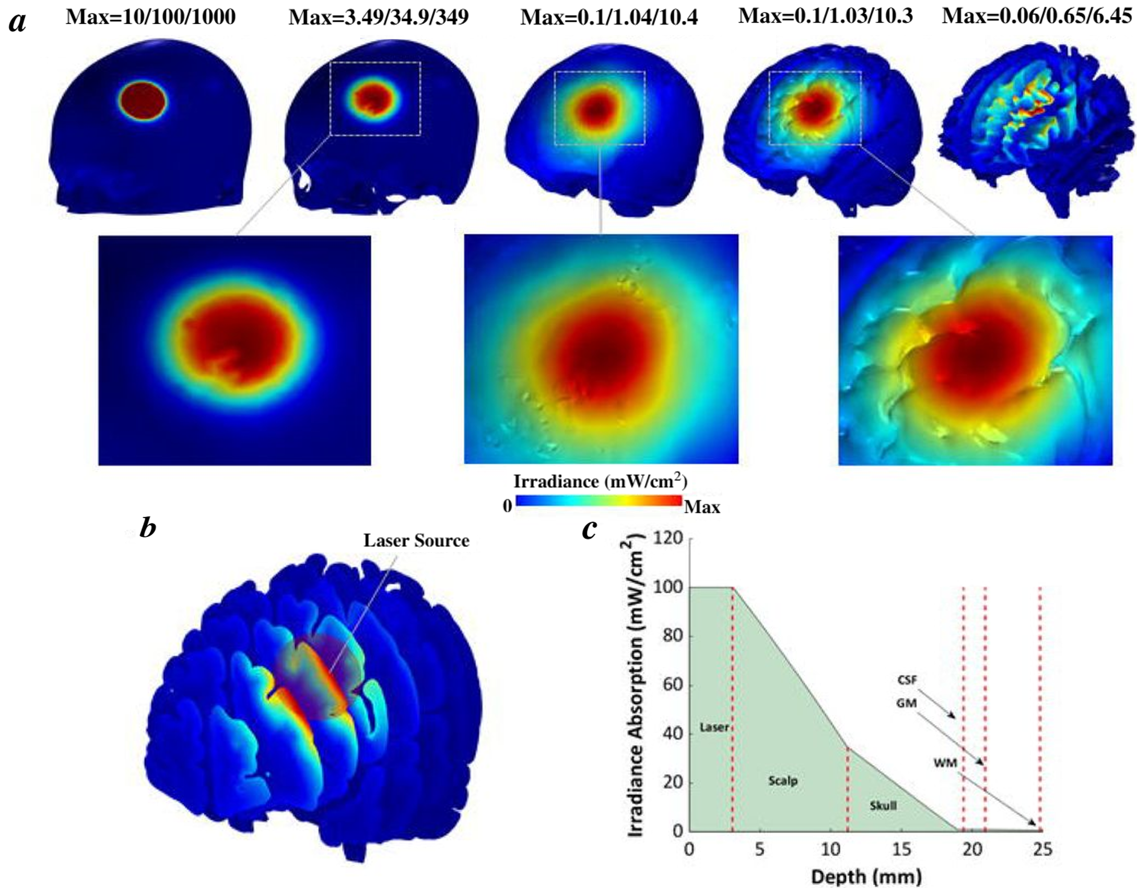

Figure 1.11: Light propagation from a 800 nm light source positioned on the scalp. ***a***) From left to right, three-dimensional surface absorption irradiance plots for: scalp, skull, CSF, gray matter and white matter. The predicted maximum irradiance values are noted in the upper section for each tissue plot. The three values noted correspond to simulation using 10, 100, and 1 000 mW/cm^2 power density, respectively. ***b***) The irradiance absorption across a series of two-dimensional cross sectional slices. ***c***) Irradiance absorption versus penetration depth in brain tissue at 100 mW/cm^2. Figures reproduced from [75].

1.4.5.2 Intracranial Photobiomodulation (iPBM)

A more invasive approach is the intracranial Photobiomodulation (iPBM), which overcomes the limitations of tPBM since it allows to deliver light directly into the brain tissue via surgically implanted devices.

Preclinical studies on the effects of iPBM are summarized in Table 1.8.

PD Model	Study	Light Source	Treatment
MPTP mouse	Moro et al., (2014) [76]	LED, 670 nm	4 sessions of 90 s over 30 h, repeated for 6 days
	El Massri et al., (2017) [77]	Laser, 670 nm	5 s ON / 60 s OFF over 30 h
6-OHDA rat	Reinhart et al., (2016) [78]	LED, 670 nm	2 sessions of 90 s per day, for 23 days
	El Massri et al., (2017) [77]	Laser, 670 nm	5 s ON / 60 s OFF over 23 days
MPTP non-human primate	Darlot et al., (2016) [79]	Laser, 670 nm	5 s ON / 60 s OFF a few minutes before each MPTP injection and turned on for the next 24-hour period. 2 groups: 5 and 7 MPTP injections
	Moro et al., (2016) [80]		5 s ON / 60 s OFF over 25 days
	El Massri et al., (2017) [77]		5 s ON / 60 s OFF over 5 days
	Moro et al., (2017) [81]		5 s ON / 60 s OFF over 7, 8 or 12 days (3 groups)
	El Massri et al., (2018) [82]		5 s ON / 60 s OFF over 5 days

Table 1.8: Summary of studies on the effects of iPBM in animal models of PD.

These preclinical trials show no adverse effects on the surrounding brain and demonstrate positive effects in alleviating motor symptoms and potential for slowing down neurodegeneration. Additionally, iPBM has enabled studies in non-human primates, as transcranial devices would likely be disrupted by the primates' attempts to remove them, increasing the risk of infection and potential fatality.

These findings led to the world's first and only clinical trial of iPBM for PD, launched by Clinatec at CEA/DRT/LETI[1] in December 2020, with completion expected in April 2028.

[1]Commissariat à l'Energie Atomique et aux Energies Alternatives/Direction de la Recherche Technologique/Laboratoire d'Electronique et de Technologie de l'Information

1.4.5.2.1 Ongoing Clinical Trial at Clinatec

This clinical trial is a randomized, open-label (a study in which both the researchers and participants are aware of the treatment being administered) and case-control trial [83]. Firstly, it aims to evaluate the safety and tolerance of intraventricular surgical implantation and intracranial illumination; and secondly, the neuroprotective potential of this new treatment. To do this, the density of dopaminergic neurons is studied via Positron Emission Tomography (PET)-scan using [^{11}C]-PE2I tracer, which is a highly selective marker for imaging dopamine transporter.

The study includes 14 PD patients (7 treated with the implantable medical device and 7 control patients who do not receive any iPBM device) meeting the following criteria: aged 25–65 years, diagnosed less than 2 years ago, idiopathic (sporadic PD), no prior anti-PD medications, and patients with mild to moderate symptoms who are still able to live independently.

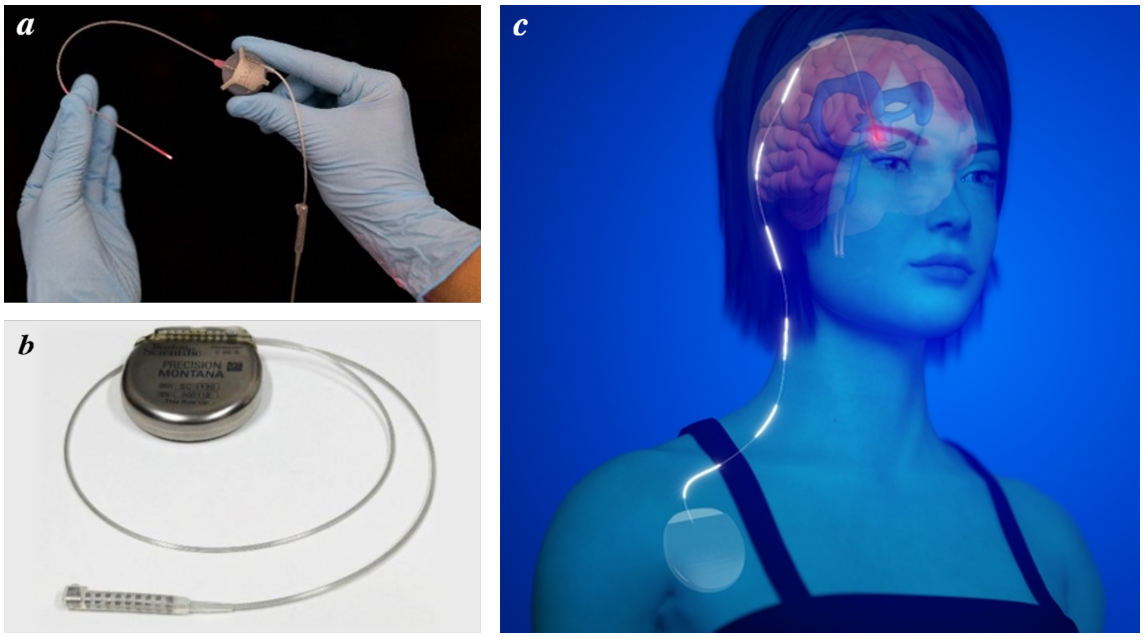

Figure 1.12: ***a***) Laser diode coupled to the optical fiber, ***b***) rechargeable battery and ***c***) illustration of the implantable device as a whole used for the current clinical trial.

The implantable medical device, illustrated in Figure 1.12, consists of a 670 nm laser diode, coupled to an optical fiber and powered by a rechargeable battery. The laser diode is implanted in the skull, the distal end of the intracerebral optical fiber is placed in the third ventricle, approximately 7.5 mm from the medial edge of each SNpc and the battery is located below the clavicle, subcutaneously. The optical fiber is implanted into the brain

through a minimally invasive endoventricular route. The electrical energy required is supplied by a battery adapted from those used for DBS, designed by Boston Scientific. The battery delivers pulsed light consisting of cycles of two pulses, each lasting 260 μs and reaching a peak power of 15 mW/cm^2, separated by a 50 μs interval. This results in a duty cycle of 7.5%. These pulse cycles are repeated at a frequency of 150 Hz. The device operates in a cyclical mode, remaining active for 1 minute followed by a 4-minute inactive period, corresponding to 20% overall activity. Consequently, the average optical power is 0.23 mW/cm^2 (detailed calculations are provided in chapter 6).

Preliminary results have been published in January 2025 on MedRxiv (non peer-reviewed) [84], reporting on the first three treated patients compared to three control PD patients. Patients report no major adverse effects, consistent with preclinical experiments already cited. The most remarkable finding is that, after 12 months, iPBM has induced a substantial increase in dopamine transporter levels, as measured by [^{11}C]-PE2I-PET across all basal ganglia in two out of three patients. Results are shown in Figure 1.13.

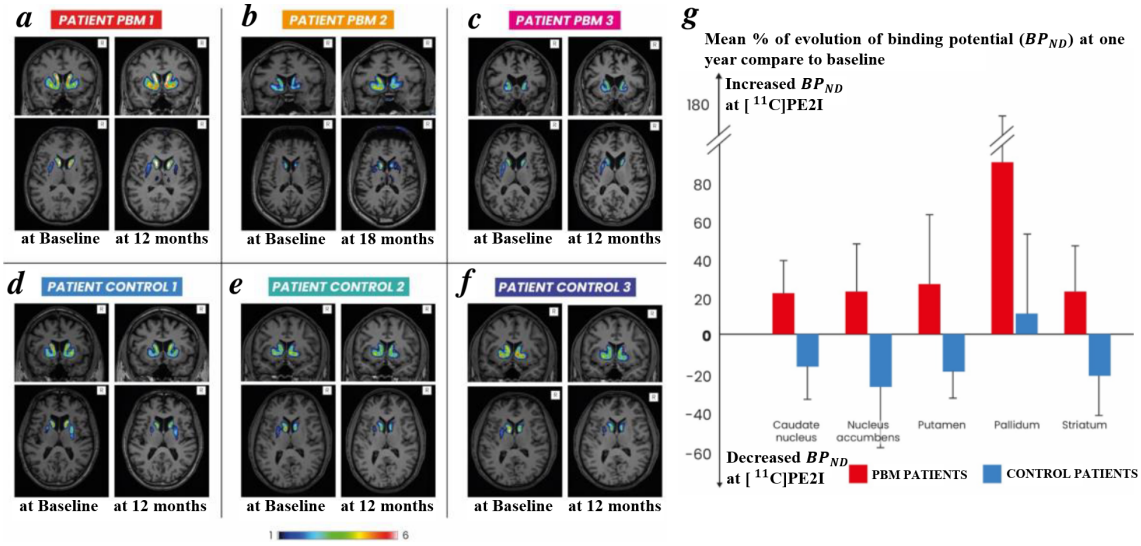

Figure 1.13: ***a, b, c, d, e, f***) Evolution of [^{11}C]-PE2I tracer binding, indicating the dopamine transporter levels, for the first three patients treated with iPBM and three control PD patients. ***g***) Mean values of [^{11}C]-PE2I tracer binding potential (BP_{ND}) between baseline and 12 months follow-up across brain regions for all patients. Figure adapted from [84].

For the third treated patient, results vary depending on the basal ganglia area. In contrast, in the control group and across all basal ganglia, [^{11}C]-PE2I uptake is reduced as expected. These findings are consistent with preclinical studies in several animal models of PD and suggest that iPBM could restore dopaminergic function, supporting a potential disease-modifying effect. Dopaminergic neurons that are suffering but still alive could thus

restore their production of dopamine. For the third treated patient, a trend toward clinical improvement has been observed after adjustment of the illumination protocol.

A definitive conclusion on the slowing down of neurodegeneration cannot be drawn due to the patient population size. Furthermore, as this is an open-label study, the possible contribution of a placebo effect in the improvement of clinical symptoms observed is no completely discounted, even if it is very unlikely to persist at 24 months. In addition, a persistent symptomatic effect of dopaminergic medications cannot be excluded, despite the 24-hour withdrawal of anti-parkinsonian drugs before performing clinical evaluations. However, residual effects cannot account for the improved [^{11}C]-PE2I-PET profiles recorded for the treated patients as it is well-established that anti-parkinsonian drugs have no effect on [^{11}C]-PE2I tracer.

Based on the data obtained from the first three implanted patients, it can be concluded that iPBM is both well tolerated and safe for use in PD patients and shows promise as a mean to modify disease progression. However, in order to validate the clinical efficacy of iPBM in slowing down PD progression, a larger number of patients with longer follow-up is necessary.

1.5 Fundamentals of Light Propagation and Interaction in Biological Tissue

The current implant based on PBM and used for the clinical trial emits light with the intent to stimulate the SNpc. However, a significant fraction of the emitted photons are absorbed and scattered by the surrounding brain tissues before reaching the target area. This limits the effective therapeutic light dose and underscores the importance of understanding how light propagates inside the brain.

Specifying the optical properties of tissue is a critical first step in designing effective light-based devices and therapeutic protocols. While tabulated optical coefficients from the literature provide a useful starting point, they must be considered carefully, as tissue optical properties vary across individuals, anatomical sites, time, and physiological state due to factors such as blood content, water content, collagen, and cellular architecture [85]. Moreover, many tabulated values come from post-mortem or *in vitro* measurements, and *in vivo* properties may differ substantially.

Light transport in biological tissue is governed primarily by three intrinsic optical parameters:

- The absorption coefficient, μ_a (in cm^{-1}): corresponds to the inverse of the mean free path traveled by photons before absorption when passing through tissue. The resulting light intensity, I(d), as a function of depth, d, in tissue follows the Beer-Lambert law:

$$\mathrm{I}_a(\mathrm{d}) = \mathrm{I}_0 \, e^{-\mu_a \cdot \mathrm{d}} \tag{1.1}$$

  where I_0 is the incident light intensity.

- The scattering coefficient, μ_s (in cm^{-1}): corresponds to the inverse of the mean free path traveled by photons before scattering by the tissue they are interacting with. Similar to absorption, the intensity attenuation due to scattering alone can be expressed as an exponential decay:

$$\mathrm{I}_s(\mathrm{d}) = \mathrm{I}_0 \, e^{-\mu_s \cdot \mathrm{d}} \tag{1.2}$$

- The anisotropy factor, g, (dimensionless, range -1 to 1): characterizes the average cosine of the scattering angle, describing the preferential forward directionality of photon scattering. For example, if the tissue tends to scatter incident photons into the forward direction, then $g \approx 1$; if the scattering tends to be isotropic, then $g \approx 0$; and if the tissue tends to scatter incident photons into the backward direction, then $g \approx -1$. Since μ_s and g are coupled, the reduced scattering coefficient $\mu_s' = \mu_s(1-\mathrm{g})$ is often used to simplify modeling. Absorption, however, is an isotropic process; photons are absorbed regardless of direction, so there is no analogous reduced absorption coefficient. Therefore, the total attenuation (extinction) coefficient μ_t, considering both absorption and scattering, is typically written as $\mu_t' = \mu_a + \mu_s'$. So the intensity is attenuated as:

$$\mathrm{I}_t(\mathrm{d}) = \mathrm{I}_0 \, e^{-\mu_t' \cdot \mathrm{d}} = \mathrm{I}_0 \, e^{-(\mu_a + \mu_s') \cdot \mathrm{d}} \tag{1.3}$$

Light transport through tissue can be predicted by integrating estimated optical parameters into computational models (e.g., Monte Carlo simulations). A key concept is the use of a generic tissue model constructed from known chromophores and their concentrations (blood volume fraction, oxygen saturation, melanin content, etc.). This approach allows researchers to estimate tissue-specific optical properties at any wavelength of interest and use them in simulation studies to predict light propagation and energy deposition. Such models enable exploring patient- or site-specific variations and guide implant design parameters.

Recent Monte Carlo light transport simulations conducted at Clinatec, reveal that up to four orders of magnitude of the clinically emitted photons are lost before reaching the SNpc due to scattering and absorption in the surrounding tissues.

Unfortunately, the current implant used in the clinical trial has several additional limitations:

- Whereas the surgical positioning of the optical fiber is non-invasive for the brain, the implantation of the battery under the clavicle is more restrictive and quite harmful for the patient.
- The laser diode's power supply requires recharging the battery, via induction, at least twice a week.
- Additionally, the current device generates only a single-point light source, suitable for illuminating small targets such as the SNpc but not for larger and more complex regions of the brain. Therefore, it cannot be used to treat other diseases like AD, where the hippocampus and cortex would need to be illuminated.

1.6 Conclusion

In this chapter, the most common neurodegenerative diseases worldwide have been presented, with PD ranked as the second most prevalent. While treatments exist that can alleviate the symptoms of this disease, they are unable to slow the cellular death of dopaminergic neurons, which are the cells affected by this disorder. Therefore, it is necessary to work on the development of new therapies aimed at slowing the progression of the disease. Among these, PBM stands out.

Currently, the world's first clinical trial is being conducted at the Clinatec research laboratory, where this thesis is carried out, proposing PBM as a potential treatment for PD. Although preliminary results are very promising, it is necessary to begin work on new light-based devices that can be implanted not only closer to the SNpc to reduce optical losses between the light emitted by the device and the amount absorbed by the target, but that are also more comfortable for the patient. Hence, there is significant interest in developing implantable radioluminescent devices.

Troubles Neurodégénératifs et Maladie de Parkinson : Traitements Actuels et Thérapies Emergentes

Résumé du Chapitre

Dans ce chapitre, les maladies neurodégénératives les plus courantes dans le monde ont été présentées (la maladie de Alzheimer (AD), la maladie de Parkinson (PD), la sclérose latérale amyotrophique (ALS) et la maladie de Huntington (HD)), étant PD classée comme la deuxième plus répandue. Bien qu'il existe des traitements permettant d'inhiber les symptômes de cette maladie, tels que les traitements pharmacologiques à base de L-DOPA ou la stimulation cérébrale profonde (DBS), ils ne ralentissent pas la mort cellulaire des neurones dopaminergiques. Ces neurones, touchés par ce trouble neurologique, se situent dans une région très profonde du cerveau appelée substance noire pars compacta (SNpc). Il est donc nécessaire de développer des nouvelles thérapies visant à ralentir la progression de la maladie. Parmi celles-ci, la photobiomodulation (PBM) se démarque.

Actuellement, le premier essai clinique mondial proposant la PBM comme traitement potentiel de PD est mené au laboratoire de recherche Clinatec, où cette thèse est réalisée. Bien que les résultats préliminaires soient très prometteurs, il est nécessaire de commencer à développer de nouveaux dispositifs lumineux pouvant être implantés non seulement plus près de la SNpc afin de réduire les pertes optiques entre la lumière émise par l'implant et la quantité absorbée par la cible, mais aussi plus confortables pour le patient, de sorte qu'il n'ait pas besoin de recharger la batterie de l'implant. C'est pourquoi un intérêt considérable est porté au développement de dispositifs radioluminescents implantables.

Chapter 2

Radioluminescence and Strategies for the Development of Radioluminescent Light Sources for Photobiomodulation

An implantable radioluminescent device for treating PD via PBM would offer multiple advantages over the electroluminescent implant used in the clinical trial: a minimally invasive approach, superior light delivery to tissues due to its compact design and diffuse illumination, and extended energy independence, all potentially contributing to enhanced patient comfort and treatment efficacy. Moreover, it would allow multiple implantations, which in the case of PD treatment would mean that a radioluminescent device could be implanted next to each SNpc.

2.1 History of Radioactivity

The history of radioactivity begins in 1895 with Wilhelm Conrad Röntgen, a German physicist, who was experimenting with cathode rays using a Crookes tube (a vacuum tube with electrodes at each end). While the tube was shielded with heavy black cardboard to block visible light, he observed that a fluorescent screen coated with barium platinocyanide placed nearby began to glow. Röntgen concluded that an unknown type of radiation, which he referred to as "X" radiation, was being emitted from the tube and it could

penetrate opaque materials. He found that these rays were capable of passing through most substances, even through the tissue of humans, but not bones and metal objects. One of Röntgen's first experiments late in 1895 was a film of his wife's hand (Figure 3.1a), revealing her bones and wedding ring, which would be the first X-ray image in history. In 1901, Röntgen was awarded the first-ever Nobel Prize in Physics for his discovery of X-rays.

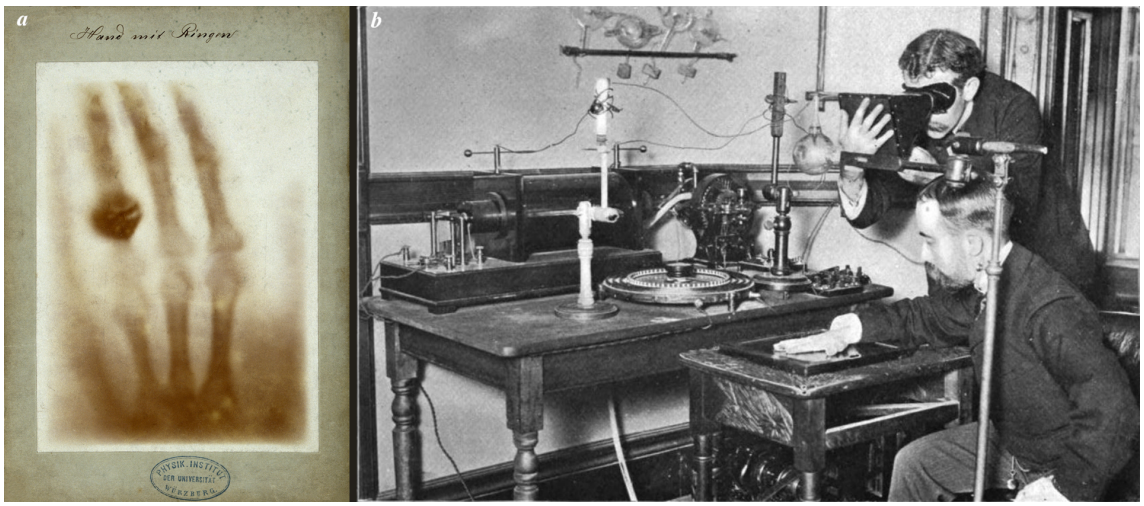

Figure 2.1: ***a***) The first X-ray image in history, the Röntgen's wife's hand. ***b***) Taking an X-ray image with early Crookes tube apparatus, late 1800s. The Crookes tube is visible in center. The standing man is viewing his hand with a fluoroscope screen. The seated man is taking a radiograph of his hand by placing it on a photographic plate.

In 1896, Henri Becquerel made another important discovery while studying phosphorescence in potassium uranyl sulfates [86]. He serendipitously found that the material emitted radiation capable of darkening photographic plates. This phenomenon, later named "radioactivity" by Marie Curie, earned Becquerel the 1903 Nobel Prize in Physics, shared with Marie and Pierre Curie for their joint research into radiation phenomena. The Curies further expanded this field by discovering two new radioactive elements, polonium and radium, in 1898. Marie Curie received her second Nobel Prize in Chemistry in 1911 for isolating radium and studying its properties, cementing her legacy as a pioneer in the field. The ability to produce artificial radioactivity came in 1934, when their daughter, Irène Joliot-Curie, and her husband, Frédéric Joliot, bombarded aluminum nuclei with alpha particles emitted from polonium. This process created a radioactive isotope of phosphorus, ^{30}P, which continued to emit positrons even after the alpha source was removed, proving that the aluminum had been made artificially radioactive. Their work was published shortly thereafter, earning them the 1935 Nobel Prize in Chemistry. This breakthrough opened

the door to producing radioisotopes for medical and industrial applications. Scientists like Enrico Fermi further advanced this field by using neutron bombardment to create new radioactive elements. The invention of the cyclotron in 1930 by Ernest Lawrence enabled the production of important isotopes, such as ^{14}C, ^{131}I, and many others, which became essential tools in nuclear medicine. The number of studies increased exponentially when the nuclear reactor in Oak Ridge, USA, was opened for radionuclide production in 1946.

Ernst Rutherford was the first to categorize the types of emitted radiation from radioactive isotopes. He sorted these ionizing radiations by their depth of penetration and called them alpha, beta and gamma in increasing order of penetration [87]:

- Alpha radiation: consists of relatively heavy and positively charged particles, which are actually helium nuclei. Despite being a highly ionizing radiation, its penetration depth is quite limited since it can be stopped by a piece of paper or even the dead outer layers of skin. However, alpha radiation can be very harmful to living cells when alpha particles are inhaled, ingested, or absorbed into the blood stream (e.g., through a cut in the skin).

- Beta radiation: involves lighter charged particles emitted during nuclear decay, which proved to be negatively charged electrons (β^--decay) or positively charged electrons, i.e., positrons (β^+-decay). Beta decay occurs when there is an imbalance between the number of protons and neutrons required for optimal nuclear stability. If there are too many protons (an excessive positive charge), the nucleus attempts to attain greater stability either by emitting a positron through β^+-decay or by capturing an orbiting electron and combining this with a proton. In either case, the excess positive charge is neutralized and a proton is transformed into a neutron. Only when the energy difference between parent and daughter nuclei involved in nuclear decay exceeds 1.022 MeV can positron emission occur; when the difference is below this threshold, electron capture is the only decay option. The general equation governing the β^+-decay from a particle perspective is [87]:

$$ {}^{1}_{1}\mathrm{p} \rightarrow {}^{1}_{0}\mathrm{n} + {}^{0}_{+1}\mathrm{e} + {}^{0}_{0}\nu_e \tag{2.1} $$

  From a nuclear perspective:

$$ {}^{x}_{y}\mathrm{A} \rightarrow {}^{x}_{y-1}\mathrm{B} + {}^{0}_{+1}\beta^+ + {}^{0}_{0}\nu_e \tag{2.2} $$

  being the superscript x the mass number (the total number of protons plus neutrons) which must remain constant during the decay, and the subscript y wich is the atomic

number (the number of protons) which changes accordingly. An example of β^+-decay, is the case of the fluorine-18 radioisotope. Through this decay, fluorine-18 transforms into stable oxygen-18 by emitting a positron and an electron neutrino:

$$^{18}_{9}\mathrm{F} \rightarrow {}^{18}_{8}\mathrm{O} + {}^{0}_{+1}\beta^{+} + {}^{0}_{0}\nu_{e} \tag{2.3}$$

Conversely, when there is a deficiency of protons (i.e., not enough positive charge), the nucleus can gain a proton and increased stability by emitting an electron via β^--decay, which converts a neutron into a proton. The general equation governing the β^--decay from a particle perspective is the following:

$$^{1}_{0}\mathrm{n} \rightarrow {}^{1}_{1}\mathrm{p} + {}^{0}_{-1}\mathrm{e} + {}^{0}_{0}\bar{\nu}_{e} \tag{2.4}$$

and from a nuclear perspective:

$$^{x}_{y}\mathrm{A} \rightarrow {}^{x}_{y+1}\mathrm{B} + {}^{0}_{-1}\beta^{-} + {}^{0}_{0}\bar{\nu}_{e} \tag{2.5}$$

An example of β^--decay, is the case of the tritium radioisotope. Through this decay, tritium transforms into stable helium-3 by emitting an electron and an electron antineutrino:

$$^{3}_{1}\mathrm{H} \rightarrow {}^{3}_{2}\mathrm{He} + {}^{0}_{-1}\beta^{-} + {}^{0}_{0}\bar{\nu}_{e} \tag{2.6}$$

It should be noted that the inclusion of neutrinos (or antineutrinos) in these equations is essential to conserve energy, momentum, and lepton number. Historically, however, the continuous energy spectrum of beta particles puzzled early researchers, such as Lise Meitner and Otto Hahn, who believed that conservation laws were being violated. In 1930, Wolfgang Pauli postulated the existence of an undetectable neutral particle to solve this issue. Enrico Fermi later named it the "neutrino", and its existence was experimentally confirmed by Cowan and Reines in 1956 through inverse beta decay experiments. Thus, β^--decay is always accompanied by an antineutrino, and β^+-decay by a neutrino. After beta decay, the daughter nucleus may still be left in an excited state, releasing excess energy as a gamma photon.

In addition, during the beta decay, electrons or positrons released are decelerated or deflected by the electric fields of atomic nuclei in the target material they interact with, producing radiation with a continuous spectrum, what it is called "bremsstrahlung radiation" or "braking radiation" [88]. This process converts the kinetic energy of the high-speed beta particles into electromagnetic radiation, typically in the form of X-rays. The energy of the bremsstrahlung X-rays has a continuous spectrum up to a maximum equal to the maximum kinetic energy of the beta particles.

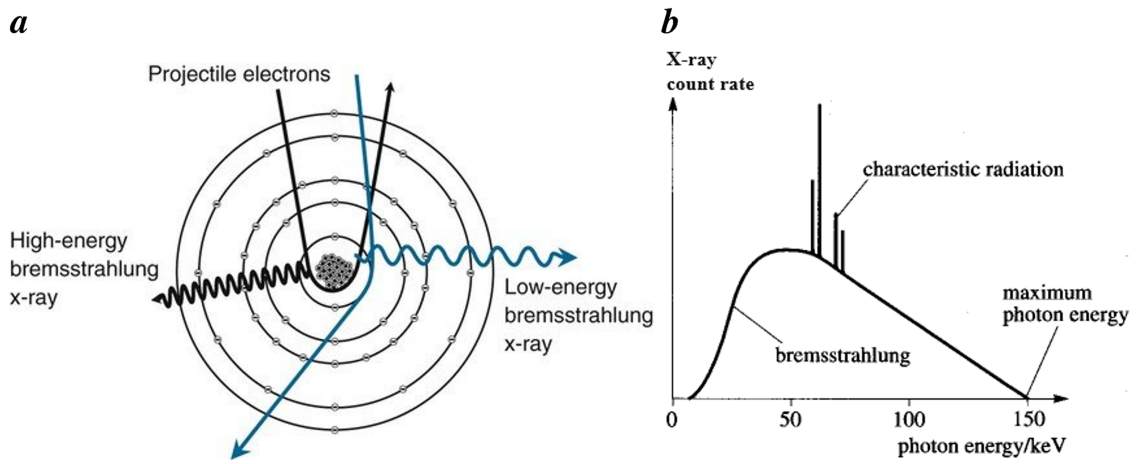

Figure 2.2: ***a)*** Schematic illustration of bremsstrahlung radiation production. ***b)*** Bremsstrahlung radiation spectrum from beta particles interacting with a heavy metal target. Adapted from [88].

This continuous spectrum arises because the energy lost by the electron can vary depending on its trajectory near the nucleus, as illustrated in Figure 2.2a. When an electron passes very close to the atomic nucleus, it undergoes strong deceleration, resulting in high-energy bremsstrahlung X-rays. Conversely, electrons that pass farther from the nucleus experience gentler deflections, producing lower-energy X-rays. The intensity of bremsstrahlung radiation is proportional to the square of the atomic number of the target material and to the energy of the incident beta particles, while being inversely proportional to the mass of the charged particle. The bremsstrahlung spectrum, as shown in Figure 2.2b, displays this continuous distribution of X-ray energies, ranging up to the maximum kinetic energy of the beta particles. In addition to the continuous background, sharp characteristic peaks are present in the spectrum. These characteristic peaks represent emissions of X-rays with discrete energies caused by electron transitions between atomic shells within the target atoms, following inner-shell electron ionization by the incoming beta particles. For instance, when an inner shell electron is knocked out, an electron from an outer shell fills the vacancy, emitting an X-ray photon with energy specific to the difference in the shell binding energies.

Beta radiation can be stopped by a sheet of aluminum or several centimeters in the air, where its mean free path is approximately 3.7 m/MeV in air [89], since unlike mono-energetic alphas, beta particles come in a continuous spectrum of energies. Compared to alpha particles, beta radiation is less ionizing but more penetrating, capable of entering the skin and causing damage such as burns. Its main biological hazard arises from ingestion or inhalation.

In this work, the focus will be placed on beta radiation as the primary type of interest.

- Gamma radiation: composed of high-energy photons, this radiation is highly penetrating and requires dense materials like lead or concrete for effective stopping. Gamma rays can easily pass through the human body; nevertheless, a fraction of the energy can be absorbed by tissue and be potentially harmful to living cells.

Radioluminescence (RL) emerged as a practical application of radioactivity when radium was mixed with phosphors to create luminous paints for watch dials and exit signs. However, this innovation came at a cost: workers who handled radium-based paints suffered severe health effects due to prolonged exposure, as exemplified by the tragic case of the "Radium Girls" in the 1920s. This led to stricter regulations on radiation safety [90].

The discovery of radioactivity has had profound implications for science and society, especially in medicine. Its applications range from diagnostic imaging, with the use of X-rays; to targeted cancer therapies, like brachytherapy using ^{226}Ra sources introduced by Marie Curie in the 1910s and used for many decades. However, with the increased use of X-rays and radium, the scientific community also became aware of the hazards of ionising radiation. Advances in nuclear medicine now focus on using lower-energy isotopes to minimize collateral damage while optimizing therapeutic efficacy.

2.2 Ideal Radioisotope Characteristics

If one were to describe the ideal radioisotope for developing an implantable radioluminescent device intended to treat PD, the criteria defining this ideal radioisotope would be based on the following questions:

- What type of radiation (alpha, beta, or gamma) would be optimal for this application?
- What energy would be necessary to produce the desired radioluminescence in the R-NIR range?
- What radiative emission spectrum, in terms of energy, would be ideal: monoenergetic or polyenergetic?
- What half-life would be appropriate for treating such chronic disease?
- Regarding device safety, how can biological damage be minimized and biocompatibility ensured?

To address the first question regarding the most suitable type of radiation for the desired application, it is important to consider that there is no advantage in using gamma radiation. Due to its high penetration power, gamma radiation cannot be effectively shielded within a compact device, potentially exposing the patient to unnecessary radiation.

Concerning alpha emitting radioisotopes, alpha particles typically have energies up to 3 MeV, which may degrade the luminescent materials too quickly. Moreover, since they are highly ionizing, thick shielding would be required to stop them increasing the overall bulk of the device. Lastly, their penetration depth may be too short to interact with the surrounding luminescent materials, reducing optical efficiency.

For all these reasons, beta emitters appear as the most suitable choice for developing a medical implantable device based on RL. As previously mentioned, beta radioisotopes are classified into β^+- and β^--emitters. Both types of radiation can produce radioluminescence [91]; however, when producing RL with β^+-radiation, each positron ultimately annihilates upon encountering an electron, resulting in the emission of two 511 keV gamma photons emitted in opposite directions. Therefore, the most convenient radiation type to use is β^--radiation.

To answer the question regarding the energy necessary to excite luminescent materials emitting in the red or NIR range, it must be considered that the beta particle energy needs to exceed the material's bandgap or excitation energy threshold, which is typically on the order of a few eV, to generate excited states that lead to the emission of photons. However, it could be that particles with only a few eV have a penetration depth that is too short, so they might not excite the entire volume of a luminescent particle. It might be better to have a beta radioisotope with several tens of eV or even reaching some keV.

However, very high-energy beta emissions (hundreds of keV to MeV) may not be ideal because they can cause structural damage or degradation of the luminescent material over time, reducing device longevity.

Regarding the energy spectrum ideal for the proposed device, a monoenergetic spectrum is preferable. Regardless of whether the luminescent material is excited by a single well-defined energy or a broad energy spectrum, the emitted light wavelengths correspond to the electronic structure of the luminescent material and will remain unchanged. Exciting a luminescent material with multiple excitation energies will not alter its intrinsic emission spectrum.

However, excitation by a broad energy spectrum can result in some excitation energies exceeding the threshold needed for photon emission, leading to excess energy dissipated as heat or via non-radiative pathways. This reduces the luminescence efficiency and may

cause damage to the luminescent material's structure and to other components of the device.

Therefore, optimizing light emission becomes more challenging with polyenergetic excitation. Additionally, higher-energy beta particles require increased shielding for safe confinement, which increases the overall device size.

The ideal half-life of the desired β^--radioisotope should balance several factors:

- It must be long enough to ensure stable and continuous light emission over years to decades, matching the chronic nature of the disease and reducing the need for frequent device replacement surgeries. The emitted light intensity by the RL device would decrease by a factor of 2 every half-life, so after about 3-4 half-lives, the brightness may drop below practical usefulness.

- It should avoid excessively long half-lives, which complicate radioactive waste management and long-term safety. Moreover, all other device materials must withstand this radiation throughout the isotope's operational lifetime. Additionally, the potential for reusing the medical device may raise ethical concerns, including issues related to patient safety, contamination risks, and device ownership. For instance, early medical devices such as plutonium-powered pacemakers [92] demonstrated remarkable longevity (since Pu-238 has a half-life of 88 years) but also highlighted safety and regulatory challenges related to long-lived radioactive materials and their disposal after patient death.

Therefore, the appropriate half-life range would be around 20 to 30 years, providing practical longevity while maintaining manageable safety concerns.

The ideal radioisotope would therefore be a pure β^--emitter with a monoenergetic spectrum limited to a few tens of eV or even some keV. Effective radiation confinement and device safety require shielding both beta particles, which may escape if not fully absorbed by luminescent particles, and bremsstrahlung X-rays produced by electron deceleration (described in the previous section). Since bremsstrahlung X-rays would have maximum energies corresponding to the beta particles, usually at most a few keV, thin layers of biocompatible materials such as borosilicate glass can effectively attenuate both radiations. Practical shielding thicknesses of several micrometers (as demonstrated in the following section) are typically required to ensure adequate protection, balancing biocompatibility and device dimensions.

Once the ideal radioisotope for the desired application has been identified, the search for the best real candidate can proceed.

2.3 Selection of the Best Radioisotope Candidate

After everything previously stated, pure β^--emitters appear to be the most suitable candidates as radioactive sources for the desired device. The four least energetic pure β^--emitting candidates are ^{3}H, ^{63}Ni and ^{90}Sr, whose characteristics are shown in Table 2.1.

Radio-isotope	**Half-life**	**Beta Particle Average Energy**	**Beta Particle Maximum Energy**	**Borosilicate Thickness Required To Shield Radiation**
^{3}H	12.3 years	5.7 keV	18.6 keV	5.4 μm
^{63}Ni	98.7 years	17.4 keV	66.9 keV	45.7 μm
^{14}C	5 730 years	49.2 keV	156.5 keV	198.8 μm
^{90}Sr	28.8 years	195.7 keV	545.9 keV	1 363.7 μm

Table 2.1: Basic properties of the four least energetic pure β^--emitting radioisotopes. The lifetime and the average and maximum energies of the electrons have been obtained from [93]. The borosilicate thickness required to shield radiation has been determined by CASINO simulations[1].

No pure β^--radioisotopes exhibit monoenergetic emission spectra, so this condition cannot be met. Regarding electron energy, ^{90}Sr emissions reach a maximum of 545.9 keV, which may degrade luminescent materials too rapidly. As for half-life, both ^{63}Ni (98.7 years) and ^{14}C (5 730 years) are excessively long.

The best candidate is then ^{3}H, which is the least radiotoxic pure β^--radioisotope in the world. Its half-life of 12.3 years means that after this period, the number of emitted electrons will be half of what it was initially. However, the device can still be operational beyond this point, potentially for 20 years or even more. Its maximum electron energy of 18.6 keV may be sufficient to produce radioluminescence and electrons would be fully stopped by 6 μm of borosilicate glass.

The penetration depths of the most energetic electrons emitted by the β^--emitting radioisotopes listed in Table 2.1 are represented in Figure 2.3, after CASINO simulations.

[1]The composition of the borosilicate glass used in the CASINO simulations was: 80% SiO_2, 13% B_2O_3, 4% Al_2O_3 and 3% Na_2O. It was manually defined as a material composed of Si (atomic fraction: 0.2442), B (0.0784), Al (0.0164), Na (0.0203), and O (0.6407), with a density of 2.23 g/cm^3. The number of incident electrons was set to 100 000, with a beam radius of 1 nm and no tilt angle.

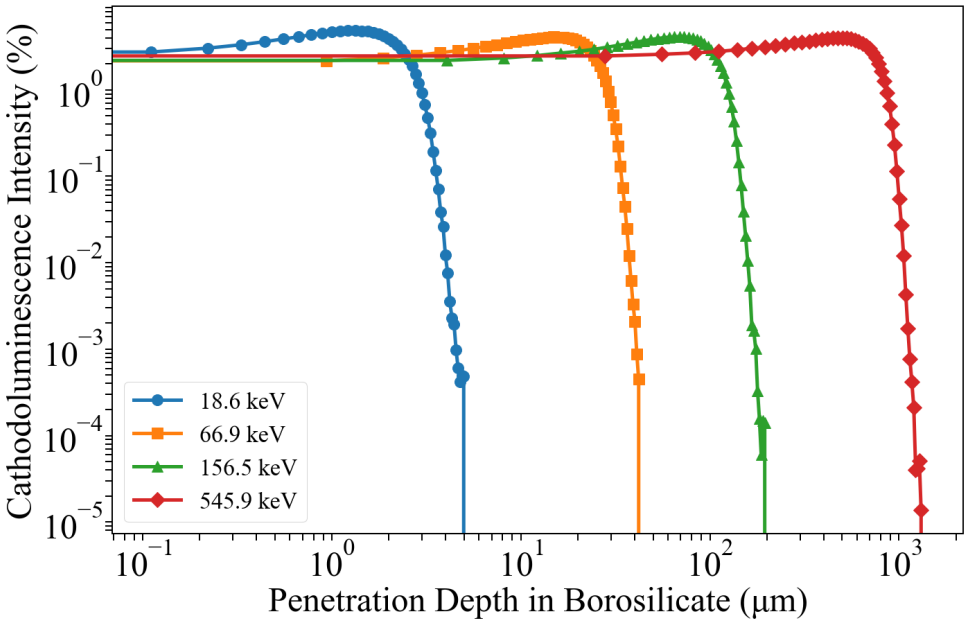

Figure 2.3: Penetration depth of electron beams at the maximum energies of radioisotopes listed in Table 2.1 in borosilicate.

However, given the critical importance of safety in such a radioluminescent implantable device, this topic will be thoroughly examined in the next section, which is fully dedicated to addressing these issues in detail.

2.4 Safety Considerations for the Proposed Radioluminescent Device

To ensure the safety of a tritium-based RL device, it is necessary to confine, on one hand, the beta radiation itself since there will be electrons that may not be absorbed by the luminescent particles, and on the other hand, the bremsstrahlung radiation.

Regarding the beta radiation, as mentioned in the previous section, the maximum electron energy of tritium is 18.6 keV, which would be fully stopped by 6 μm of borosilicate glass.

Concerning bremsstrahlung radiation, the most energetic X-rays will have a maximum energy of 18.6 keV. The attenuation length of these X-rays in borosilicate glass is approximately 1.6 mm [2].

[2]The estimation of the attenuation length was performed using the Henke X-Ray Attenuation Length Calculator [94], simulating: borosilicate glass as SiO_2 with a density of 2.23 g/cm^3 and Y_2O_3:Eu^{3+} with 5.01 g/cm^3.

The attenuation length is defined as the thickness at which the intensity of X-rays passing through the material decreases to $1/e \approx 37\%$ of its initial value, according to the Beer-Lambert law [95]:

$$I = I_0 \cdot e^{-\mu \cdot x} \tag{2.7}$$

where I_0 is the initial intensity, μ the linear attenuation coefficient, and x the material thickness. The attenuation length, x= λ_{att}, is given by $\lambda_{att} = 1/\mu$ and represents the characteristic distance at which the intensity drops by a factor of e. Consequently, after one attenuation length, only about 37% of the initial X-ray intensity remains, but it must be taken into account that the surrounding luminescent materials will also absorb this radiation. For example, X-rays at 18.6 keV have an attenuation length of 30 μm in Y_2O_3:Eu^{3+}.

The concept of critical energy for bremsstrahlung production must also be considered, defined as the energy at which radiative losses equal ionization losses. For materials such as CMC, Y_2O_3:Eu^{3+}, and borosilicate glass, this critical energy is on the order of tens of MeV. Thus, tritium beta electrons (with a maximum energy of 18.6 keV) primarily cause ionization rather than bremsstrahlung radiation.

In case of an unlikely breaking event, effects in case of inhalation or ingestion of tritium are already known [96]:

- On the one hand, 97% of tritium atoms could interact with the water accumulated in the patient's body, giving rise to HTO, which takes about 10 days to be evacuated from the body.
- On the other hand, a 3% of tritium atoms could be stored in organic molecules and that could be retained in our organism for 40 days.

Finally, once the required amount of tritium for the desired RL device will be determined, it will be possible to estimate the dose that the patient would receive in the worst-case scenario of device rupture. Dose is defined as the amount of energy deposited by ionizing radiation per unit mass of tissue.

In radiation protection, the most relevant quantities are equivalent dose and effective dose, which take into account not only the absorbed energy, but also the type of radiation and its biological impact. The unit of both equivalent and effective dose is the sievert (Sv). By definition, one sievert corresponds to one joule of radiation energy deposited per kilogram of tissue, adjusted by a dimensionless weighting factor that reflects the biological effectiveness of the radiation. The Sv is the standard SI unit used to quantify the biological risk associated with exposure to ionizing radiation, and allows for comparison of risk regardless of radiation type.

2.5 Approaches for Tritium-Based Radioluminescent Device Development

Different strategies to design radioluminescent devices based on tritium have been disclosed, including the use of tritium gas, tritiated water or a solid tritiated matrix as a β-reservoir.

2.5.1 Gaseous Tritium Light Sources (GTLS)

The earliest and most established approach for producing radioluminescent gas tubes, known as Gaseous Tritium Light Sources (GTLS), involves the use of glass capillaries internally coated with inorganic phosphors and subsequently filled with tritium gas before being hermetically sealed. The first GTLS devices were developed and patented in the late 1950s and early 1960s [97, 98, 99].

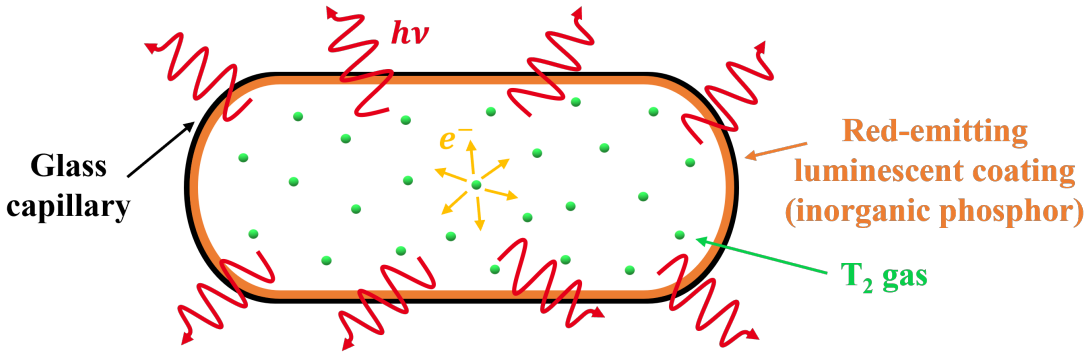

Figure 2.4: Diagram showing the operating principle of a GTLS.

As illustrated in Figure 2.4, the beta particles emitted by tritium interact directly with the phosphor coating, exciting it to emit visible light. Although green-emitting phosphors have historically dominated the literature and commercial applications, this approach remains very relevant for the development of the desired RL device targeting red emission by selecting appropriate luminescent materials.

The tritium content in GTLS is typically done by monitoring the tritium gas pressure in the tritium gas handling system. According to the Organisation for Economic Co-operation and Development (OECD) Radiation Protection Standards [100] for GTLS, devices with tritium activity up to about 2 to 5 Ci are considered within common safety and regulatory limits for general use with controlled conditions.

The work of Korin et al. [98] published in 1975 provides valuable insights into the behavior of these devices. Their studies show that the luminescence intensity at the inner surface of the tube scales approximately linearly with tritium gas pressure below 5 torr ($7{\cdot}10^{-3}$ bar), independent of tube size, as shown in Figure 2.5a. However, as the tube diameter increases, the luminous intensity begins to flatten off. This result highlights the first limitation of this approach: as the tube diameter increases, electrons emitted by tritium are absorbed within the gas ("self-absorption") before reaching the phosphor coating on the inner wall of the tube. Therefore, the innermost part of the tube becomes less effective. It is worth noting that self-absorption does not mean that the emitted electrons are directly captured by other tritium nuclei as in electron capture. It means that the emitted electrons lose their energy by interacting with surrounding matter, which in this case include other diatomic tritium molecules, which could stop them before interacting with the luminescent coating.

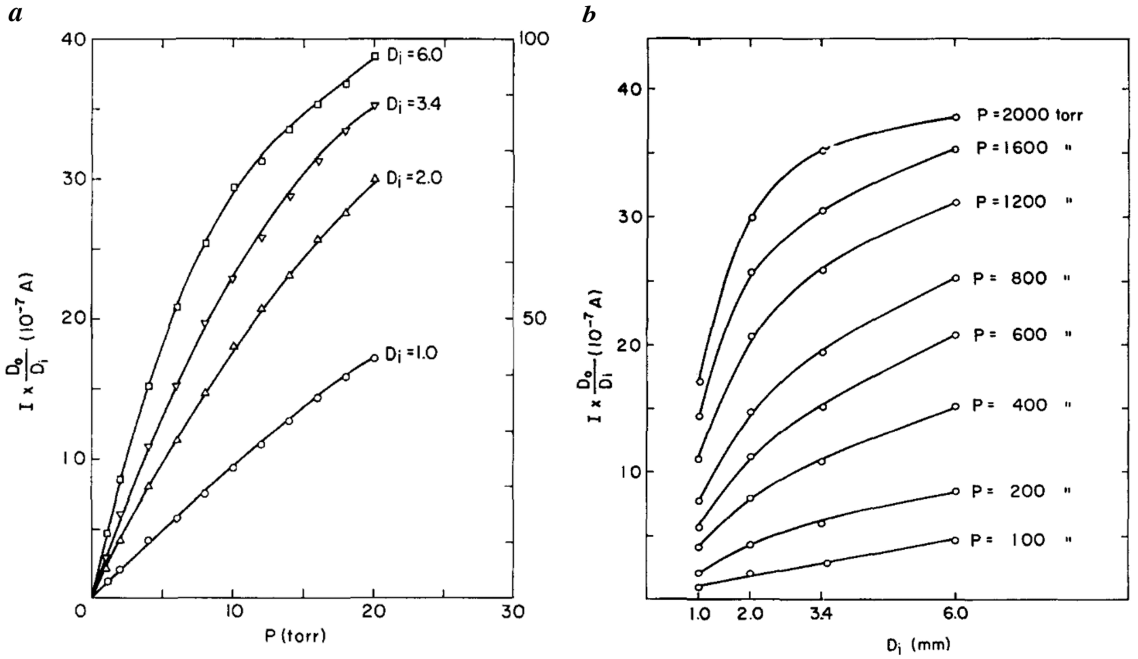

Figure 2.5: ***a***) Intensity of the glass tube as a function of pressure for four tube sizes. ***b***) Dependence of the intensity on the tube diameter for different pressures. Reproduced from [98].

Further experiments by Korin et al. revealed additional dependencies of the intensity in the glass tube as a function of the tube diameter at higher pressures. Results shown in Figure 2.5b indicated that, at low pressures, below 200 torr ($2.7{\cdot}10^{-1}$ bar), the relationship between emitted intensity and tube diameter is practically linear. However, at high pressures, the intensity starts to flatten off, reaching near saturation at the maximum pressure of 2 000 torr (2.7 bar). Self-absorption of tritium becomes significant and the relationship between intensity and tube diameter becomes more complex. This is another critical limitation to

be considered in this approach.

When the luminous intensity is plotted as a function of the coating density, curves such as those shown in Figure 2.6a are obtained. When the coating density increases, the geometrical cross-section for radioluminescence increases too. Nevertheless, after a certain coating density, the phosphor layer becomes less transparent and the photons produced inside the glass tube are not able to pass through it so the intensity outside the tube starts to decrease again.

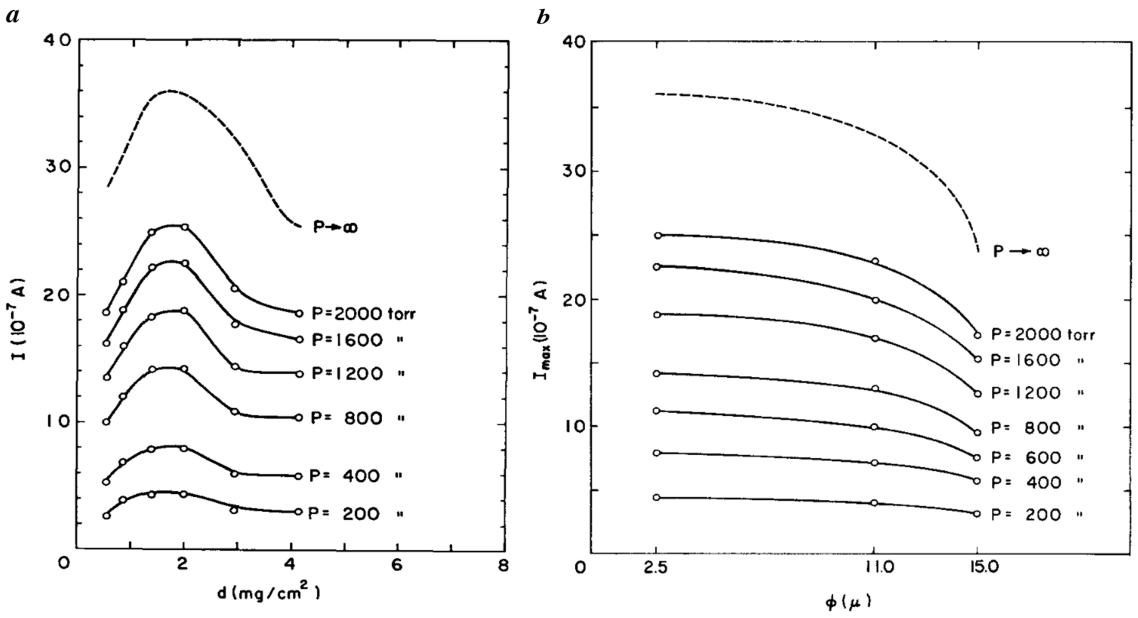

Figure 2.6: ***a***) Intensity as a function of the coating density of the phosphor (grain size $\phi = 2.5\ \mu$m). ***b***) Dependence of the maximum intensity on the grain size. Figures reproduced from [98].

Finally, these authors also studied the dependence of the luminous intensity on the phosphor grain size. As shown in Figure 2.6b, the maximum intensity values decrease when increasing grain size and this decrease becomes more pronounced as the pressure increases. The use of smaller phosphor grains implies then a higher light output but it cannot be forgotten either that the radiation damage is greater in small particles. It would then be necessary to find a compromise between the phosphor grain size that produces a good amount of light and also offers a strong resistance to radiation.

In recent years, research efforts have focused on optimizing the phosphor materials and the optimal coating conditions [101].

This self-powered illumination technology has found wide-ranging commercial applications, including illuminated watch hands and dials, fishing lures for night-time visibility, emergency exit signs, and military equipment. Prominent manufacturers in the U.S. include

Cammenga, Inc., known for its regulated tritium gas tube products used in military knives and compasses, as well as watch brands like Marathon and Ball Watch Company, who integrate tritium tubes into their tactical and luxury timepieces. In Europe, companies specialize in various niche applications of tritium gas technology. MB-Microtec (Switzerland) is a leading global provider of tritium gas tubes for military and safety signage, known for its high-reliability self-luminous products. Betalight (Netherlands) focuses on tactical illumination devices, including weapon sights and emergency lighting. Escape Light B.V. (Netherlands) develops compact safety and emergency lighting systems using tritium light sources. Smolsys Ltd. (Switzerland) advances applications in precision instrumentation and industrial safety.

Furthermore, the adaptability of this approach also enables emerging medical applications, such as the treatment of diabetic retinopathy using tritium-based radioluminescent contact lenses [102].

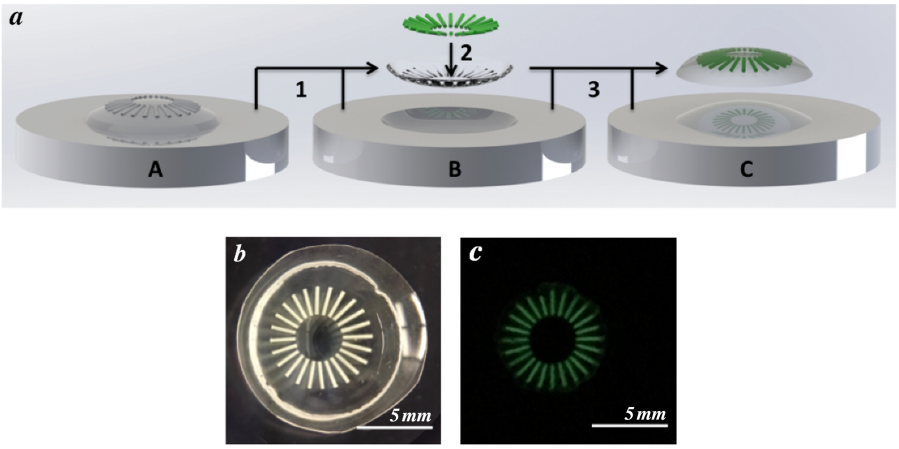

Figure 2.7: ***a***) Radioluminescent contact lens fabrication. ***b***) Image of lens under light conditions. ***c***) Image of lens under dark conditions. Figures reproduced from [102].

This approach may be interesting for this work, but the light production is greatly constrained by electron self-absorption, suggesting that other methods should be explored.

2.5.2 Liquid Tritium Light Sources

Another approach proposed in the literature involves the use of an inorganic liquid scintillator, which combines tritiated water (T_2O or HTO) with a luminescent solution [99, 103]. This mixture can then be encapsulated to create a RL device.

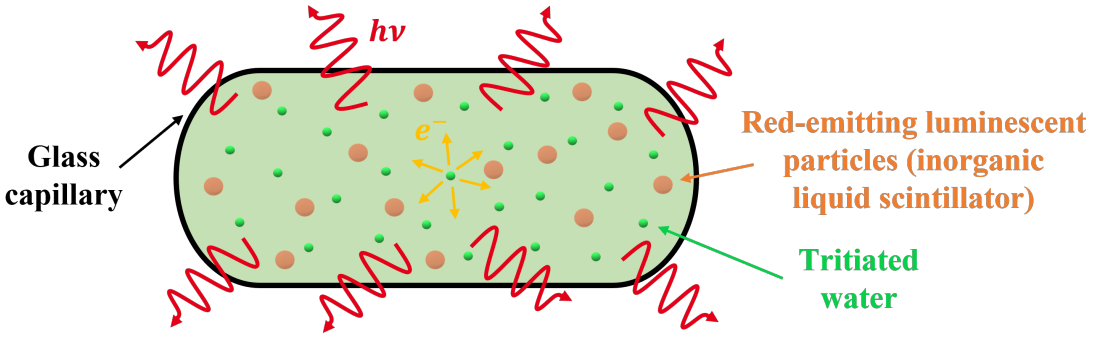

Figure 2.8: Diagram showing the operating principle of RL devices based on tritiated luminescent water.

The study by Hara et al. (2017) presents findings that may be valuable for the future development of the intended RL device.

The tritium content is measured using Liquid Scintillation Counting (LSC), a standard and sensitive technique for quantifying tritium in liquid samples. The authors have reported a radioactivity of approximately 12.3 MBq/mL, equivalent to about 0.33 μCi/mL.

The measured Photomultiplier Tube (PMT) output current, proportional to the emitted RL intensity, is plotted in Figure 2.9 as a function of the amount of tritiated water. This dependence exhibits a positive linear correlation, indicating that the emitted intensity scales directly with the amount of tritium present in the mixture.

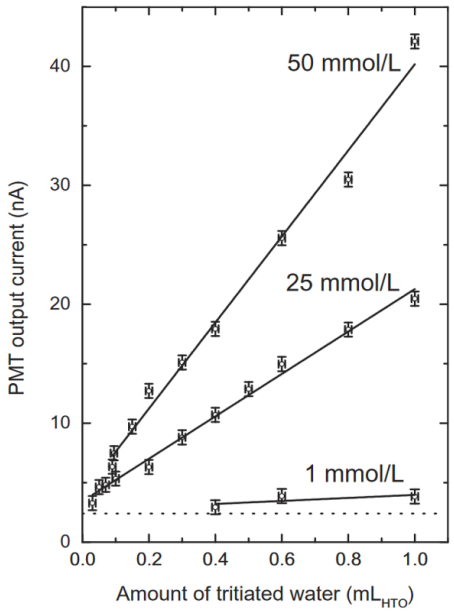

Figure 2.9: Dependence of the PMT output current on the amount of tritiated water. Figure reproduced from [103].

Moreover, the authors have also observed that the slope of this linear relationship depends on the concentration of the luminescent species, increasing with higher concentrations. This behavior arises because the RL intensity is influenced by how many luminescent particles are excited along the path of a beta electron; therefore, a higher concentration of luminescent materials generates a stronger output. However, care must be taken to avoid excessive concentrations, which can lead to photon self-absorption within the mixture, reducing emitted light.

Other limitations of this approach to consider include:

- Limited brightness: the mean free path of the most energetic tritium beta electrons is roughly 4 mm in air, but shrinks to approximately 8 μm in water, significantly restricting light output.

- Production complexity: manufacturing HTO-based scintillators is intricate and costly.

- Radiolysis: both T_2O and HTO molecules are able to self-radiolyze into free radicals and molecular gases (H_2, T_2, HT, O_2); generating internal pressures and complicating long-term device stability [99].

- Environmental exchange: tritiated water interacts readily with its surroundings, making containment challenging.

- Safety concerns: the chemical reactivity and mobility of tritiated water pose significant storage and safety issues. Because tritiated water is chemically identical to ordinary water, it can easily diffuse through materials, permeate biological tissues, and integrate into metabolic pathways, making containment and decontamination particularly difficult.

Therefore, these factors limit the practical use of tritiated water-based liquid scintillators for the purpose envisioned in this work. Despite these drawbacks, scintillation counting using tritiated mixtures remains indispensable in bioscience and nuclear technology, particularly for radiolabeling to monitor the biodistribution of protein-drug conjugates in medical treatments [104], where HTO and organic phosphors are typically employed.

2.5.3 Solid-state Tritium Light Sources

A third strategy also discussed in the literature involves Solid-state Radioluminescent Light Sources (SRLS), where a host solid matrix contains both luminescent materials and tritium, as illustrated in Figure 2.10.

The existing kinds of SRLS can be classified according to the composition of their host matrices and luminescent materials into: pure organic, organic/inorganic mixed (hybrid) and pure inorganic.

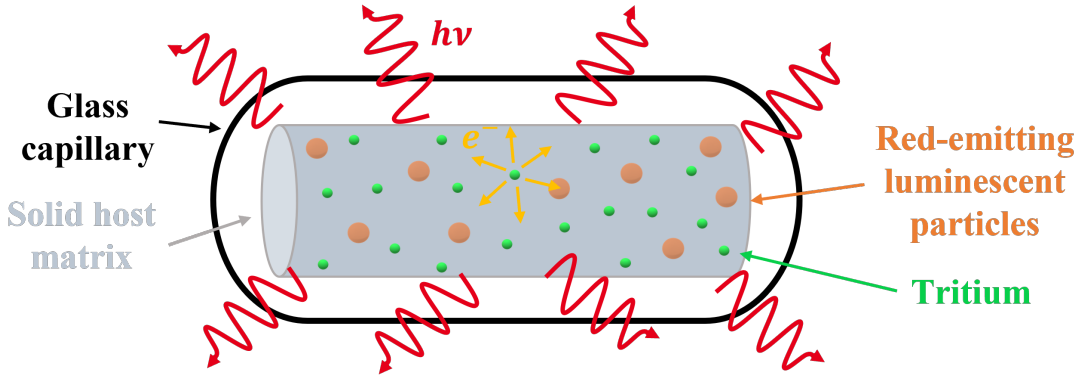

Figure 2.10: Diagram showing the operating principle of a SRLS.

2.5.3.1 Pure Organic Formulations

2.5.3.1.1 Tritiated DEB Matrix Containing Organic Phosphors

A pure organic formulation involves blending tritium with organic materials. Specifically, tritium is covalently bound within a transparent polymeric matrix containing soluble organic scintillant dyes [105, 106]. Figure 2.11 schematizes the resulting structure of the proposed approach.

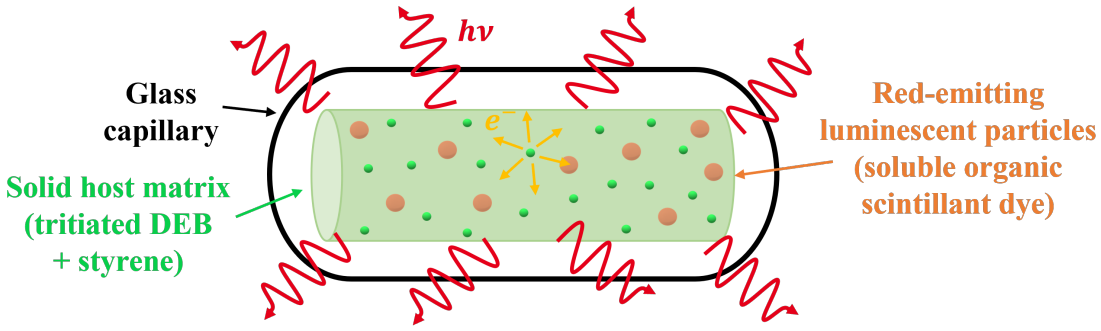

Figure 2.11: Diagram showing the operating principle of a SRLS based on a tritiated DEB matrix containing organic phosphors.

The host matrix is an optically clear organic matrix based on 1,4-bis(phenylethynyl)benzene (DEB). In order to tritiate the DEB matrix, tritium is added across the ethynyl linkages in the presence of Pd catalyst loaded on carbon black. Once the compound is tritiated, it is separated from the catalyst and mixed with a liquid styrene solution already containing the organic scintillant dye. Subsequently, styrene polymerizes incorporating both the tritiated DEB and the luminescent dye particles into the solid polymer matrix.

Renschler at al., the authors of this 1994 study, have demonstrated interesting results. For example, brightness increases proportionally with the amount of tritium incorporated (shown in Figure 2.12a), reaching up to about 75 Ci/mL. The tritium loading is inferred indirectly through precise control of gas pressure and measurement of tritium gas consumption during the chemical tritiation reaction of DEB.

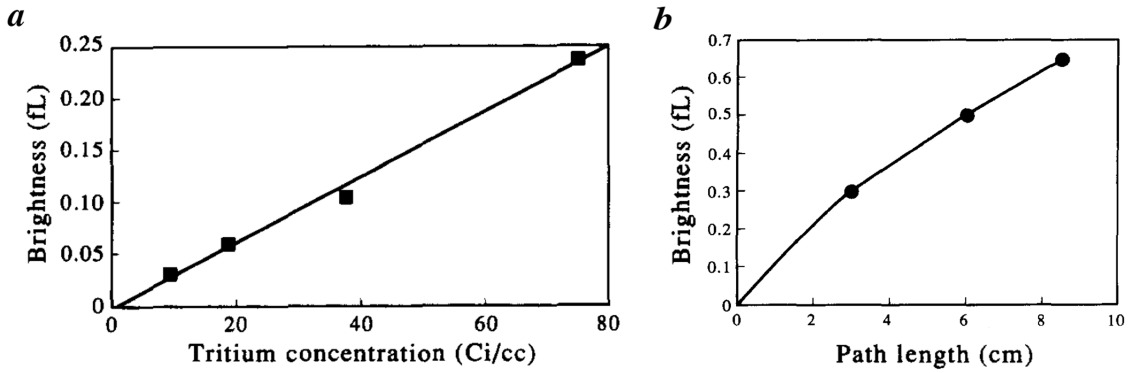

Figure 2.12: ***a***) Brightness measured (in fL, being 1 fL $\sim$ 0.6 mW/(sr·m^2)) from a tritiated DEB matrix and sealed in a 3 cm ampoule, plotted as a function of tritium concentration. ***b***) Brightness measured from several tritiated DEB samples and 9.2 Ci/ml of tritium placed in glass tubes of 3, 6 and 9 cm in length. Reproduced from [106].

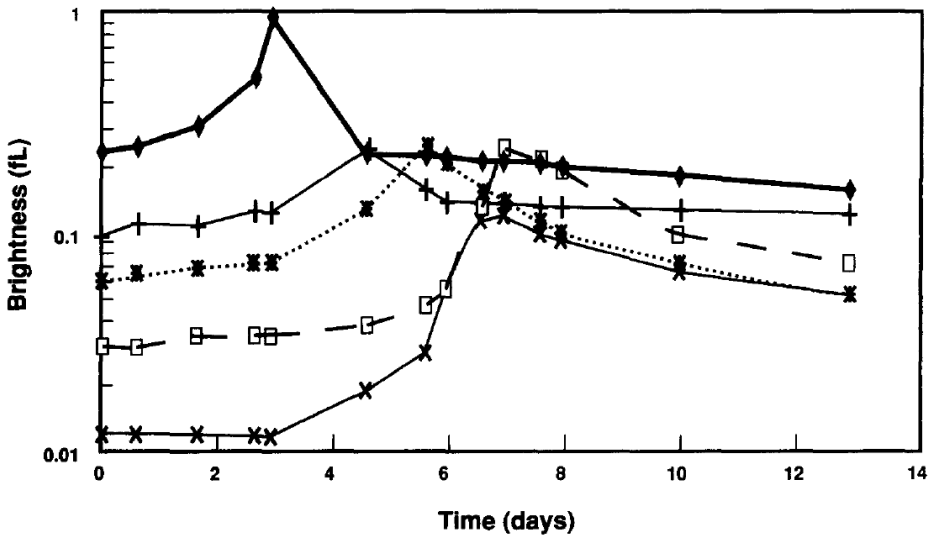

Figure 2.13: Brightness measured from several tritiated DEB samples containing rubrene and different concentrations of tritium placed in glass tubes of different lengths, as a function of time. 75 Ci/ml and 3 cm (♦), 37 Ci/ml and 3 cm (+), 19 Ci/ml and 3 cm (∗), 9.4 Ci/ml and 3 cm (□) and 9.4 Ci/ml and 1.3 cm (×). Reproduced from [106].

Additionally, the light output rises as the thickness of the RL device increases, but beyond

a certain size, the gain becomes less significant. This trend, displayed in Figure 2.12b, establishes an upper limit on the practical size of these all-organic SRLS, with the maximum effective glass tube length being approximately 8–10 cm.

These results coincide with what has been observed in the other approaches described in previous sections, but what is truly interesting about this work is the study of the evolution of brightness over time. The brightness of these SRLS increases markedly over the first few days following the preparation, as styrene polymerizes. The output reaches a maximum at the point of solidification, as shown in Figure 2.13. After complete polymerization, the light intensity begins to decrease, likely due to radiation-induced aging effects.

Despite these promising features, and although purely organic compounds allow for high tritium incorporation, they exhibit several drawbacks. These include the very low radiation resistance of organic phosphors, rapid degradation of brightness over time, and limited ability to retain tritium within the matrix.

2.5.3.2 Hybrid Formulations

2.5.3.2.1 Tritiated Rare Earth-Exchanged Dried Zeolites

A hybrid SRLS approach described in the literature involves the use of dried zeolites whose mobile sodium ions are exchanged for rare earth ions. After that, tritiated water (T_2O) is sorbed by the dried zeolites. The structure resulting from this approach is illustrated in Figure 2.14.

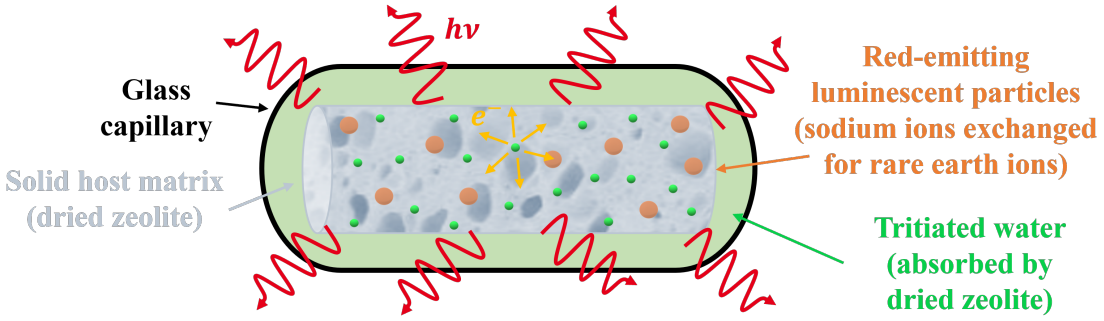

Figure 2.14: Diagram showing the operating principle of a SRLS based on tritiated rare earth-exchanged dried zeolites.

Zeolites are well-known drying agents owing to their porous structure, which strongly attracts small molecules like water. They have also been widely used as ion-exchange media, where the sodium ions in their lattice are replaced by other positively charged ions

via immersion in aqueous solutions. Their exceptional radiation stability has made them useful for capturing radioactive ions from nuclear power plant waste water, producing isotopes through neutron irradiation, and trapping tritiated water from tritium handling exhausts.

Gill et al. (1992) explored this concept where sodium ions in the zeolite were exchanged for rare earth ions, and the dried zeolite subsequently absorbed tritiated water. In a glass tube containing 53 mg of such zeolite, the total tritium content was estimated to be 36 Ci. The total tritium content is estimated from the known quantity of tritiated water vapor introduced and sorbed by the zeolite, which has been previously determined by LSC measurements.

Regarding longevity, the light output remained stable without diminishing over six weeks, as shown in Figure 2.15.

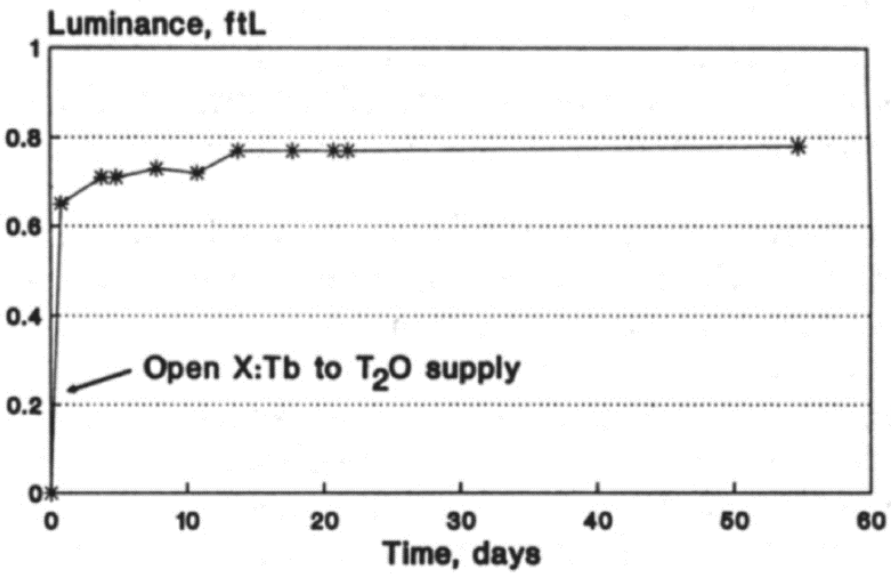

Figure 2.15: Evolution of luminance over time for a SRLS based on zeolites (being 1 fL $\sim$ 5.02 mW/(sr$\cdot$ m^2)). Reproduced from [107].

However, zeolite-based SRLS devices are less efficient than conventional tritium gas tubes, suggesting suboptimal coupling between the β^--emissions from tritium and the luminescent rare earth centers in the zeolites. To address this, the authors proposed combining different zeolite lattice types and rare earth ions, potentially including small organic molecules within the lattice to improve energy transfer and brightness.

They also pointed out that the zeolite bulk impedes the exit of photons, since they have observed that when there were gaps in the bulk, the luminous intensity was higher in

that area. To mitigate this, zeolites have been dispersed in transparent matrices such as methylmethacrylate and styrene-butadiene copolymers. Unfortunately, these composites showed reduced light output compared to pure zeolites and darkened within a week. The authors attributed this to possible T_2O leakage during sample preparation and noted the overall instability of these samples under beta radiation. They suggested that alternative host matrices, such as methane or acetylene polymers, may offer improved stability and performance.

2.5.3.2.2 Tritiated Siloxane Matrix and Inorganic Phosphors

Another hybrid RL approach, schematized in Figure 2.16, utilizes a tritiated siloxane embedded within a polydimethylsiloxane (PDMS) matrix, and containing suspended inorganic phosphor particles [106].

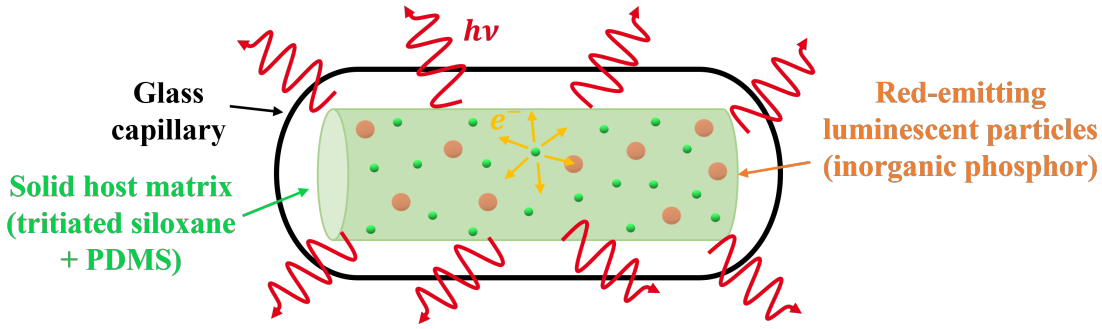

Figure 2.16: Diagram showing the operating principle of a SRLS based on tritiated siloxane embedded within a PDMS matrix, containing inorganic phosphor particles.

Each siloxane compound is mixed with an activated carbon catalyst (5% Pd on carbon), and tritium gas is introduced to tritiate the siloxane via chemical addition. After the tritiation reaction, the mixture is dissolved in petroleum ether to allow the removal of the catalyst. Petroleum ether is then evaporated by vacuum distillation, yielding purified tritiated siloxane. The next step involves adding the PDMS compound and the selected inorganic phosphor.

The tritium loading is determined by stoichiometric calculation during synthesis and by monitoring gas uptake during the tritiation process, specifically by measuring the decrease in gas pressure, which indicates the amount of tritium consumed in the reaction. The tritium loadings achieved in these experiments range from 10 Ci/cm^3 up to 193 Ci/cm^3.

Renschler at al. plotted in 1994 the evolution of sample brightness over time, as shown in Figure 2.17. Samples 1 and 2 incorporate a PDMS matrix, while samples 3-7 are composed

only of the siloxane and the phosphor. As it can be observed, the absence of PDMS result in higher brightness values. Sample 7 employs a phosphor whose surface has been modified by treatment with hexyl alcohol, resulting in a more hydrophobic surface and thereby improving the compatibility with the hydrophobic PDMS and/or siloxane matrix. This treatment has had a significant effect, as sample 7 exhibits the highest brightness level, even though it does not contain the highest tritium concentration.

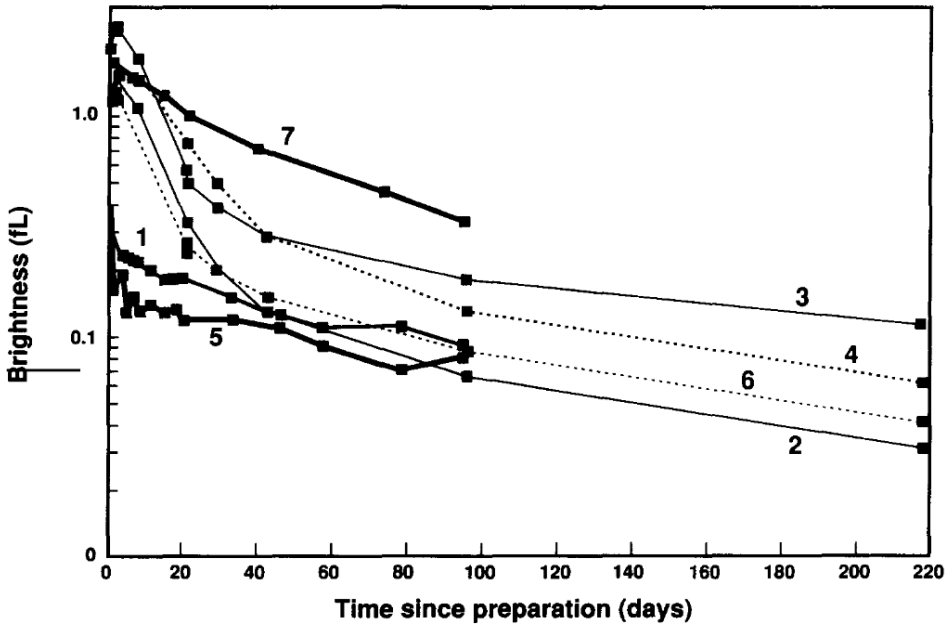

Figure 2.17: Brightness (being 1 fL $\sim$ 7.97 mW/(sr$\cdot$ m^2)) measured as a function of time, for several formulations of tritiated siloxanes and inorganic phosphors.

However, a major complication encountered in all siloxane-based experiments is the volatility of the tritiated siloxane compounds, which tend to vaporize, migrate, and even recondense elsewhere in the vial, sometimes leading to yellowing of the epoxy vial seal. The decay in brightness over time arises from both migration-induced matrix yellowing and loss of tritiated siloxane. Additionally, although inorganic phosphors themselves are generally radiation-resistant, these hybrid tritiated formulations show rapid degradation in brightness due to energy transfer losses within the matrix and degradation of the tritiated siloxane component.

2.5.3.3 Inorganic Formulations

2.5.3.3.1 Tritiated Titanium with Inorganic Phosphor Coating

An inorganic formulation found in the literature is coating a phosphor screen on a tritiated titanium substrate [108]. The schematic structure of the desired RL device based on this approach is shown in Figure 2.18.

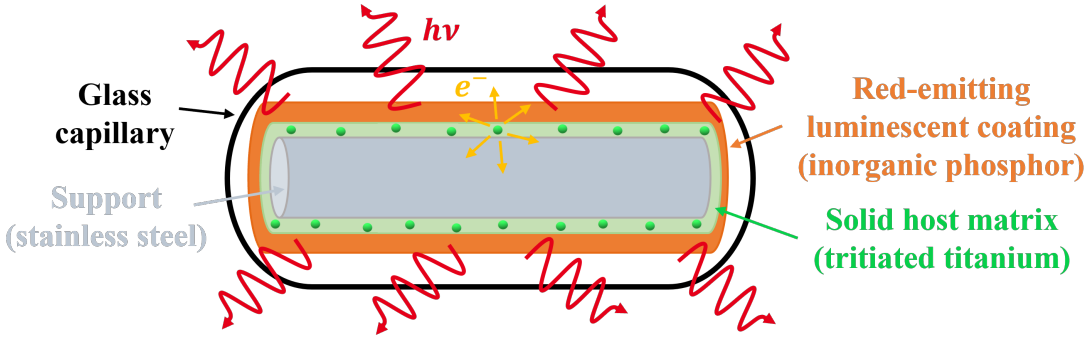

Figure 2.18: Diagram showing the operating principle of a SRLS based on tritiated titanium with an inorganic phosphor coating.

In order to provide the tight contact between phosphor and tritium, the phosphor screens are coated directly on the tritiated titanium matrix. For this reason, the phosphor coating has to meet several requirements, such as the strength of fixation on the substrate, the coating uniformity and the coating thickness. The optimal thickness of the phosphor screen is an important factor that should be taken into account. If it is too thin, it will not be able to provide high brightness while if it is too thick, it will absorb most of the produced photons. Moreover, the coating should be uniform enough to cover all the surface of the tritiated matrix and provide uniform lightning.

Zelenina et al. (2019) have developped a laboratory prototype featuring a titanium plate with a thickness of 0.5 μm, resulting in a tritium tank with a surface area of 1 cm^2 and 420 mCi (authors do not specify the technique used to determine the tritium activity). This titanium layer is deposited on a stainless steel plate, which serves as mechanical support. The authors have determined that the optimal phosphor mass density is approximately 4–5 mg/cm^2, corresponding to a phosphor screen thickness of about 20 μm.

Regarding limitations, depending on the dimensions of the desired RL device and the amount of tritium that can be loaded into the titanium layer, it would be necessary to evaluate whether the thickness of the titanium layer is mechanically stable enough on its own or if the steel plate is required. In any case, this approach is not the most interesting if

the volume of the matrix is not entirely active, in the sense that the steel plate would not act as a β-reservoir but only provide support.

2.5.3.3.2 Inorganic Phosphors Embedded in Tritiated Silica Aerogels

A second and last inorganic SRLS formulation found in the literature is the tritiation of silica aerogels containing inorganic phosphors [106]. The resulting structure of the proposed approach is illustrated in Figure 2.19.

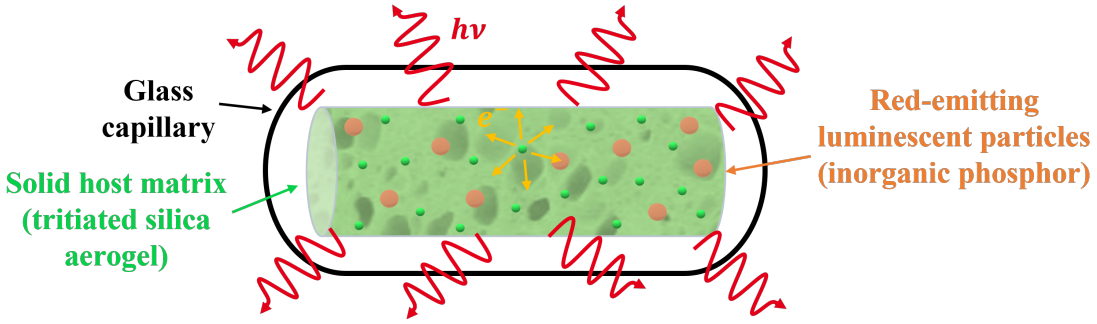

Figure 2.19: Diagram showing the operating principle of a SRLS based on inorganic phosphors embedded in tritiated silica aerogels.

To load tritium in aerogels, authors have followed three different strategies: (i) filling the aerogel pores with tritium gas, (ii) using Hydrogen Isotope Exchange (HIE) from tritium gas, where exchangeable hydrogens residing on the aerogel would be replaced by tritium, and (iii) absorption of tritiated water by the aerogel.

Results from Renschler et al., published in 1994, are particularly interesting and could inspire the development of the desired RL device. However, they employ green-emitting phosphors.

For tritium gas experiments, aerogels are placed in glass tubes and exposed to a tritium gas atmosphere while the pressure increases up to 0.14 MPa (1.4 bar), the maximum pressured used. Figure 2.20 shows the brightness of a silica aerogel loaded with inorganic phosphors (represented by ○) as a function of the tritium gas pressure. A nearly linear increase in optical brightness is observed up to the experimental limit of 0.14 MPa (1.4 bar). At the time of pressurization, the excitation is assumed to result solely from the tritium gas trapped within the pores of the aerogel. For comparison, data for bulk phosphor (represented by ●) are also provided, exhibiting a lower increase in brightness.

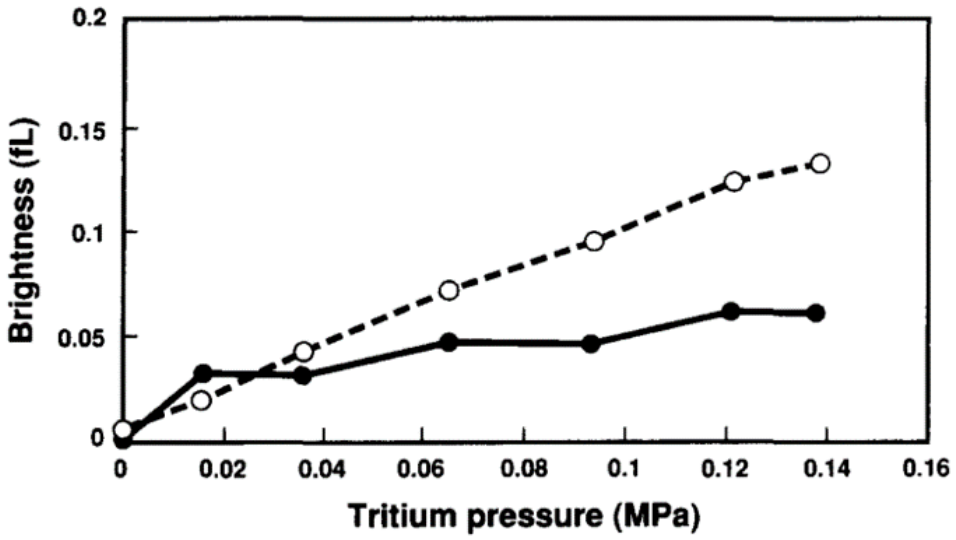

Figure 2.20: Brightness measurements of a silica aerogel loaded with inorganic phosphors (○) as a function of the tritium gas pressure. Data obtained on bulk phosphor (●) is provided for comparison. Reproduced from [106].

The glass tubes are then sealed at 0.14 MPa (1.4 bar), resulting in an initial brightness of 0.12 fL (0.6 mW/(sr·m^2)). However, the light output increases with time and reaches a maximum brightness of 0.31 fL (1.6 mW/(sr·m^2)) after about 60 days, as shown in Figure 2.21. At 135 days, the gas is evacuated from the tube and found to contain more than 60% hydrogen, approximately 30% tritium and traces of tritiated methane (CT_4) as well as around 4% ^{3}He. After removal of the tritium gas, the sample retains a brightness of 0.2 fL (5.2 mW/(sr·m^2)), corresponding to about 65% its maximum light output, as a stable residual glow. This result suggests that most of the tritium becomes chemically bound to the composite, effectively forming a SRLS.

A second tritiation of the sample shown in Figure 2.21 is carried out after approximately 180 days. This second exposure results in an even higher light output equal to 0.44 fL (2.2 mW/(sr·m^2)) with a shorter time constant compared to the first exposure. This difference is likely due to changes in the surface population of exchangeable species at the time of tritium loading. These results suggest that controlled loading of tritium in multiple time steps may be a route to brighter SRLS.

The sample remains clear (i.e., no radiation-induced darkening) and retains a brightness level of approximately 0.44 fL (2.2 mW/(sr·m^2)) after 850 days. A slight decrease in brightness, corresponding to a 5% per year and shown as a dashed line, is expected due to tritium decay.

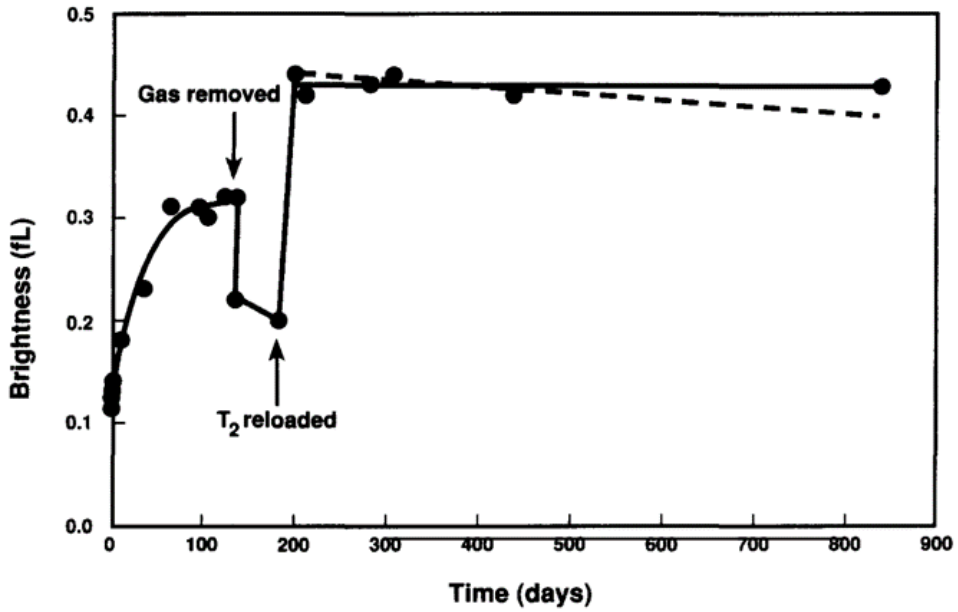

Figure 2.21: Brightness measurements of a silica aerogel loaded with 0.25 g/cm^3 of ZnS:Cu,Al (○) and sealed in a glass tube at 0.14 MPa (1.4 bar), as a function of time. Dashed line represents expected loss due to tritium decay. Reproduced from [106].

To estimate the optimal phosphor concentration, aerogels with different phosphor concentrations, ranging from 0.01 to 0.5 g/cm^3, are prepared and loaded with tritium gas to a pressure of 0.14 MPa (1.4 bar). As shown in Figure 2.22, light output increases with higher phosphor loading. Samples with phosphors concentrations greater than 0.5 g/cm^3 contain aggregates of phosphor particles, as observed by SEM. These samples are not loaded with tritium gas because particle aggregation would severely limit light output. Improved dispersion of phosphor particles should allow for higher phosphor concentrations and result in higher light output. Phosphor concentration cannot be increased indefinitely, even in the absence of aggregation. Eventually, the light output will diminish to a level comparable to that of the bulk phosphor powder, where most of the light originates in the near surface region.

Authors have also studied the behaviour of silica aerogels under high pressures of tritium gas. Figure 2.23a shows a plot of the light output as a function of tritium pressure in 1 MPa (10 bar) increments up to 10 MPa (100 bar). As can be seen, the output is not quite linear with pressure over the entire range, suggesting some absorption of beta energy by tritium gas.

The sample is introduced in a glass tube and sealed at 10 MPa to study the evolution of RL over time. Its light output is periodically measured over a 235-day period. As can be seen

in Figure 2.23b, the intensity initially decreases by a 10% within the first few days, but then declines to 13% of its initial value over the remaining time. The expected intensity based on tritium decay is also plotted. As observed, the experimental decay is considerably faster. Several explanations are possible for this relatively rapid decline in light intensity; however, the authors suggest that the most likely cause is deactivation of the luminescent centers in the phosphor by high pressure tritium.

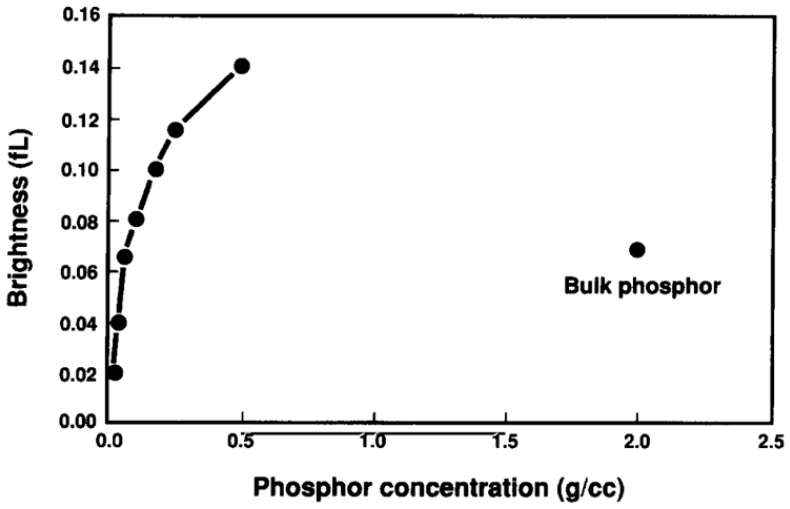

Figure 2.22: Brightness measurements of silica aerogels loaded with inorganic phosphors, sealed in a glass tube at 0.14 MPa (1.4 bar). For comparison, the brightness of the bulk phosphor powder is also plotted. Reproduced from [106].

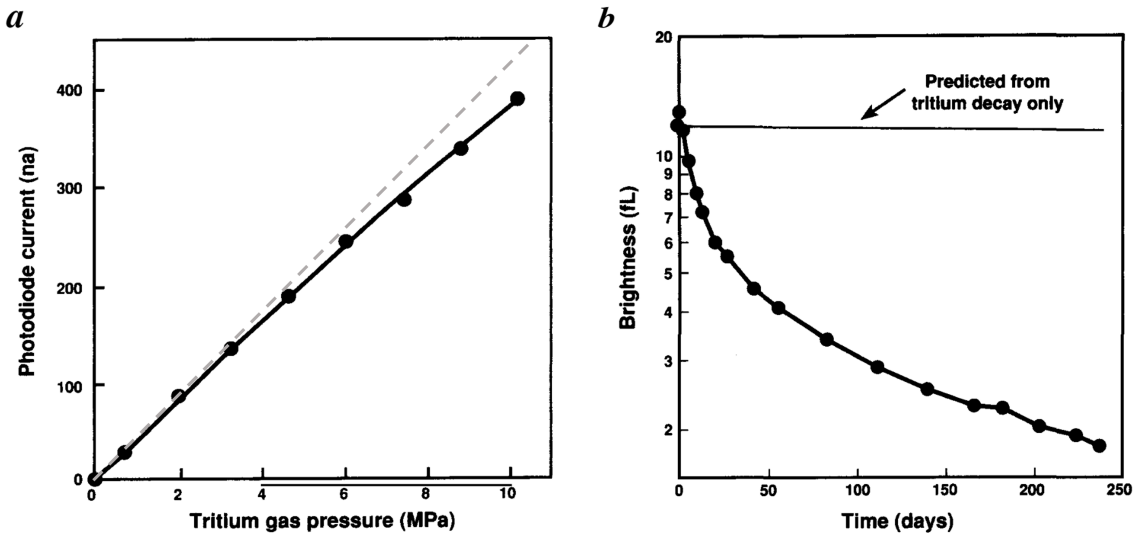

Figure 2.23: ***a***) Light output from a silica aerogel as a function of tritium gas pressure. ***b***) Brightness measured for the same sample placed in a glass tube and sealed at 10 MPa of tritium gas, as a function of time. Reproduced from [106].

Regarding tritiated water experiments, authors also placed silica aerogels containing inorganic phosphors in small glass tubes and exposed them for several days to vapors from tritiated water. The brightness increases immediately upon exposure, reaching a peak value of 4.6 fL (23.1 mW/(sr·m^2)). Although this approach produced significantly higher brightness than that achieved with tritium gas, its practical application is limited by the biohazard associated with tritiated water.

The proposed strategy of a SRLS based on an aerogel tritiated with gaseous tritium therefore stands out as the most promising approach.

2.6 Conclusion

In summary, among the various strategies for developing radioluminescent devices, tritiated water is unsuitable due to the limited mean free path of β-particles in water, which significantly reduces light output, and its inherent biohazard. Traditional GTLS radioluminescent systems based on tritium gas face major limitations from β-particle self-attenuation and the opacity of thick phosphor layers, which restrict their overall efficiency. In contrast, SRLS present a more promising pathway.

Among the SRLS investigated in this chapter, approaches based on aerogels loaded with tritium gas and containing phosphors emerge as the most advantageous strategy due to their high specific surface area, transparency, and ability to uniformly disperse phosphor particles throughout the matrix, closely approximating the ideal configuration for efficient light production. Moreover, aerogels offer enhanced robustness, safety, and design flexibility compared to gas tubes. However, optimizing SRLS still requires addressing several critical challenges, such as the incorporation of tritium within the aerogel matrix, the development of efficient luminescent materials, and ensuring the radiation stability of the system as well as an effective radiation containment.

Radioluminescence et Stratégies pour le Développement des Sources Lumineuses Radioluminescentes pour la Photobiomodulation

Résumé du Chapitre

En résumé, parmi les différentes stratégies de développement des dispositifs radioluminescents, l'utilisation de l'eau tritiée est inadaptée en raison du parcours moyen limité des particules beta dans l'eau, ce qui réduit significativement la production lumineuse, ainsi que de son danger biologique inhérent. Les systèmes radioluminescents traditionnels à base de gaz de tritium (GTLS) sont confrontés à d'importantes limitations dues à l'auto-atténuation des particules beta et à l'opacité des couches épaisses de matériaux luminescents, ce qui restreint leur efficacité globale. En revanche, les sources radioluminescentes solides (SRLS) représentent une voie plus prometteuse.

Parmi les SRLS étudiées dans ce chapitre, les approches basées sur des aérogels chargés de gaz tritium et contenant des matériaux luminescents apparaissent comme la stratégie la plus avantageuse, grâce à leur grande surface spécifique, leur transparence et leur capacité à disperser uniformément les particules luminescentes dans toute la matrice hôte, ce qui se rapproche de la configuration idéale pour une production lumineuse efficace. De plus, les aérogels offrent une robustesse, une sécurité et une flexibilité de conception accrues par rapport aux tubes à gaz. Cependant, l'optimisation des SRLS nécessite encore de relever plusieurs défis critiques, tels que l'incorporation du tritium dans la matrice hôte d'aérogel, le développement de matériaux luminescents performants, ainsi que la stabilité face aux radiations et un confinement efficace des radiations.

Chapter 3

Design and Fabrication of a Radioluminescent Device

Having adopted the strategy of using a radioluminescent aerogel for the development of an implantable radioluminescent device, several key technical questions arise. Which host materials are suitable for simultaneously containing tritium and luminescent particles? At what wavelength should the emitted light be, given that this will influence the choice of luminescent materials? What level of luminous intensity is required? What should be the dimensions of the device? These questions, along with the development of the radioluminescent device itself, will be addressed in detail in the following chapter, considering that the radioluminescent implant must meet the safety standards required for medical applications.

3.1 Device Specifications

The desired radioluminescent device must meet several requirements:

- The host matrix must play the role as both tritium and luminescent material reservoir.
- It must emit light in the [600, 1000] nm range. More specifically, to achieve light emission near 670 nm, which is the wavelength currently used in the ongoing clinical trial at Clinatec.
- As for the minimum optical power required, no standard has been established to date and it is largely application-dependent, as already discussed in section 1.4.5 of

chapter 1. However, the device used in the clinical trial delivers pulsed light with a peak power of 15 mW/cm^2 and an average power of 0.23 mW/cm^2. Therefore, the objective here for the radioluminescent device is to maximize the achievable optical power.

- To overcome safety issues, the radioluminescent material will be encapsulated in borosilicate glass to confine both the beta particles emitted by tritium and the bremsstrahlung radiation, as detailed in section 2.4 of chapter 2. Additionally, this encapsulation prevents the possible release of tritiated species.

- In terms of dimensions, the radioluminescent device could be assimilated to the electrodes used in DBS (neurosurgical treatment described in section 1.3.2 of chapter 1), which have an outer diameter of 1.27 mm. It must also be noted that for the ongoing clinical trial, the optics fiber is inserted in a PTFE cathether (permanently implanted) whose outer diameter is 2 mm. However, in this exploratory work, the first proof-of-concept will consist of an aerogel with a diameter of 3 mm, selected for technical convenience, encapsulated in borosilicate glass with a thickness of 500 μm to 1 mm. The resulting device will therefore have an overall diameter of 4–5 mm. The aerogel will have a length of 10 mm, resulting in a total device length of 11–12 mm after encapsulation. The ultimate objective of this work will be to develop a smaller aerogel with a 1 mm diameter.

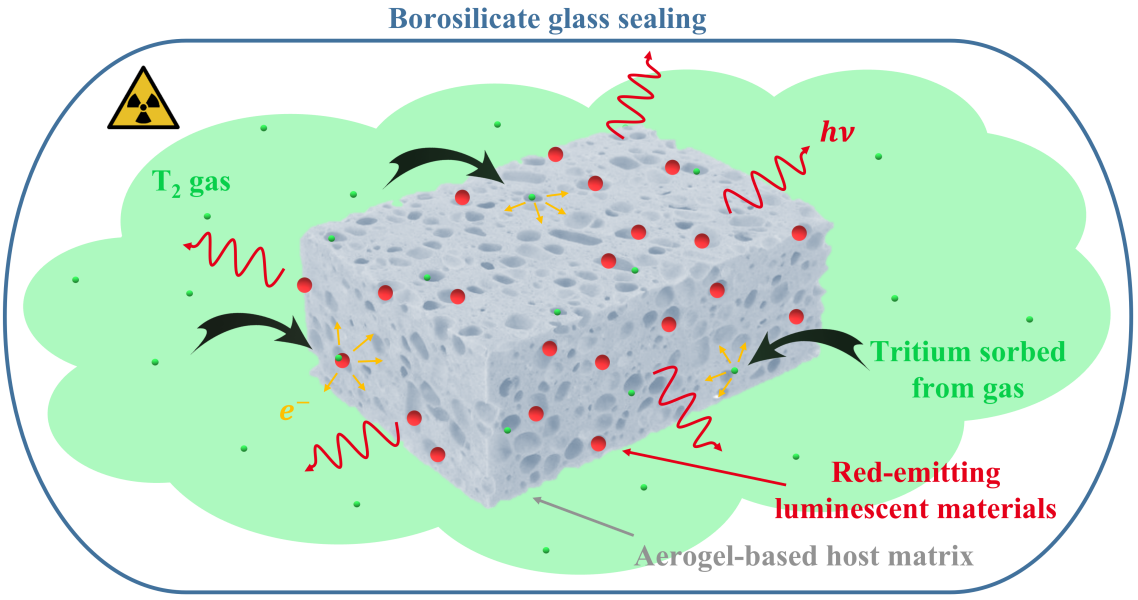

Figure 3.1: Design of the future implantable radioluminescent device.

Therefore, the above proposed SRLS device contains (i) a host matrix acting as a reservoir for both (ii) tritium sorbed from gas and (iii) red-emitting luminescent materials. The whole will be integrated inside a borosilicate glass capsule, which will then be sealed to ensure that the radioactivity is fully contained within, making the device safe for external handling, as illustrated in Figure 3.1.

3.2 Choice of Materials

The role of the host matrix is not only to maximize the interaction between tritium gas and luminescent particles, but also to allow the photons emitted by the luminescent materials to pass through. First, this can be achieved with a highly porous material, which increases the penetration depth of electrons due to their longer mean free path in porous structures and provides a larger accessible surface area for tritium gas compared to bulk materials. Second, the host matrix must be transparent in the 600–1000 nm range.

An aerogel-based matrix fulfills these criteria due to its unique properties, including extremely low density from approximately 0.05 to 0.5 g/cm^3, high porosities ranging from 80% to nearly 99.9%, and specific surface areas between 10 and over 1600 m^2/g [109]. These values are highly sensitive to synthesis routes, gelation mechanisms, aging conditions, and drying processes, which collectively determine the final porous structure of the aerogel. In this work, two types of aerogels have been selected for study: sodium carboxymethyl cellulose (CMC) aerogels and silica aerogels. They are compared with the aim of identifying potential differences in behavior or performance between organic and inorganic approaches.

Regarding the radioactive source, tritium has been selected for this purpose as previously discussed in section 2.3 of chapter 2. Tritium, $^3_1$H, has one proton and two neutrons in its nucleus. This distinguishes it from protium, $^1_1$H, which has one proton and no neutrons; and from deuterium, $^2_1$H, which has one proton and one neutron. The tritium beta decay is described by Equation 2.6 from the previous chapter. Through this decay, there is the emission of an electron as well as an antineutrino, and it transforms into a helium-3 nucleus. The emitted beta particles have a mean energy of 5.7 keV and a maximum energy of 18.6 keV, as shown in Figure 3.2, making them easy to confine and enabling the design of a non-radiotoxic device, even if it is powered by a radioactive source. Tritium's half-life of about 12.3 years suggests that medical devices incorporating it could operate for 20 years or even more, making them suitable for the treatment of chronic conditions. Furthermore, tritium and the risks associated with its use have been extensively studied [96].

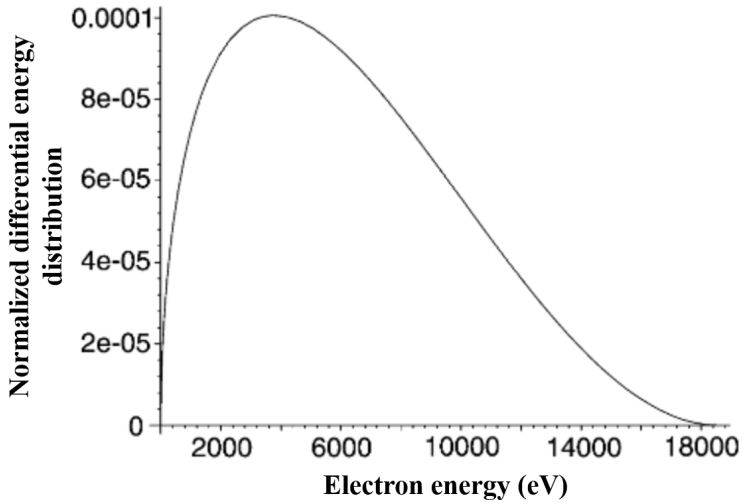

Figure 3.2: Tritium beta spectrum. Figure adapted from [110].

As for the red-emitting luminescent materials, four different types have been selected and evaluated in terms of performance:

- Europium-doped yttrium oxide (Y_2O_3:Eu^{3+}) phosphor, provided by Phosphor Technology (ref. QK63/N-C1), with a particle size of approximately 8.0 μm and an emission wavelength at 611 nm. Its crystal lattice is the ordered cubic-C bixbyite phase [111].

- Europium-doped yttrium vanadate (YVO_4:Eu^{3+}) phosphor, synthesized in-house (at CEA/DES/LITEN[1]), featuring a particle size of 20 nm and emitting at 614 nm. It exhibits a tetragonal zircon-type structure [112].

- Quantum Dots (QDs) with a core of silver indium sulfide and a shell of zinc sulfide ($AgInS_2$/ZnS), also synthesized in-house (at CEA/DRF/IRIG[2]), with a size of 2.5 nm and an emission wavelength of 646 nm. It typically crystallizes in a chalcopyrite crystal structure [113].

- QDs with a core of copper indium sulfide and a shell of zinc sulfide ($CuInS_2$/ZnS), likewise prepared in-house (at CEA/DRF/IRIG), measuring close to 3 nm in size and emitting at 686 nm. It also has a chalcopyrite crystal structure [113].

[1]Commissariat à l'Energie Atomique et aux Energies Alternatives/Direction des Energies/Laboratoire d'Innovation pour les Technologies des Energies Nouvelles et les Nanomatériaux

[2]Commissariat à l'Energie Atomique et aux Energies Alternatives/Direction de la Recherche Fondamentale/Institut de Recherche Interdisciplinaire de Grenoble

Within these luminescent materials, a distinction is made between phosphors and QDs, which exhibit different luminescence mechanisms.

Figure 3.3 illustrates the energy diagram of the phosphorescence process in inorganic phosphors doped with Eu^{3+}. The incident energy, either from a photon in Photoluminescence (PL) or an electron in Cathodoluminescence (CL) or RL, is absorbed by the system, promoting an electron from the ground state of the host lattice to an excited state. The excited electron seeks to return to a relaxed state, releasing the excess energy in the process. Part of this energy is dissipated through internal energy conversion, a non-radiative process, where the electron relaxes to the excited $^5D_0$ state among the discrete energy levels introduced by the Eu^{3+} dopants within the band gap. From this excited state, several radiative transitions occur down to lower-energy ^7F_J states (notably $^7F_2$, $^7F_1$, and $^7F_0$), leading to the emission of photons in a process known as phosphorescence. Finally, electrons residing in these ^7F_J ground states relax back to the ground state of the host lattice through non-radiative pathways, completing the energy dissipation cycle.

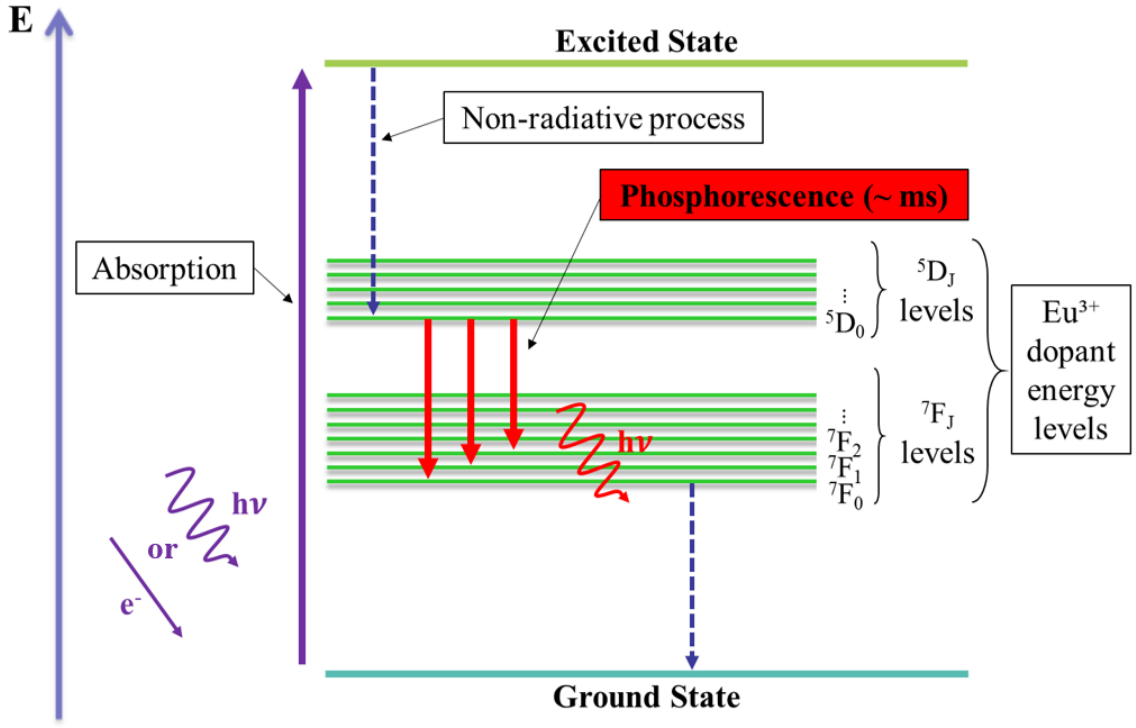

Figure 3.3: Simplified energy diagram, also called Perrin-Jablonski diagram, illustrating the phosphorescence process in inorganic phosphors doped with Eu^{3+}.

This phosphorescence process contrasts with the fluorescence observed in QDs. In QDs such as $AgInS_2$ and $CuInS_2$, the luminescence process is dominated by fluorescence emission. Due to their nanoscale size, these semiconductor quantum dots exhibit discrete, quantized energy levels that replace the continuous Valence Band (VB) and Conduction Band (CB) of bulk materials. As shown in Figure 3.4, as the QDs become smaller, the energy gap between the quantized ground and excited states increases, and therefore the wavelength of the photons emitted by fluorescence becomes shorter, shifting towards the blue.

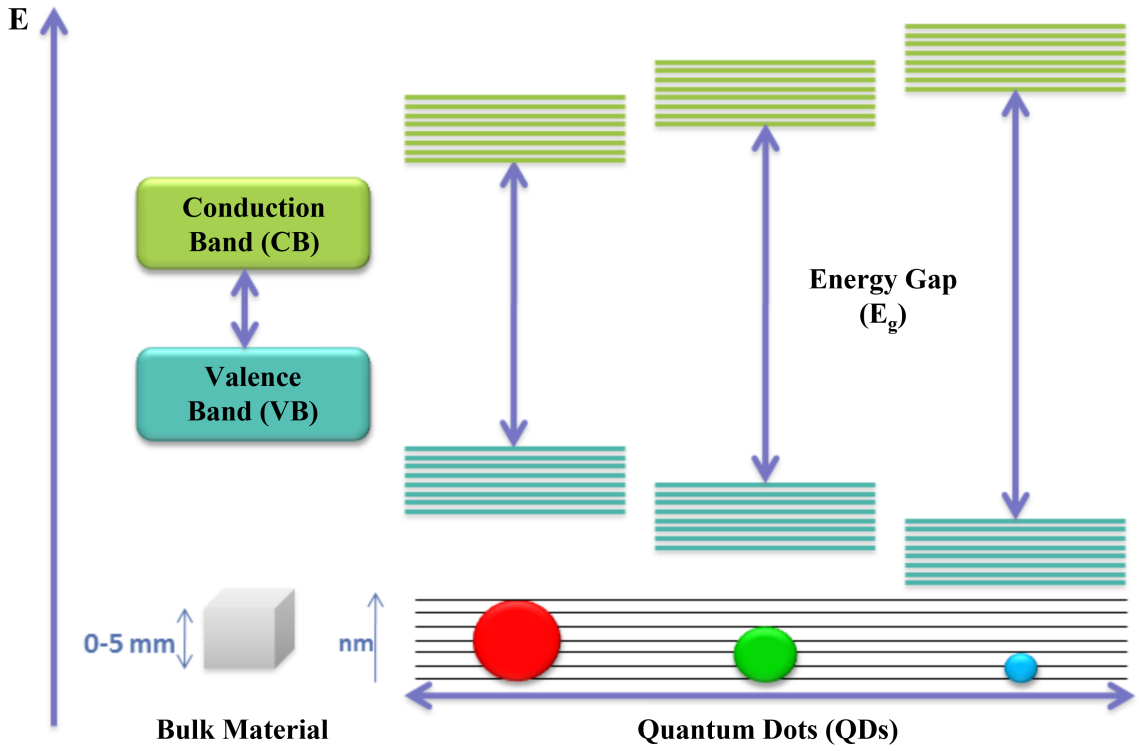

Figure 3.4: Evolution of fluorescence properties for decreasing sizes of QDs. Adapted from [114].

Upon excitation, electrons in QDs are promoted to quantized CB states and subsequently recombined radiatively with holes in the VB or in defect/trap states within the band gap. Figure 3.5 schematizes the fluorescence process in QDs. This radiative recombination results in photon emission with relatively short lifetimes, typically on the order of nanoseconds to hundreds of nanoseconds, characteristic of fluorescence, whereas phosphorescence lifetimes, such as those observed in Eu^{3+}-doped inorganic phosphors, are significantly longer, often ranging from milliseconds to seconds. Both $AgInS_2$ and $CuInS_2$ QDs share similar luminescence mechanisms involving band-edge and defect-related transitions, although there may be some variations due to their specific defect chemistries.

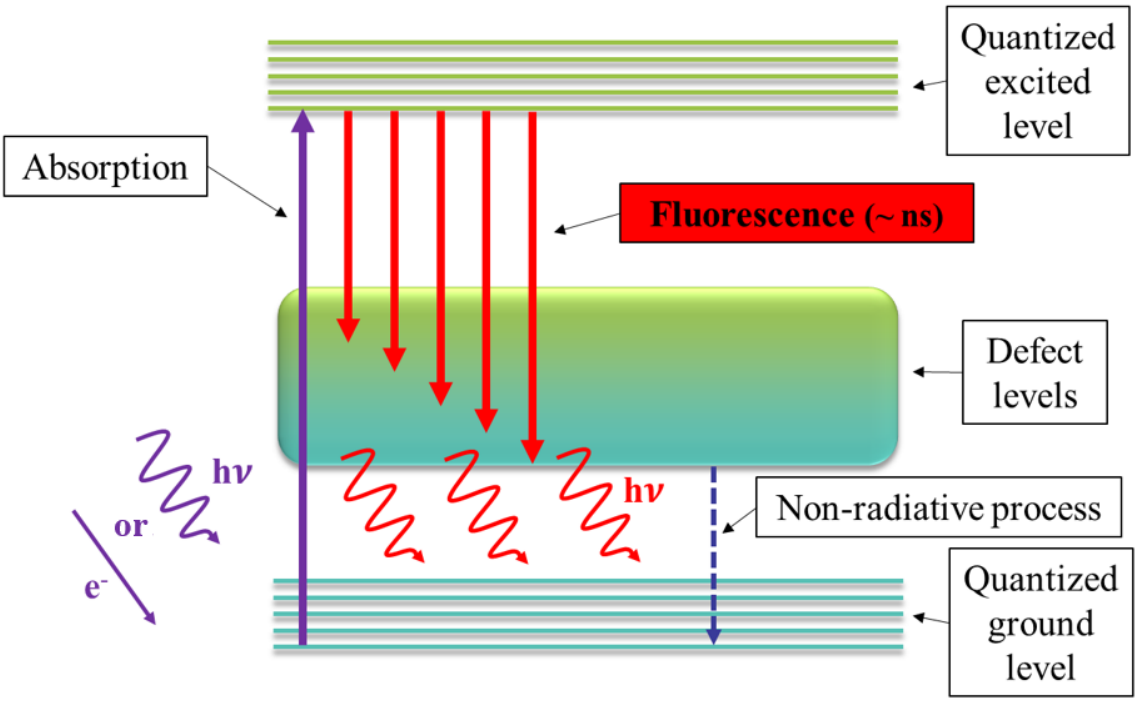

Figure 3.5: Simplified energy diagram, also called Perrin-Jablonski diagram, illustrating the fluorescence process in QDs.

Once the different mechanisms of luminescence generation in these materials have been understood, their synthesis is presented.

3.3 Synthesis and Formulation of Materials

With the exception of Y_2O_3:Eu^{3+} that has been commercially sourced, all other luminescent materials have been synthesized at CEA. In this subsection, protocols used for the in-house synthesis of these luminescent materials are described and their subsequent integration into the aerogel matrix.

3.3.1 Luminescent Materials

3.3.1.1 YVO_4:Eu^{3+} Nanophosphors

The following synthesis protocol of YVO_4:Eu^{3+} has been used at CEA/DES/LITEN, and can be divided into these main steps:

1. Preparation of the stack solution:

- 0.1 g of europium(III) nitrate hexahydrate ($Eu(NO_3)_3 \cdot (H_2O)_6$) and 1.8 g of yttrium(III) nitrate hexahydrate ($Y(NO_3)_3 \cdot (H_2O)_6$) are dissolved in 50 mL of deionized water, to prepare the nitrate solution.
- 1.1 g of sodium citrate dihydrate ($HOC(COONa)(CH_2COONa)_2 \cdot 2H_2O$) are dissolved in 37.5 mL of deionized water, to prepare the sodium citrate solution.
- 0.7 g of sodium orthovanadate (Na_3VO_4) are dissolved in 37.5 mL of deionized water, to prepare the vanadate solution.

2. Synthesis of the $YVO_4:Eu^{3+}$ nanoparticles:

   - The nitrate solution is poured into a round-bottom flask, heated to 60°C in an oil bath, and stirred continuously.
   - Once the temperature stabilizes between 58 – 62°C, the sodium citrate solution is added. A white precipitate (lanthanide citrate) will form immediately.
   - While maintaining stirring at 60°C, the vanadate solution is quickly added. The white precipitate will dissolve instantly, and the pH will rise to approximately 8. The flask is covered with a septum and count t_0.
   - At t_0 + 30 min, the heat is turned off, allowing the mixture to cool to room temperature.

3. Purification:

   - The final solution is purified via dialysis against 4 – 5 L of deionized water using Zellutrans dialysis tubing (Roth – 46 mm width, 48 µm thickness, 6.74 mL/cm capacity, approximately 25 cm of tubing for 120 mL of solution). The dialysis bath is replaced at t_0 + 24 h and t_0 + 48 h.
   - A drop of the dialyzed solution diluted in 2 mL of deionized water yield particles around $\sim$ 20 nm in size, as measured by Dynamic Light Scattering (DLS). The solution obtained is completely transparent.

In this way, a colloidal solution of $YVO_4:Eu^{3+}$ nanoparticles with sodium citrate ligands is obtained. Ligands help control the particle size during synthesis.

3.3.1.2 $AgInS_2$/ZnS Quantum Dots (QDs)

The following synthesis of both $AgInS_2$/ZnS and $CuInS_2$/ZnS QDs is performed in-house at CEA/DRF/IRIG via a microwave-assisted aqueous route [115]. The team at IRIG

has established solid expertise in quantum dot synthesis and surface engineering through several years of research.

The synthesis of the QDs involves two main steps: the initial formation of the core ($AgInS_2$ or $CuInS_2$) with glutathione (GSH) as surface ligands, followed by the growth of a ZnS shell to complete the core/shell structure.

The formation of the $AgInS_2$ core follows the steps outlined below:

1. Preparation of the indium – GSH complex:

   - 2 mmol of GSH are solubilized in 5 mL of Milli-Q water in a 30 mL microwave-compatible reaction vessel. GSH acts as a metal chelator (binding to metal ions and forming stable ring-like structures known as chelates) and as a surface ligand, stabilizing the nanocrystals.
   - In a separate vial, 2 mmol of indium(III) chloride ($InCl_3$) are dissolved in 2 mL of 0.25 M nitric acid (HNO_3) to ensure the complete solubilization of the indium salt.
   - The two solutions are combined and 1 mL of Milli-Q water is added to form a homogeneous mixture containing indium–thiol complexes. Milli-Q water is ultrapure deionized water to minimize contamination from ions and organics, typically produced by a Milli-Q purification system.

2. pH adjustment and precursor addition:

   - All sequential additions are performed under intense stirring. 2.7 mL of 5.0 M ammonium hydroxide (NH_4OH) are added to increase the pH. The addition of NH_4OH induces the formation of a white precipitate. After 2 – 3 min of stirring, the precipitate is dissolved, indicating formation of soluble intermediates.
   - 0.2 mmol of silver nitrate ($AgNO_3$) diluted in 2 mL of Milli-Q water are added.
   - The pH is adjusted to approximately 7.5 by adding some drops ($\sim$ 0.8 mL) of a 2.0 M citric acid solution.
   - Finally, a freshly prepared solution of 1 mmol of sodium sulfide (Na_2S) is added in 4 mL of Milli-Q water as the sulfur source.
     $AgNO_3$ and Na_2S are the key chemical precursors that actually form the $AgInS_2$ nanocrystals.

3. Microwave-assisted heating:

- The reaction vessel is subsequently sealed and heated to 100°C for 20 min under microwave irradiation (using a CEM Discover 2.0 system) and magnetic stirring.
- The solution color changes from light yellow before heating to red, indicating the formation of colloidally stable $AgInS_2$ QDs, remaining dispersed in solution without precipitation.

A ZnS shell is grown around the $AgInS_2$ core particles to improve colloidal stability and enhance the overall quantum yield by passivating surface traps on the $AgInS_2$ core and reducing non-radiative recombinations. This leads to a more efficient emission of light regardless of how the QDs are excited.

The ZnS shell is formed via a second microwave step:

1. Preparation of ZnS precursor stock solution:
   - In a separate vial: 0.8 mmol of GSH, 0.8 mmol of zinc acetate dihydrate ($Zn(OAc)_2 \cdot 2H_2O$), and 0.8 mmol of thiourea ($SC(NH_2)_2$) are dissolved in 9 mL of Milli-Q water.
   - The pH is adjusted to 7.5 by adding 1 mL of 5 M NH_4OH.
2. Shell growth reaction and microwave-assisted heating:
   - The ZnS precursor solution is added to the crude $AgInS_2$ core solution.
   - The mixture is heated to 100°C for 15 min under microwave irradiation with magnetic stirring.
   - The solution color shifts from red to orange, indicating successful growth of a ZnS shell around the $AgInS_2$ core, which alters the optical properties of the nanocrystals.

3.3.1.3 $CuInS_2$/ZnS Quantum Dots (QDs)

Regarding the synthesis of $CuInS_2$/ZnS QDs, the initial steps for the formation of the $CuInS_2$ core are similar to those used for the $AgInS_2$ core, particularly the preparation of the indium – GSH complex, which is performed in the same way. However, there are slight differences in the pH adjustment and precursor addition. To adjust the pH to 7.5, a smaller volume of NH_4OH ($\sim$ 0.2 mL) is used. In this case, the first metal precursor added is copper nitrate (0.4 mmol of $Cu(NO_3)_2$), replacing the 0.2 mmol of $AgNO_3$. This

quantity corresponds to twice the amount of silver precursor and reflects a stoichiometric adjustment based on the minor cation (Ag^+ in $AgInS_2$ and Cu^+ in $CuInS_2$). The second precursor, Na_2S, remains unchanged to enable the formation of $CuInS_2$ nanocrystals. The final step involving microwave-assisted heating and magnetic stirring is carried out under the same conditions as for the $AgInS_2$ synthesis.

The growth of the ZnS shell on the $CuInS_2$ core follows a procedure similar to that used for $AgInS_2$/ZnS QDs, with adjusted reagent quantities. Specifically, the amount of ZnS precursors is doubled to account for the stoichiometric adjustment based on the concentration of the minority cation Cu^+, which is twice the concentration of Ag^+ used in the $AgInS_2$ synthesis. The ZnS stock solution is prepared by dissolving 1.6 mmol each of GSH, $Zn(OAc)_2{\cdot}2H_2O$, and $SC(NH_2)_2$ in 18 mL of Milli-Q water. The pH is then adjusted to 7.5 by the addition of 2 mL of 5 M NH_4OH. This ZnS precursor solution is added to the crude $CuInS_2$ core solution and the mixture is subjected to microwave-assisted heating under the same conditions used for $AgInS_2$/ZnS (at 100°C for 15 min with magnetic stirring).

$AgInS_2$/ZnS and $CuInS_2$/ZnS QDs are purified by adding 1.5 volumes of isopropanol (C_3H_8O). The addition of C_3H_8O results in the precipitation of the QDs, and the precipitate can be separated by centrifugation (10 min at 8500 rpm) and redissolved in the required volume of deionized water.

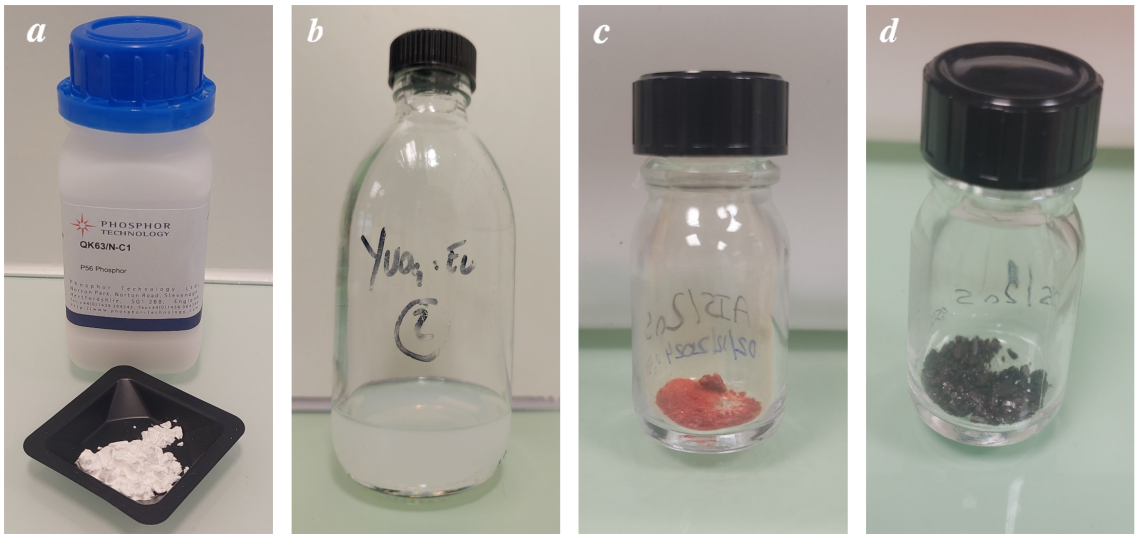

Figure 3.6: ***a***) Commercial Y_2O_3:Eu^{3+} microphosphors in white powder form. ***b***) YVO_4:Eu^{3+} nanophosphors synthesized at CEA/DES/LITEN in a colloidal solution concentrated at 2%. ***c***) and ***d***) Dried $AgInS_2$/ZnS and $CuInS_2$/ZnS QDs, respectively, synthesized at CEA/DRF/IRIG, before solubilization in deionized water.

Figure 3.6a corresponds to the commercially available Y_2O_3:Eu^{3+} microphosphors in white powder form. The YVO_4:Eu^{3+} nanophosphors synthesized at CEA/DES/LITEN are presented as a concentrated 2% colloidal solution, shown in Figure 3.6b. In Figures 3.6c and 3.6d, the dried $AgInS_2$/ZnS and $CuInS_2$/ZnS QDs synthesized at CEA/DRF/IRIG are shown, respectively, prior to solubilization in deionized water.

3.3.2 Synthesis of Luminescent Aerogels

Once the various luminescent materials have been successfully synthesized, the next step is their integration into the aerogel matrix, either cellulose- or silica-based [3].

3.3.2.1 Cellulose Aerogels

CMC (CAS 9004-32-4, Sigma-Aldrich, weight-average molecular weight (M_w) $\sim$ 90000), one of the most widely used cellulose-derived polymers, has been proposed by the LITEN team as the basis for the cellulose aerogel matrix, due to their experience using this polymer and literature available [116].

The process of preparation of luminescent CMC aerogels, shown in Figure 3.7, along with visual and qualitative verification of their luminescent properties under PL is mainly based on the following six steps:

1. Luminescent soft gel:

    - The starting point consists of preparing a soft gel by mixing an aqueous solution of 2%wt CMC with the luminescent particles. Different concentrations have been prepared depending on the type of luminescent material used.
    - For Y_2O_3:Eu^{3+} phosphor, which is supplied as a white powder, any concentration can be prepared without difficulty. Accordingly, samples with the following concentrations have been prepared: 0.5, 3, 16, 30, 50, 60, 75, and 99%wt.
    - In the case of YVO_4:Eu^{3+} phophor, a stock solution at 2%wt was available, which limited the achievable concentrations. From this solution, the following concentrations have been prepared: 0.05, 0.3, and 3%wt. To reach the 3%wt concentration and ensure consistency across all sample compositions, a portion

[3] The preparation of the aerogels loaded with luminescent materials is carried out in the CEA/DES/LITEN laboratories located at the CEA Grenoble site.

of the vanadate solution was left to evaporate in an open vial, thereby increasing its concentration.

- As for the $AgInS_2$ and $CuInS_2$ QDs, both materials have been initially obtained in dry form and subsequently dispersed in deionized water to form colloidal solutions. These have been used to prepare aerogels with luminescent material concentrations of 0.2, 0.5, 1.5, 3, 10, and 16%wt.

All solutions are then stirred for at least 15 min until fully dispersion of the particles in the CMC solution.

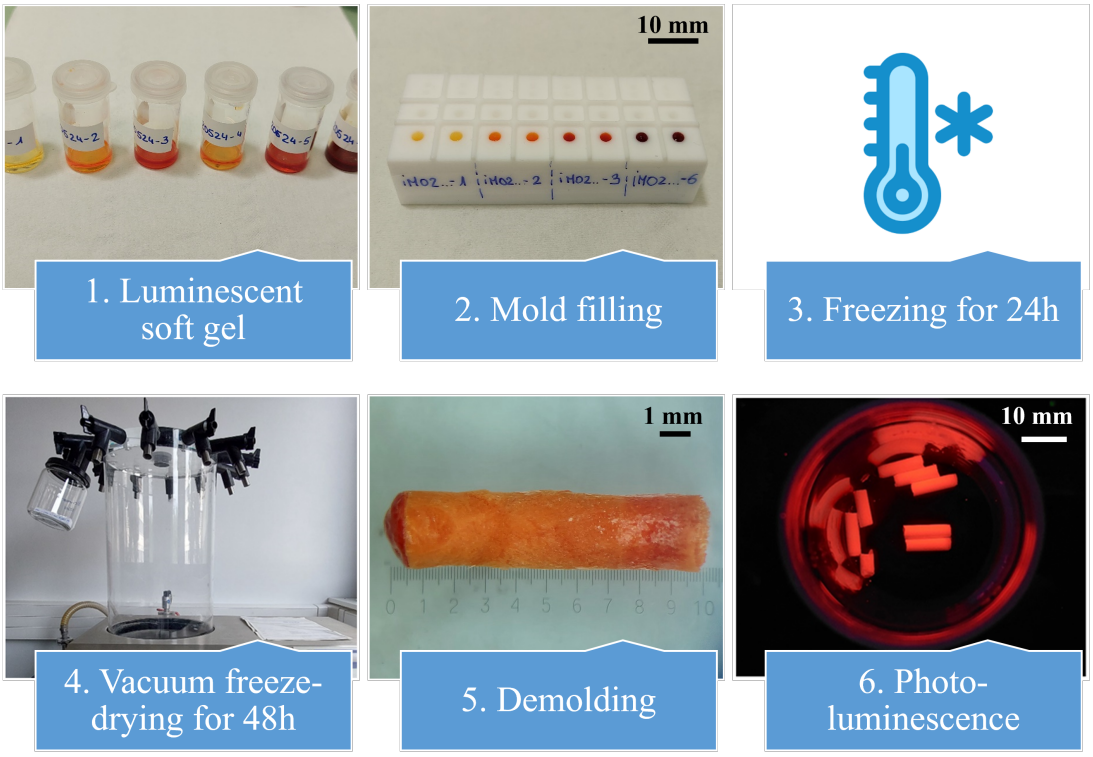

Figure 3.7: Schematic of preparation of CMC aerogels loaded with luminescent materials along with visual and qualitative verification of their luminescent properties under PL.

2. Mold filling:

- Molds, which are cylindrical wells of 1, 2 or 3 mm in diameter and 10 mm in depth drilled in a polytetrafluoroethylene (PTFE) plate, are filled with the prepared soft gels. Custom molds have been designed in SolidWorks and subsequently manufactured by Mecanic 3D. As will be shown in later chapters, all the aerogels characterized prior to exposure to tritium have a diameter of 3 mm, for technical simplicity, as well as the aerogels used during the first tritium

exposure experiments. As these latter experiments progress, smaller diameters (2 and 1 mm) will be studied to investigate the dependence of luminous intensity on aerogel diameter and to perform encapsulation and hermeticity tests. All this with the final objective of developing a device with a diameter of 1 mm, as mentioned in section 3.1.

3. Freezing for 24 h:

   - This plate is then placed in a freezer at -21°C for 24 hours to completely freeze soft gels. When the water inside the soft gel freezes, it creates ice crystals. These crystals create a porous network, pushing the CMC polymers into the interstitial zones between the crystals.

4. Vacuum freeze-drying for 48 h:

   - After freezing, the PTFE plate is introduced in a freeze-dryer for 48 hours in order to dry frozen soft gels by vacuum freeze-drying, also called lyophilization, and get aerogels.

5. Demolding:

   - Once dry, the aerogels are demolded. The appearance of pure CMC aerogels is opaque and white, as seen in Figures 3.8a and 3.8b (in particular, the aerogel located in the upper left corner of each image). After the addition of phosphors, either Y_2O_3:Eu^{3+} microparticles (Figure 3.8a) or YVO_4:Eu^{3+} nanoparticles (Figure 3.8b), no visible difference can be observed between the pure CMC aerogel and those containing different phosphor concentrations. In contrast, the incorporation of QDs gives an orange hue to the aerogel, which intensifies with increasing concentration (as observed in Figure 3.8c). $CuInS_2$ QDs produce a more intense coloration than $AgInS_2$ at the same luminescent material concentration.

6. Photoluminescence (PL):

   - Finally, aerogels are exposed under UV light (254 and 365 nm) to visually check their PL features. Upon UV light exposure, a sedimentation effect on samples containing Y_2O_3:Eu^{3+} particles has been observed. The sedimentation of these micrometric particles occurred during the freezing process. In order to prevent this sedimentation, a new step was introduced in the aerogel preparation, which consisted on freezing instantaneously the samples containing the mixture of

2%wt CMC and Y_2O_3:Eu^{3+} particles with liquid nitrogen. Figure 3.9 shows Y_2O_3:Eu^{3+} particles embedded at different concentrations (16, 30, and 50 %wt) in CMC aerogels, using the modified method including liquid nitrogen. Under UV light, no sedimentation effect is observed. It should be noted that the light emitted by these aerogels appears yellow in Figure 3.9, but this is due to the camera contrast. In reality, the emitted light is red, as shown in other images throughout this document.

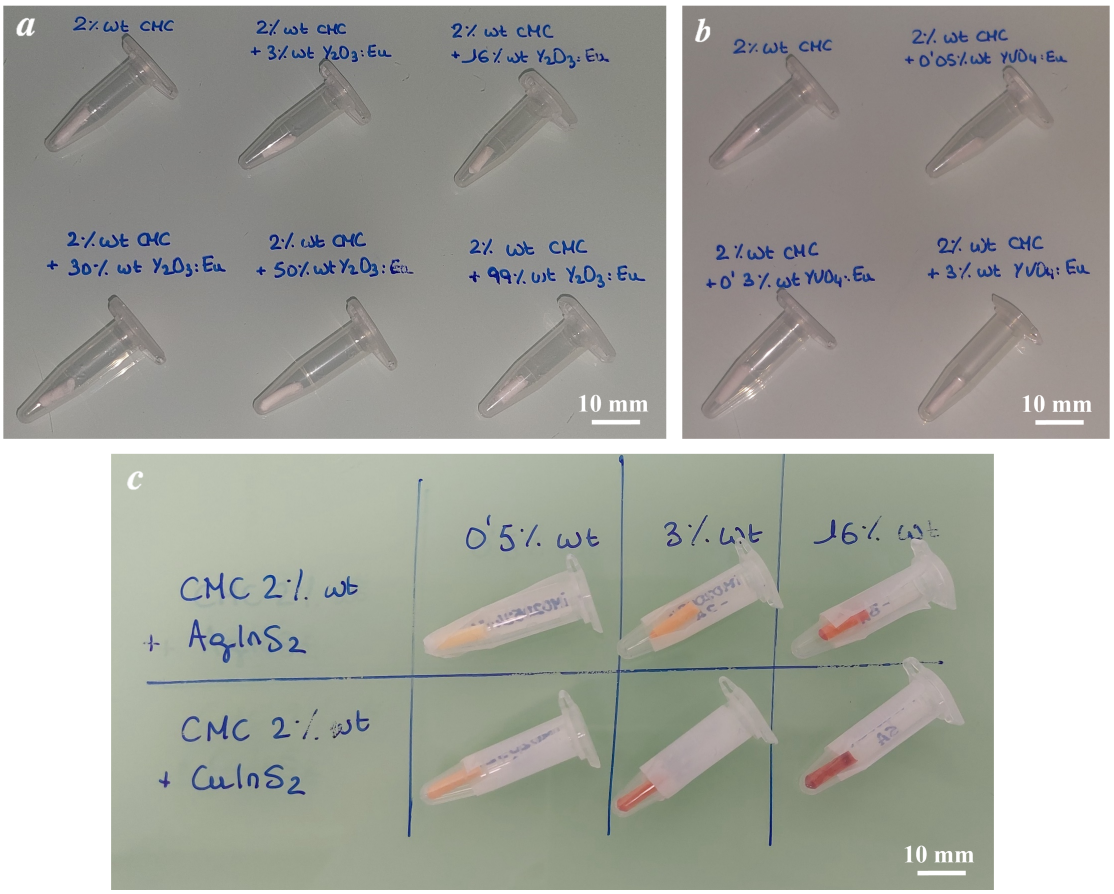

Figure 3.8: ***a***) A pure CMC aerogel and CMC aerogels loaded with Y_2O_3:Eu^{3+} microphosphors at different concentrations (3, 16, 30, 50 and 99%wt). ***b***) A pure CMC aerogel and CMC aerogels loaded with YVO_4:Eu^{3+} nanophosphors at different concentrations (0.05, 0.3 and 3%wt). ***c***) CMC aerogels loaded with $AgInS_2$ and $CuInS_2$ QDs at different concentrations (0.5, 3 and 16%wt).

It is important to note that for the preparation of the 2%wt CMC and 99%wt Y_2O_3:Eu^{3+} sample, the preparation is different since the sample has to be extremely concentrated. For this purpose, a mold is completely filled with 119.4 mg of Y_2O_3:Eu^{3+} powder, which is then compacted under applied pressure. Following this, 20.9 mg of the aqueous solution

of 2%wt CMC are added. The sample is then kept at a temperature of 100°C for 2 hours in order to evaporate water. After this time, the sample is demolded, resulting in a fragile material resembling a powdered bulk of Y_2O_3:Eu^{3+} rather than an aerogel structure.

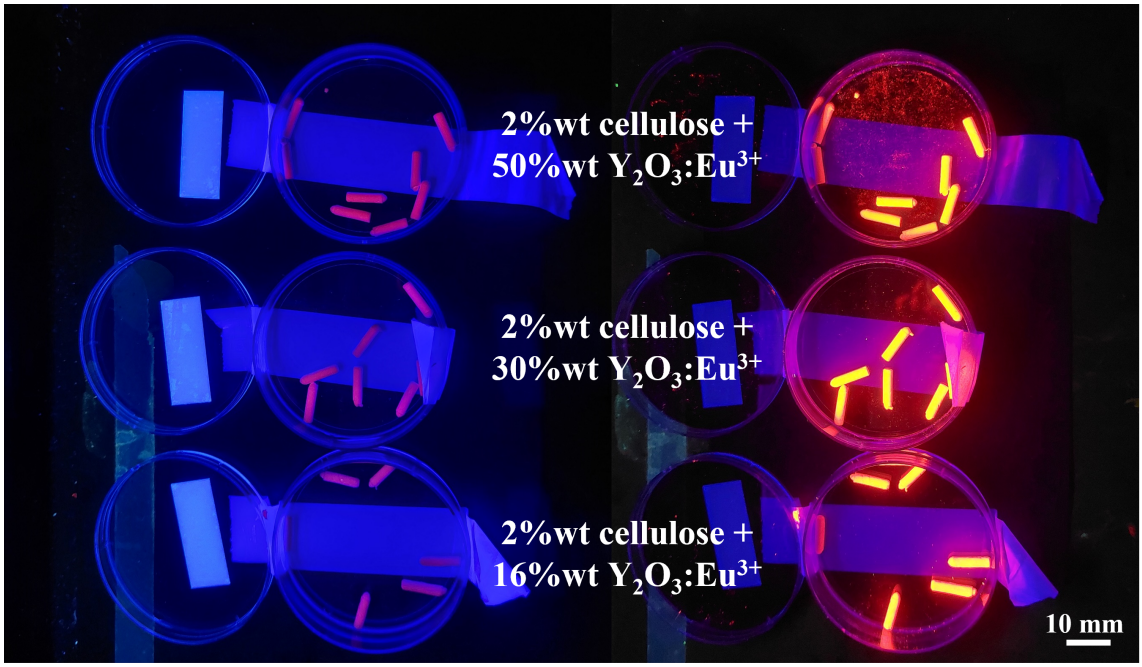

Figure 3.9: CMC aerogels loaded with different concentrations (16, 30 and 50%wt) of Y_2O_3:Eu^{3+}, exposed under UV light at two different wavelengths (254 and 365 nm).

It has been observed that during storage of the aqueous colloidal solution of $CuInS_2$ at room temperature in the laboratory and protected from UV rays, this solution turns black in just a couple of weeks, while the $AgInS_2$ solution remains orange. However, CMC aerogels loaded with $CuInS_2$ remain orange months after synthesis, which would indicate encapsulation of the QDs in the aerogel, making them much more stable.

3.3.2.2 Silica Aerogels

The preparation of silica aerogels along with visual and qualitative verification of their luminescent properties under PL follows a distinct process, outlined as follows and illustrated in Figure 3.10.

1. Luminescent soft gel:

    - 15 mL of tetraethyl orthosilicate (TEOS) ($Si(OC_2H_5)_4$) are mixed with 12 mL of deionized water. TEOS is the silica precursor and it undergoes hydrolysis

and condensation reactions when reacting with deionized water to form a three-dimensional silica network. During the TEOS hydrolysis, the ethoxy groups -(OC_2H_5) are gradually replaced with hydroxyl groups -OH and ethanol (C_2H_5OH) is released. This can happen up to four times, until $Si(OH)_4$ is obtained:

$$Si(OC_2H_5)_4 + H_2O \rightarrow Si(OC_2H_5)_3(OH) + C_2H_5OH \quad (3.1)$$

$$Si(OC_2H_5)_3(OH) + H_2O \rightarrow Si(OC_2H_5)_2(OH)_2 + C_2H_5OH \quad (3.2)$$

$$Si(OC_2H_5)_2(OH)_2 + H_2O \rightarrow Si(OC_2H_5)(OH)_3 + C_2H_5OH \quad (3.3)$$

$$Si(OC_2H_5)(OH)_3 + H_2O \rightarrow Si(OH)_4 + C_2H_5OH \quad (3.4)$$

However, TEOS is fairly stable on its own in water so the hydrolysis reaction is slow. The addition of an acid, lowering the pH, serves as a catalyst for the TEOS hydrolysis by making the ethoxy -(OC_2H_5) groups more willing to leave. Thus, 140 μL of 5.2 M nitric acid (HNO_3) are added to the solution. The -Si(OH) groups produced during the hydrolysis reaction, called silanols, are essential for the condensation step. The TEOS solution is left in agitation for 24 h for the hydrolysis process to be completed correctly.

- The luminescent materials are added to the solution of hydrolyzed TEOS, at the desired concentration, before gelation to ensure they become embedded in the silica matrix.
- 6.25 mL of 0.1 M ammonium hydroxide (NH_4OH) are added to the solution, raising the pH and initiating a fast gelation via a base-catalyzed condensation step. The amount of NH_4OH directly affects the gelation time: the more that is added, the faster the gelation occurs. During condensation, two -OH groups or one -OH and one -OC_2H_5 react to form a siloxane bond (Si-O-Si), releasing a small molecule like water or ethanol:

$$\text{Si-OH + HO-Si} \rightarrow \text{Si-O-Si + } H_2O \quad (3.5)$$

$$\text{Si-OH + Si-}OC_2H_5 \rightarrow \text{Si-O-Si + } C_2H_5OH \quad (3.6)$$

This process builds up a three-dimensional network of Si–O–Si bounds extensively interconnected, forming the silica polymer network. At this stage, the silica polymer is a wet gel, a solid structure filled with solvent (usually water and ethanol). Since the addition of HNO_3 pushes the reaction toward fully hydrolyzed TEOS as already discussed, it reduces the presence of remaining

-(OC_2H_5) groups, which in turn lowers the probability of the alcohol-type condensation (reaction 3.6). Therefore, condensation primarily occurs between –OH and –OH groups, which is slower and leads to a more uniform and better-controlled network.

Different concentrations have been prepared depending on the type of luminescent material used:

- For Y_2O_3:Eu^{3+} phosphor, samples with the following concentrations have been prepared: 3, 16, 30 and 50%wt (with respect to the total weight of the soft gel).
- In the case of YVO_4:Eu^{3+} phosphor, the following concentrations have been prepared: 0.05, 0.3, 1.7 and 3%wt.
- As for the $AgInS_2$/ZnS and $CuInS_2$/ZnS QDs, silica aerogels could not be obtained due to issues arising during the mixing of the hydrolyzed TEOS solution with the QDs. This may be attributed to interactions between the acidic ligands on the QDs and the HNO_3 used in the sol–gel process.

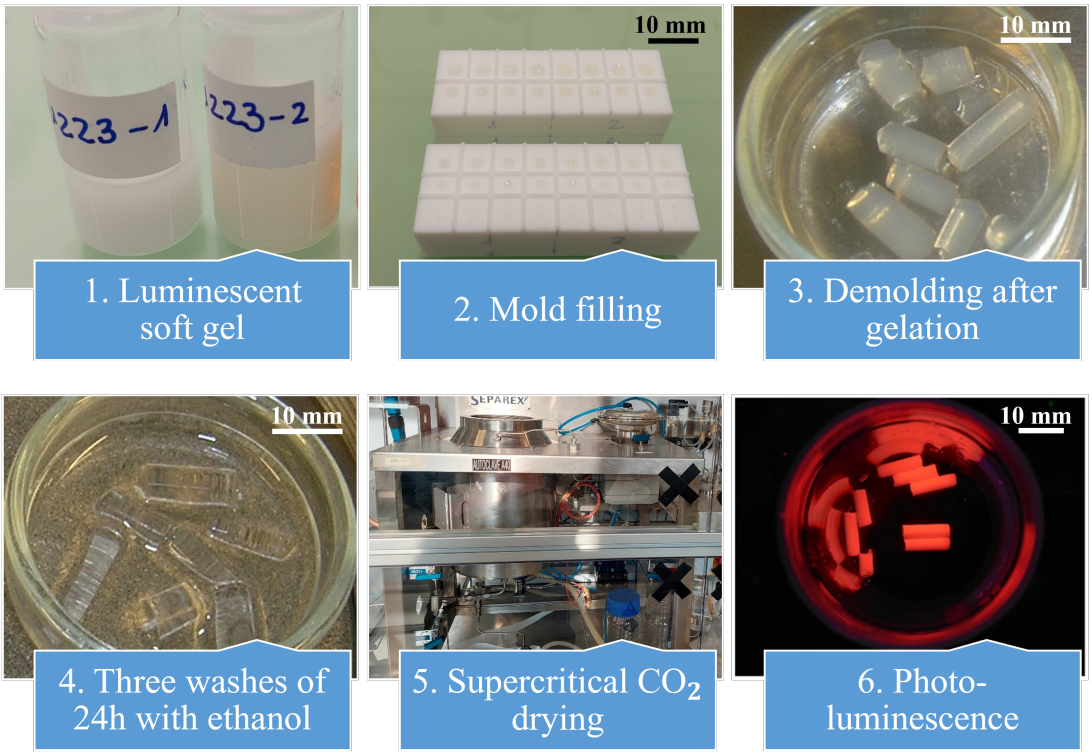

Figure 3.10: Schematic of preparation of silica aerogels loaded with luminescent materials along with visual and qualitative verification of their luminescent properties under PL.

2. Mold filling:

    - Immediately after adding NH_4OH, the solution is poured into molds to allow polymerization to occur within them.

3. Demolding after gelation:

    - After fully gelation, gels are carefully removed from the mold and placed into a flask. At this point, the gel still contains water and ethanol so it is mechanically fragile.

4. Three washes of 24 h with ethanol:

    - After demolding, the gels are immersed in ethanol to replace the water in the pores via solvent exchange. This step is important to remove unreacted chemicals, catalysts, and water. Consequently, the gel pores are filled solely with ethanol which, being miscible with liquid CO_2, prepares the gel for supercritical drying.

5. Supercritical CO_2 drying:

    - The process begins with liquid CO_2 to ensure that no liquid–gas interface forms within the pores, which could otherwise lead to cracking.
    - The system is then brought into the supercritical region by heating, allowing the removal of ethanol through continuous CO_2 circulation.
    - Finally, the pressure is reduced to return to the gaseous state. During ethanol extraction (i.e., drying), capillary forces never form inside the pores, thereby preventing the gels from cracking.
    - The cycle followed during supercritical CO_2 drying is illustrated in Figure 3.11.

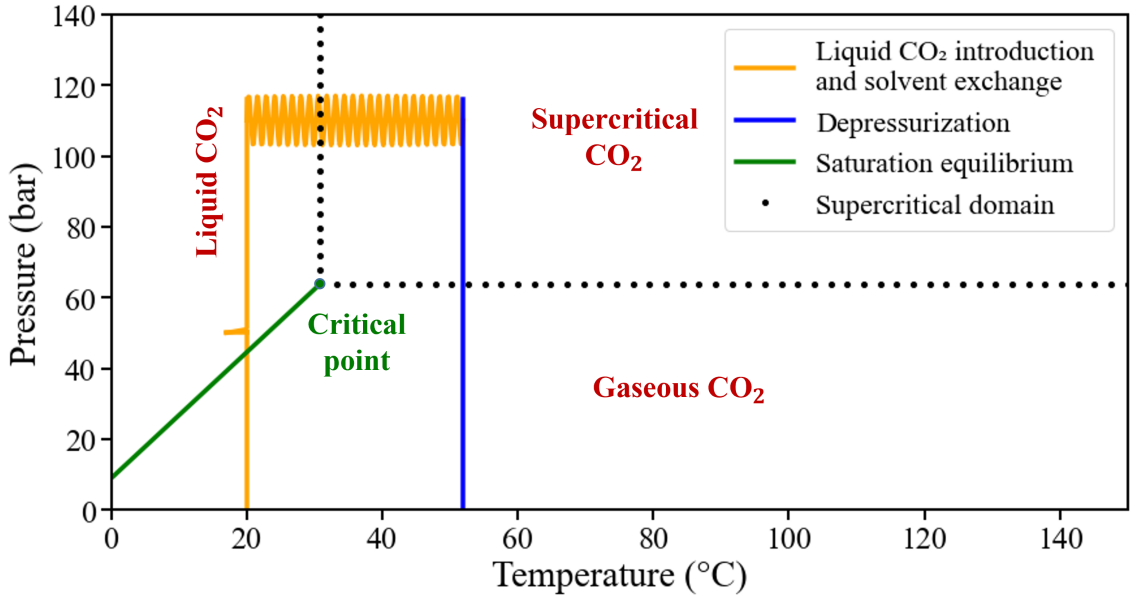

Figure 3.11: Pressure–temperature cycle followed during gel drying using supercritical CO_2.

- After drying, pure silica aerogels are nearly transparent, as shown in Figure 3.12a. However, after the addition of micrometric Y_2O_3:Eu^{3+} or nanometric YVO_4:Eu^{3+} phosphors, both types of loaded silica aerogels appear visually identical, being opaque white in color. Unlike CMC aerogels, silica aerogels exhibit a noticeable change in appearance with increasing concentrations of luminescent materials. Specifically, they become progressively more opaque and whiter, as illustrated in Figure 3.12b, which displays silica aerogels loaded with varying concentrations of Y_2O_3:Eu^{3+}.

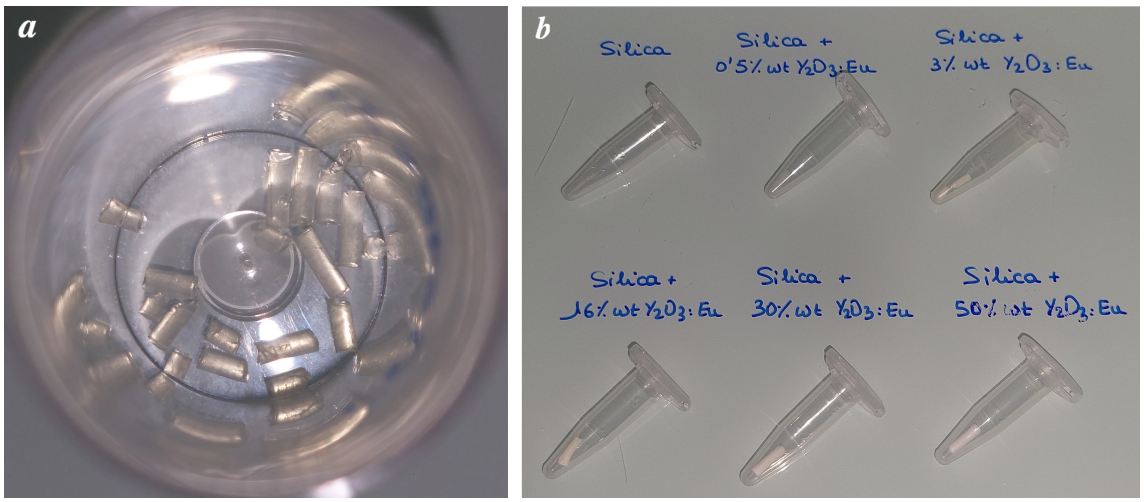

Figure 3.12: ***a***) Pure silica aerogels. ***b***) A pure silica aerogel and silica aerogels loaded with Y_2O_3:Eu^{3+} microphosphors at different concentrations (0.5, 3, 16, 30 and 50 %wt).

6. Photoluminescence (PL):

    - Finally, the aerogels are exposed to UV light at 254 nm and 365 nm to visually examine their PL properties. Sedimentation of micrometric Y_2O_3:Eu^{3+} phosphors was again observed. To prevent this issue, gelation parameters were optimized to ensure the microparticles had insufficient time to settle.

Having detailed the luminescent aerogel fabrication process, the procedure for exposing them to a tritium atmosphere will be discussed in the next section.

3.4 Tritium Production and Exposure to Tritium Gas

Tritium is primarily produced in nuclear reactors through the interaction of fission neutrons with the heavy water (D_2O, water in which the hydrogen atoms are replaced by deuterium) moderator and coolant, such as in the Canadian Deuterium Uranium (CANDU) reactors [117]. A moderator is a material used to slow down fast neutrons produced during fission, increasing the likelihood of sustaining the chain reaction. In these reactors, heavy water serves this function by moderating the neutron speed while also acting as the coolant that removes heat from the core. Over time, tritium accumulates in the heavy water as a byproduct of nuclear fission reactions. Tritium can only be extracted from the heavy water moderator by means of a Tritium Removal Facility (TRF), of which only two are currently in operation, one in Canada (the tritium source used in this work comes from this facility) and one in South Korea, although there are plans for a third in Romania. The extracted tritium is then processed and incorporated into sources such as depleted uranium cartridges (U-beds), which are used in laboratory settings for controlled tritium gas release. These cartridges enable safe and regulated exposure to tritium gas. The CANDU reactor system represents a significant industrial source of tritium, producing approximately 130 g of tritium per year, which is also considered a radioactive waste product requiring careful handling and containment.

The depleted uranium cartridge employed in this work is purchased from RC Tritec AG and is stored at room temperature. Images of this uranium source located inside the glovebox are shown in Figure 3.13a. By heating this uranium cartridge, the tritium gas can be released in a controlled manner. Tritium gas pressure can be finely modulated by adjusting the oven temperature, as illustrated in Figure 3.13b.

Concerning the sample, it is introduced into a 3.5 mL Fischer-Porter glassware with a ground glass joint that allows to be connected to a tritium gas transfer line in a completely watertight and gastight manner[4].

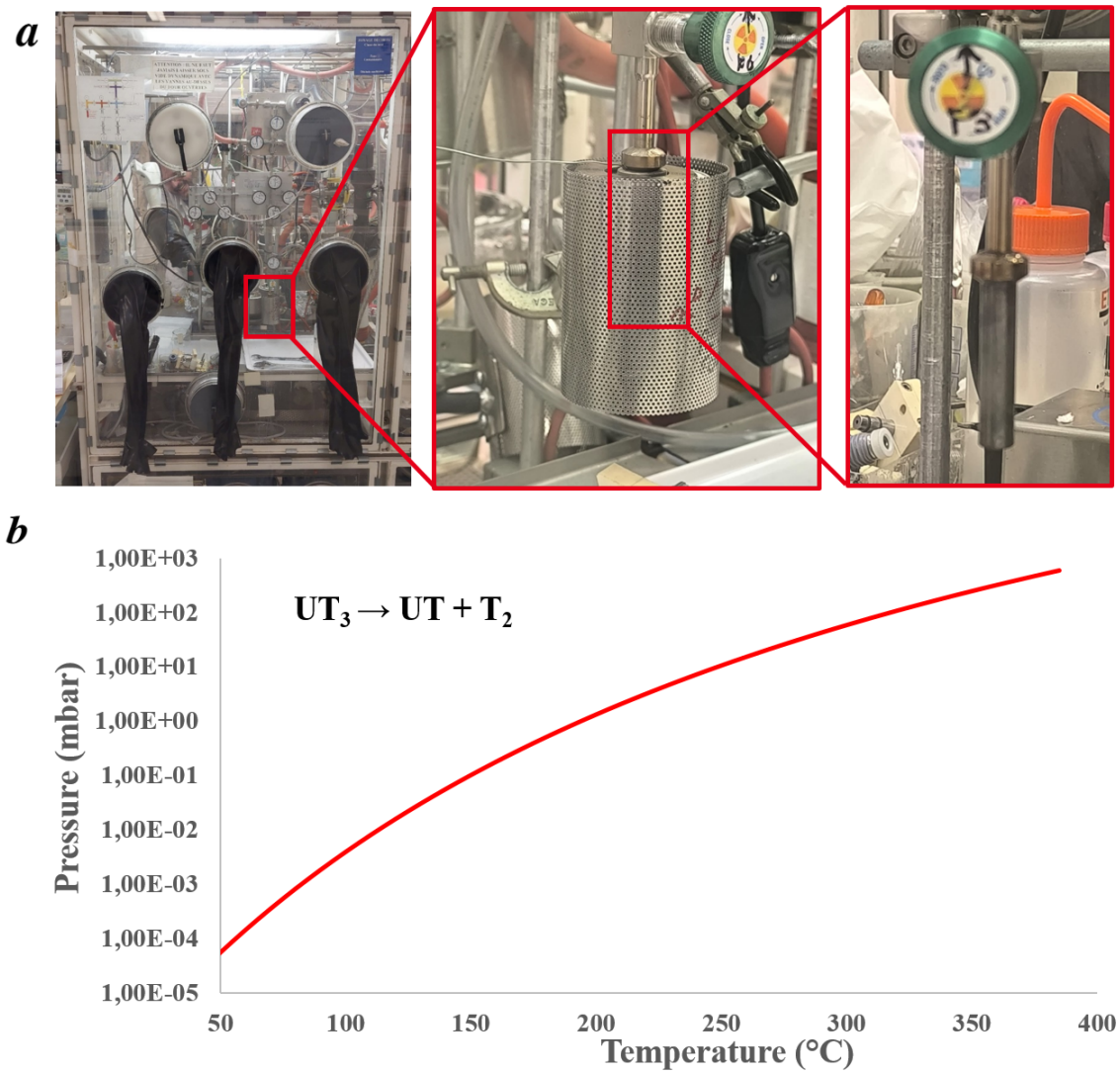

Figure 3.13: ***a***) The tritium gas is stored on a depleted uranium cartridge. ***b***) Pressure of the tritium gas released by the depleted uranium cartridge as a function of its temperature.

The tritium gas is then transferred from the U-bed to the sample using a custom-built tritium manifold, shown in Figure 3.14a. The gaseous tritium released from the depleted uranium cartridge (FII) when heated above 200°C travels along the route marked by the solid yellow arrows in Figures 3.14b and 3.14c, passing through valves F4, F2, 7, 4, 2, and 1, until it reaches the Fisher-Porter vessel containing the sample.

[4]The aerogels are exposed to the tritium gas atmosphere in the CEA/DRF/JOLIOT laboratories at the CEA Saclay site.

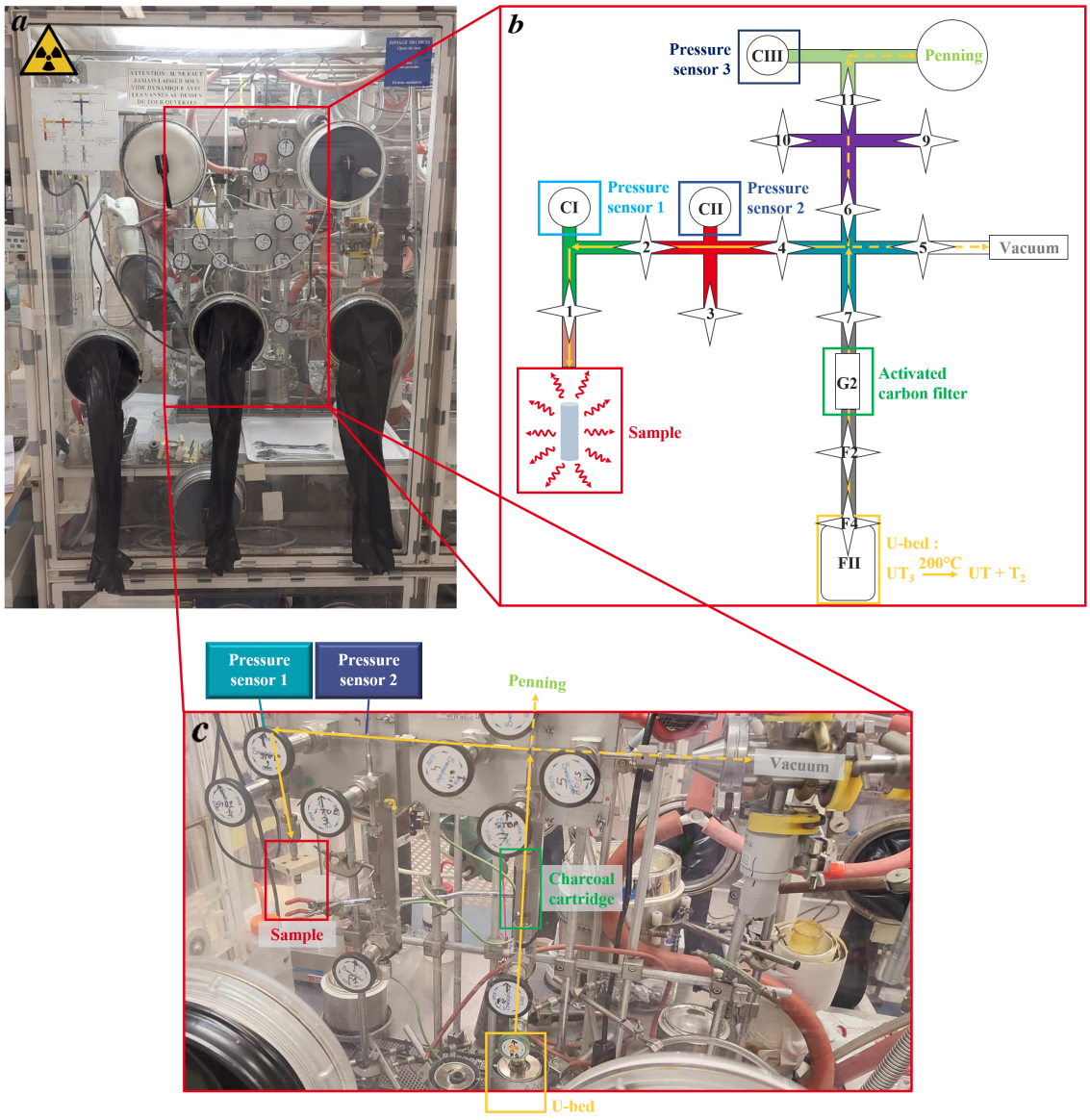

Figure 3.14: ***a***) Image of the glovebox used at the CEA/DRF/JOLIOT laboratory. ***b***) Schematic diagram showing the main components within the glovebox, including the U-bed (FII) and the sample exposed to the tritium atmosphere. When the U-bed is heated above 200°C, tritium gas is released and follows the path indicated by the solid yellow arrows. The dashed yellow arrows represent the alternate path taken by the gas flow during vacuum operations or Penning measurements. ***c***) Photograph highlighting the complexity of the tritium transport system between the U-bed and the sample.

To reduce the pressure of the gaseous tritium to which the sample is exposed, the furnace is cooled, allowing the circulating tritium to be reabsorbed into the uranium cartridge. In this reverse process, the tritium follows the same path in the opposite direction, passing through valves 1, 2, 4, 7, F2, and F4. Between valves 7 and F2, an activated carbon filter

(G2) is placed to trap solvents and organic impurities potentially present in the gas stream, thereby preventing contamination of the tritium bed.

Prior to exposing the sample to the tritium atmosphere, a vacuum must be applied to reabsorb any moisture that may have been stored in the aerogel from the time it was dried. In this case, the gaseous fluid is evacuated along the path through valves 1, 2, 4, and 5, leading to the vacuum pump.

For calibration purposes, a Penning measurement can be performed via the chimney stack to determine the tritium activity in the gas phase. The corresponding flow path runs through valves 1, 2, 4, 6, and 11. This measurement relies on a Penning ionization detector, which operates by applying a high voltage between two electrodes, generating a strong electric field within a low-pressure chamber. When tritium gas enters the chamber, free electrons in the gas are accelerated by this field and can ionize the diatomic tritium molecules through collisions. These ionization events lead to a cascade of secondary electrons, which are collected as an electric current. This current is proportional to the number of ionizations, and therefore directly related to the tritium concentration. The output current signal is plotted against time, producing a curve with distinct peaks. Each peak corresponds to a different tritium species, and is interpreted based on empirical calibration data. Since T_2 is a small, non-polar, inert gas molecule, it moves quickly and freely through the gas line without sticking much to surfaces inside tubing and valves. When it reaches the Penning cell, it enters rapidly and exits rapidly, resulting in a sharp and well-defined peak. However, HTO vapor behaves very differently from T_2 since HTO is polar and interacts with internal surfaces of the system. As a result, it takes longer to reach the detector after valve opening and it continues to release slowly. This produces a delayed, broader peak with a longer tail.

Once the sample has been exposed to the gaseous tritium atmosphere, the aerogel can be encapsulated in a borosilicate glass capillary by melting the glass to create a seal. After sealing, the upper part of the capillary (above the seal) remains connected to the ground glass joint, which allows connection to the tritium gas transfer line and ensures that no tritium escapes from the manifold. The aerogel sample remains isolated and sealed within the lower section of the borosilicate capillary (below the seal).

After sealing, the outer surface of the capsule is cleaned to remove any radioactive residues that may have been deposited during handling. For this purpose, compressed air, or a mixture of compressed air and water, is ionized using an electric arc to generate a plasma jet. This jet is directed onto the surface, degreasing and activating it, which enhances the removal of any residual tritium.

To verify the hermeticity and safety of the borosilicate-encapsulated aerogel, surface smear

tests can be performed. These involve wiping the outer surface with filter papers soaked in ethanol or water, which are then analyzed by Liquid Scintillation Counting (LSC).

Once the production of tritium and the exposure of the aerogels to this gaseous tritium atmosphere have been understood, the setup used for the measurement of the luminescence intensity emitted by these aerogels via RL will be presented in the following section.

3.4.1 Home-Built System for Radioluminescence (RL) Measurements under Tritium Atmosphere

Characterizing the light emitted by luminescent aerogels exposed to a radioactive tritium atmosphere presents significant challenges due to safety constraints limiting access to radioactive samples. Furthermore, only a minimal amount of material can be exposed to the radioactive atmosphere to minimize radioactive waste.

The main challenge lies in exposing the samples to the tritium atmosphere and measuring the emitted light as the tritium gas pressure varies[5].

As already mentioned in section 3.4, the aerogel to be exposed to the tritium gas atmosphere is previously introduced into a 3.5 mL Fischer-Porter glassware with a ground glass joint that allows to be connected to a tritium gas transfer line. This glassware is then placed inside an integrating sphere (Thorlabs, 2P4/M, 50 mm diameter), which serves to collect all the scattered photons in order to estimate the optical power of the light source over 4π sr since the radioluminescent aerogel is a Lambertian source, an extended light source that produces diffused light. The integrating sphere is supported by a clamp that is fixed to a vertical support rod and covered with aluminum foil to prevent external photons from entering the measurement system. When the aerogel starts to be in contact with the gaseous tritium atmosphere, the electrons from the β-decay begin to interact with the luminescent particles contained in the aerogel. These particles absorb the electrons and emit photons by RL. An optical fiber of 10 m long (commercialized by SEDI-ATI, ref. 18.055, Numerical Aperture (NA) 0.22, 1000 µm silica core, silica cladding, stainless steel jacket and attenuation of 0.008 dB/m for a wavelength of 650 nm) will guide these photons from the integrating sphere to the detector (Atik 414EX Monochrome Charge Coupled Device Camera), which is located outside the glove box. For the fiber-sphere and fiber-detector connections, 2 supports 2P-SMA (Thorlabs) have been used. The detector is connected to a computer via a USB connection which allows it to be controlled by the

[5]It should be noted that all manipulations were observed and priorities coordinated with the team. Although I did not perform the tritium handling for safety reasons, I managed data acquisition and proposed the home setup used in the RL experiments.

Artemis Capture software. A scheme of the described setup is illustrated in Figure 3.15.

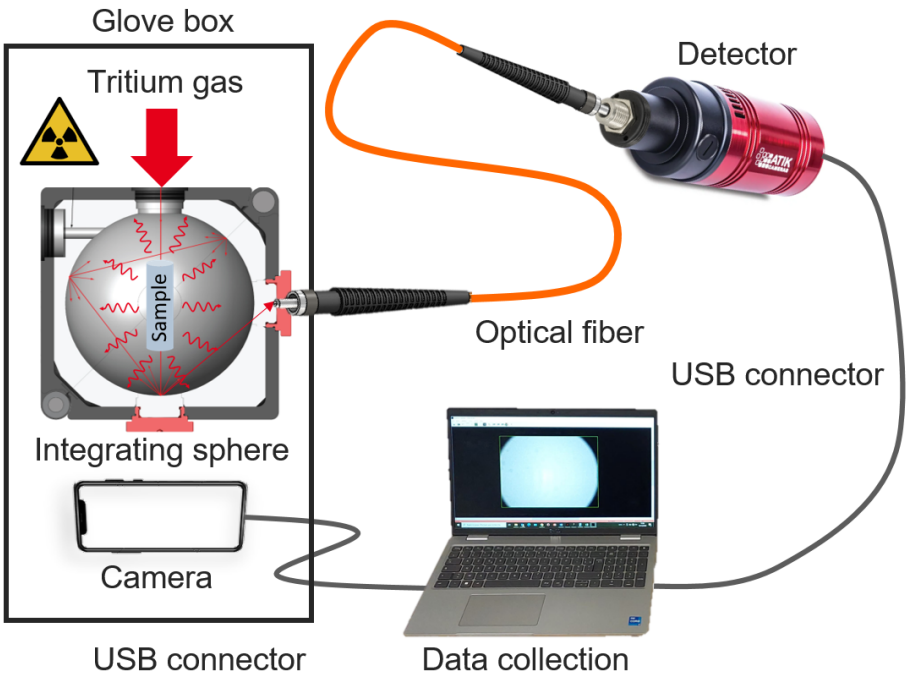

Figure 3.15: Schematic view of the RL measurement setup. The image is not to scale.

This setup allows quantification of the number of photons emitted from the sample but does not provide imaging of the sample. To address this, a compact camera (a repurposed smartphone remotely controlled) was introduced inside the glove box, positioned under the integrating sphere, as shown in Figure 3.16c.

To image the sample, the aluminum foil covering the integrating sphere must be removed, and the bottom port of the sphere opened. The picture is then taken using this camera that is remotely controlled via a USB connection to the computer.

As a result, the whole setup acts, not only as a light output quantification, but also as an imaging system.

The protocol followed while quantifying emitted photons is as follows:

1. Make a dynamic vacuum to reabsorb any moisture that may have been stored in the aerogel from the time it was dried.

2. Once the aerogel has finished degassing, a static vacuum is created and the oven begins heating.

3. When the oven reaches 200°C, tritium gas is released from the U-bed cartridge and the pressure of tritium gas begins to increase. Aerogel starts to emit photons and

an acquisition, of 20 seconds integration time, is launched with the detector every 100 mbar aimed at studying the dependence of the light ouput with the pressure of tritium gas.

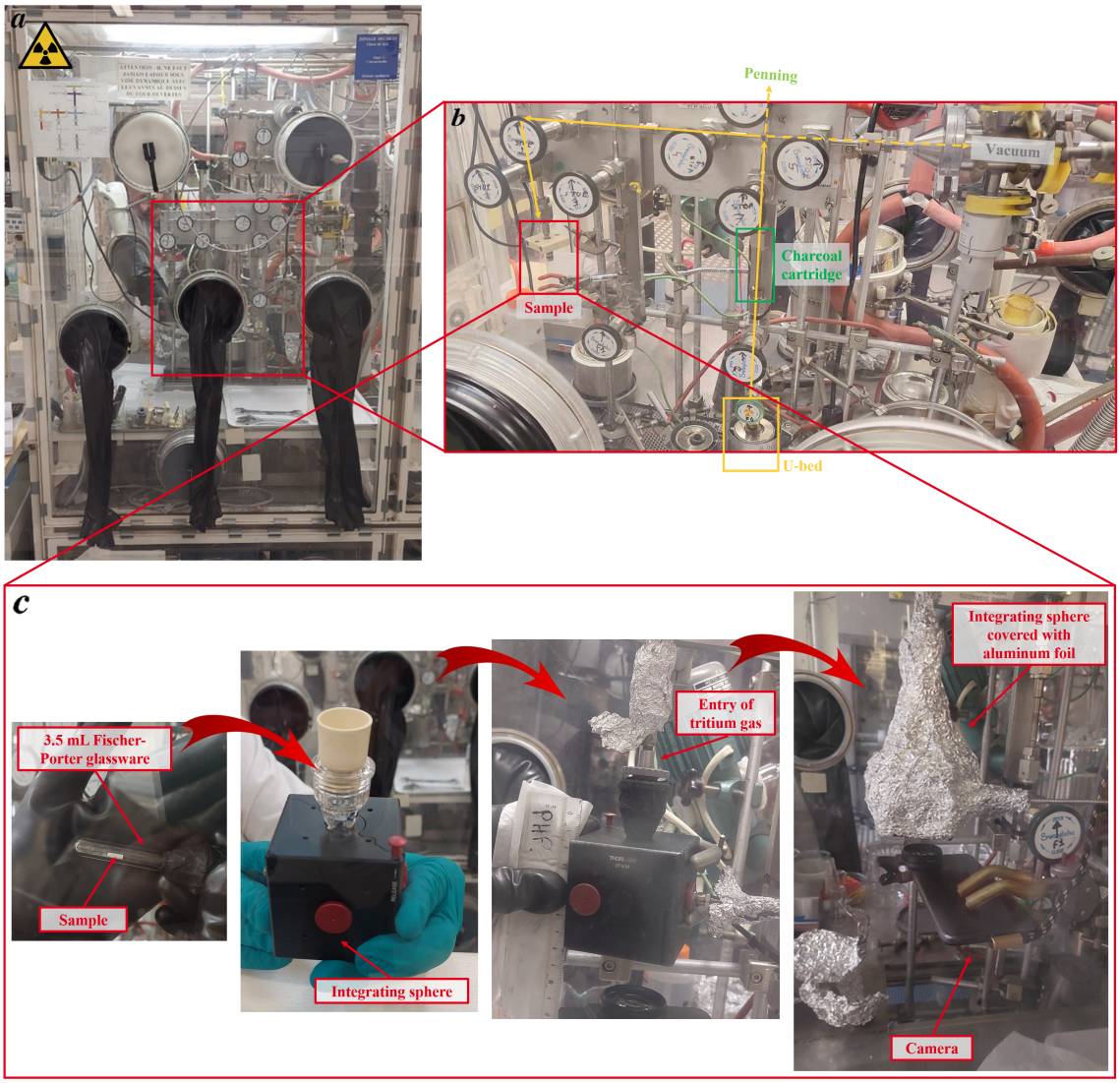

Figure 3.16: ***a***) Image of the glovebox used at the CEA/DRF/JOLIOT laboratory. ***b***) Photograph highlighting the complexity of the tritium transport system between the U-bed and the sample. ***c***) Images showing the aerogel being introduced into the 3.5 mL Fisher-Porter glassware, which is then placed into the integrating sphere. The camera is placed below the integrating sphere.

4. When the maximum pressure is reached, defined to be 1200 mbar for safety reasons, the sample remains exposed to this pressure for 30 minutes while the oven starts to being cooled down.

5. During this time, the pressure in the volume V_1 is also recorded, to check whether

or not the sample has already absorbed tritium after 30 minutes of exposure. At the same time, a picture of the sample is taken with the camera. In order to optimize the experimental time, some samples are exposed to the tritium gas atmosphere at 1200 mbar overnight (about 13 hours).

6. After that, the tritium gas pressure is gradually decreased, with acquisitions taken every 100 mbar, if possible.

7. After having launched the last acquisition at 0 mbar, the sample is brought to ambient pressure, a last picture of the sample is taken with the camera and the sample is removed from the Fischer-Porter glassware. It is important to note that the glassware must be cleaned between two experiments since it could contain luminescent particles that could contaminate the next sample and thus, falsify the results.

It is worth mentioning that the sample is exposed to a tritium gas atmosphere whose volumetric activity is 2.55 Ci/(mL·bar) under standard conditions (P = 1 bar, T = 273.15 K). The total tritium activity can be determined from the tritium gas pressure (in bar) in a volume of 8.71 mL that includes the Fischer-Porter glassware and a section of the gas transfer line up to the first isolation valve. In this volume, the aerogel volume is neglected. Equation 3.7 gives us the relationship between activity and pressure:

$$\text{Total activity} = \text{Isotopic purity} \cdot \text{Volumetric activity} \cdot \text{Volume} \cdot \text{Pressure} \tag{3.7}$$

where the isotopic purity of the tritium source is 85%.

This optical setup allows to obtain black-and-white images in which a halo of light is observed against a black background, corresponding to the light emitted from the optical fiber and captured by the detector. Regarding the processing of data obtained from this system, a Region of Interest (ROI), centered on the image with dimensions 0.6 times those of the acquisition image, is defined in order to determine the mean gray value. Calibration measurements are performed using an in-house reference light source, which is a prototype of the electroluminescent implants used in the clinical trial, whose optical power has been previously measured using sensors calibrated annually[6].

The setup used during the calibration measurements follows the same configuration as that used for the RL experiments conducted at CEA Saclay. The light source, which is the output of the optical fiber from the electroluminescent implant, is introduced into an integrating sphere identical to the one used in the tritium experiments. The photons emitted

[6]Detector calibration measurements are performed at Clinatec's facilities at the CEA Grenoble site.

by the implant at 670 nm are directed to the detector, which is the same as the one used in the RL setup. However, access to the optical fiber used during those RL experiments (NA = 0.22 and core = 1000 μm) was not available. Instead, two optical fibers with the same numerical aperture (NA = 0.22) but different core diameters (105 and 400 μm) were used to determine a correction factor corresponding to the original fiber (NA = 0.22, core = 1000 μm).

Additionally, the Python calibration code accounts for the attenuation factor associated with the fiber used in the RL experiments (0.008 dB/m at a wavelength of 650 nm).

The whole detector calibration process, previously described, is outlined in Figure 3.17.

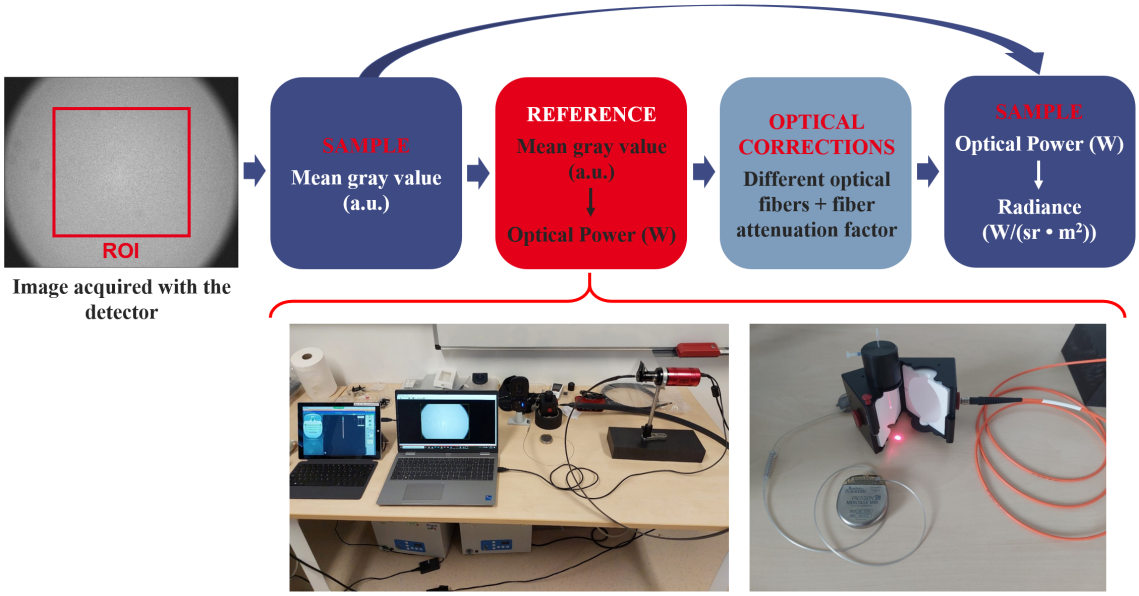

Figure 3.17: Diagram illustrating the different stages of the detector calibration process used to convert the mean gray value (in a.u.) into radiance values (in W/(sr · m^2)), performed at Clinatec's facilities at the CEA Grenoble site.

These calibration measurements enable to correlate the mean value of an image with the optical power emitted by the device under study. Consequently, the optical power emitted by a radioluminescent aerogel can be quantified.

However, the optical power does not give any information about the light source such as its size and the angular distribution of its emitted light. To address these limitations, the concept of *radiance* will be used, a standard quantity in radiometry.

3.4.2 Fundamentals of Radiometry

Radiance, L, is defined as the optical power emitted per unit solid angle and per unit emitting area in a specific direction:

$$L = \frac{\text{Optical power}}{\text{Solid angle} \cdot \text{Surface area}} \tag{3.8}$$

Therefore, radiance has units W/(sr $\cdot$ m^2). For a Lambertian source, as it is the case here, radiance relates to emittance, M, by $L = M/\pi$, where M = Optical power / Surface area. The total cylindrical surface area of the aerogel is:

$$\text{Surface area} = 2\pi rl + 2\pi r^2 \tag{3.9}$$

with r the radius and l the length of the aerogel. Experimentally, the optical power will be measured, the surface area of the sample defined, the emittance determined, then radiance calculated by $L = M/\pi$.

The radiance values are an estimation, likely an underestimation, considering the integrating sphere is not entirely perfect and additional losses may be due to the Fischer-Porter glassware. Furthermore, these radiance values are the maximum it can achieve at t_0, without considering the possible future degradation of the different materials.

When comparing the radiance values obtained in this work with those reported in the literature, it is important to note that most RL studies from the 1970s to 1990s report luminance values, which are photometric units rather than radiometric units. It means that luminance accounts for the eye's spectral luminous efficiency function, which describes the wavelength-dependent sensitivity of human vision. Converting luminous flux (lm) to radiant flux (W), also known as optical power, requires the photopic (daylight) and scotopic (night vision) luminous functions representing the average visual response under different lighting conditions, which are used as weighting factors in this conversion.

The curves for these luminous functions are displayed in Figure 3.18 and serve as a reference for calculating radiometric values from photometric units. To convert the reported luminance values given in

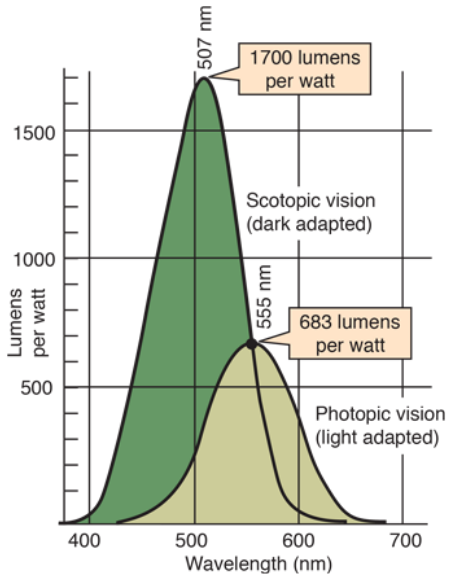

Figure 3.18: Luminous functions for human vision: scotopic (night light) in dark green and photopic vision (daylight) in light green. Figure reproduced from [118].

units of cd/m^2 (candelas per square meter) or fL (foot-lamberts) to the radiance unit used here, W/(sr · m^2), the following relationships are relevant: 1 fL corresponds to 3.426 cd/m^2, and 1 cd equals 1 lm/sr (1 lumen per steradian).

Now that the RL experiments have been explained, the characterization techniques required to study the samples before and after tritium exposure to interpret the RL results will be presented in the following section.

Radioactivity amounts, expressed in curie or becquerel, loaded in the aerogels have not been discussed in this section, as the primary objective here was to describe the methodology followed during the RL experiments. The quantity of tritium and related radioactivity considerations will be addressed in detail later in this document.

Before moving on to the next section, it is important to acknowledge that this work was made possible through the collaborative efforts of numerous colleagues from the laboratory, safety, management, and infrastructure teams at CEA Saclay, whose collective efforts made these exceptional experiments possible. Also to be acknowledged is the invaluable expertise and guidance provided by colleagues from CEA/DES/LITEN and CEA/DRF/IRIG at the Grenoble center, whose know-how greatly contributed to the sample preparation.

3.5 Characterization Techniques

To investigate both the luminescent materials in their pure form (before integration into the aerogels, to better know the luminescent materials that are being using in this work) and the luminescent aerogels, various characterization techniques are employed. These techniques can be grouped into those performed prior to tritium exposure and those carried out after tritium exposure.

3.5.1 Prior to Tritium Exposure

3.5.1.1 Spectral Characterization by Photoluminescence (PL)

The first of these techniques is PL spectroscopy, a non-destructive spectral characterization technique that provides valuable information on the electronic properties and composition of materials under photon excitation.

3.5.1.1.1 Instrumentation

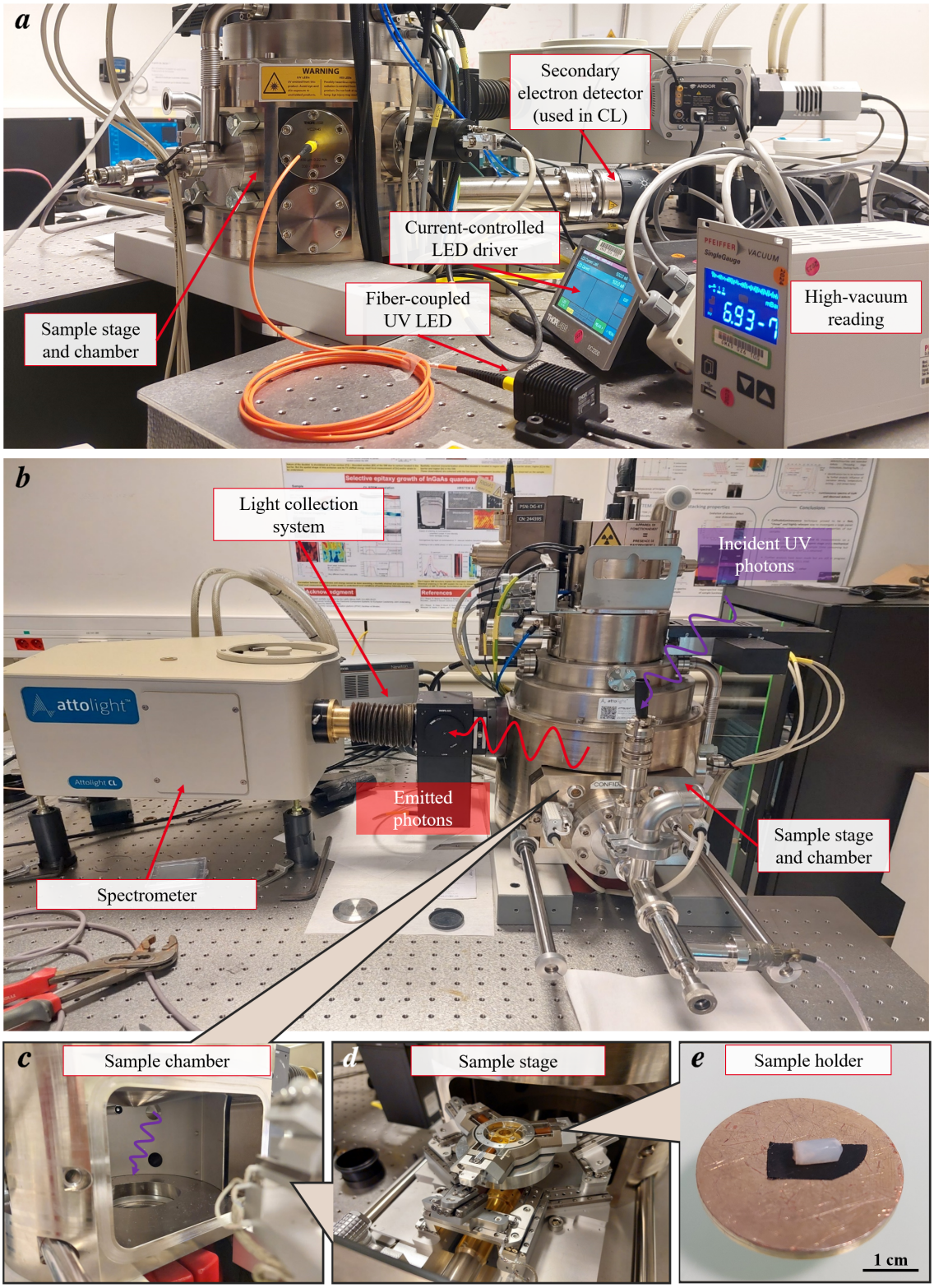

Figure 3.19: ***a***) Custom-built PL spectroscopy setup showing the integration of the UV excitation source. ***b***) Custom-built PL spectroscopy setup adapted from the CL system, highlighting the photon collection optics and the spectrometer. ***c***) Vacuum sample chamber with ***d***) the sample stage, which supports ***e***) the sample holder, where the sample is fixed using double-sided carbon tape.

In this work, PL measurements are performed using a custom-built setup fully integrated into the CL chamber[7].

Regarding the excitation source, a fiber-coupled UV LED (emission centered at 280 nm, ref. M280F5[g] from Thorlabs) is powered by a current-controlled LED driver, and the optical fiber is introduced into the CL chamber, as shown in Figure 3.19a.

Thus, these UV photons strike the sample located inside the vacuum chamber (Figure 3.19c), placed on the sample stage (Figure 3.19d) and fixed to the sample holder with double-sided carbon tape (Figure 3.19e) since other adhesive and conductive agents, such as silver lacquer, would be absorbed by the sample. This excitation produces the emission of photons that are collected by an optical system and detected with a spectrometer equipped with a CCD detector, as shown in Figure 3.19b.

The integration of the PL excitation source within the existing CL setup allows for rapid switching between measurement modes during the same experimental session.

3.5.1.1.2 Sample Preparation

As already mentioned, this characterization technique is used both for pure luminescent materials and for luminescent aerogels, prior to their exposure to the tritium atmosphere. But it must be noted that, to characterize the pure luminescent materials before their incorporation into the aerogels, luminescent coatings must be prepared.

For this purpose, the spray coating technique is employed, with a liquid solution containing the luminescent material diluted in deionized water, which is then deposited on a silica wafer as fine aerosol droplets. As shown in Figure 3.20a, the silica wafers are placed on a plate heated to 120°C to evaporate the water.

Profilometry measurements show that the resulting luminescent coatings have thicknesses of 5 μm for YVO_4:Eu^{3+}, 50 μm for the QDs, and 80 μm for Y_2O_3:Eu^{3+}. Figures 3.20b and 3.20c show the coatings of $AgInS_2$ and Y_2O_3:Eu^{3+}, respectively, under a binocular microscope.

[7]The PL spectroscopy is carried out at the nanocharacterization platform shared by the LETI, LITEN, and IRIG laboratories, located at the CEA Grenoble site.

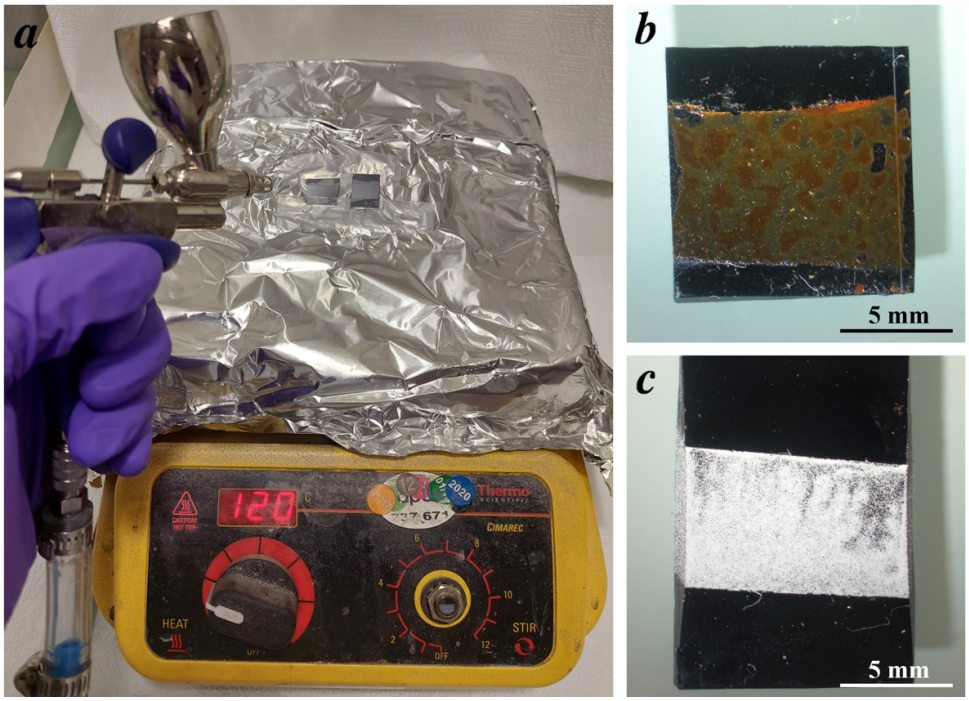

Figure 3.20: ***a***) Preparation of the luminescent coatings, in particular the YVO_4:Eu^{3+} coating, by spray coating. ***b***) $AgInS_2$ coating. ***c***) Y_2O_3:Eu^{3+} coating.

3.5.1.2 Two-Dimensional Morphological and Spectral Characterization by Cathodoluminescence (CL)

Another spectroscopy technique used in this work is CL, performed with the Allalin instrument commercialized by Attolight, in which the excitation source is electrons [8]. The main objective of this study is to simulate the behavior of sample under tritium exposure, although the excitation mechanism is not exactly the same. In the case of tritium, the excitation is polyenergetic, with electrons having an average energy of 5.7 keV and a maximum of 18.6 keV, whereas in CL the electron beam is monoenergetic and its maximum energy is 11 keV.

When an energetic electron beam interacts with a material, it generates a characteristic pear-shaped interaction volume whose size and depth depend on the electron energy and sample composition, as illustrated in Figure 3.21. Within this region, numerous signals are produced, including:

- Secondary Electrons (SE): low-energy electrons ejected from atoms near the sample's surface after energy transfer from the incoming electron beam.

[8]The CL spectroscopy is carried out at the nanocharacterization platform shared by the LETI, LITEN, and IRIG laboratories, located at the CEA Grenoble site.

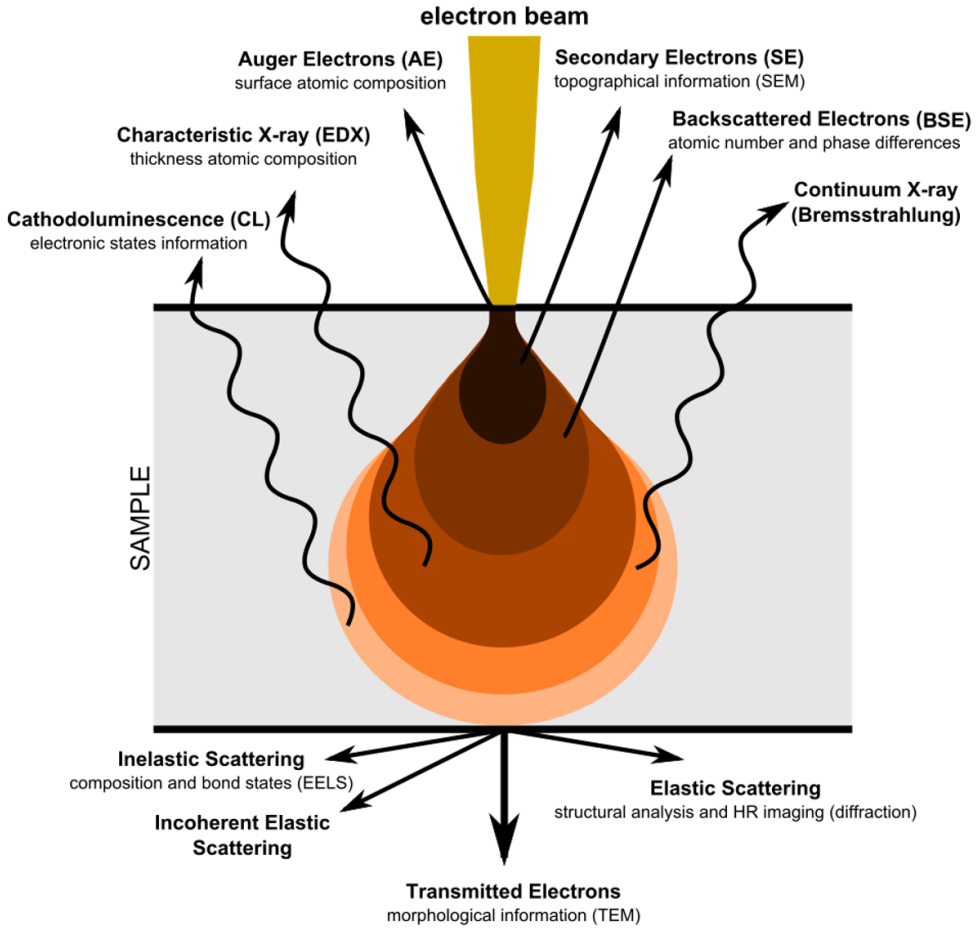

Figure 3.21: Characteristic pear-shaped interaction volumes when an electron beam interacts with a material. Figure reproduced from [119].

- Backscattered Electrons (BSE): primary electrons from the incident beam that are scattered back out of the sample by elastic interactions with atomic nuclei.
- Auger Electrons (AE): when core-shell electrons are ejected (inner-shell ionization), a higher-shell electron can fill the vacancy. The excess energy is transferred to another electron, which is then ejected (the Auger electron).
- Characteristic X-ray (EDX): when a higher-energy electron fills a lower-energy shell vacancy, an X-ray photon is emitted with an energy characteristic of the atomic species.
- CL photons: when struck by the electron beam, if the sample contains luminescent materials as it is the case, photons are emitted.
- Continuum X-ray (bremsstrahlung): produced by the deceleration of the primary

electron as it passes near the nucleus, resulting in a broad spectrum of X-ray emissions.

In addition, some electrons and other radiations can penetrate through the entire sample, producing transmitted electrons and other signals. With the use of CL spectroscopy, only the SE and CL photons will be utilized, as will be explained now.

Moreover, the shape and size of the interaction volume are influenced by factors such as the atomic number (Z) and density of the material. On one hand, as demonstrated in Figures 3.22a, 3.22b, and 3.22c, increasing the electron beam energy (5, 10, and 20 keV, respectively, in Si) results in a larger interaction volume, as shown by Monte Carlo simulations with CASINO. In these figures, blue lines represent absorbed electrons and red lines indicate the trajectories of BSE, with the largest interaction volume observed at 20 keV. On the other hand, the use of higher atomic number materials increases electron scattering, thereby reducing the penetration depth and shrinking the interaction volume. This effect is illustrated in Figures 3.22d, 3.22e, and 3.22f, which show simulations at 5 keV for Si, Ti, and Au, respectively.

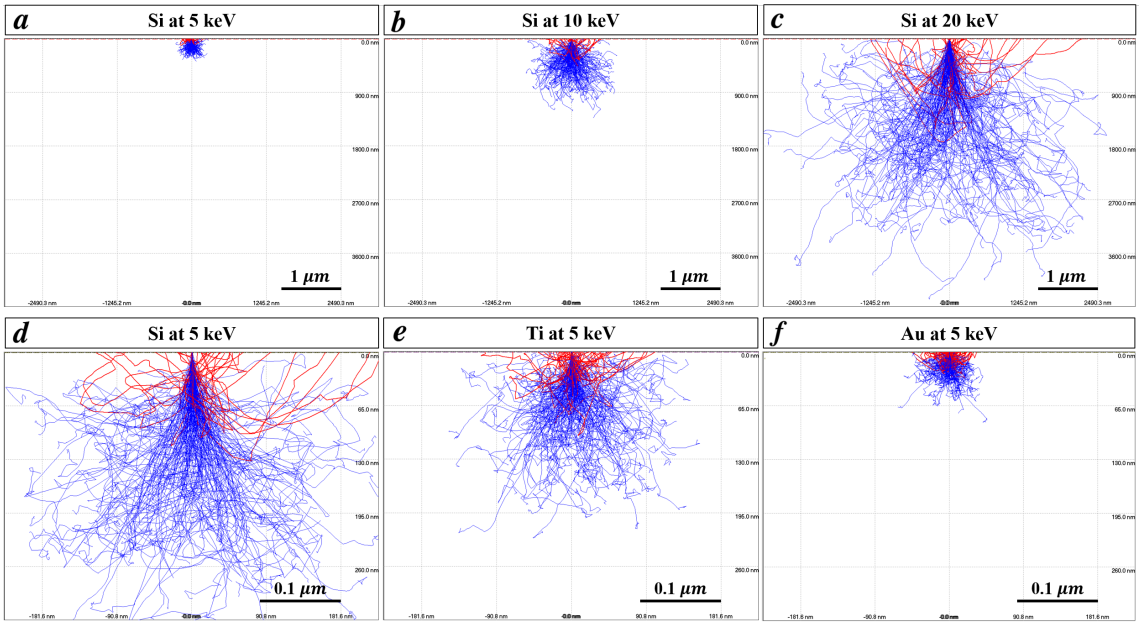

Figure 3.22: Monte Carlo simulations using CASINO of electron trajectories[9]: ***a***) Si at 5 keV, ***b***) Si at 10 keV, ***c***) Si at 20 keV, ***d***) Si at 5 keV (on a different scale), ***e***) Ti at 5 keV, and ***f***) Au at 5 keV. Blue lines correspond to trajectories of absorbed electrons and red lines to BSE.

[9]The number of incident electrons was set to 100 000, with a beam radius of 1 nm and no tilt angle.

3.5.1.2.1 Instrumentation

The excitation source in CL experiments is a Field Emission Gun (FEG) electron source [120]. An FEG generates electrons using the quantum tunneling effect. A sharply pointed single-crystal tungsten tip is placed under a very strong electric field. This field lowers the potential barrier confining the electrons at the emitter surface, enabling them to tunnel through and escape into the vacuum. This type of electron source produces an electron beam that is smaller in diameter (typically around 3 to 10 nm), more coherent, and brighter than what can be achieved with conventional thermionic emitters such as tungsten.

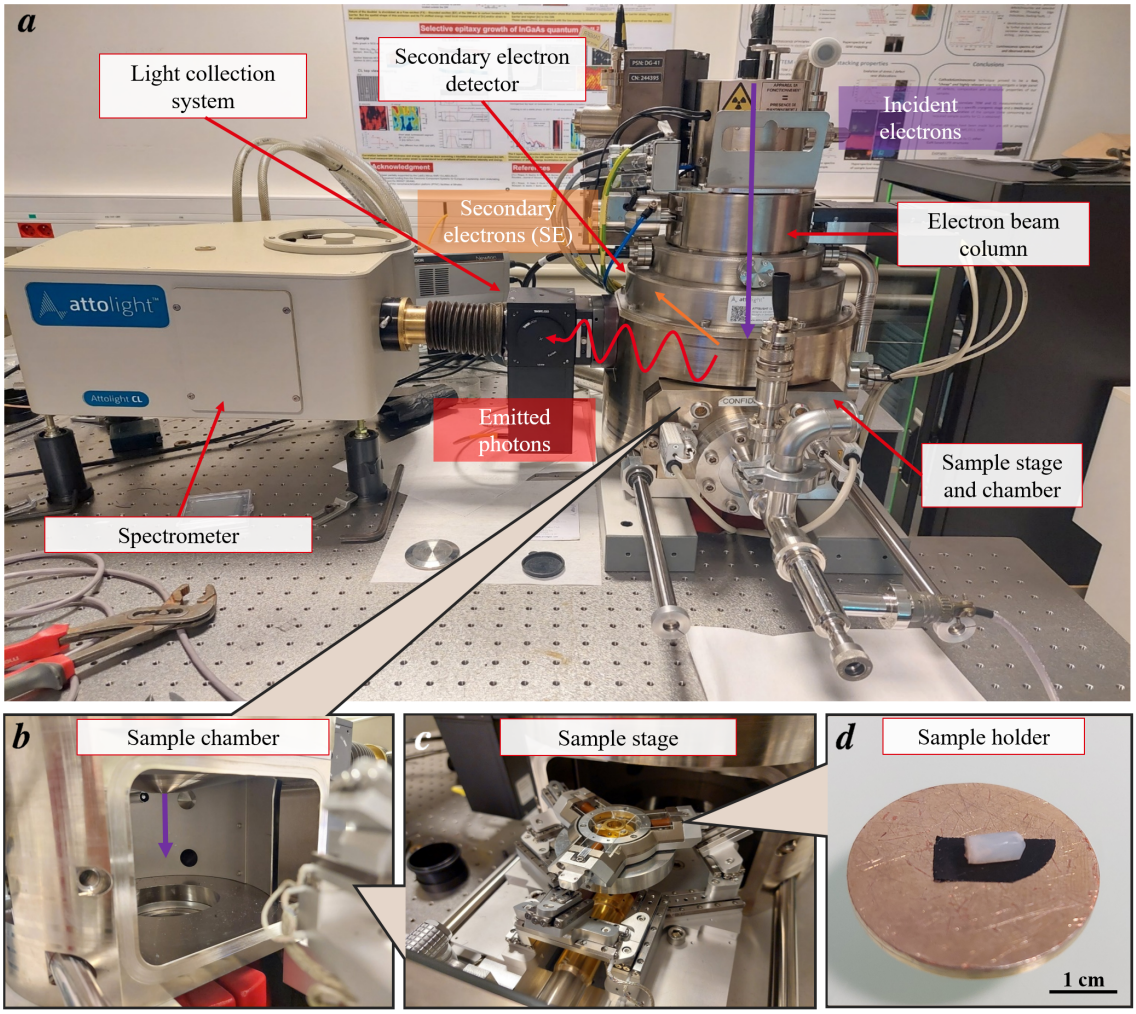

Figure 3.23: ***a***) CL spectroscopy setup, highlighting the electron beam column, the SE detector, the photon collection system and the spectrometer. ***b***) Vacuum sample chamber with ***c***) the sample stage, which supports ***d***) the sample holder, where the sample is fixed using double-sided carbon tape.

This electron source, together with the system of optical elements used to focus the beam,

are located in the electron beam column shown in Figure 3.23a. The electron beam strikes the sample inside the vacuum chamber (Figure 3.23b), placed on the sample stage (Figure 3.23c) and fixed to the sample holder (Figure 3.23d), in the same way as for PL spectroscopy.

The sample emits, on one hand, SE, among others, which are collected (by the detector best seen in Figure 3.19a) to form an image of the analyzed sample surface (SE imaging). On the other hand, the sample also emits photons, which are collected by an optical system and detected with the spectrometer coupled to the CCD. The system therefore includes an electron microscope coupled to an optical microscope.

Regarding sample preparation, either the luminescent coatings prepared by spray coating or the aerogels with the luminescent materials already integrated are used, as is done in PL spectroscopy (section 3.5.1.1.2).

3.5.1.3 Three-Dimensional Morphological Characterization by Gas Adsorption/Desorption Measurements

Another characterization technique used is gas adsorption and desorption measurement, aimed at studying the porous structure of the aerogel and how it varies depending on the type and concentration of the embedded luminescent material [10].

3.5.1.3.1 Physical Principles of Adsorption and Desorption

Gas adsorption is the process by which gas molecules (the *adsorptive*) adhere to the surface of a solid (the *absorbent*), a process favored when pressure increases. Physical adsorption (physisorption) and chemical adsorption (chemisorption) are two fundamental mechanisms by which gases interact with material surfaces [121, 122]. Physisorption involves weak bonding between gas molecules, mainly through van der Waals forces, which are reversible. Chemisorption involves the formation of stronger chemical bonds between gas molecules and atoms or molecules on the surface of the solid.

A gas molecule can collide either with a bare surface or with a surface already covered by a layer of *adsorbate* (gas molecules already attached to the solid surface), as illustrated in Figure 3.24a [123]. On the covered surface, there exists a potential similar to that of the bare surface, but with a significantly lower interaction energy, as plotted in Figure 3.24b. Multilayer adsorption is possible but will only occur under conditions close to liquefaction,

[10] The gas adsorption/desorption technique is carried out at the nanosafety platform of the CEA/DES/LITEN laboratories, located at the CEA Grenoble site.

that is, at high pressures close to the saturation vapor pressure of the adsorptive at the given temperature.

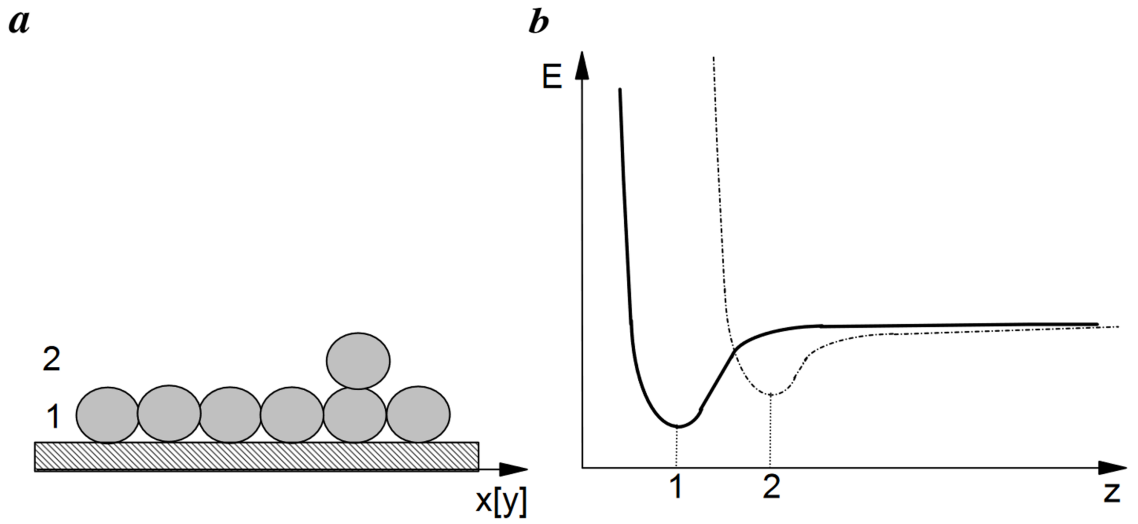

Figure 3.24: ***a)*** Diagram of a surface with a gas molecule adsorbing onto an already covered surface. ***b)*** The interaction energy is lower when adsorption occurs on an already covered surface. Figure reproduced from [123].

Desorption is the opposite process, where gas molecules leave the solid surface, a process favored when pressure decreases.

3.5.1.3.2 Measurements

Gas adsorption analyses are generally, and particularly in this work, carried out using nitrogen gas (N_2) due to its strong affinity for solid surfaces. This type of measurement follows the steps listed below:

1. Pretreatment of sample:

    - The sample is initially exposed to a degazing to remove any moisture that has accumulated since its preparation and to clean its pores. For this, the sample is exposed to a high vacuum, and heated to 110°C at a rate of 5°C/min for 1320 min (22h).

2. Adsorption process (steps illustrated in Figure 3.25):

    - Stage 1:

  - Isolated sites on the solid surface begin to adsorb gas molecules at low pressure.

- Stage 2:

  - As gas pressure increases, coverage of gas molecules increases to form a monolayer (one gas molecule thick).

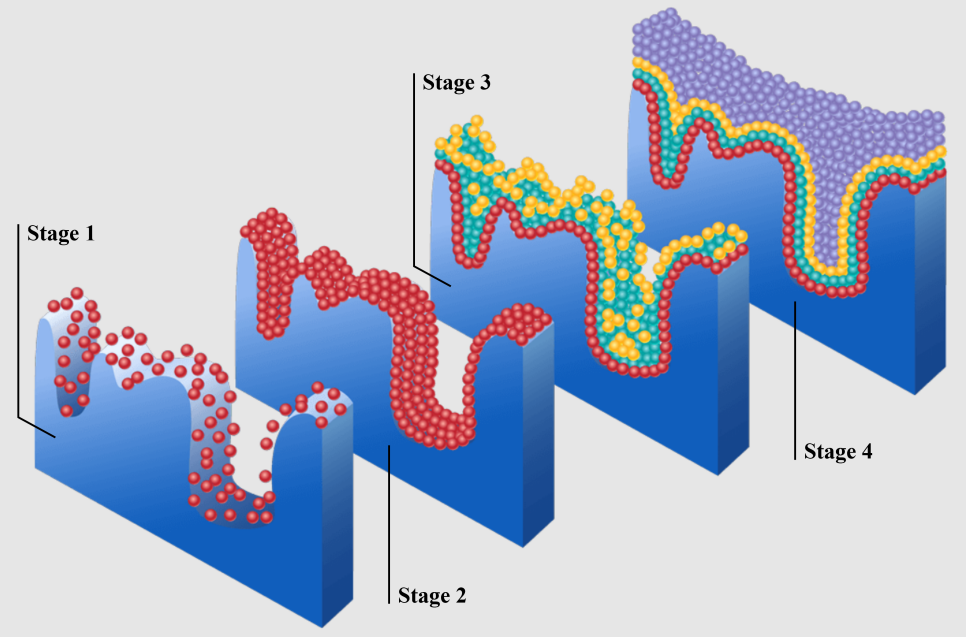

Figure 3.25: Schematic representation of the stages involved in the gas adsorption process. Figure adapted from [122].

  - The Brunauer–Emmett–Teller (BET) model is used to calculate the specific surface area from the quantity of adsorbed gas. The specific surface area corresponds to the area accessible to gas molecules, including both the external surface of the sample and the internal surfaces of pores. The BET model is applied within a relative pressure (P/P_0) range between 0.05 and 0.25 (corresponding to the linear behavior), with P being the actual pressure and P_0 the saturation vapor pressure (the highest pressure it can be reached before condensation occurs) of nitrogen at 77 K, which is very close to 1 bar.

- Stage 3:

  - As the gas pressure increases further, multilayer adsorption begins, with smaller pores in the sample filling first.

- Stage 4:

  - At sufficiently high gas pressures, the sample surface becomes fully covered and all pores are filled.
  - The Barret-Joyner-Halenda (BJH) model is applied to determine pore diameter, volume and distribution.

3. Desorption process:

   - Basically, the same steps as in the adsorption process are followed, but in reverse order and with a particular feature. The interior of a pore, called the core, evaporates suddenly as soon as the critical pressure (specific relative pressure at which capillary evaporation occurs) for that core radius is reached. Once the core has evaporated, a layer of adsorbate remains on the pore walls. This layer becomes progressively thinner with each subsequent decrease in pressure, so the amount of desorbed gas measured at each step corresponds to the amount of gas evaporated from the pore cores at that stage, plus the amount desorbed from the walls of pores whose cores have already been evaporated in previous steps.
   - The BJH model is again applied during desorption, as it is fundamentally a desorption-based model, although it can also be used with data obtained during adsorption. This model is used to determine the pore size distribution as well as other parameters such as pore volume (both incremental and cumulative) and pore surface area (both incremental and cumulative), although here only the results related to pore size distribution will be presented. In addition, this model can determine the relationship between the core radius and the critical pressure using the Kelvin equation, and the thickness of the layer that remains on the pore walls for each value of relative pressure. This model, which assumes cylindrical pore geometry, is applied within a relative pressure range of 0.4 to 0.98 to determine the distribution of mesopores (with diameters between 2 and 50 nm) and macropores (with diameters greater than 50 nm). For relative pressures above 0.98 or below 0.4, the model is no longer valid. Therefore, the t-plot model is employed to analyze the distribution of micropores (with diameters smaller than 2 nm).

4. Isotherm acquisition:

   - After the desorption process is complete, the system is returned to ambient pressure, and the full isotherm, comprising both the adsorption and desorption branches, is obtained. International Union of Pure and Applied Chemistry

(IUPAC) has classified isotherms into six types according to their shape, as shown in Figure 3.26. This classification provides valuable insights into the porous structure of the sample.

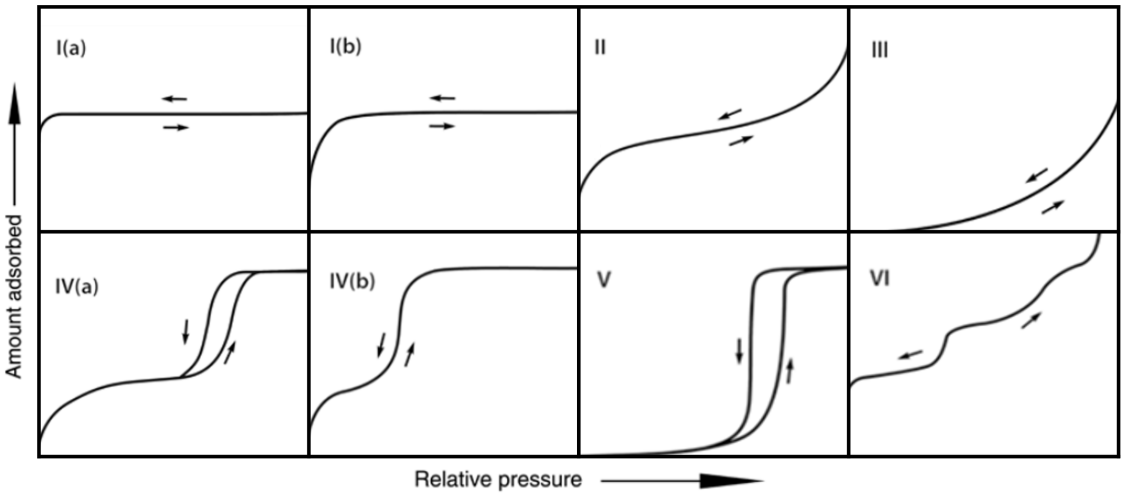

Figure 3.26: IUPAC classification of isotherms. Figure adapted from [121].

As can be observed in isotherms IV(a) and V, hysteresis loops may appear. Many different forms of hysteresis loops have been reported, but the main types classified by IUPAC are illustrated in Figure 3.27.

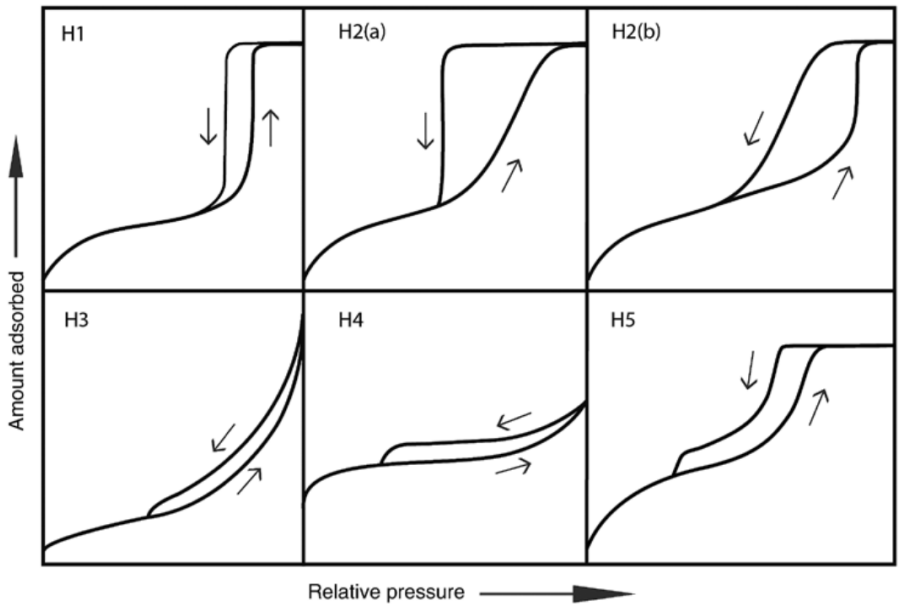

Figure 3.27: IUPAC classification of hysteresis loops. Figure reproduced from [121].

Hysteresis loops may arise from several physical mechanisms [121], such as:

- Capillary condensation in mesopores: during adsorption, gas condenses in the pores at a certain relative pressure but during desorption, evaporation from the pores occurs at a lower pressure, creating a loop between the two branches. It has been reported in mesopores wider than $\sim$ 4 nm for nitrogen at 77 K.
- Capillary condensation in open-ended pores, like straight cylindrical pores.
- Blocking effects in ink-bottle pores: these pores have a large cavity connected to the external surface by a narrow neck and during desorption, the large cavity cannot empty until the narrow neck empties, which happens at a much lower relative pressure.
- Cavitation: when the neck diameter is smaller than a critical size, the liquid in the cavity can become metastable and evaporate suddenly via cavitation (i.e., the spontaneous nucleation and growth of gas bubbles in the metastable condensed fluid). For nitrogen at 77 K, this critical neck diameter has been reported to be approximately 5-6 nm.

Finally, it is also important to note that the slope of the adsorption curves can vary, and the BET model relates this slope to the number of layers that have been filled with the gas, as illustrated in Figure 3.28.

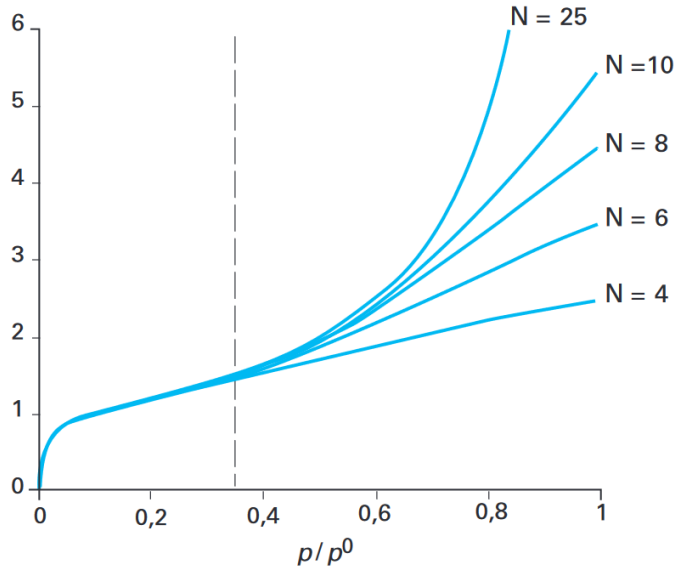

Figure 3.28: Adsorption isotherms calculated using the BET model for different values of the number N of adsorbed layers. Figure reproduced from [124].

3.5.1.3.3 Instrumentation

The equipment used for nitrogen gas adsorption/desorption measurements, a Micromeritics ASAP 2420 instrument, is shown in Figure 3.29a [11]. It consists of two distinct zones: in the lower zone (Figure 3.29c), sample pretreatment is performed, whereas in the upper zone (Figure 3.29b), the samples are subsequently exposed to nitrogen gas inside cylindrical chambers (Dewars). In the image, the Dewars are in their lowered position within the instrument. After initial filling with liquid nitrogen, the Dewars are raised to enclose the glass tubes containing the samples, enabling the gas absorption/desorption measurements to be performed [125].

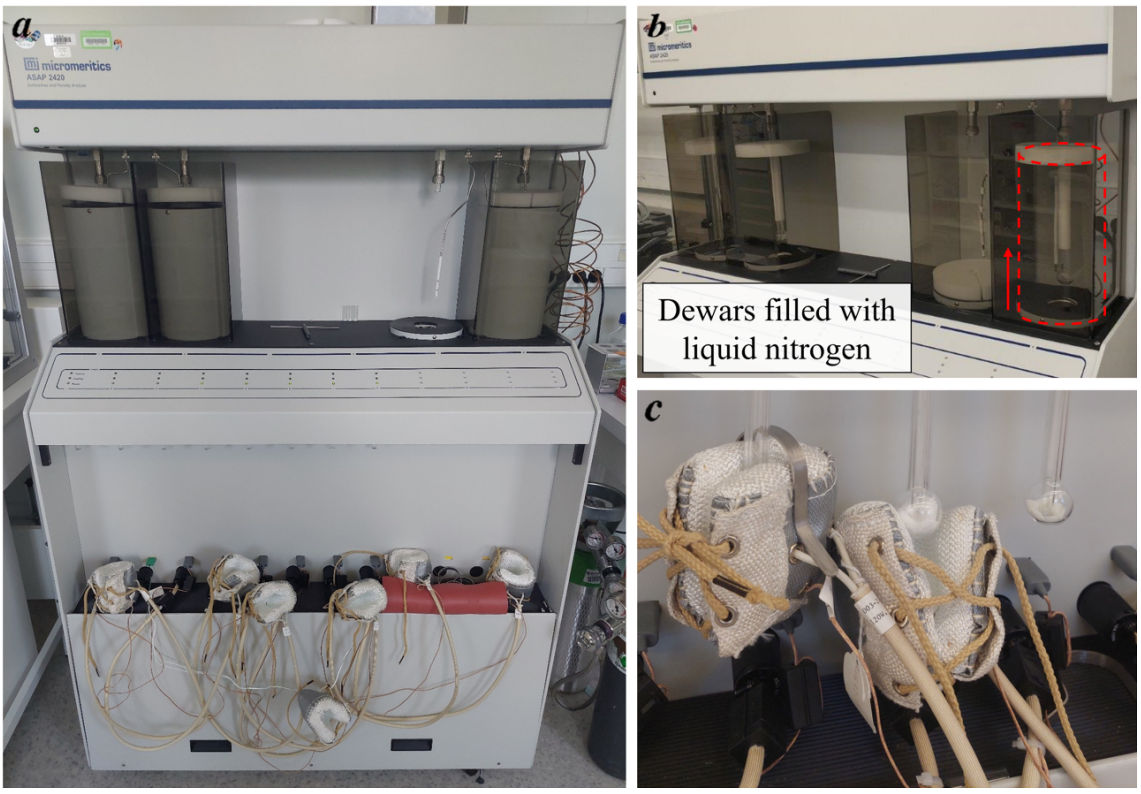

Figure 3.29: ***a)*** The Micromeritics ASAP 2420 instrument used for the nitrogen gas adsorption/desorption measurements in the CEA/DRT/LETI laboratories located at the CEA Grenoble site. ***b)*** Nitrogen gas exposure zone for adsorption/desorption measurements. ***c)*** Pretreatment zone.

As will be discussed in the following section, this equipment allows the analysis of silica aerogels but not of CMC aerogels or the pure luminescent powders, which have much lower specific surface areas. For this reason, a BEL Japan BELSORP instrument is used

[11] The nitrogen gas absorption/desorption measurements using the Micromeritics ASAP 2420 instrument are carried out in the CEA/DRT/LETI laboratories located at the CEA Grenoble site.

for the analysis of CMC aerogels and pure luminescent powders[12], which works with smaller volumes for both samples and nitrogen, thereby increasing the sensitivity of the equipment. In addition, it features a supplementary cell that is always kept empty and serves as a reference, which improves the precision of the measurements. This instrument is shown in Figure 3.30, where the oven used for sample pretreatment can be seen; this oven is later replaced by the Dewar filled with liquid nitrogen. In order to try to perform all the analyses under the closest possible conditions, the pretreatment conditions are the same as those defined for the Micromeritics ASAP 2420 instrument.

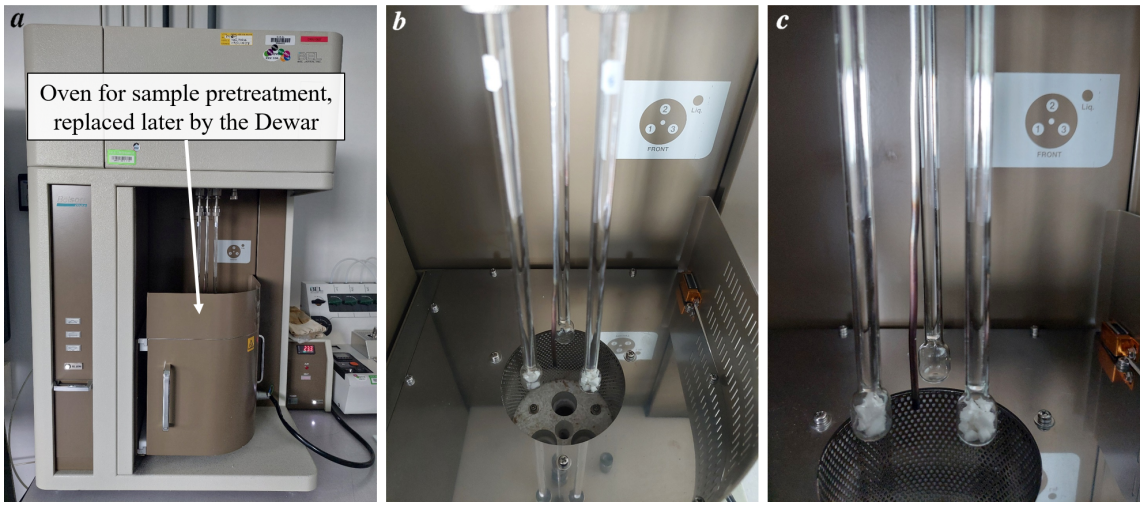

Figure 3.30: ***a)*** The BEL Japan BELSORP instrument used for the nitrogen gas adsorption/desorption measurements in the CEA/DES/LITEN laboratories located at the CEA Grenoble site. ***b)*** Three glass tubes, two of them containing the samples to be analyzed (ports 1 and 3) and the empty reference tube (port 2). ***c)*** Glass tubes more closely, where the volume of the bulbs can be better appreciated.

3.5.1.3.4 Sample Preparation

This technique is also used to characterize both pure luminescent materials and luminescent aerogels.

Regarding the analysis of the luminescent materials, they can only be studied in the dry state, so the Y_2O_3:Eu^{3+} phosphors are in powder form, which is their commercial format, and the QDs are dry as well, which corresponds to their state immediately after synthesis. YVO_4:Eu^{3+} phosphors are not characterized because they are initially diluted. Figure 3.31 shows the glass tubes containing the luminescent materials used for the measurements.

[12]The nitrogen gas absorption/desorption measurements using the BEL Japan BELSORP instrument are carried out in the CEA/DES/LITEN laboratories located at the CEA Grenoble site.



Figure 3.31: From left to right: Y_2O_3:Eu^{3+} phosphors, $CuInS_2$, and $AgInS_2$ QDs introduced into the measuring cells for gas adsorption/desorption measurements.

Regarding the luminescent aerogels, two-thirds of the volume of the bulbs of the glass tubes must be filled for both instruments, which implies a large number of aerogels. To achieve this, instead of using the cylindrical aerogels of 3 mm in diameter and 10 mm in length, a disk-shaped sample with a diameter of 30 mm and a thickness of 5 mm is prepared using the same stock solution and at the same time as the cylindrical aerogels. In this way, the disk-shaped aerogel is later cut into small pieces that are easier to introduce into the glass tubes. For both inserting and removing the samples from these cells, it is helpful to use a U-shaped antistatic tool that allows neutralizing static charges, as the CMC aerogels are highly electrostatically charged.

The porosity and specific surface area of the aerogel are intrinsic to its composition and synthesis conditions. The additional surface created by cutting the disk-shaped aerogel into small pieces is negligible compared to the internal porosity of the aerogel itself, and does not affect the measured values of these properties.

In Figure 3.32a, the aqueous solution can be seen, which specifically contains 2%wt CMC and 0.3%wt YVO_4:Eu^{3+}, and is used for the preparation of a disk-shaped aerogel. This solution is the same as that used for the cylindrical aerogels of the same composition. In Figure 3.32b, this same solution is shown under a UV lamp. The same procedure as for the cylindrical aerogels is followed; thus, after freezing and freeze-drying, the disk shown in Figure 3.32c is obtained, which is displayed under UV light. Finally, Figure 3.32d shows this disk cut into small pieces so that it can be introduced into the glass tubes.

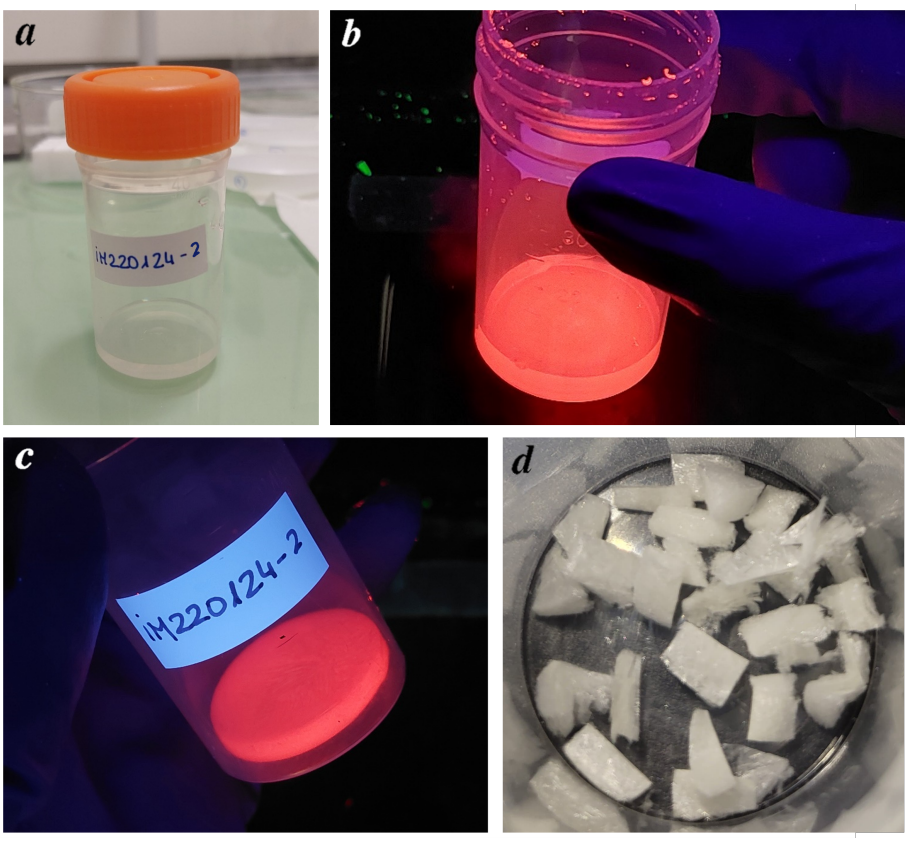

Figure 3.32: ***a)*** Aqueous solution of 2%wt CMC and 0.3%wt YVO_4:Eu^{3+}. ***b)*** Same aqueous solution under UV light. ***c)*** Aerogel of 2%wt CMC and 0.3%wt YVO_4:Eu^{3+} under UV light. ***d)*** Same aerogel cut in small pieces to be introduced into the measuring cell for gas adsorption/desorption measurements.

3.5.1.4 Three-Dimensional Morphological Characterization by X-Ray Tomography

With the aim of studying the distribution of luminescent particles in aerogels, laboratory X-ray tomography experiments are carried out[13]. X-ray tomography is a non-destructive three-dimensional imaging technique that uses X-rays to visualize the internal structure of objects without damaging them.

A sample is placed in the laboratory X-ray tomography system, which consists of an X-ray source and a detector. The laboratory X-ray source, typically a micro-focus tube, operates by accelerating electrons onto a metal target, producing a broad spectrum of X-rays with a controllable energy range. For this experiment, X-rays at 40 keV are

[13]The laboratory X-ray tomography experiments are carried out at the nanocharacterization platform shared by the LETI, LITEN, and IRIG laboratories, located at the CEA Grenoble site.

used, providing suitable penetration for aerogel-based samples. The sample is rotated, and X-rays pass through it from various angles. The detector captures a series of two-dimensional projections, which are processed using reconstruction algorithms to generate a three-dimensional image of the analyzed sample.

However, as will be shown in section 6.1.4 of chapter 6, the spatial resolution and contrast achievable with laboratory X-ray tomography at 40 keV are not sufficient to resolve the distribution of luminescent particles within the aerogel. To overcome these limitations, more energetic and highly coherent X-rays from synchrotron radiation sources can be employed. Synchrotron X-rays enable advanced imaging techniques, such as phase contrast tomography, which provide significantly enhanced sensitivity and resolution for visualizing low-density or weakly absorbing features.

Therefore, a request for beamtime at the European Synchrotron Radiation Facility (ESRF) in Grenoble, France, was sent. Our proposal (ref. MA-6408) was accepted, and we were allocated three shifts of beamtime (a shift typically corresponds to an 8-hour block of experimental time) in September 2024 (from Friday, September 13th to Sunday, September 15th).

3.5.1.4.1 European Synchrotron Radiation Facility (ESRF)

The ESRF is a large, circular accelerator of electrons that produces extremely bright and focused beams of X-rays, 10 trillion times brighter than medical X-rays. It functions like a giant microscope, that reveals the structure of materials and living matter in all their complexity thanks to the brilliance, penetration depth and coherence properties of synchrotron X-rays.

The generation of X-rays at the ESRF is based on the following steps [126]:

1. Electron production in the Linear Accelerator (Linac):
    - Electrons are produced in a triode electron gun, where a heated cathode emits electrons that are accelerated to an initial energy of about 200 MeV. These electrons are organized into bunches and further accelerated in subsequent accelerator sections to reach energies suitable for injection into the booster synchrotron.
2. Injection into the booster synchrotron:
    - The high-energy electrons are then injected into a ring of 300 meters, where they are accelerated under ultra-high vacuum ($1{\cdot}10^{-9}$ mbar [127]) from 200

MeV up to 6 GeV (highly relativistic electrons), the full operational energy required for the storage ring.

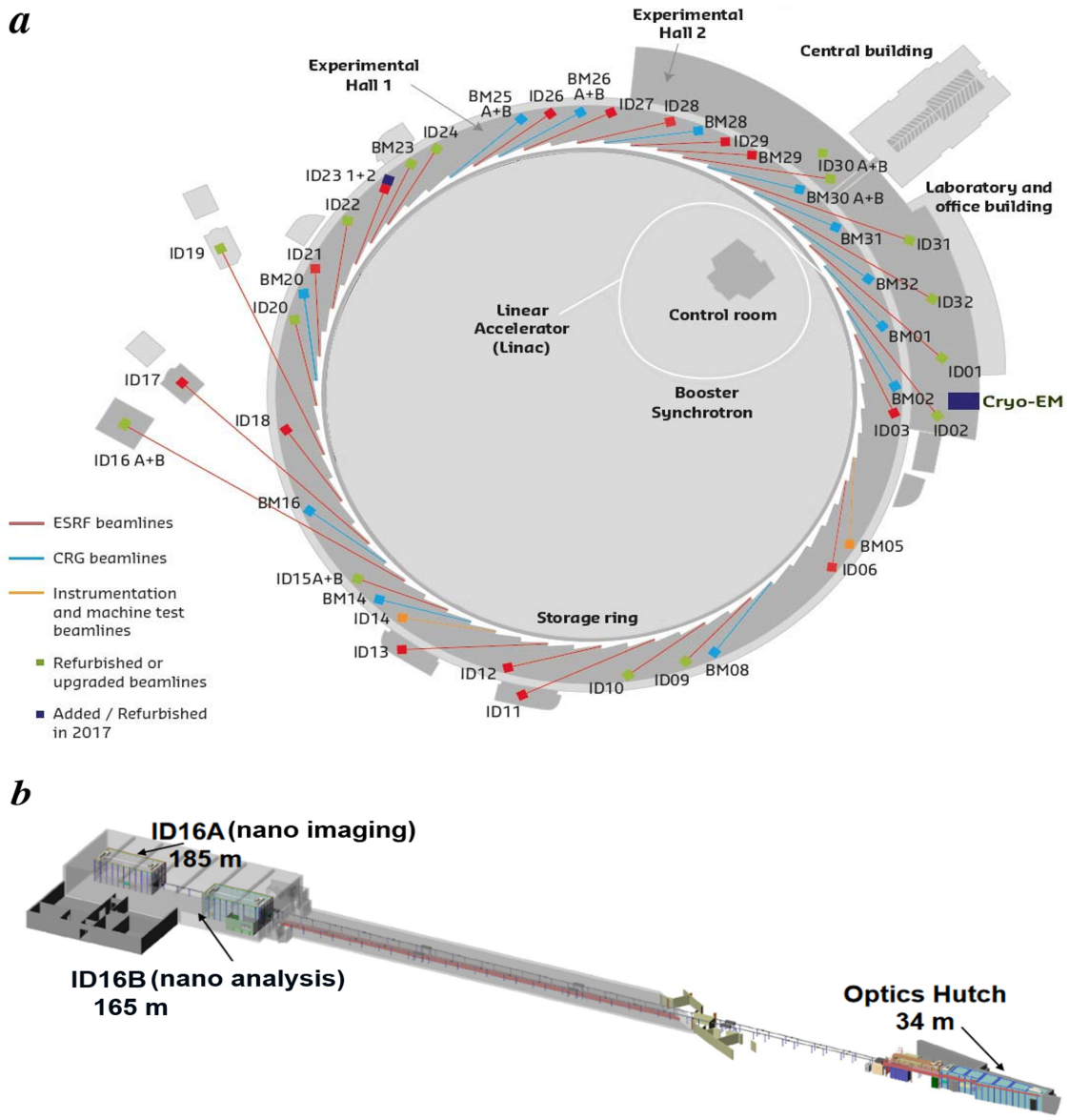

Figure 3.33: ***a)*** Illustration showing the different elements of the ESRF: the Linac, the booster synchrotron, the storage ring and the different beamlines. ***b)*** Layout of beamlines ID16A and ID16B. Figures reproduced from [126].

3. Injection into the storage ring:

   - Electrons enter the main and much larger ring of 844 meters, where they circulate for many hours.

- In an X-ray tube, electrons emitted by the cathode decelerate when approaching the anode, producing Bremsstrahlung X-rays. In contrast, synchrotrons produce X-rays by bending the electron beam from its original path. The storage ring consists of straight sections containing insertion devices (also called undulators) separated by curved sections with bending magnets, similar to second-generation synchrotrons. These bending magnets serve both to produce synchrotron radiation and to guide the electrons along a closed orbit. The undulators induce horizontal oscillations in the electron beam, enhancing X-ray emission characteristic of third-generation synchrotrons.

4. Delivery of X-rays to the beamlines:

   - The emitted X-rays are directed to experimental stations, called beamlines, where the beam is conditionned using different X-ray optics elements (grazing incidence mirrors, monochromators, collimating optics, focusing optics) whose description is beyond the scope of this work.

All these ESRF's elements are illustrated in Figure 3.33a.

Our beamtime has been carried out on the ID16A beamline, which is illustrated in Figure 3.33b and will be described more in detail in the following section. This beamline provides a high-brilliance beam focused down to nanometer size, allowing quantitative tridimensional characterization of the morphology and the elemental composition of specimens [126].

3.5.1.4.2 ID16A Beamline

ID16A is a recent 185 meters long nano-imaging beamline, designed to deliver a high-energy X-ray beam at 17.0 or 33.6 keV (in our experiments, we worked at 33.6 keV) with a sub-13 nm beam spot size, a world first at energies above 20 keV. Such a tiny and intense beam (6 billion photons per second) enables imaging of thick and highly absorbing samples, as well as direct visualization of nanoscale structures. To achieve this, the beamline uses advanced X-ray focusing optics based on a Kirkpatrick-Baez (K-B) system, consisting of a pair of multilayer coated, curved mirrors, one for horizontal and one for vertical focusing. ID16A's K-B mirrors require the highest possible level of perfection for the surface of these two small mirrors, only 36 and 70 mm in length. The mirrors are permanently installed in the optics hutch and supported by a custom-designed optomechanical assembly.

When a sample object is exposed to the X-ray source, X-rays transmitted through the sample at various angles propagate over a certain distance between the object and the

detector [128]. Variations in the X-ray refractive index within the sample cause changes in the shape of the X-ray wavefront as it passes through. In conventional X-ray imaging (illustrated in Figure 3.34a), the detector is placed directly behind the sample, resulting in a conventional absorption image. However, materials composed of low-Z elements absorb X-rays weakly, making it difficult to distinguish fine structures.

The ID16A beamline enables phase-contrast X-ray imaging (schematized in Figure 3.34b), a technique that enhances image contrast by exploiting the phase shifts X-rays undergo as they traverse the sample. By positioning the detector at a greater distance from the object, the X-ray beam is allowed to propagate after passing through the sample, leading to interference effects that produce a phase-contrast image (Fresnel diffraction). The most noticeable feature of phase-contrast enhancement is edge enhancement at interfaces between components with differing X-ray refractive indices.

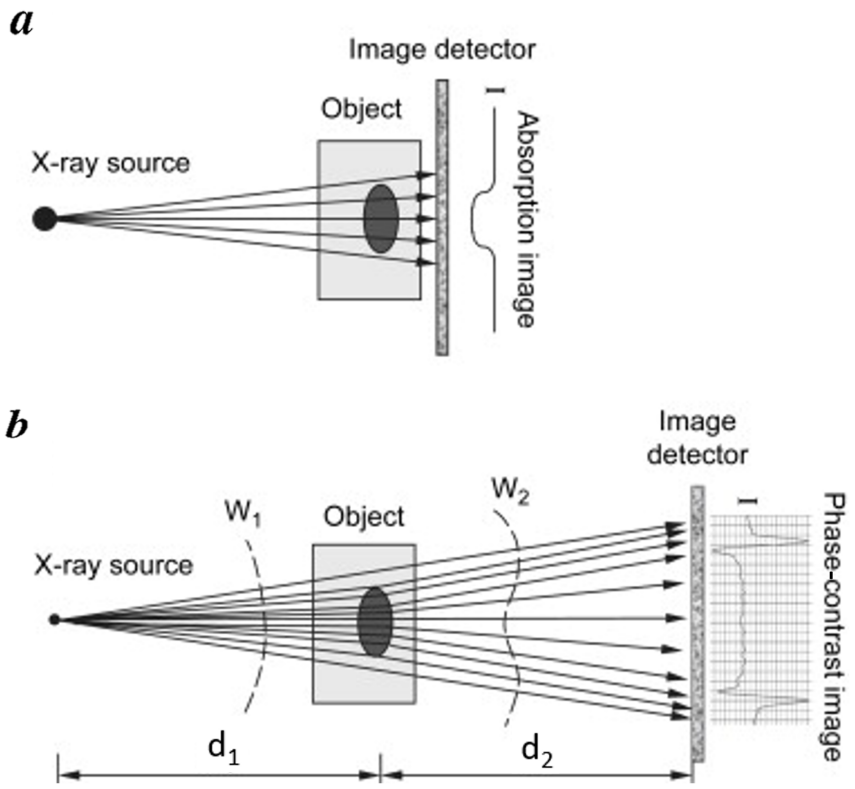

Figure 3.34: ***a)*** Conventional X-ray imaging setup. ***b)*** Phase-contrast imaging setup. Figures reproduced from [128].

After acquiring an initial phase-contrast image of the sample object, the sample is rotated incrementally around its axial axis (z-axis) so that at each angle, a phase-contrast image is recorded. Since the X-rays propagate along the x-direction, this technique, known as tomography, results in a series of two-dimensional projections in the (y, z) plane.

Since the detector only measures intensity, specialized computational algorithms are applied to extract the phase information from the recorded images. This step, called holotomography and illustrated in Figure 3.35, involves acquiring images at multiple sample-to-detector distances.

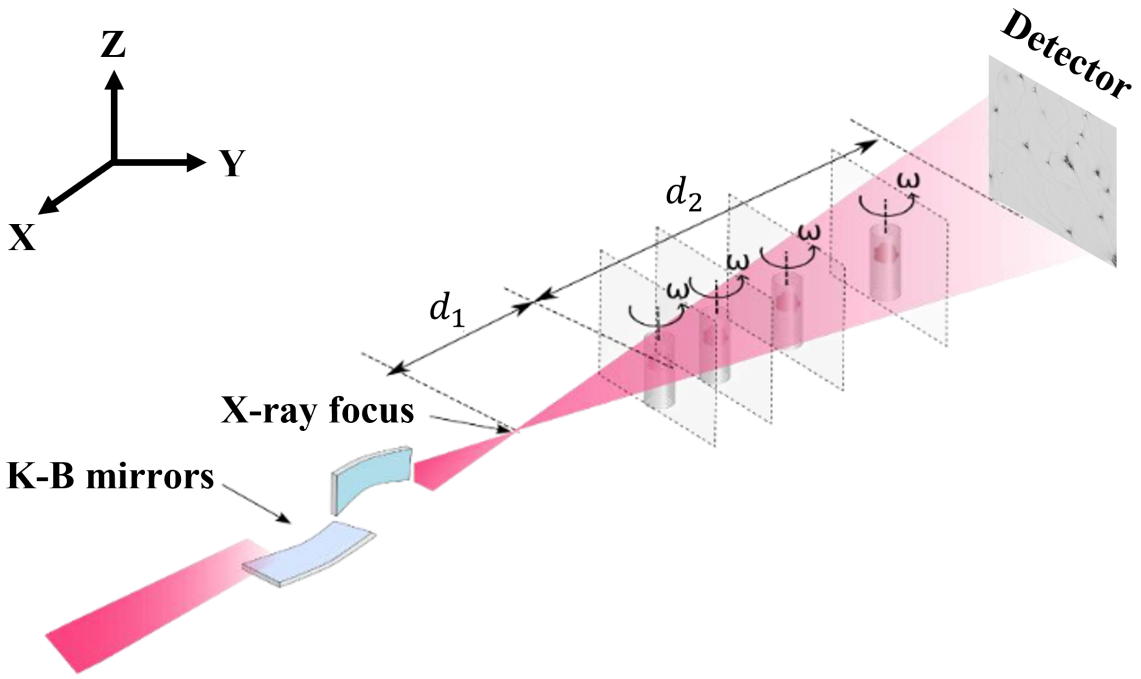

Figure 3.35: Holotomography setup in the ID16A beamline at ESRF in Grenoble, France. Figure adapted from [129].

High-Z or high electron density materials produce greater attenuation of X-rays than low-Z materials, as they absorb and scatter more X-rays. These materials also cause a larger phase shift and typically appear brighter (white) in holotomography images. In contrast, low-Z materials or low electron density materials usually appear darker (black). However, the images presented in this chapter are inverted during data processing. As a result, high-Z materials, such as the luminescent particles, appear dark (black), while the host CMC matrix appear bright (white).

The retrieved phase projections are fed into tomographic reconstruction software, generating a quantitative tridimensional map of the sample's internal structure. The visualization of the sample's internal structure gives us information about its morphology, internal interfaces and electron density distribution.

The three-dimensional distribution of luminescent particles within the aerogel structure will be studied combining phase-contrast imaging with holotomography. Due to the limited beamtime allocated, the current study has been restricted to CMC-based aerogels, in order

to prioritize exploring a greater variety of luminescent materials rather than varying the aerogel host matrix.

As far as sample requirements are concerned, limitations related to sample size must be considered. As shown in Figure 3.36, the sample should not exceed 5 mm in height above the sample holder. Additionally, due to the limited offset range, the sample must be positioned within ±0.7 mm of the center of the axis of rotation of the pin.

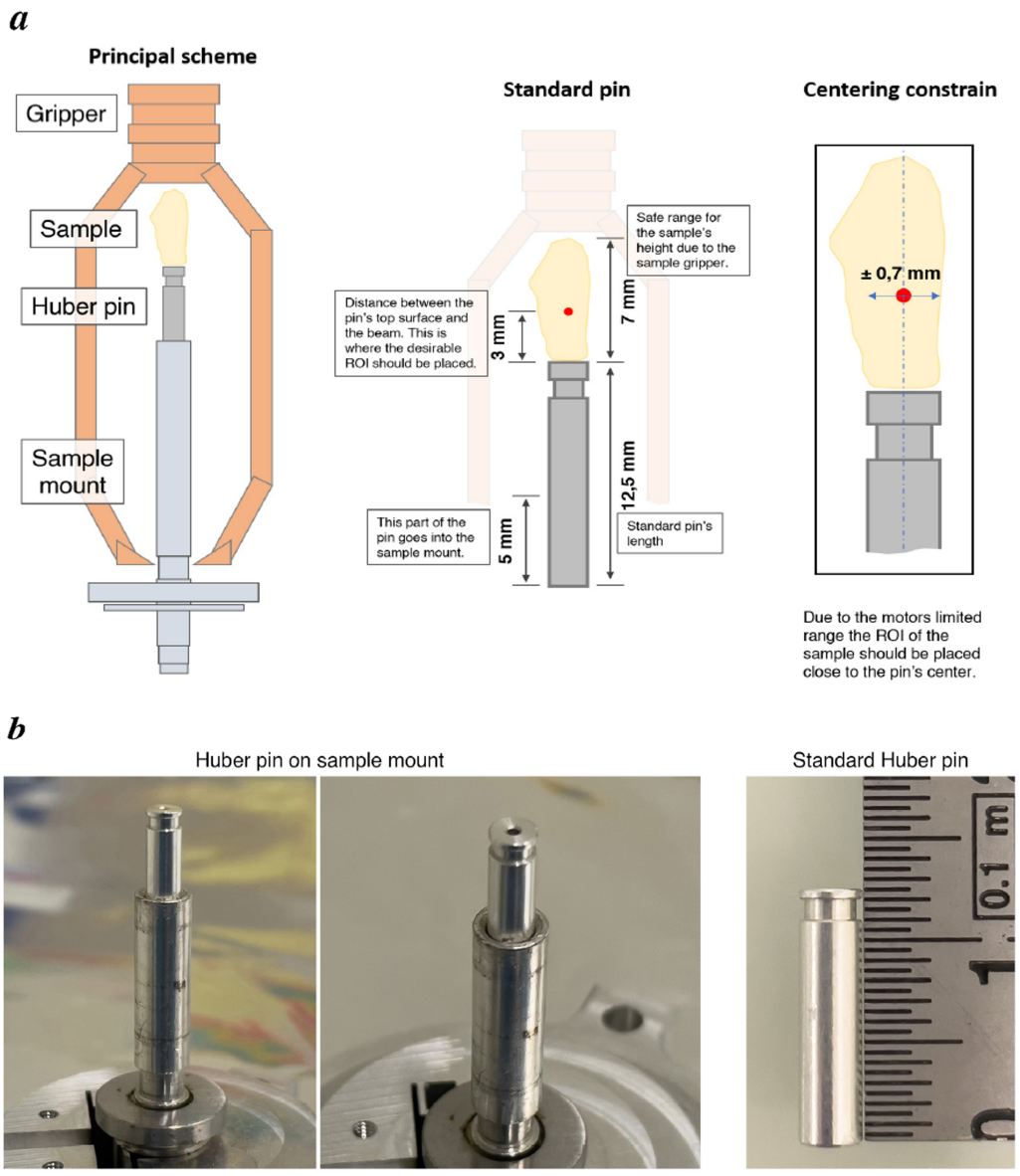

Figure 3.36: ***a)*** Schematic of the sample holder used in the experiments performed on the ID16A beamline at the ESRF in Grenoble, France. ***b)*** Images of the Huber pin that will hold the sample. ***c)*** Dimensions of the Huber pin. Figures reproduced from [130].

For tomography reconstruction to operate well, the diameter of the sample should be equal

to or smaller than the Reference Field of View (FoV). The latter depends on the X-ray magnification, i.e., the distance between the focal spot and the sample. It is typically around 60–290 μm (using a 2048×2048 pixel detector with a virtual pixel size of approximately 30–140 nm, as it has been the case in these experiments). However, it is possible to work in so-called *local tomography*, where the sample diameter reasonably exceeds the FoV. Since this facilitates sample preparation, although at the expense of image quality, it was decided to prepare samples whose typical diameter is around 800 μm.

This implies that smaller samples than those described in section 3.3.2 have to be prepared.

3.5.1.4.3 Sample Preparation

The initial approach to prepare the micrometric samples is to follow the same procedure used for millimetric aerogels, employing micrometric glass tips and capillaries as molds. However, the issue arises when attempting to fill the capillary with the CMC solution containing luminescent materials, since even when using micro-volume syringes, the tip of the syringe is wider than the diameter of the capillaries. The capillaries can only be filled by capillarity, by vertically immersing them in a vial containing the luminescent solution. This process is not immediate and may take up to 2 hours to fill just 10 mm in height. As a result, it is likely that sedimentation of the luminescent materials occurs at the bottom of the vial containing the solution.

Using this procedure, it is possible to prepare samples with diameters ranging from 120 to 160 μm, of CMC and nanometric luminescent particles (YVO_4:Eu^{3+}, $AgInS_2$, and $CuInS_2$), but not with micrometric ones (Y_2O_3:Eu^{3+}). This occurs despite using CMC solution and luminescent materials at a mass concentration of 3%wt to ensure the resulting solution is not too viscous.

A second strategy for preparing micrometric samples involves using millimettric aerogels, approximately 1 mm in diameter, synthesized following the method described in section 3.3.2. Upon drying, the aerogels typically shrink slightly, resulting in final sample diameters of around 750 to 900 μm, as measured under a binocular microscope. This technique enables the fabrication of samples incorporating various types of luminescent materials, including micrometric Y_2O_3:Eu^{3+} particles. However, the fact of analyzing wider samples implies that it will not be possible to perform a complete scan of the sample by holotomography, but it will be limited to perform a local tomography.

Figure 3.37 shows samples containing YVO_4:Eu^{3+}, $AgInS_2$, and $CuInS_2$ prepared using the first procedure (microcapillary filling) in panels a–c, with diameters ranging from 120–160 μm. Samples created through the second method (millimetric aerogel) appear in

panels d–f. The samples containing Y_2O_3:Eu^{3+}, $AgInS_2$, and $CuInS_2$ samples show larger diameters, of 750–900 μm.

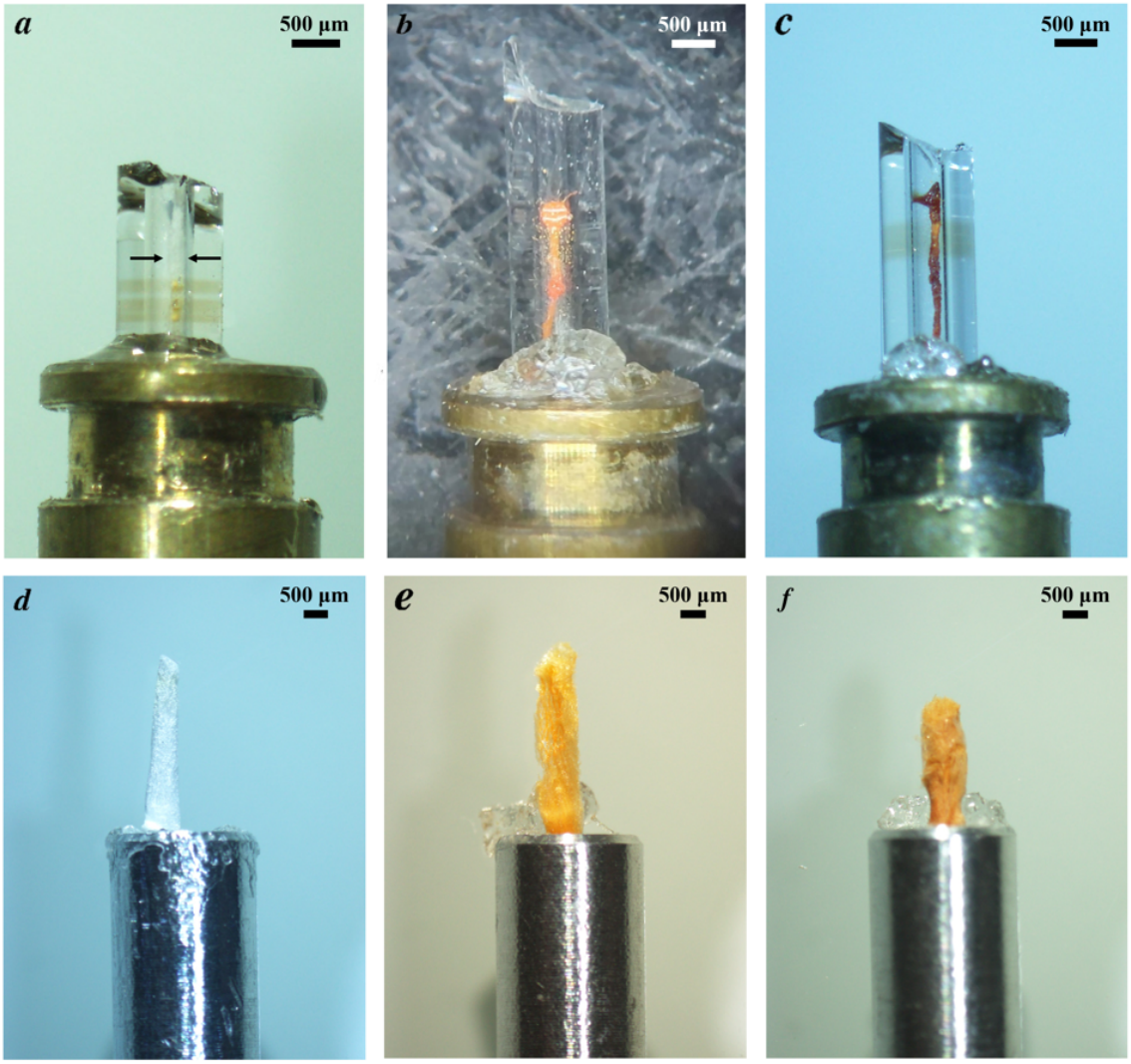

Figure 3.37: ***a)*** CMC sample loaded with YVO_4:Eu^{3+} at 3%wt concentration, prepared by microcapillary filling. ***b)*** CMC sample loaded with $AgInS_2$ at 3%wt concentration, prepared by microcapillary filling. ***c)*** CMC sample loaded with $CuInS_2$ at 3%wt concentration, prepared by microcapillary filling. ***d)*** CMC sample loaded with Y_2O_3:Eu^{3+} at 3%wt concentration, prepared from the 1 mm-diameter aerogel. ***e)*** CMC sample loaded with $AgInS_2$ at 3%wt concentration, prepared from the 1 mm-diameter aerogel. ***f)*** CMC sample loaded with $CuInS_2$ at 3%wt concentration, prepared from the 1 mm-diameter aerogel.

The equipment of the ID16A beamline is shown in Figure 3.38a. The different samples are introduced into the first vacuum chamber (shown in Figure 3.38b), where an initial vacuum is created. They are then analyzed one by one in the second chamber (which appears in Figure 3.38c) under the exposure of X-rays.

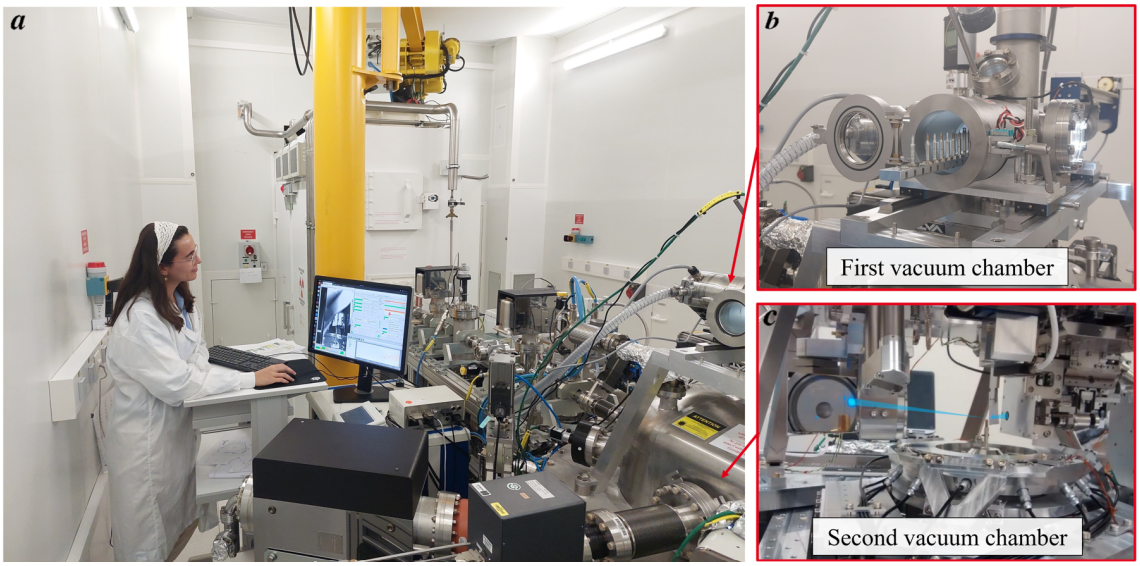

Figure 3.38: ***a)*** Nano-imaging equipment in the ID16A beamline at the ESRF in Grenoble, France. ***b)*** First vacuum chamber where the different samples can be observed. ***c)*** The second vacuum chamber where it can be observed the sample exposed to X-rays (image reproduced from [129]).

3.5.1.4.4 Data Treatment

The protocol followed for each of the samples is schematized in Figure 3.39 and is as follows:

1. Holotomography:
    - For the same sample, several holotomographies are performed at different distances along the axial axis (z-axis).
2. Three-dimensional reconstruction:
    - A three-dimensional reconstruction for each holotomography/local tomography is obtained. This process combines all the two-dimensional projections acquired at different angles and distances to generate a three-dimensional volume[14].
3. Definition of ROIs:
    - For this PhD work, a basic three-dimensional image processing process has been defined to extract interesting features. After reconstructing the three-dimensional volumes, specific ROIs are defined within each reconstructed

[14]This work was largely performed by ID16A beamline staff, namely Dmitry Karpov.

volume. These ROIs are typically cubic sub-volumes (as shown in red in the image) and are centered at the same z position in each reconstruction. Focusing on ROIs rather than the entire volume allows to manage data size and facilitate more detailed analysis within manageable sub-volumes.

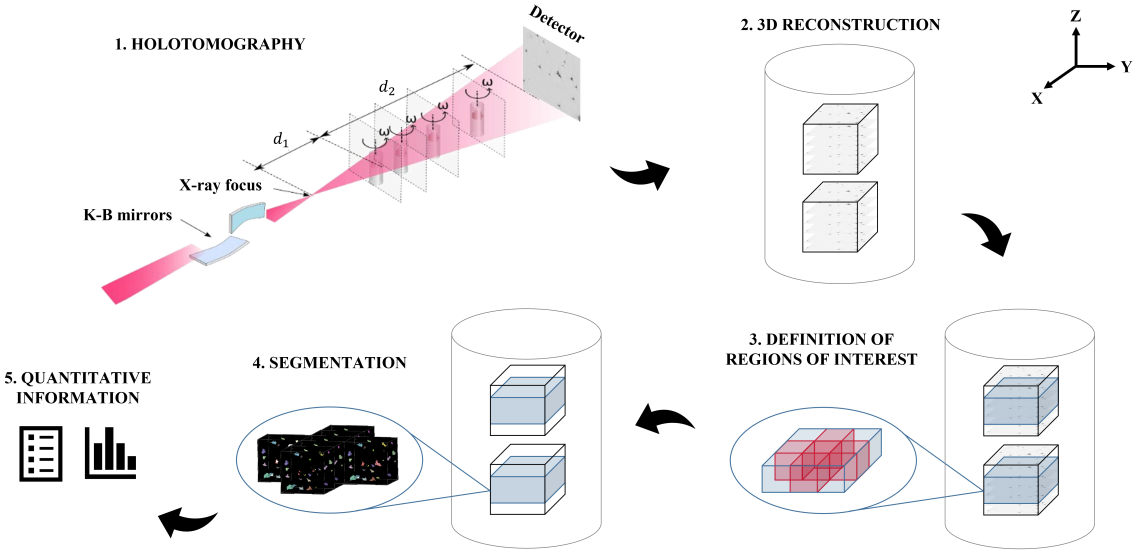

Figure 3.39: Step-by-step explanation of the data treatment followed for each sample after exposure to X-rays in the ID16A beamline at ESRF in Grenoble, France.

4. Segmentation:

   - For each ROI, segmentation is performed to identify individual particles. This is typically done by applying a threshold to separate the particles from the background. The segmentation step allows us to track and quantify each particle within the ROI.

5. Quantitative information:

   - After segmentation, quantitative information for each ROI is extracted, including:
     - The number of identified particles ($N_{particles}$)
     - The average particle volume ($\bar{V}_{particle}$)
     - The total volume occupied by particles ($V_{particles}$)
     - The total volume of the ROI (V_{ROI})
     - The volumetric concentration of particles ($C_V = V_{particles}/V_{ROI}$)
     - The average particle area ($\bar{A}_{particle}$)

- The total area occupied by particles ($A_{particles}$)
- The total area of the ROI (A_{ROI})
- The surface concentration of particles ($C_S = A_{particles}/A_{ROI}$)
- The average particle diameter ($\bar{d}_{particle}$)
- The average sphericity of the particles ($\bar{S}_{particle}$)

From the volumetric concentration, the mass concentration (C_M) can be determined from the following equation:

$$C_M = \left(\frac{\rho_{particles}}{\rho_{solution}} \cdot C_V \right) \cdot 100 \tag{3.10}$$

with $\rho_{particles}$ being the density of the luminescent particles in its massive (bulk) crystal structure and $\rho_{solution}$ the density of the liquid solution containing the host material, which is CMC for all the samples, and the luminescent particles used for the sample preparation.

It is therefore useful to estimate the mass concentration from the segmentation of three-dimensional reconstructions obtained via holotomography/local tomography, and compare it with the theoretical mass concentration used during sample preparation. This comparison can help assess whether the procedure followed during the aerogel preparation is accurate and consistent.

3.5.1.5 Optical Efficiency Characterization via Quantum Yield Measurements

Another technique employed during the characterization, both of the luminescent materials (both in the dry state and in liquid solution) and of the aerogels containing the luminescent materials, is the measurement of the absolute PL quantum yield [15].

The quantum yield expresses the efficiency with which a material or system converts an excitation (photon, electron, or radiation) into a specific event (such as photon emission, chemical reaction, etc.). In particular, the absolute PL quantum yield is defined as:

$$\eta_{PL}^{ref} = \frac{N_{h\nu\ em,\ PL}^{ref}}{N_{h\nu\ abs,\ PL}^{ref}} \tag{3.11}$$

being:

- $N_{h\nu\ em,\ PL}^{ref}$ the total number of photons emitted by the sample under excitation.
- $N_{h\nu\ abs,\ PL}^{ref}$ the number of incident photons at the excitation wavelength that are absorbed by the sample.

[15] The absolute PL quantum yield measurements are carried out at the CEA/DES/LITEN laboratories, located at the CEA Grenoble site.

3.5.1.5.1 Instrumentation

The instrument used for these measurements is a Hamamatsu absolute quantum yield spectrometer (C11347), shown in Figure 3.40b. It consists of a xenon lamp coupled to a monochromator as the excitation light source, an integrating sphere, and a photonic multichannel analyzer for detection. These components are illustrated in Figure 3.40a.

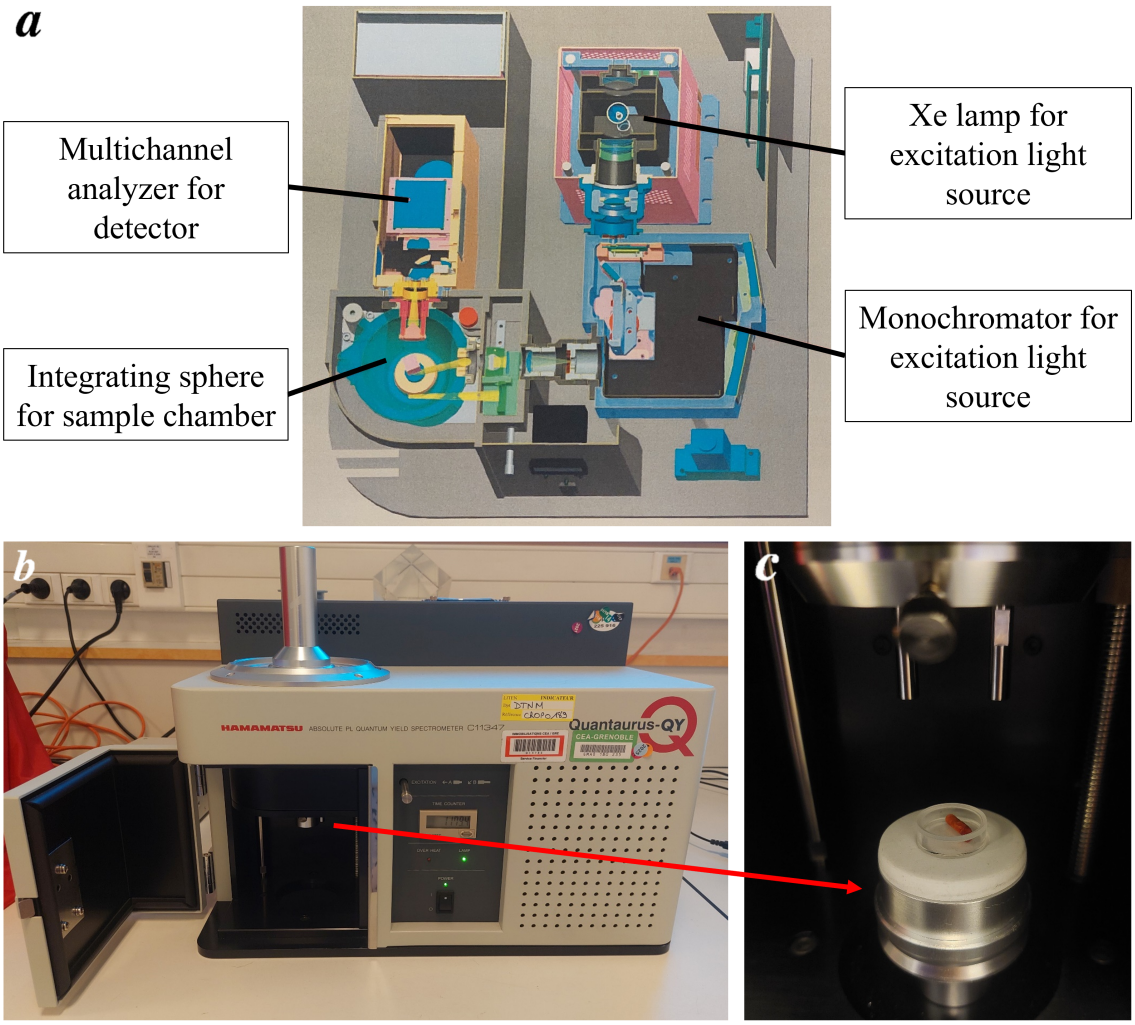

Figure 3.40: ***a)*** Diagram showing the different components of the instrument used for absolute PL quantum yield measurements. Figure reproduced from [131]. ***b)*** Photograph of the instrument used in the laboratory. ***c)*** Placement of the sample inside a quartz laboratory dish, covered with its quartz cover.

The sample is placed inside the integrating sphere, where it is illuminated by the excitation source. The monochromator allows the excitation wavelength to be selected sequentially, so that the PL quantum yield can be measured as a function of excitation wavelength. For

each chosen excitation wavelength, the multichannel analyzer records the corresponding emission spectrum.

Figure 3.41 shows the excitation light profile and the emission spectrum of a sample obtained from reference and sample measurements. In the reference measurement, excitation light is directed into an empty quartz cell placed inside the integrating sphere. The resulting spectrum contains only the scattered excitation light. In the sample measurement, the same quartz cell contains the sample (Figure 3.40c). The acquired spectrum then contains both residual excitation light that has not been absorbed, whose intensity is typically lower than in the reference due to absorption by the sample, and the PL emission characteristic of the sample.

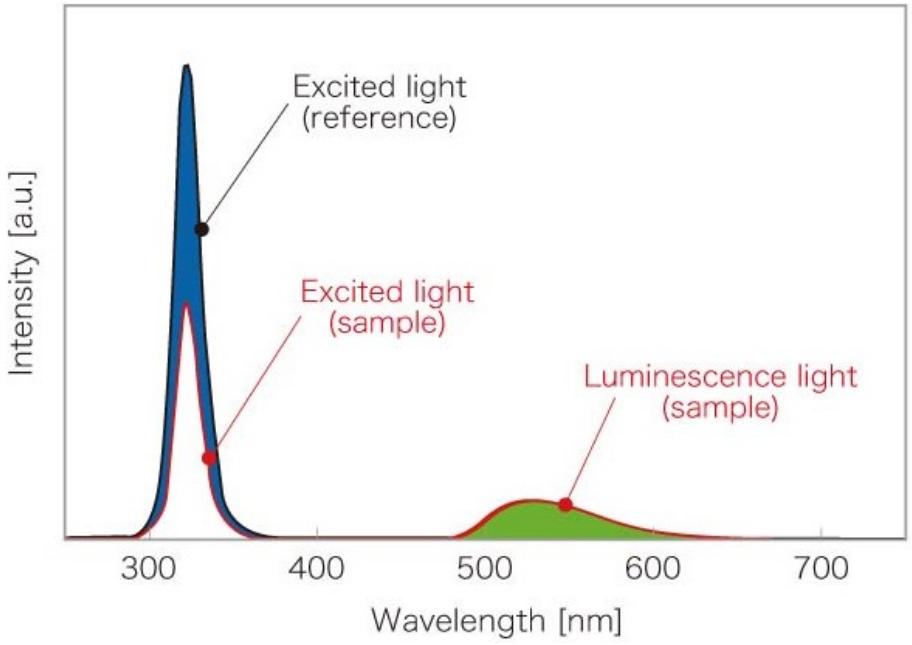

Figure 3.41: Spectra acquired during the reference and sample measurements. Figure reproduced from [131].

The number of absorbed photons, $N^{ref}_{h\nu\ abs,\ PL}$, is proportional to the difference between the areas of the excitation light profiles in the reference and sample measurements. The number of emitted photons, $N^{ref}_{h\nu\ em,\ PL}$, is proportional to the integrated area of the PL emission spectrum.

Once all the characterization techniques to be used for analyzing the samples prior to exposure to the tritium gas atmosphere have been understood, the next section will describe the techniques employed after exposing aerogels to the tritium exposure. Therefore, these techniques will only be applied to aerogels and not to the pure luminescent materials.

3.5.2 After Tritium Exposure

These techniques aim to quantify the amount of tritium remaining in the aerogel after exposure.

3.5.2.1 Liquid Scintillation Counting (LSC)

The first of these techniques is Liquid Scintillation Counting (LSC)[16]. This technique allows for quantifying the amount of tritium in the aerogel, but exclusively the tritium resulting from HIE. The reason why gaseous tritium that might have remained trapped in the gas structure cannot be quantified is that, to carry out this type of measurement, the sample must be dissolved.

Indeed, LSC involves dissolving the sample and mixing it with a scintillation cocktail in such a way that the beta radiation emitted by the tritium contained in the sample excites the scintillation cocktail, which then emits photons. The emitted photons are converted into an electrical signal by PMT to quantify the radioactivity present in the sample.

The instrument used for these measurements is a Tri-Carb 2910TR model, which is shown in Figure 3.42. The aerogels are dissolved in an HCl solution, and the scintillation cocktail used is Ultima Gold, whose photons are emitted at a wavelength of 420 nm.

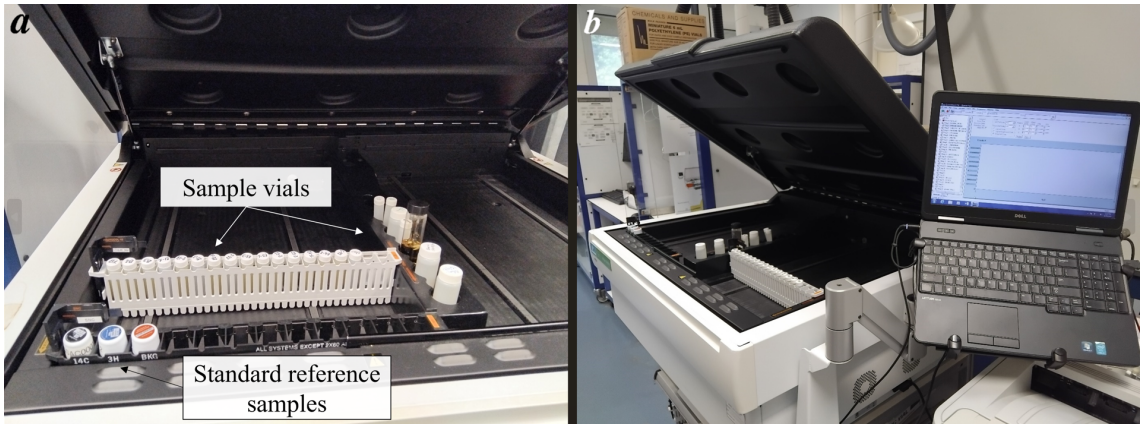

Figure 3.42: Instrument used for the LSC measurements.

[16]The LSC measurements are carried out by Pierre Colonna, a postdoctoral colleague funded by the Programmes Exploratoire et Transversaux de Compétences (PE-PTC), in the CEA/DRF/JOLIOT laboratories at the CEA Saclay site.

3.5.2.2 Thermodesorption Measurements

Thermodesorption measurements enable determination of the amount of tritium gas trapped in the porous structure of the aerogel by observing the release of trapped tritium gas as the sample temperature is gradually increased[17]. As temperature rises, trapped tritium atoms are released from the sample. The released gas is collected in vials and quantified by LSC, indicating the amount of radioactivity stored in the pores.

The sample is first held at 20°C for 18 hours to allow stabilization, then heated successively at increasing temperatures: 2 hours at 153°C, 2 hours at 350°C, 2 hours at 700°C, 2 hours at 950°C, and finally cooled back to 20°C for 12 hours. The furnace employed is shown in Figure 3.43a, with the emission of light from a sample containing tritium in Figure 3.43b.

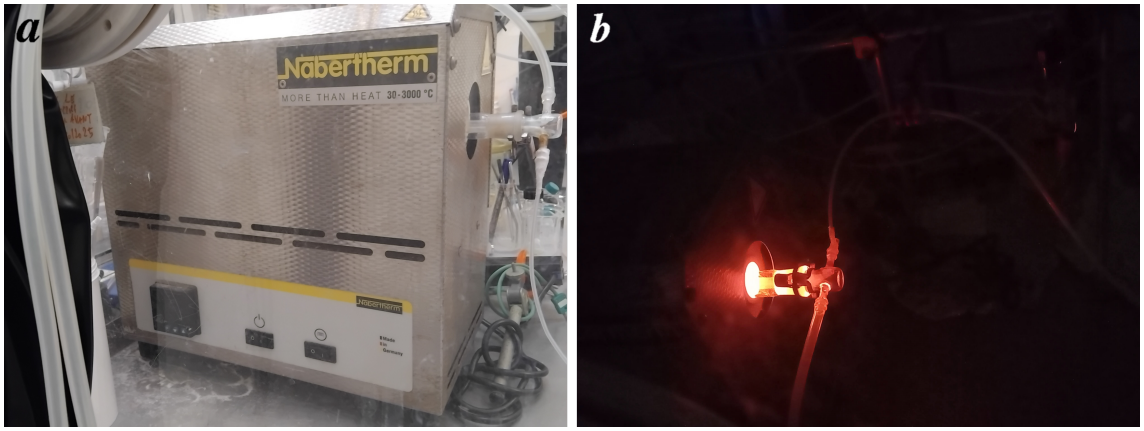

Figure 3.43: Instrument used for the thermodesorption measurements.

At each temperature step, different fractions of trapped tritium atoms are thermally released. Lower temperatures liberate more weakly bound fractions, while higher temperatures free more tightly bound or confined tritium.

3.6 Conclusion

This chapter covered many aspects in detail. Initially, the technical specifications needed for designing our future implantable radioluminescent device were presented. This device is based on an aerogel that serves both as a reservoir for luminescent particles and tritium. Two types of host materials were selected: silica aerogels and cellulose aerogels.

[17]The thermodesorption measurements are carried out by Pierre Colonna, a postdoctoral colleague funded by the Programmes Exploratoire et Transversaux de Compétences (PE-PTC), in the CEA/DRF/JOLIOT laboratories at the CEA Saclay site.

Four types of luminescent materials with dominant emission wavelengths between 611 and 686 nm were supplied: commercially available micrometric Y_2O_3:Eu^{3+} phosphor; nanometric YVO_4:Eu^{3+} phosphor synthesized at CEA/DES/LITEN; and two types of quantum dots, $AgInS_2$/ZnS and $CuInS_2$/ZnS, synthesized at CEA/DRF/IRIG. The synthesis protocols for all these luminescent materials, as well as the preparation of aerogels loaded with them, have been described.

The production of gaseous tritium, the method employed to expose the aerogels to this gas, and the home-made setup designed for measuring the emitted radiance were also detailed.

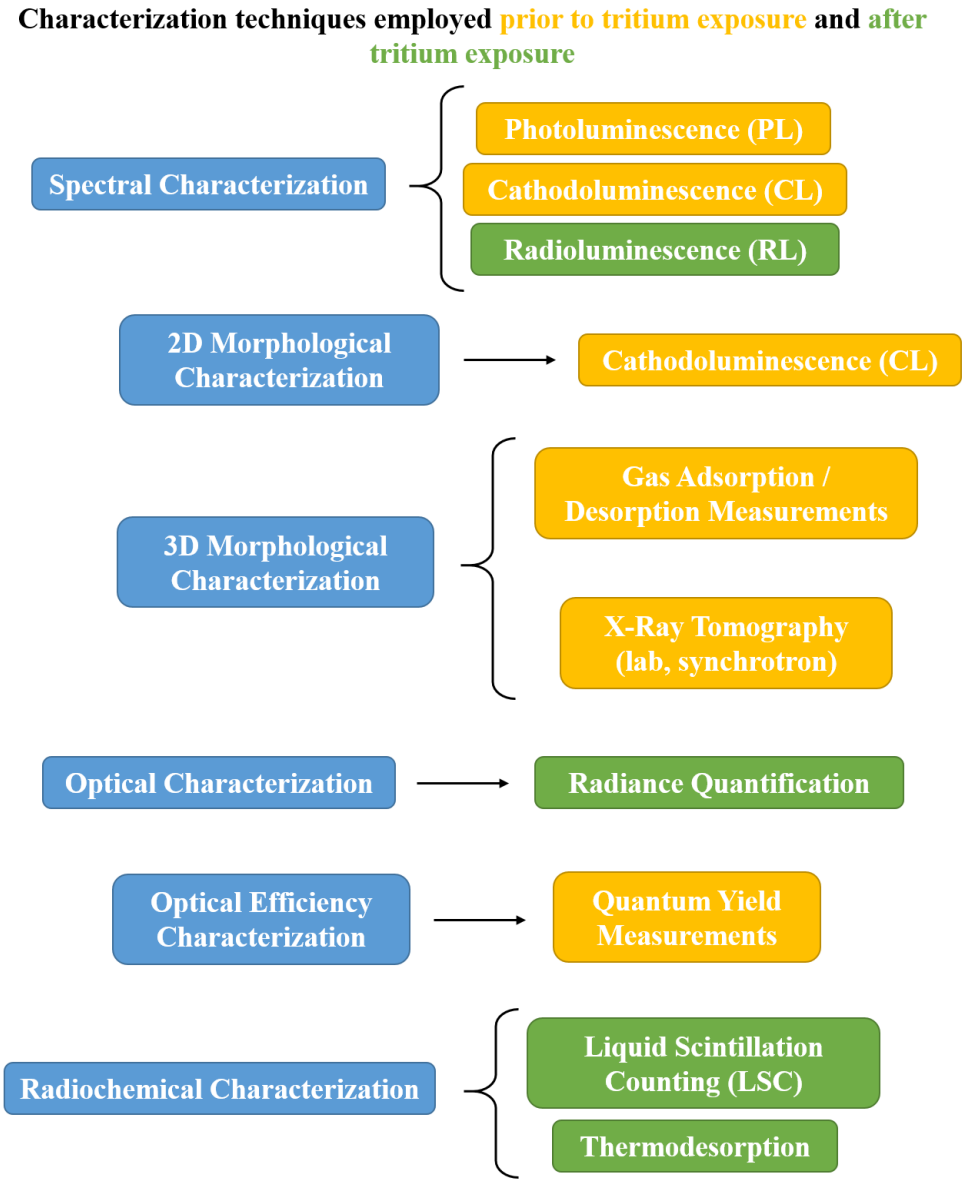

Figure 3.44: Summary of the characterization techniques used in this work.

Finally, the characterization techniques that will be used to study not only the aerogels but

also the luminescent materials, since understanding the properties of these materials prior to integration is important, have been introduced. Figure 3.44 summarizes the different characterization techniques that have been described in the chapter.

In the next chapter, we will present the results obtained from the characterization of these luminescent materials.

Conception et Fabrication d'un Dispositif Radioluminescent

Résumé du Chapitre

Ce chapitre a couvert de nombreux aspects en détail. Dans un premier temps, les spécifications techniques nécessaires à la conception du futur dispositif radioluminescent implantable ont été présentées. Ce dispositif est basé sur un aérogèl qui sert à la fois de réservoir pour les particules luminescentes et pour le tritium. Deux types de matériaux hôtes ont été sélectionnés: les aérogels de silice et les aérogels de cellulose.

Quatre types de matériaux luminescents présentant des longueurs d'onde d'émission dominantes comprises entre 611 et 686 nm ont été fournis: un luminophore micrométrique Y_2O_3:Eu^{3+} disponible dans le commerce; un luminophore nanométrique YVO_4:Eu^{3+} synthétisé au CEA/DES/LITEN; ainsi que deux types de boîtes quantiques, $AgInS_2$/ZnS et $CuInS_2$/ZnS, synthétisées au CEA/DRF/IRIG. Les protocoles de synthèse de l'ensemble de ces matériaux luminescents, ainsi que la préparation des aérogels les intégrant, ont été décrits.

La production de tritium gazeux, la méthode employée pour exposer les aérogels à ce gaz, ainsi que le montage conçu pour mesurer la radiance émise ont également été détaillés.

Enfin, les techniques de caractérisation qui seront utilisées pour étudier non seulement les aérogels mais également les matériaux luminescents, puisque la compréhension des propriétés de ces matériaux avant leur intégration est importante, ont été présentées. La Figure 3.44 résume les différentes techniques de caractérisation qui ont été décrites dans le chapitre.

Chapter 4

Characterization of Luminescent Materials

In this chapter, the results obtained from the characterization of the different luminescent materials using the previously described techniques are presented.

4.1 Spectral Characterization by Photoluminescence (PL)

First of all, a spectral characterization of the emission of these luminescent coatings is performed by PL spectroscopy using the custom setup described in section 3.5.1.1.1, in order to identify the principal emission peaks.

To enable direct comparison of the spectral shapes, the measured intensities $I_{em,\,PL}^{meas}$ are normalized by dividing by the following factors:

$$I_{em,\,PL}^{norm} = \frac{I_{em,\,PL}^{meas}}{t_{exp} \times P_{UV} \times S_{exc}} \tag{4.1}$$

and finally divided by the maximum intensity value of each spectrum. This normalization takes into account:

- The exposure time t_{exp} of the Charge-Coupled Device (CCD), representing the total measurement time.
- The power P_{UV} of the UV lamp, from which the number of photons emitted (and thus incident on the sample, assuming minimal losses) per second can be estimated.

- The excitation surface area S_{exc}, corresponding to the portion of the aerogel illuminated by the UV lamp.

This yields an intensity normalized per photon, per unit surface area, and per unit time.

Figure 4.1 shows the comparison of the normalized photoluminescence emission spectra of each of the luminescent coatings, when excited with UV light at 280 nm.

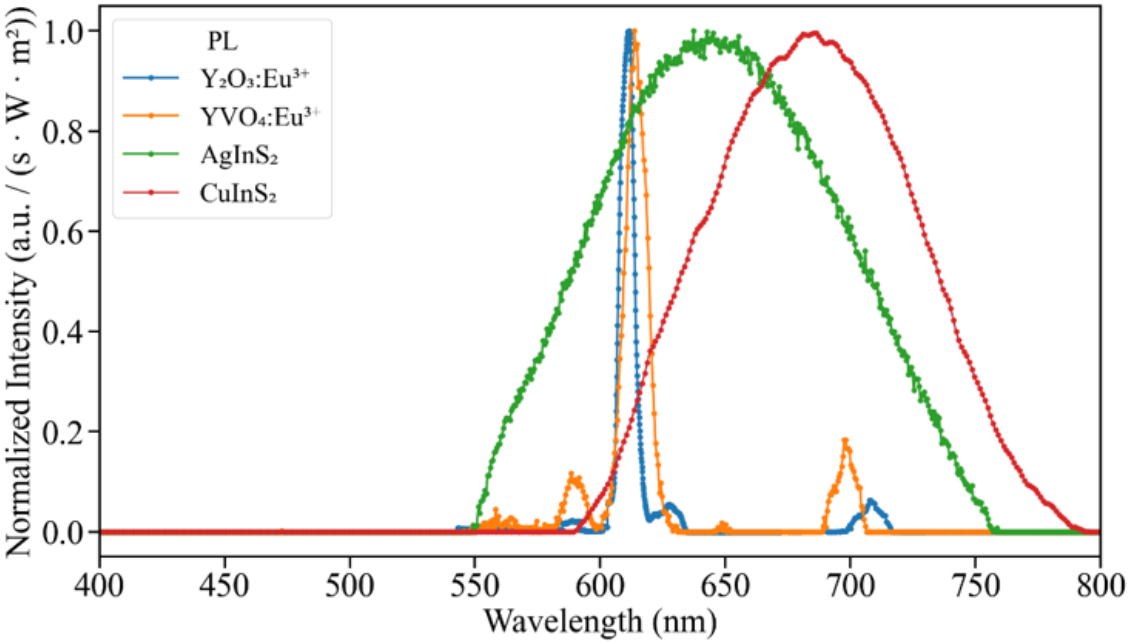

Figure 4.1: Emission spectra of luminescent materials deposited on a silicon wafer under UV excitation at 280 nm.

The spectra for the Y_2O_3:Eu^{3+} and YVO_4:Eu^{3+} phosphors are quite similar, which is unsurprising since, as explained in section 3.2, the mechanism of photon generation in these phosphors is mainly dependent on the dopant ion, in this case Eu^{3+}. Both materials show a prominent peak: 611 nm for Y_2O_3:Eu^{3+} and 614 nm for YVO_4:Eu^{3+}, corresponding to the $^5D_0 \rightarrow {}^7F_2$ transition. Secondary peaks are also observed: one at 589 nm, corresponding to the $^5D_0 \rightarrow {}^7F_1$ transition, and another at 698 nm, associated with the $^5D_0 \rightarrow {}^7F_4$ transition. All these transitions are illustrated in Figure 3.3. Minor differences between Y_2O_3:Eu^{3+} and YVO_4:Eu^{3+} spectra are due to host matrices (Y_2O_3 and YVO_4, respectively) effects. Spectra of these phosphors are well documented [132, 133].

In contrast, the QDs have much broader spectra, spanning a wider wavelength range, whereas the phosphor spectra display sharp peaks at distinct wavelengths. The $AgInS_2$ QDs have an emission centered at 646 nm, and the $CuInS_2$ QDs at 686 nm. The literature supports these emission spectra although, unlike the phosphors, the quantum dot emission

spectra vary depending on different parameters, such as the synthesis procedure, including the X:In:S ratio, synthesis temperature, ZnS shell thickness, and ligand nature [134, 135].

4.2 Spectral Characterization by Cathodoluminescence (CL)

Subsequently, a CL spectroscopy study of these luminescent coatings is carried out using the setup described in section 3.5.1.2.1, with the samples excited by an electron beam at 5.7 keV.

To enable direct comparison of the spectral shapes, the measured intensity $I^{meas}_{em,\,CL}$ from a ROI in the sample is normalized as follows:

$$I^{norm}_{em,\,CL} = \frac{I^{meas}_{em,\,CL}}{N_{pix} \times t_{dwell} \times I_{beam} \times S_{exc}} \tag{4.2}$$

and finally divided by the maximum intensity value of each spectrum. This normalization takes into account:

- The number of pixels N_{pix} in the ROI, to obtain the intensity per pixel.
- The dwell time t_{dwell}, i.e., the irradiation time of the electron beam per pixel.
- The emission current I_{beam}, which represents the number of electrons in the beam per second (assuming minimal losses, this approximates the incident electrons).
- The excitation surface area S_{exc}, corresponding to the physical surface area of the ROI.

This yields an intensity normalized per electron, per unit surface area, and per unit time.

The comparison of the normalized emission spectra for each of the different luminescent coatings is shown in Figure 4.2.

The most striking observation is the large difference between the spectra of Y_2O_3:Eu^{3+} and YVO_4:Eu^{3+}, since in PL they are practically identical. For the QDs, the emission spectra retain the same overall shape as in PL, although some differences are observed. The $AgInS_2$ spectrum, centered at 646 nm under PL, shifts to 644 nm under CL, corresponding to a 2 nm blueshift. In contrast, the $CuInS_2$ spectrum, which is centered at 686 nm under PL, shifts to 706 nm under CL, resulting in a 20 nm redshift. While the blueshift of $AgInS_2$ could be attributed to calibration adjustments or spectrometer sensitivity (even though the

same instrument is used as in the custom PL setup), the significant redshift of $CuInS_2$ cannot be neglected and likely reflects an intrinsic property of the luminescent material, whose emission response may vary depending on the type of excitation.

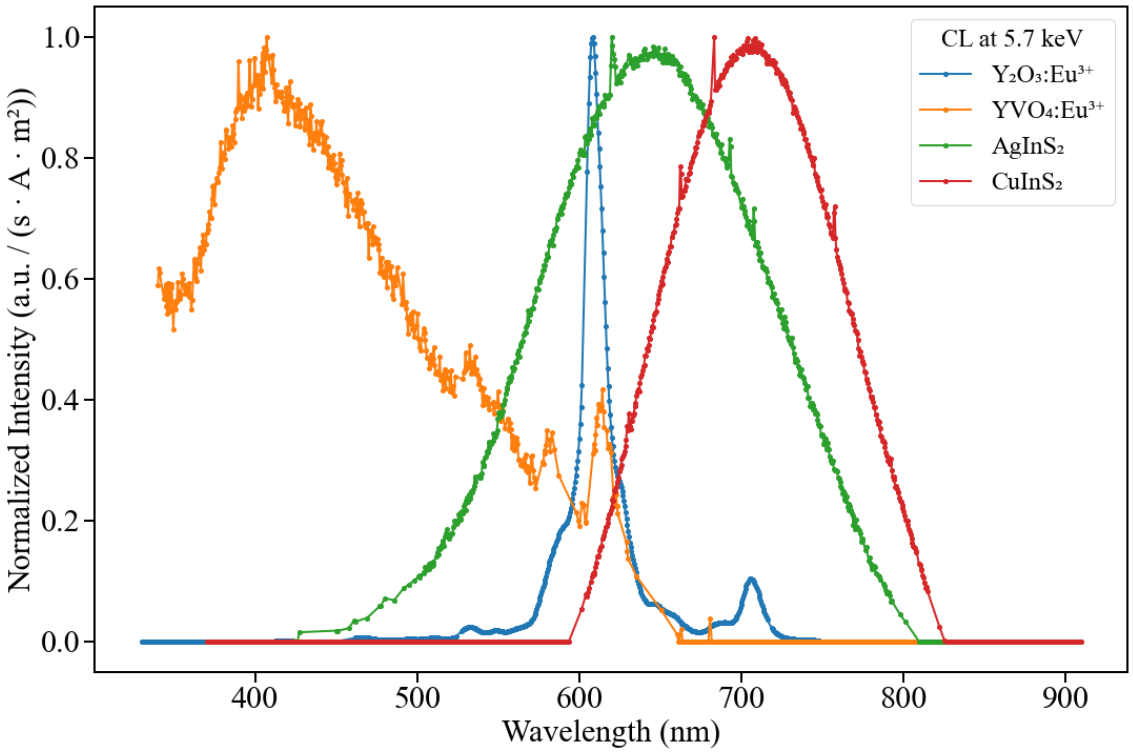

Figure 4.2: Emission spectra of luminescent materials deposited on a silicon wafer under excitation with a 5.7 keV electron beam.

Regarding the phosphors, the Y_2O_3:Eu^{3+} spectrum preserves the same shape as in PL, but the main peak shifts from 611 nm to 608 nm, corresponding to a slight 3 nm blueshift. On the other hand, the emission spectrum of YVO_4:Eu^{3+} differs completely from that observed under PL. In CL, a continuous emission appears below 600 nm, reaching a maximum at 407 nm. The dominant peak in PL, observed at 614 nm, shifts to 612 nm in CL, corresponding to a 2 nm blueshift. Interestingly, this blueshift has the same magnitude as those observed for Y_2O_3:Eu^{3+} and $AgInS_2$, suggesting that it may indeed be linked to the instrumentation, or alternatively, that these materials undergo slight but consistent variations in their emission spectra, much smaller, however, than the shift observed in the case of $CuInS_2$.

Table 4.1 shows the characteristic wavelengths of the different luminescent materials under photoluminescence (PL) and cathodoluminescence (CL).

Luminescent Coating	λ_{PL} (nm)	λ_{CL} (nm)
Y_2O_3:Eu^{3+}	611	608
YVO_4:Eu^{3+}	614	612
$AgInS_2$	646	644
$CuInS_2$	686	706

Table 4.1: Summary of characteristic emission wavelengths for the different luminescent coatings under PL and CL.

One hypothesis to explain why the emission spectrum of YVO_4:Eu^{3+} shows emission below 600 nm is that this emission could correspond to the ligands of sodium citrate. If these ligands do not withstand the radiation, exposing the sample for some time to the electron beam or increasing the electron beam energy could cause a decrease in the spectrum below 600 nm due to the ligands possibly blocking the emission spectrum of the YVO_4:Eu^{3+} particles. To test this hypothesis, three mappings of the YVO_4:Eu^{3+} luminescent coating are performed in the same ROI, with the electron beam energy increasing from 2 keV to 5.7 keV, passing through 4 keV. The evolution of the emission spectrum is shown in Figure 4.3.

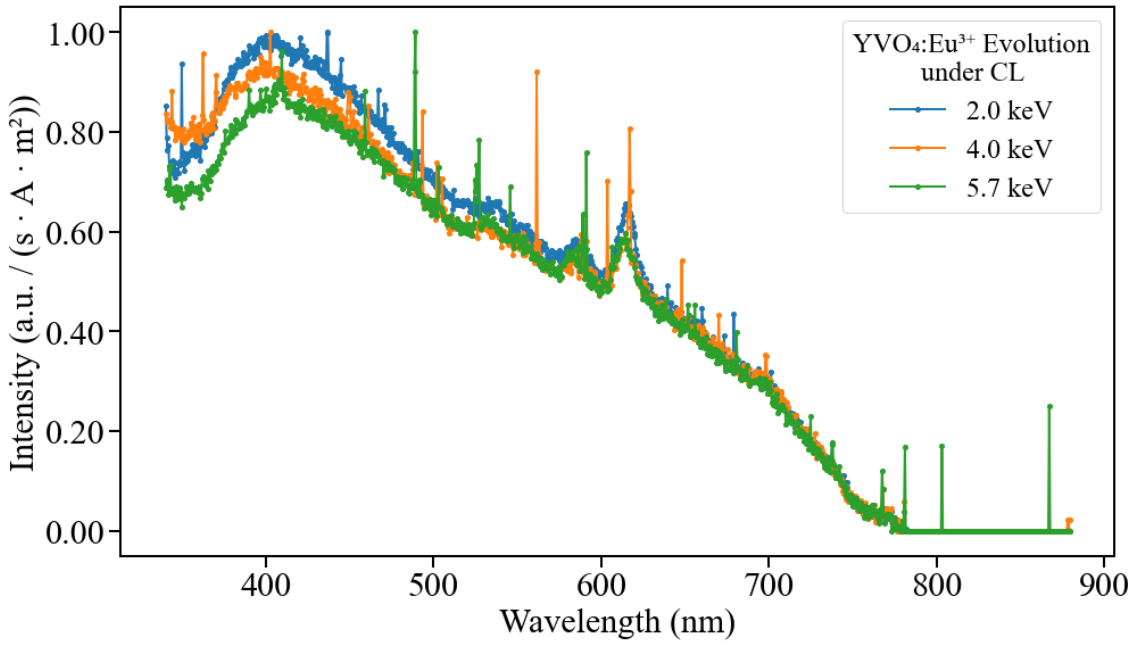

Figure 4.3: Evolution of YVO_4:Eu^{3+} under CL, starting with the first mapping performed at 2 keV, followed by subsequent mappings (in the same ROI) at progressively higher energies, up to 5.7 keV.

It is observed that indeed, the emission spectrum decreases as the electron beam energy

increases, which could confirm the hypothesis stated above. These ligands might be blocking the emission of the YVO_4:Eu^{3+} particles themselves. This is surprising since, in PL, a very clean spectrum is observed without that contribution below 600 nm. This could indicate that the response of this material is not the same under different excitation sources.

In any case, it would be necessary to have a sodium citrate coating to study in more detail the intrinsic emission of these ligands and to investigate their evolution under the electron beam in order to confirm this hypothesis.

4.3 Three-Dimensional Morphological Characterization via Gas Adsorption and Desorption Measurements

Gas adsorption and desorption measurements provide insight into the porosity of the luminescent materials. In this work, nitrogen adsorption and desorption measurements at 77 K, performed with the instrumentation described in section 3.5.1.3.3, are used to evaluate the isotherm shapes, specific surface area, pore volume, and pore size distribution of the samples. These analyses are performed on the luminescent materials (Y_2O_3:Eu^{3+}, $AgInS_2$, $CuInS_2$) in powder form; YVO_4:Eu^{3+} is excluded since it is only available as a liquid solution.

First, this technique allows the study of the characteristic isotherm shape of each sample, as shown in Figure 4.4a. Based on the IUPAC classification (Figure 3.26), the isotherms of these three luminescent materials correspond to type II. These isotherms begin with a rapid increase in the amount of gas adsorbed at low pressures, followed by an almost linear section, and finally a gradual increase at very high pressures. The point at which the nearly linear section begins (0.05 P/P_0) corresponds to the completion of the monolayer and the onset of multilayer adsorption. This type of isotherm is typical of nonporous or macroporous materials, with weak to moderate interactions between the adsorbent (the luminescent particles) and the adsorbate (gaseous nitrogen).

It is also observed that the adsorption (lower curve) and desorption (upper curve) curves do not overlap for any of these luminescent materials at low temperatures, which could indicate that some nitrogen gas may be trapped in these particles and could not be released.

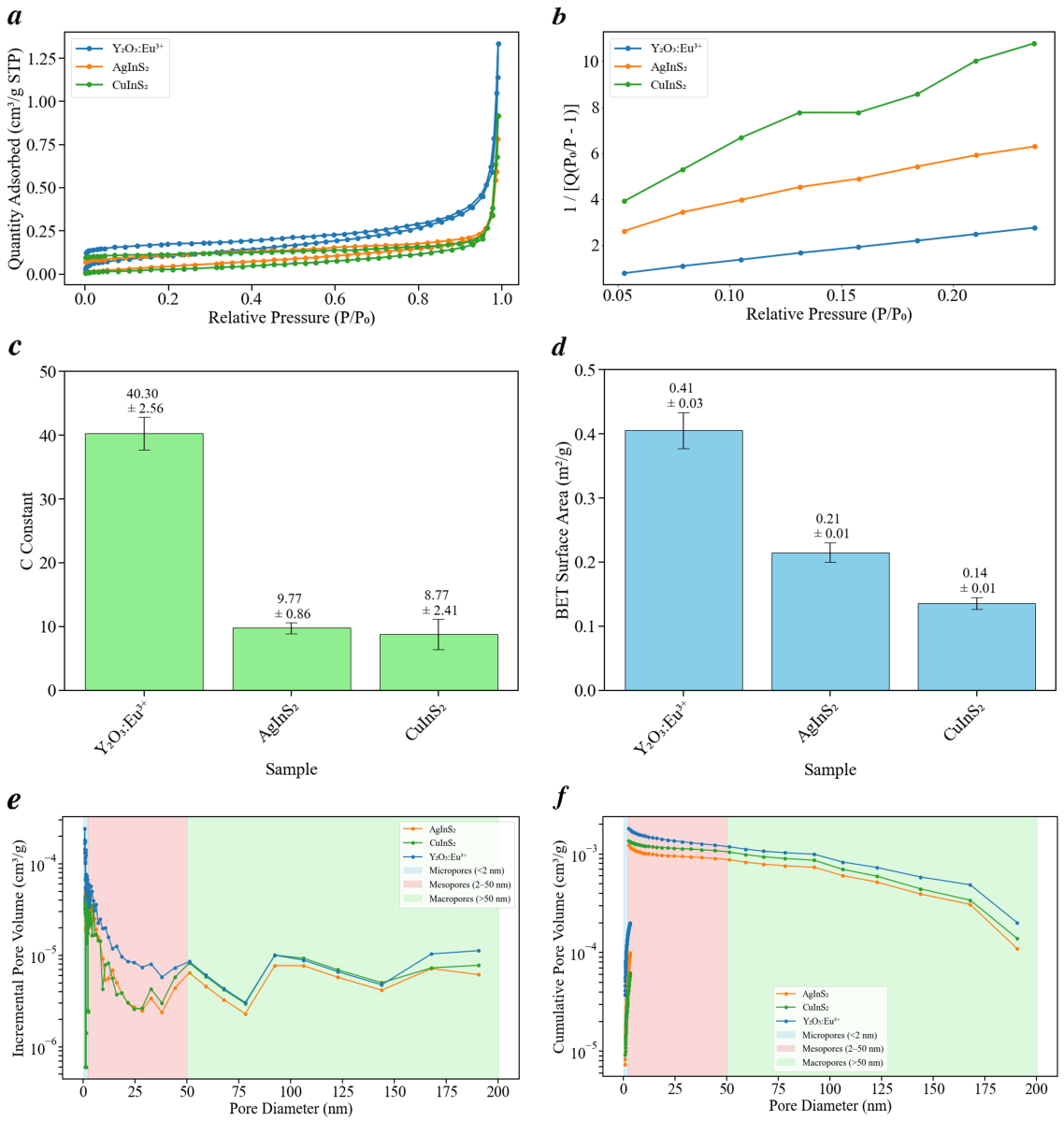

Figure 4.4: Characterization of luminescent materials in powder form via gas adsorption and desorption measurements. ***a***) Adsorption and desorption isotherms. ***b***) The variable $1/[Q(P_0/P - 1)]$ as a function of the relative pressure in the range $0.05 < P/P_0 < 0.25$. ***c***) C constant values. ***d***) BET surface area values. ***e***) Incremental pore volume. ***f***) Cumulative pore volume.

In any case, the amount of nitrogen gas adsorbed by the Y_2O_3:Eu^{3+} microparticles is greater than that adsorbed by either the $AgInS_2$ or $CuInS_2$ QDs, which show very similar values. At the highest pressure, Y_2O_3:Eu^{3+} microparticles have adsorbed 1.33 cm^3 of nitrogen per gram of sample at standard temperature and pressure, while the QDs of $AgInS_2$ and $CuInS_2$ have adsorbed 0.92 and 0.78 cm^3/g, respectively. After the measurements, 0.12 cm^3/g remained adsorbed in Y_2O_3:Eu^{3+} microparticles, 0.09 cm^3/g in $AgInS_2$ QDs

and 0.06 cm^3/g in $CuInS_2$ QDs.

To apply the BET model in order to determine the specific surface area, the variable $1/[Q(P_0/P - 1)]$ (with Q being the quantity of gas adsorbed) is plotted in Figure 4.4b as a function of the relative pressure in order to verify a linear behaviour, typically in the range $0.05 < P/P_0 < 0.25$. This approach works because, in this range, the BET theory predicts a linear relationship, leading to reliably determine the monolayer capacity and thus the BET surface area. By checking the linearity of this plot, it can be verified that the BET model is appropriate for our data.

Another way to verify that the BET model is applicable is by examining the value of the constant C. This constant is obtained from the BET plot using the following equation, based on the slope and intercept of the linear plot:

$$C = \frac{\text{Slope}}{\text{Intercept}} + 1 \tag{4.3}$$

The C constant must always be positive so if it is negative, the data obtained are not valid. The constant C is related to the shape of the isotherm. The higher the value of C, the stronger the interaction between the surface and the first adsorbed layer compared to the subsequent layers. This results in significant adsorption at low pressure, and the isotherm more closely resembles a type II isotherm. Conversely, if C is low (less than 2), it indicates weak interactions, typical of type III isotherms.

The values of the constant C obtained for the luminescent materials are shown in Figure 4.4c. For the three luminescent materials, the constant C is positive. Moreover, the constant C for Y_2O_3:Eu^{3+} is higher than that obtained for both QDs, indicating a stronger interaction between the Y_2O_3:Eu^{3+} microparticles and the nitrogen gas compared to the QDs.

Therefore, the BET model can be applied to determine the specific surface area of each sample. These results are shown in Figure 4.4d. The microparticles of Y_2O_3:Eu^{3+} exhibit a surface area of 0.41 m^2/g, which is higher than that obtained for the $AgInS_2$ QDs with 0.21 m^2/g, which in turn is greater than the surface area of the $CuInS_2$ QDs at 0.14 m^2/g.

Finally, this technique allows determining the pore size distribution, both incremental and cumulative, as shown in Figures 4.4e and 4.4f, respectively. The Y_2O_3:Eu^{3+} microparticles exhibit higher porosity compared to the QDs, particularly in the micropore regime. The two types of QDs show similar behavior.

All these results are consistent and allow the conclusion that, on one hand, the Y_2O_3:Eu^{3+} phosphor microparticles present a larger surface area accessible to the gas, thereby increasing the interactions between these particles and the gas and potentially retaining some gas

within them. On the other hand, the QDs are much less porous and therefore interact very little with the gas.

4.4 Optical Efficiency Characterization via Quantum Yield Measurements

The last technique employed to characterize the luminescent materials is the measurement of the absolute PL quantum yield, using the setup described in section 3.5.1.5.1. The results obtained are shown in Figure 4.5.

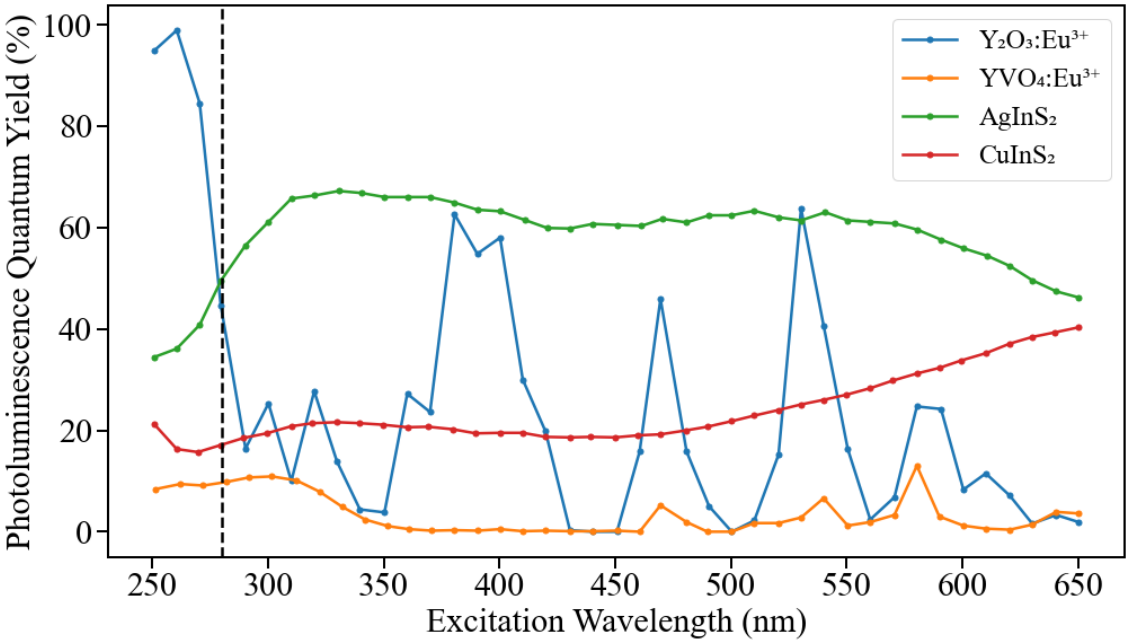

Figure 4.5: Absolute PL quantum yield of luminescent materials in powder form, except for YVO_4:Eu^{3+} which is measured in liquid solution, as a function of the excitation wavelength. The black dashed vertical line indicates the quantum yield values for an excitation wavelength of 280 nm.

Different behaviors are observed between the phosphors and the QDs. The phosphors exhibit excitation preferences at specific wavelengths, whereas QDs display a broad excitation spectrum. This could lead to self-absorption of photons emitted by the QDs themselves, thereby reducing output light intensity. The luminescent material with the highest PL quantum yield is the Y_2O_3:Eu^{3+} microphosphor, reaching nearly 98% efficiency when excited by UV light at 260 nm. This is followed by the $AgInS_2$ QDs, with a PL quantum yield of 67% when excited at 330 nm, and then the $CuInS_2$ QDs with 40% under

650 nm excitation (which is surprising since they are more effectively excited by red light than by UV light, contrary to the $AgInS_2$ QDs). Finally, the YVO_4:Eu^{3+} nanophosphors show a PL quantum yield of 11% when excited at 300 nm, but they also present this yield when excited at 580 nm, which could cause the self-absorption of their own emitted photons.

4.5 Conclusion

In this chapter, the different luminescent materials have been characterized. Their spectral properties were studied via PL and CL, their porous structure was analyzed through nitrogen gas adsorption and desorption measurements, and their luminous efficiency was determined by measuring the quantum yield in PL.

The following chapter will present the results obtained after exposing the luminescent aerogels to the radioactive tritium gas atmosphere.

Caractérisation des Matériaux Luminescents

Résumé du Chapitre

Dans ce chapitre, les différents matériaux luminescents ont été caractérisés. Leurs propriétés spectrales ont été étudiées par photoluminescence (PL) et cathodoluminescence (CL), leur structure poreuse a été analysée grâce à des mesures d'adsorption et de désorption d'azote, et leur efficacité lumineuse a été déterminée par la mesure du rendement quantique en PL.

Chapter 5

Tritium Exposure Results

After the preparation of the different aerogels loaded with luminescent materials, they are exposed to a gaseous tritium atmosphere to induce RL. To analyze the resulting light emission, a dedicated setup, already described in section 3.4.1 of chapter 3, has been designed for collecting and quantifying the photons emitted by the samples. The results obtained from these experiments are presented in this chapter.

5.1 Dependence of Radiance on Tritium Activity

Firstly, aerogels of 3 mm in diameter and 10 mm in length, prepared according to the synthesis process detailed earlier in chapter 3, section 3.3.2 are studied.

Figure 5.1 shows the radiance values measured for each scintillating aerogel, whether with a silica or CMC host matrix and the different luminescent materials, as a function of the tritium activity, which itself depends on the tritium pressure, as described by Equation 3.7.

The different families of aerogels can be ordered from highest to lowest radiance as follows: CMC aerogels loaded with micrometric Y_2O_3:Eu^{3+} particles, which show maximum radiance values of up to 30 mW/(sr·m^2) and up to 2 times higher than the radiance values obtained for silica aerogels with these same micrometric particles and same concentrations. Next are the CMC aerogels with $AgInS_2$ and $CuInS_2$ QDs, both materials showing very similar behavior with radiance values close to 7 mW/(sr·m^2). Then come the silica aerogels loaded with nanometric YVO_4:Eu^{3+} particles, with maximum values of 4 mW/(sr·m^2). Finally, and with values 10 times lower than the previously mentioned ones, are the CMC aerogels with nanometric YVO_4:Eu^{3+} particles.

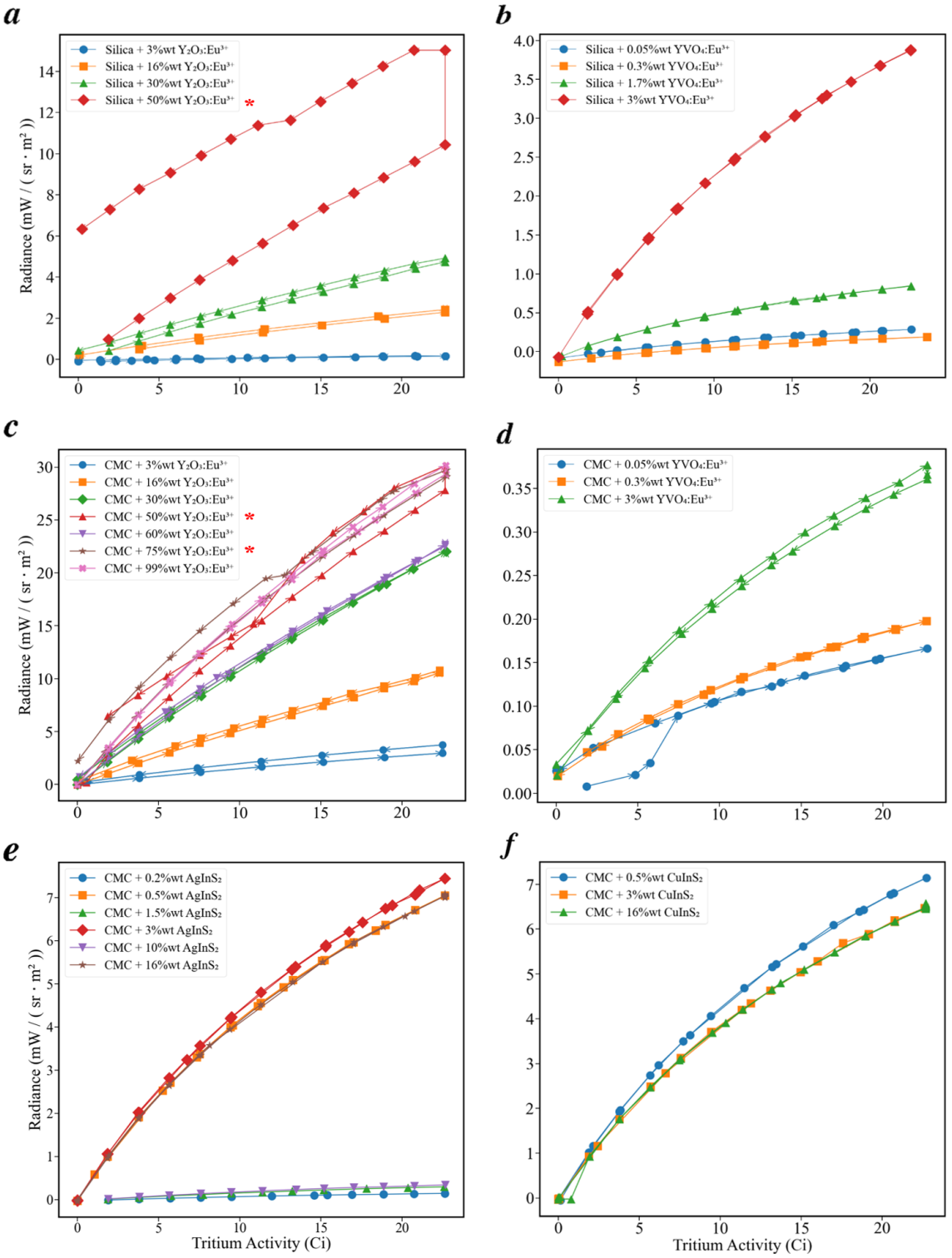

Figure 5.1: Dependence of radiance on the tritium activity for ***a)*** silica aerogels containing micrometric Y_2O_3:Eu^{3+} particles, ***b)*** silica aerogels containing nanometric YVO_4:Eu^{3+} particles, ***c)*** CMC aerogels containing micrometric Y_2O_3:Eu^{3+} particles, ***d)*** CMC aerogels containing nanometric YVO_4:Eu^{3+} particles, ***e)*** CMC aerogels containing nanometric $AgInS_2$ particles, and ***f)*** CMC aerogels containing nanometric $CuInS_2$ particles. The symbol * indicates samples that have been exposed to 1200 mbar overnight (about 13 hours), while the other samples have been exposed for 30 minutes.

Let us now analyze each type of aerogel in more detail. The aerogels containing micrometric Y_2O_3:Eu^{3+} particles, regardless of the host matrix, show a radiance dependence that is proportional to the concentration of luminescent materials. In the case of CMC, once the concentration exceeds 50%wt of luminescent particles, the radiance begins to saturate and there is no further gain. The aerogel with a 60%wt concentration shows a slightly lower radiance than that obtained at 50%wt and higher concentrations.

Furthermore, for these aerogels, the radiance values obtained during the pressure decrease of tritium gas are higher than those measured during the pressure increase. This is due to the fact that radiance increases during continuous exposure, whether for 30 minutes or overnight (approximately 13 hours), to a constant tritium atmosphere of 1200 mbar. Thus, a kind of hysteresis cycle is observed, a cycle that remains constantly open since, even at pressures close to atmospheric pressure, the descending pressure branch does not necessarily overlap with the ascending pressure branch.

Regarding the aerogels containing YVO_4:Eu^{3+} nanoparticles, the radiance values are proportional to the concentrations of the luminescent material, since for both the silica and CMC aerogels, the highest radiance is reached at the maximum concentration of 3%wt. In these aerogels, no hysteresis loop is observed.

Finally, the CMC aerogels loaded with QDs, whether $AgInS_2$ or $CuInS_2$, exhibit very similar behavior. In both cases, the highest radiance is not reached at the highest nanoparticle concentration; for $AgInS_2$, the maximum radiance is achieved at a concentration of 3%wt, and for $CuInS_2$, at 0.5%wt. This phenomenon may be due to a photoquenching effect in the QDs, potentially caused by the self-absorption of photons as discussed in section 4.4 of chapter 4. Confirming this would require additional data points (i.e., more concentrations). Additionally, as in the case of the aerogels containing YVO_4:Eu^{3+} nanoparticles, there is no hysteresis loop.

Among the six concentrations prepared of the CMC aerogels containing QDs, it is observed that the concentrations of 0.2, 1.5, and 10%wt exhibit lower radiance values compared to the other three concentrations. Upon reviewing the laboratory notebook, a change in the synthesis procedure of the aerogels has been identified. For the concentrations of 0.5, 3, and 16%wt, the QDs were initially diluted in deionized water and subsequently mixed with the 2%wt CMC solution. In contrast, for the concentrations of 0.2, 1.5, and 10%wt, the QDs were directly diluted in the 2%wt CMC solution. The significant difference in radiance between these two groups of aerogels could be explained as follows: when the QDs are first diluted in water, they are more homogeneously dispersed in the solution, and this dispersion is maintained upon the addition of the 2 %wt CMC. However, when the QDs are directly diluted in the 2%wt CMC solution, the intermolecular interactions between

the QDs and the polymeric matrix may promote aggregation, leading to the formation of clusters with poorer dispersion [136]. The formation of such clusters or aggregates may reduce the exposed active surface area and enhance quenching processes, thereby decreasing the measured radiance.

As it can also be observed, only the aerogels containing micrometric particles exhibit a hysteresis loop. This phenomenon could be explained by the results obtained during the adsorption/desorption measurements, where the aerogels containing micrometric Y_2O_3:Eu^{3+} particles show smaller pores compared to those containing YVO_4:Eu^{3+} nanoparticles, which may promote the trapping of tritium gas. On the other hand, aerogels containing YVO_4:Eu^{3+} nanoparticles would have larger pores, favoring a reversible process during the exposure cycle to the atmosphere of gaseous tritium.

In addition to this, differences in radiance are observed between aerogels that contain the same luminescent materials but different host matrix materials. For example, for Y_2O_3:Eu^{3+} microparticles, CMC aerogels exhibit 4 times more radiance than silica aerogels, whereas for nanometric YVO_4:Eu^{3+} particles, silica matrices show radiance levels 10 times higher than those with CMC matrices. All of this suggests that radiance may depend not only on pore size but also on other parameters such as chemical structure. The micrometric Y_2O_3:Eu^{3+} particles may be more compatible with the micropores and small mesopores of the CMC network, whereas the nanometric YVO_4:Eu^{3+} particles may be more compatible with the larger mesopores of the silica network. In any case, further research is needed to better understand these complex mechanisms.

The hysteresis can be studied in more detail by quantifying the increase in radiance as a function of the exposure time of the aerogels to gaseous tritium at 1200 mbar. Figure 5.2 presents these results, from which different trends can be identified for each aerogel family.

For silica aerogels containing micrometric Y_2O_3:Eu^{3+} particles, the radiance increase rate rises proportionally with the concentration of luminescent particles. The radiance measured instantaneously at 1200 mbar (prior to continuous exposure at this constant pressure) shows a progressive increase with the concentration of micrometric Y_2O_3:Eu^{3+} particles, reaching a maximum at 50%wt. In the case of CMC aerogels, the radiance increase rate does not increase proportionally with the particle concentration. This rate reaches its maximum at the lowest concentration (3%wt), and then remains relatively low and stable across the other concentrations, showing only a slight increase at the highest concentration of 99%wt. The instantaneous radiance measured at 1200 mbar increases with the concentration of micrometric particles up to 50%wt, beyond which the radiance increase rate begins to saturate.

It is true that for silica aerogels, concentrations above 50%wt have not been studied, so it cannot be predicted whether the radiance increase rate will also reach a saturation point or not.

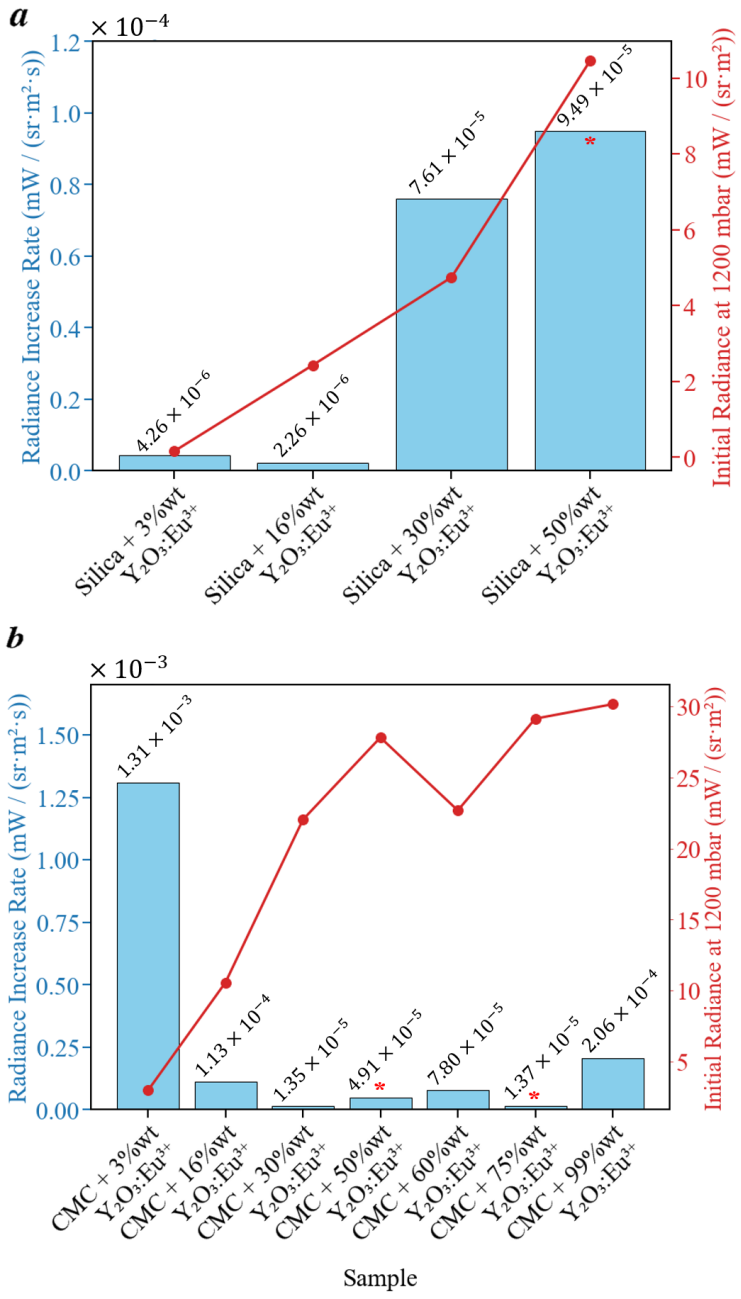

Figure 5.2: Radiance increase rate at 1200 mbar (left y-axis, bargraph) and initial radiance at 1200 mbar (right y-axis, points) for ***a)*** silica aerogels containing micrometric Y_2O_3:Eu^{3+} particles, and ***b)*** CMC aerogels containing micrometric Y_2O_3:Eu^{3+} particles. The symbol * indicates samples that have been exposed to 1200 mbar overnight (about 13 hours), while the other samples have been exposed for 30 minutes.

After all these results, the CMC aerogel with micrometric Y_2O_3:Eu^{3+} particles has been selected as the best candidate for the following experiments, as it offers a good compromise between the instantaneous radiance values (reaching the highest absolute radiance levels) and a reasonable radiance increase rate.

5.2 Influence of Sample Size on Radiance

After studying the dependence of radiance on the tritium quantity and the exposure time at 1200 mbar, let us study the dependence of radiance on the size of the aerogel. For this purpose, different CMC aerogels with 50%wt Y_2O_3:Eu^{3+} microparticles have been prepared using the standard method, but employing cylindrical molds of 1 and 2 mm diameter and a constant length of 10 mm.

After exposing these aerogels to the tritium atmosphere, in the same way as was done with the 3 mm diameter aerogels, the results shown in Figure 5.3a are obtained. On one hand, it is observed that the radiance is not clearly proportional to the diameter of the aerogel. For the aerogels that contain 16%wt and 50%wt of Y_2O_3:Eu^{3+}, the radiance increases with the aerogel radius, but this is not the case for those that contain a 30%wt concentration of Y_2O_3:Eu^{3+}, where the aerogel with a diameter of 1 mm exhibits a higher radiance than the one with a diameter of 2 mm.

On the other hand, it is confirmed that, regardless of the aerogel radius, the concentration of luminescent particles at 50%wt always shows higher radiance than the 30%wt concentration, which in turn is higher than that of the 16%wt concentration.

Figure 5.3b shows an image taken of the CMC aerogel loaded with 50%wt luminescent materials, with a diameter of 2 mm, after its exposure at 1200 mbar.

To attempt a more quantitative analysis, Figure 5.3c plots the radiance increase rate for each of these groups of aerogels and the instantaneous radiance value at 1200 mbar. These results show that for the 16%wt concentration of luminescent materials, the highest radiance increase rate occurs with a diameter of 3 mm, followed by 2 mm, and then 1 mm. While for the other two concentrations (30 and 50%wt), the highest radiance increase rate occurs with 2 mm diameter, then 3 mm, and finally 1 mm diameter.

Regarding the instantaneous value of radiance at 1200 mbar (right y-axis in Figure 5.3c), it is observed that this increases with concentration but it is difficult to distinguish whether it depends on the surface area or the volume of the aerogel.

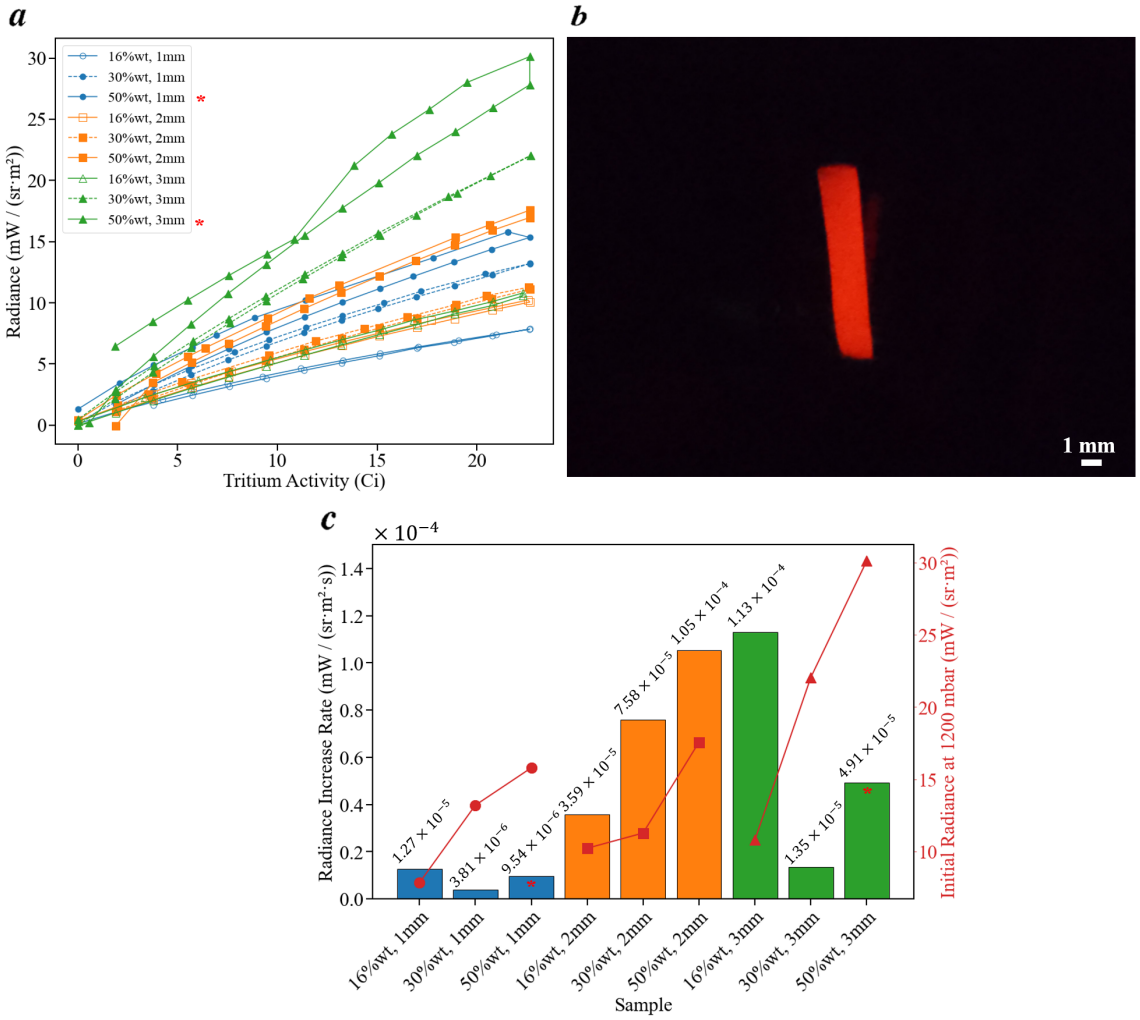

Figure 5.3: ***a)*** Dependence of radiance on the tritium activity for CMC aerogels with different diameters, loaded with different concentrations of micrometric Y_2O_3:Eu^{3+} particles. ***b)*** Image of the CMC aerogel loaded with 50%wt of Y_2O_3:Eu^{3+} microparticles, with 2 mm in diameter, at 1200 mbar. ***c)*** Radiance increase rate at 1200 mbar (left y-axis, bargraph) and initial radiance at 1200 mbar (right y-axis, points) for the same set of aerogel samples. The symbol * indicates samples that have been exposed to 1200 mbar overnight (about 13 hours), while the other samples have been exposed for 30 minutes.

5.3 Radiance Evolution Over Time

To continue studying the radiance produced by the CMC aerogel loaded with 50%wt of micrometric Y_2O_3:Eu^{3+} particles, the evolution of the radiance over time on a larger timescale is analyzed, over the course of a week. For this purpose, two identical aerogels with 3 mm in diameter are prepared.

It is recalled that the ultimate goal of these exploratory works will be the development of a medical device, so it would be interesting in reducing the tritium activity to what is strictly necessary. Hence, a study of the radiance evolution at high and low tritium gas pressures will be carried out.

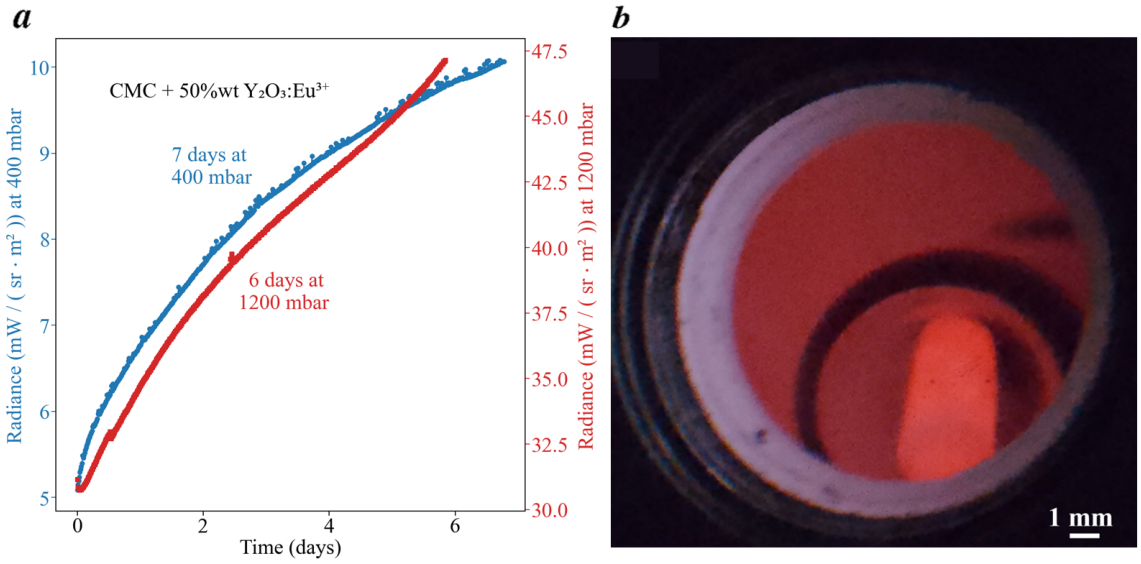

Figure 5.4: ***a)*** Radiance evolution for CMC aerogels loaded with 50%wt of micrometric Y_2O_3:Eu^{3+} particles, after 7 days of exposure to a tritium gas atmosphere at 400 mbar (left y-axis) and 6 days at 1200 mbar (right y-axis). ***b)*** Image taken with the smartphone placed inside the glove box, showing the radioluminescent CMC aerogel loaded with 50%wt of micrometric Y_2O_3:Eu^{3+} particles after 6 days of exposure at 1200 mbar.

Figure 5.4a compares the evolution of RL over time when the sample is exposed at 1200 and 400 mbar during 6 and 7 days, respectively. Whereas the sample exposed at 1200 mbar has gone from 30 to 47 mW/(sr·m^2) in 6 days (an increase of 53%), the sample exposed at 400 mbar has gone from 5 to 10 mW/(sr·m^2) in 7 days (an increase of 100%). After the exposure time, the radiance at 1200 mbar is 4.7 higher than at 400 mbar. However, it appears that the aerogel exposed at 400 mbar is approaching a saturation radiance value, whereas the curve describing the behavior of the aerogel exposed at 1200 mbar shows an increased slope after the fifth day.

After having the aerogel of CMC and 50%wt Y_2O_3:Eu^{+3} at the 1200 mbar tritium atmosphere for 6 days, a picture of the sample has been taken with the camera placed inside the tritium gas handling system. Figure 5.4b illustrates the red light emitted by the sample positioned at the bottom of the Fischer-Porter glassware within the integrating sphere. The viewpoint is from below, looking up at the inclined cylindrical aerogel.

In any case, even if the aerogel had to be exposed to 22 Ci of tritium with the purpose to

load the sample with as much tritium as possible, this does not imply that the final medical device will have to operate with this amount of tritium. This just indicates that this quantity of tritium will be necessary to prepare our radioluminescent device but then, it will operate at lower tritium gas pressures since the final aim would be to encapsulate the device into a borosilicate capillary.

5.4 Encapsulation

For this purpose, encapsulation experiments are carried out to assess the hermeticity of the device. Therefore, smaller aerogels (in particular, with a diameter of 1.7 mm) are placed inside capillaries instead of the Fisher-Porter glassware used previously, with the aim of directly sealing the capillary after exposure to tritium.

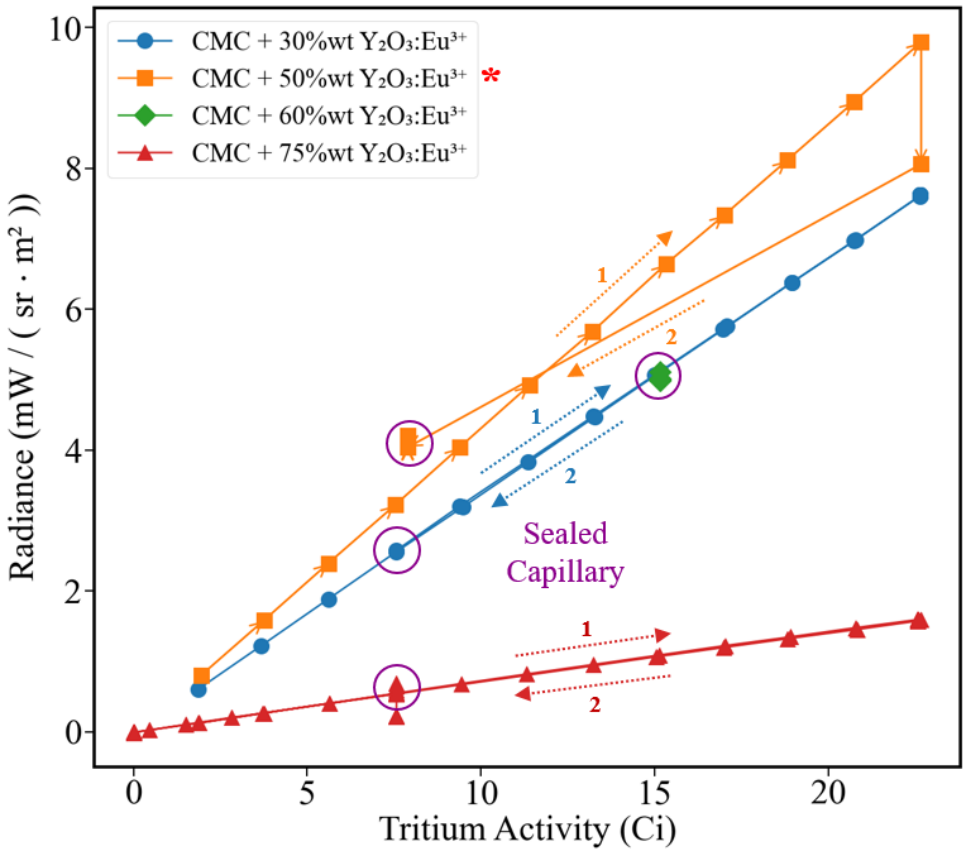

Figure 5.5: Dependence of radiance on tritium activity for CMC aerogels with a diameter of 1.70 mm, loaded with different concentrations of micrometric Y_2O_3:Eu^{3+} particles. The samples are subsequently sealed at 400 mbar (for aerogels loaded with 30, 50, and 75%wt microparticles) and at 800 mbar (for the sample loaded with 60%wt microparticles).

Regarding encapsulation pressure, note that the laboratory operates under negative pressure relative to atmospheric pressure outside, and the glove box maintains even lower pressure relative to the laboratory. This setup ensures that any potential tritium gas leak remains contained within the glove box. Consequently, a maximum encapsulation pressure of 800 mbar is selected to ensure safe working conditions.

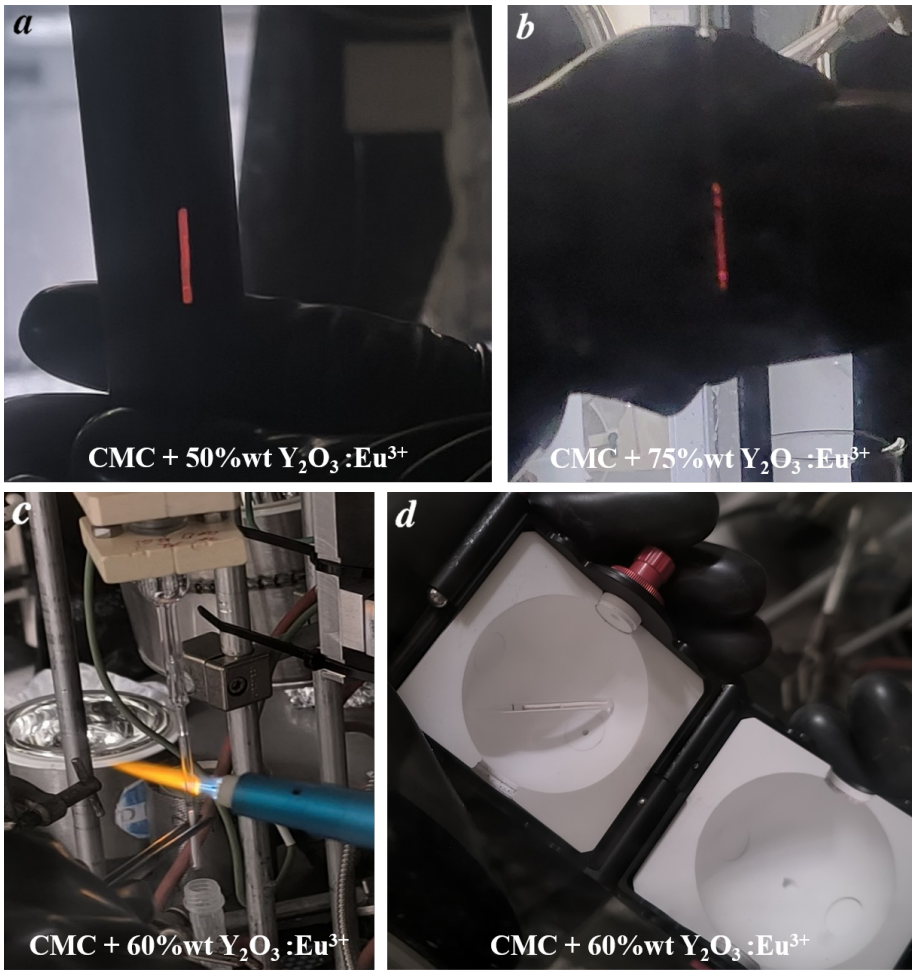

Figure 5.6: ***a)*** Capillary containing the CMC aerogel loaded with 50%wt of Y_2O_3:Eu^{3+} microparticles, at 400 mbar before sealing. ***b)*** Capillary containing the CMC aerogel loaded with 75%wt of Y_2O_3:Eu^{3+} microparticles, at 400 mbar before sealing. ***c)*** Sealing of the capillary containing the CMC aerogel loaded with 60%wt of Y_2O_3:Eu^{3+} microparticles, at 800 mbar. ***d)*** The same sealed capillary inside the integration sphere.

Figure 5.5 shows the dependence of radiance on tritium activity. CMC aerogels loaded with Y_2O_3:Eu^{3+} at concentrations of 30, 60, and 75%wt are exposed to a constant pressure of 1200 mbar for 30 minutes, while the aerogel with a concentration of 50%wt is exposed overnight. It can be observed that, for the aerogels exposed for only 30 minutes, there is

little variation between the curves corresponding to the increase and decrease of tritium activity. In contrast, for the aerogel exposed overnight, a significant drop in radiance is observed, corresponding to a decrease of 17.6%. This loss of radiance is linked to a leak in the hermeticity of the valve system inside the glovebox, as a loss of 1.9 Ci has been detected over the course of the night.

The capillaries containing aerogels with concentrations of 30, 50, and 75%wt are sealed at a pressure of 400 mbar. In the case of the aerogel with a 60%wt concentration of luminescent materials, the full pressure increase process up to 1200 mbar is not shown, only the radiance value measured at 800 mbar, just before encapsulation. This radiance value, recorded right before sealing, is highlighted with a purple circle in Figure 5.5 for all samples.

Figures 5.6a and 5.6b show images of the capillaries containing CMC aerogels loaded with 50 and 75%wt of Y_2O_3:Eu^{3+} microparticles at 400 mbar, taken just before encapsulation. Figure 5.6c shows the encapsulation process, in which the capillary is sealed in order to close and hermetically isolate it. Subsequently, these capillaries are inserted one by one into the integrating sphere, as shown in Figure 5.6d, to monitor the radiance and check whether it remains stable during the first few minutes.

5.5 Aging Effects

After carrying out the first encapsulation tests of aerogels inside borosilicate capillaries and studying the evolution of radiance over the course of a week, surprisingly observing that it increases steadily throughout the entire week, an experiment is designed to study long-term aging. A CMC aerogel containing 50%wt of Y_2O_3:Eu^{3+} microparticles is subjected to increased gaseous tritium pressure up to 1200 mbar in order to loaded it as much as possible with tritium, then the pressure was reduced to 600 mbar before encapsulation. Once encapsulated, the sample is placed inside the integrating sphere and radiance measurements are taken with the camera every 3 hours to monitor its evolution.

This experiment was launched at the end of January 2025, and the aim is to keep it running, at least, until the end of the present doctoral thesis project. Figure 5.7 shows the evolution of radiance over time.

It is surprising to observe that, despite a slight decrease in radiance during the first two weeks, it begins to increase shortly afterward and continues to rise up to the month of August, six months after the experiment was launched. A 30% increase has been recorded compared to the initial radiance value at the time of sealing, despite the natural radioactivity

decrease and the potential aging of luminescent materials. The radiance appears to stabilize at 7.58 mW/(sr·m^2) after the sixth month.

Initially, it was suspected that this increase in radiance could be due to an instrumental issue, as the camera was starting to heat up from continuous operation. In addition, the camera is located in the airlock (SAS) of the glove box, where ventilation is limited. Although the setpoint temperature of the camera is -20°C, it was reaching -15°C. However, after introducing dry ice into the airlock in an attempt to lower the camera's temperature, the same radiance values continued to be obtained across multiple acquisitions, thereby demonstrating that the increase in radiance is indeed due to the sample itself.

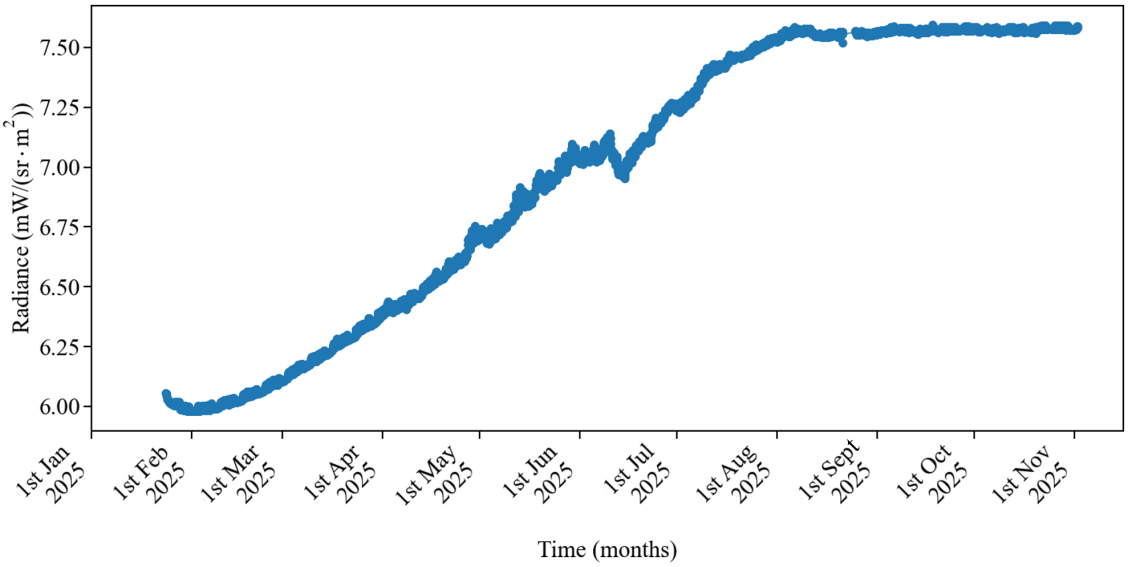

Figure 5.7: Radiance evolution over time for a CMC aerogel loaded with 50%wt of micrometric Y_2O_3:Eu^{3+} particles, with a diameter of 1 mm and 30 mm in height, after sealing at 600 mbar.

This increase in radiance, which has only been observed in RL, whereas in PL and CL, the luminescent materials show degradation from the beginning, may be attributed to several hypotheses that have already been discussed in the literature:

1. Phase changes that have been described in Y_2O_3:Eu^{3+} thin films irradiated by ions (Kr^{2+} at 300 keV and Ne^{+} at 150 keV) [137, 138]. These films show an order to disorder transition in the oxygen sublattice. Although in our case the energies are much lower (18.6 keV maximum), a similar phenomenon may be occurring. This would lead to a random distribution of oxygen vacancies, where the electrons released from these vacancies become mobile, increasing charge carrier mobility and enhancing energy transfer to Eu^{3+} dopants, thereby amplifying the radiance. Filling oxygen vacancies would also reduce non-radiative recombination.

2. Beta radiation may also destabilize Eu^{3+} sites and alter the crystal environment of Y_2O_3:Eu^{3+}, increasing local asymmetry [139]. This favors electric dipole radiative transitions such as $^5D_0 \rightarrow ^7F_2$, which corresponds to the dominant emission peak at 612 nm.

3. The incorporation of $^3He^+$, emitted by tritium atoms, could also be the trigger for phenomena 1 and 2 [140].

4. Beta particles might degrade the CMC matrix, creating free radicals that could interact with Y_2O_3:Eu^{3+} microparticles and alter its luminescent properties.

5. Beta radiation could influence the diffusion of impurities from the CMC and Y_2O_3:Eu^{3+} materials, and modify covalent bonds and their luminescence efficiency.

6. A HIE may be taking place even without a catalyst.

5.6 Maximum Tritium Dose

The calculation of the maximum tritium dose in the event of device failure, based on [102], is 20 mSv/μmol. With the device sealed at 400 mbar, 7.5 Ci of tritium would be present according to Equation 3.7, corresponding to 257 μmol. However, this amount is experimentally measured in a container volume of approximately 9 mL, whereas even aerogels with a 3 mm diameter have smaller volumes than 0.1 mL. In the worst-case scenario, the aerogel would be loaded with 2.9 μmol of tritium. The total dose would then amount to 58 mSv. For reference, a full-body CT scan delivers about 20 mSv.

5.7 Comparison with Radiance Values Reported in the Literature

The proposition of Korin et al. [98], involving a capillary with a luminescent coating on its inner surface filled with tritium gas, achieved $4{\cdot}10^{-4}$ mW/(sr·m^2) at a tritium gas pressure of 2666 mbar. In comparison, the RL device developed in this work reached 24 mW/(sr·m^2) at 1200 mbar (prior to the 30-minute exposure), which represents the maximum pressure defined. Regarding the SRLS devices, the stainless steel plate with a micrometric layer of tritiated titanium proposed by Zelenina et al. [108] delivers a maximum radiance value of $6{\cdot}10^{-2}$ mW/(sr·m^2) at 1 Ci, whereas the present device reaches 1 mW/(sr·m^2) at the

same tritium gas activity (prior to the 30-minute exposure). According to Gill et al. [107], tritium-loaded zeolites registered a maximum radiance of 12 mW/(sr·m^2) at 36 Ci, which is lower than the maximum value attained with the current device. Finally, Renschler et al. [106] reported 3 mW/(sr·m^2) at 1400 mbar using a silica aerogel containing phosphors, a value lower than the maximum radiance obtained here.

5.8 Conclusion

In this chapter, the set of results obtained from the experiments exposing various aerogels to a gaseous tritium atmosphere is presented. These experiments aimed to study the dependence of radiance on the pressure of the tritium gas and, consequently, on the amount of tritium contained in that atmosphere; its dependence on the aerogel diameter; and, of course, its dependence on time. Additionally, tests carried out to encapsulate what has been considered the best candidate for the radioluminescent device, the CMC aerogel loaded with 50%wt Y_2O_3:Eu^{3+}, in a borosilicate glass capsule are shown. This encapsulation enabled launching an ongoing experiment to study the long-term evolution of radiance, from which very interesting results are being obtained. Furthermore, the radiance values achieved in this work exceed those reported in the current literature.

In the following chapter, the results obtained from the analysis of different aerogels before and after their exposure to the tritium atmosphere will be presented, using the characterization techniques described in chapter 3, which will help to better understand the RL results just presented in this chapter.

Résultats de l'Exposition au Tritium

Résumé du Chapitre

Dans ce chapitre, l'ensemble des résultats obtenus lors des expériences d'exposition de différents aérogels à une atmosphère de tritium gazeux est présenté. Ces expériences visaient à étudier la dépendance de la radiance à la pression du gaz de tritium et, par conséquent, à la quantité de tritium contenue dans cette atmosphère; sa dépendance au diamètre de l'aérogel; et, bien entendu, sa dépendance au temps. De plus, des essais réalisés pour encapsuler ce qui a été considéré comme le meilleur candidat pour le dispositif radioluminescent, à savoir l'aérogel de CMC chargé à 50% en masse de Y_2O_3:Eu^{3+}, dans une capsule en verre borosilicate, sont présentés. Cette encapsulation a permis de lancer une expérience en cours visant à étudier l'évolution à long terme de la radiance, dont des résultats très intéressants sont en train d'être obtenus. En outre, les valeurs de radiance atteintes dans ce travail dépassent celles rapportées dans la littérature actuelle.

Chapter 6

Characterization Techniques and Supporting Analyses

To gain insight into the mechanisms of tritium integration in aerogels and to better understand the results presented in the previous chapter, various samples will be analyzed using the characterization techniques described in chapter 3, and the obtained results will be presented here. Finally, this chapter will compare the radioluminescent device developed and characterized throughout this work with the electroluminescent device currently used in the clinical trial conducted at Clinatec.

6.1 Characterization of Luminescent Aerogels Before Tritium Exposure

To begin, the luminescent aerogels will be characterized prior to their exposure to tritium.

6.1.1 Spectral Characterization by Photoluminescence

This first technique aims to investigate the spectral emission of various aerogels via PL and to evaluate whether the emission spectra of the luminescent materials remain unchanged after their integration into the aerogel matrix.

The spectra recorded for the different aerogel samples, upon excitation with 280 nm UV light, are presented in Figure 6.1. Intensity is normalized following Equation 4.1 and divided by the maximum intensity value of each spectrum.

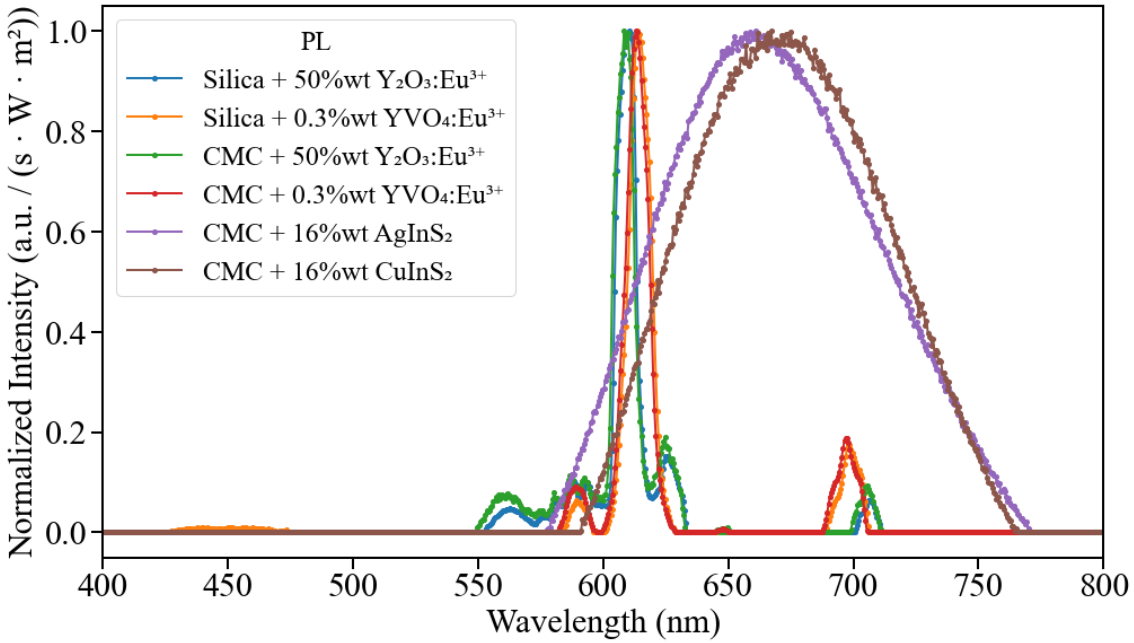

Figure 6.1: Normalized emission spectra of CMC and silica aerogels loaded with different luminescent materials under UV light at 280 nm.

The emission spectra of these luminescent aerogels can be compared with those obtained from characterizing the luminescent material coatings presented in chapter 4. Table 6.1 shows the different wavelengths.

Luminescent Material	**Sample**	**λ_{PL} (nm)**
Y_2O_3:Eu^{3+}	Coating	611
	Embedded in Silica Aerogel	610
	Embedded in CMC Aerogel	609
YVO_4:Eu^{3+}	Coating	614
	Embedded in Silica Aerogel	615
	Embedded in CMC Aerogel	613
$AgInS_2$	Coating	646
	Embedded in CMC Aerogel	660
$CuInS_2$	Coating	686
	Embedded in CMC Aerogel	671

Table 6.1: Summary of characteristic emission wavelengths for various luminescent materials under PL, in coatings or embedded in silica or CMC aerogels.

The phosphors (Y_2O_3:Eu^{3+}, YVO_4:Eu^{3+}) preserve their characteristic emission wave-

lengths, with only a 2 nm difference between the values measured in the coating and in the aerogel samples. This slight shift could be attributed either to instrumental sensitivity of the spectrometer or to modifications in their local environment. Although it is difficult to determine whether this effect is purely instrumental, the fact that the redshift of 2 nm consistently appears for both phosphors specifically in the CMC aerogel makes it suspicious, suggesting that a real change in the emission wavelength may indeed occur due to structural or environmental effects.

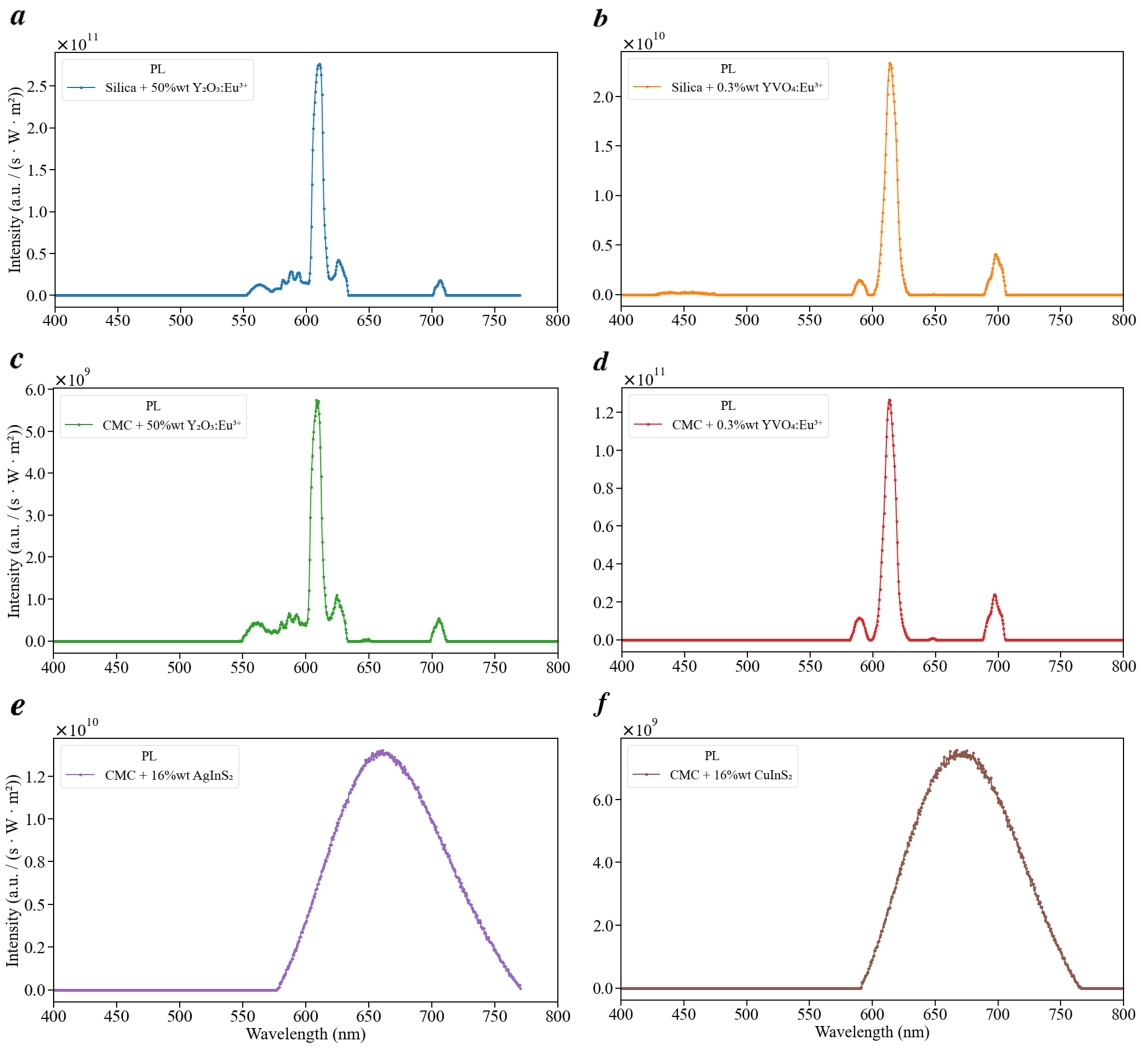

Figure 6.2: Emission spectra under exposure to a 280 nm UV light from: ***a)*** a silica aerogel loaded with 50%wt Y_2O_3:Eu^{3+}, ***b)*** a silica aerogel loaded with 0.3%wt YVO_4:Eu^{3+}, ***c)*** a CMC aerogel loaded with 50%wt Y_2O_3:Eu^{3+}, ***d)*** a CMC aerogel loaded with 0.3%wt YVO_4:Eu^{3+}, ***e)*** a CMC aerogel loaded with 16%wt $AgInS_2$, and ***f)*** a CMC aerogel loaded with 16%wt $CuInS_2$. The intensity is calculated using Equation 4.1.

For the QDs, the spectral shifts are more pronounced. In the case of $AgInS_2$ QDs, a redshift

of 14 nm is observed when embedded in the aerogel, with the emission moving from 646 to 660 nm. Conversely, for $CuInS_2$ QDs, a blueshift of 15 nm occurs, with the emission shifting from 686 nm in the coating to 671 nm in the aerogel. Such wavelength variations in QDs have been recently reported [141], and they are generally attributed to changes in local environment, surface chemistry, strain, and inter-dot interactions.

Figure 6.2 shows the spectra of each aerogel individually, where intensity has been normalized following Equation 4.1.

The silica aerogel loaded with Y_2O_3:Eu^{3+} exhibits the most intense spectrum, followed by the CMC aerogel loaded with YVO_4:Eu^{3+}. Next in intensity is the silica aerogel loaded with YVO_4:Eu^{3+}, followed by the CMC aerogel loaded with $AgInS_2$ QDs. The CMC aerogel loaded with $CuInS_2$ comes next, and finally, the CMC aerogel loaded with Y_2O_3:Eu^{3+}.

6.1.2 Two-Dimensional Morphological and Spectral Characterization by Cathodoluminescence

The next step involves analyzing various samples using CL to investigate both the surface morphology and the optical emission of the aerogels under electron beam excitation. This method provides insight into their expected behavior in a gaseous tritium atmosphere. However, it is important to note that the excitation conditions differ between the two contexts: in CL, excitation is localized, with the electron beam having a diameter of several hundreds of nm, whereas in RL experiments, the entire aerogel surface is uniformly exposed to tritium.

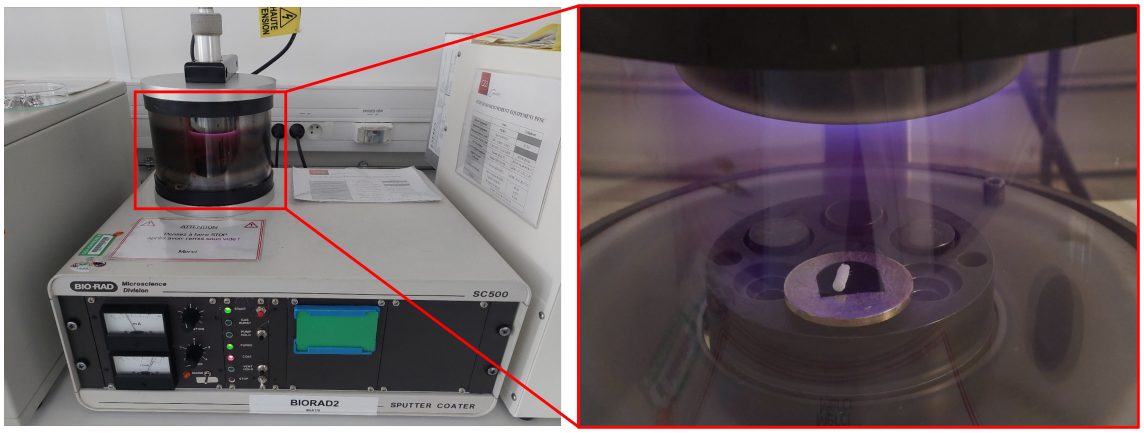

Figure 6.3: Process of depositing a platinum coating on the surface of an aerogel by plasma sputter coating. To mount the aerogel on the cathodoluminescence sample holder, Scotch carbon tape is used.

For reference, the emission spectrum of beta particles from tritium decay has an average energy of 5.7 keV and a maximum energy of 18 keV, as already mentioned. In these CL experiments, monoenergetic electron beams with energies ranging from 2 to 10 keV are employed, corresponding to the energy range accessible on the available equipment.

Due to the electrically insulating nature of aerogels, a 10 nm platinum layer is deposited on the sample surface via plasma sputter coating, as shown in Figure 6.3, to prevent surface charge accumulation under electron-beam exposure. Without this conductive layer, accumulated charges would distort the electron interactions needed for CL, leading to signal loss or image artifacts that make analysis unreliable.

6.1.2.1 Surface Imaging with Secondary Electrons

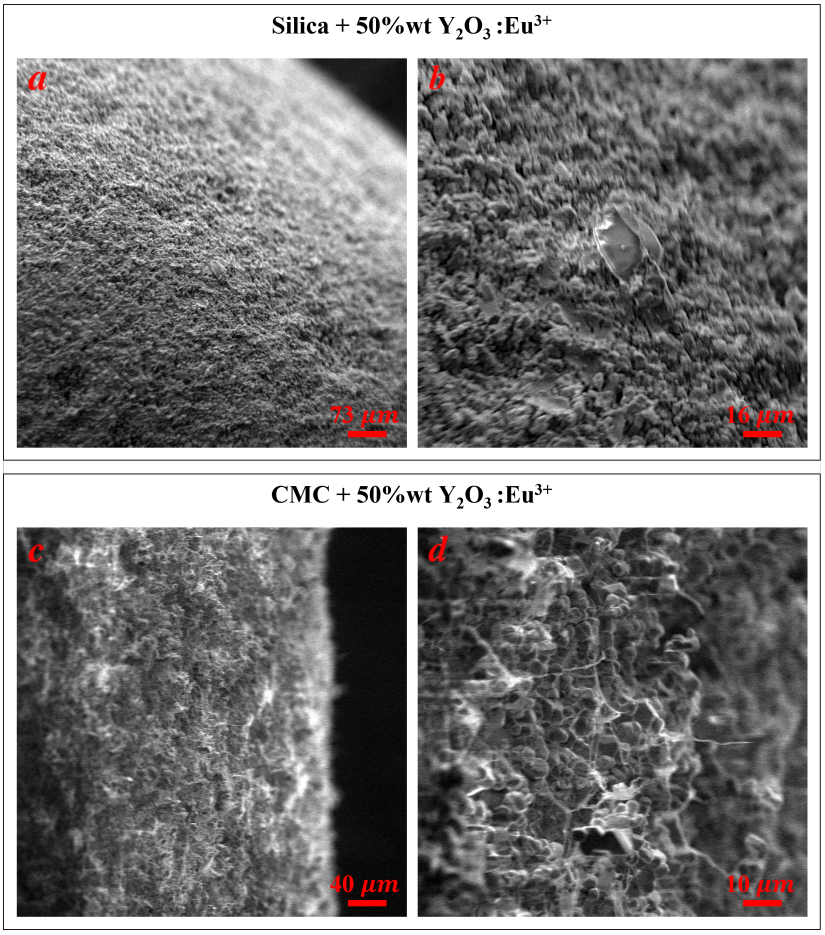

Figure 6.4: Electron microscope images of ***a)*** zoomed-out view of the region shown in ***b)***, corresponding to a silica aerogel loaded with 50%wt Y_2O_3:Eu^{3+} microparticles; and ***c)*** zoomed-out view of the region shown in ***d)***, corresponding to a CMC aerogel loaded with 50%wt Y_2O_3:Eu^{3+} microparticles.

Figures 6.4a and 6.4b shows images obtained using secondary electrons emitted upon bombardment of the surface of a 3 mm diameter, 10 mm long aerogel composed of a silica matrix loaded with Y_2O_3:Eu^{3+} microparticles at a concentration of 50%wt. Meanwhile, Figures 6.4c and 6.4d correspond to a CMC aerogel loaded with 50%wt Y_2O_3:Eu^{3+}. Differences can be observed between the two types of aerogels. On one hand, the silica aerogel shows a grainy texture uniformly distributed across the surface, where most particles have a diameter close to 8 μm (which matches their commercial specifications), although larger agglomerates can sometimes be seen (like the one in Figure 6.4b). On the other hand, the CMC aerogel displays a more sponge-like texture, where the Y_2O_3:Eu^{3+} particles appear to be surrounded by a fibrous network, which are likely CMC fibers.

All of this is consistent with observations made when handling these aerogels: the silica aerogel has a smoother texture and is much harder and more brittle, breaking easily into powder when fractured. In contrast, the CMC aerogel behaves more like a sponge, it can be touched and deformed under pressure, not fully returning to its original shape, but it does not break; to tear it, it has to be pulled apart.

Moreover, no surface pores are observed in either of the aerogels, which may suggest the presence of pores smaller than the spatial resolution of the instrument, indicating that these pores are likely on the nanometer scale.

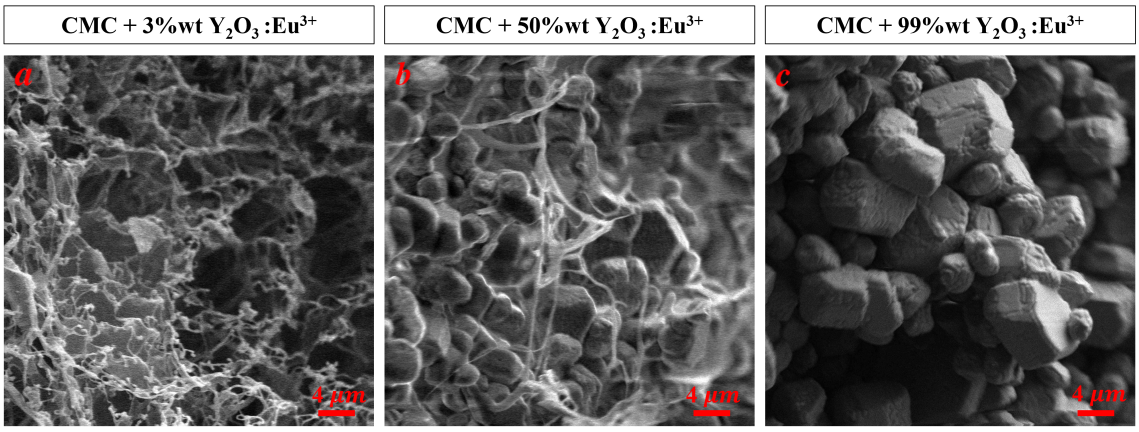

Figure 6.5: Electron microscope images of a CMC aerogel loaded with Y_2O_3:Eu^{3+} microparticles at a concentration of: ***a)*** 3%wt, ***b)*** 50%wt, and ***c)*** 99%wt.

In order to study the structure of CMC aerogels in more detail as a function of the concentration of Y_2O_3:Eu^{3+} microparticles, images are taken of aerogels loaded with three different concentrations: 3, 50, and 99%wt. At the lowest concentration, 3%wt (Figure 6.5a), a very airy and porous structure is observed, with pores in the CMC network reaching up to 8 μm, and no Y_2O_3:Eu^{3+} particles are visible. As the concentration of

the luminescent material increases, in the case of 50%wt (Figure 6.5b), fewer pores are observed, and Y_2O_3:Eu^{3+} particles begin to appear, surrounded by fibrous CMC networks. At a concentration of 99%wt of luminescent material (Figure 6.5c), only micrometric particles are visible, and no CMC fibers are observed.

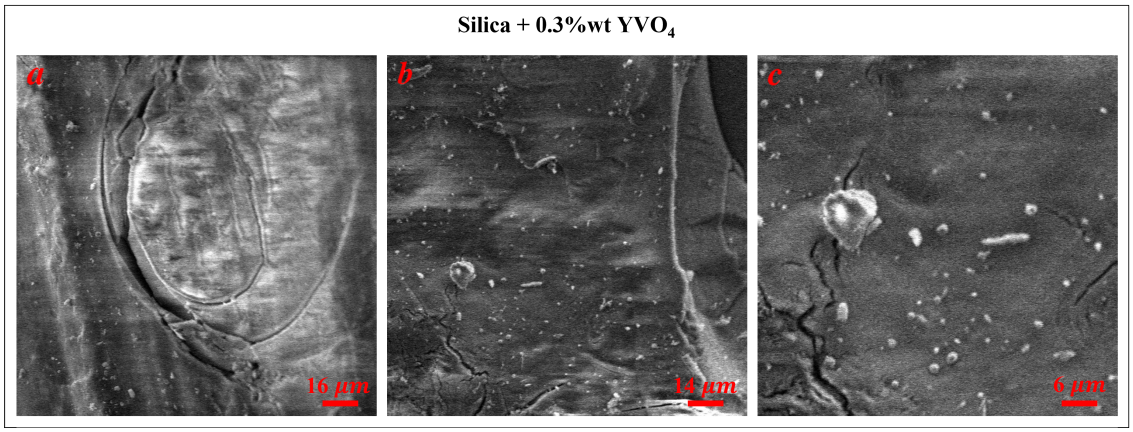

Figure 6.6: Electron microscope images of a silica aerogel loaded with YVO_4:Eu^{3+} nanoparticles at a concentration of 0.3%wt, taken from the same region at different magnifications: ***a)*** 163 μm, ***b)*** 146 μm, and ***c)*** 65 μm.

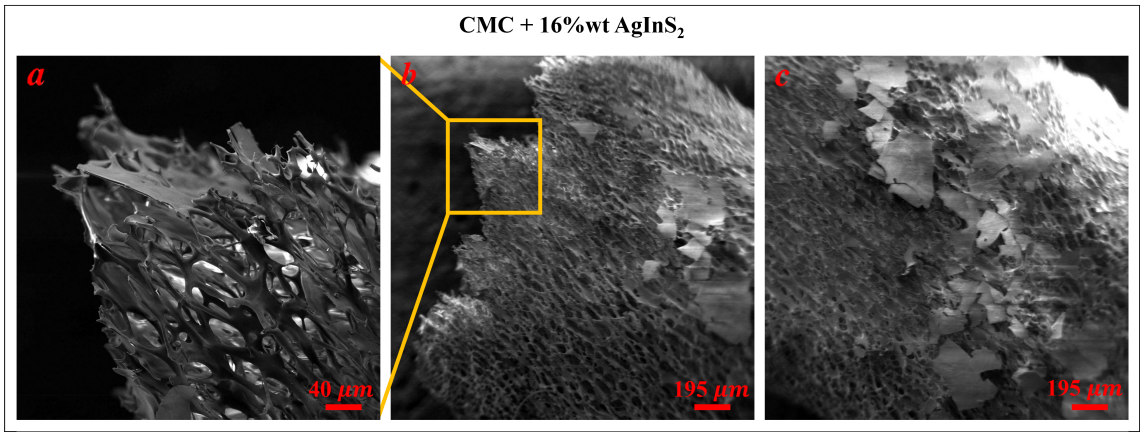

Figure 6.7: Electron microscope images of a CMC aerogel loaded with $AgInS_2$ QDs at a concentration of 16%wt. ***a)*** Zoomed-in view of the region shown in ***b)***, corresponding to a fracture in the aerogel structure caused during handling. ***c)*** Another area of the same aerogel surface, where regions with a non-porous texture can be observed.

The surface of silica aerogels loaded with nanometric YVO_4:Eu^{3+} particles is also studied. Specifically, Figure 6.6 shows different images of a silica aerogel containing 0.3%wt nanoparticles, taken from the same region at different magnifications. These images confirm that silica aerogels exhibit much finer porosity than CMC aerogels, as even when

loaded with nanoparticles, no pores on the micrometer scale are observed. This suggests that the pores are smaller than the spatial resolution of the instrument. Slight surface fractures can also be seen, along with particles that could be agglomerates of YVO_4:Eu^{3+}.

Figure 6.7 shows images of a CMC matrix loaded with $AgInS_2$ QDs at a concentration of 16%wt. The surface appears highly porous, and smoother regions can also be observed. These smoother areas may correspond to remnants of the colloidal quantum dot solution that were not fully mixed with the CMC solution, resulting in regions with a smoother and less porous texture, as shown in Figure 6.7c. Figures 6.7a and 6.7b show a fracture in the aerogel structure that occurred during handling, where pores approximately 40 μm in diameter can be observed.

Let us now move on to characterize the spectral emission of these aerogels under electron beam exposure.

6.1.2.2 Emission Spectra at 5.7 keV

First, the emission spectra of the different aerogels is studied with the aim of determining whether their emission spectra match, or not, those of the pure luminescent materials. To do this, various aerogels are exposed to a 5.7 keV electron beam.

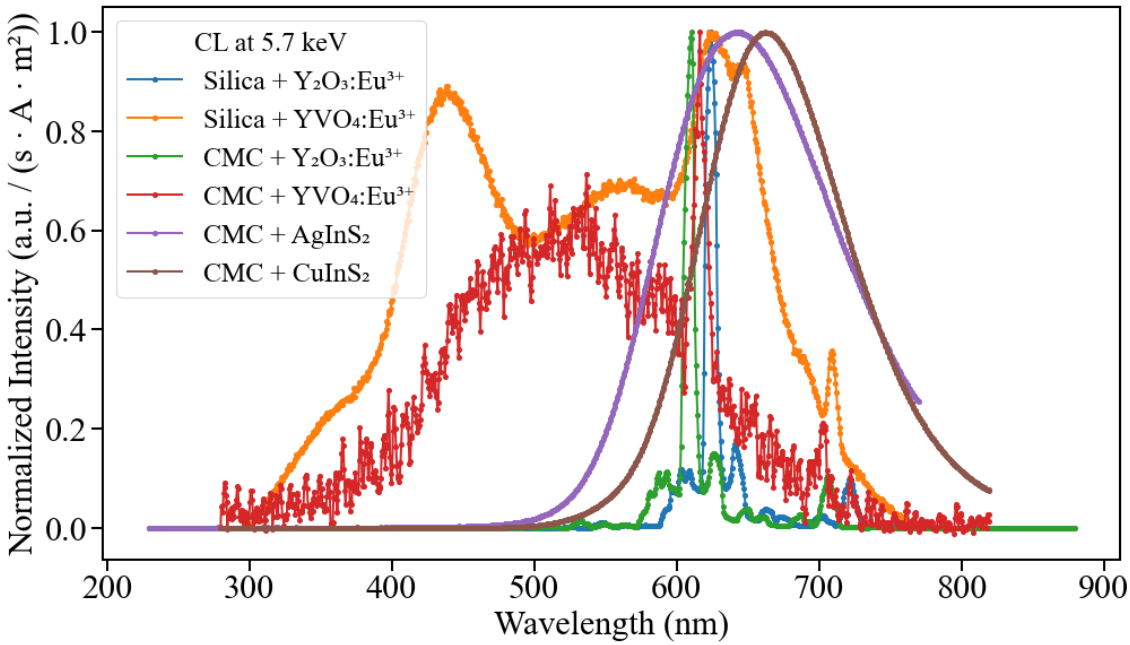

Figure 6.8: Emission spectra of CMC and silica aerogels loaded with different luminescent materials under the exposure of a 5.7 keV electron beam.

Figure 6.8 shows the normalized emission spectra of CMC and silica aerogels loaded with

different luminescent materials, allowing direct comparison of their spectral shapes. The spectra are normalized using Equation 4.2 and subsequently divided by the maximum intensity value of each spectrum.

At first glance, the emission spectra of the aerogels, both silica and CMC, loaded with $YVO_4:Eu^{3+}$, appear different from those observed under PL, since the emission peaks are not sharp and instead there is a broad light emission starting from 400 nm, which may be due to sodium citrate ligands as mentioned in seccion 4.2 of chapter 4. However, this has already been observed for $YVO_4:Eu^{3+}$ coatings under CL (section 4.2 of chapter 4). By contrast, the PL spectra do show sharp emission peaks, both for the $YVO_4:Eu^{3+}$ coating and once integrated into the aerogel. This suggests that the phenomenon depends on the excitation mechanism.

Table 6.2 compares the emission wavelengths of the different luminescent materials when excited under CL, whether in a coating or embedded in an aerogel. In contrast to what has been observed under PL (previous section), here the wavelength shifts are much more pronounced for all luminescent materials. For the phosphor $Y_2O_3:Eu^{3+}$, a redshift of up to 16 nm is observed between the coating and the silice aerogel, while the shift is only 2 nm with the CMC aerogel. A similar behavior is found for the $YVO_4:Eu^{3+}$ phosphor, where a redshift of 12 nm occurs with the silica aerogel, compared to 5 nm with the CMC aerogel.

Luminescent Material	**Sample**	λ_{CL} **(nm)**
$Y_2O_3:Eu^{3+}$	Coating	608
	Embedded in Silica Aerogel	624
	Embedded in CMC Aerogel	610
$YVO_4:Eu^{3+}$	Coating	612
	Embedded in Silica Aerogel	624
	Embedded in CMC Aerogel	617
$AgInS_2$	Coating	644
	Embedded in CMC Aerogel	641
$CuInS_2$	Coating	706
	Embedded in CMC Aerogel	662

Table 6.2: Summary of characteristic emission wavelengths for various luminescent materials under CL, in coatings or embedded in silica or CMC aerogels.

Regarding the QDs, in the case of $AgInS_2$, embedding them in the aerogel results in a blueshift of only 3 nm, whereas under PL a redshift of 14 nm was observed. Finally, for

the $CuInS_2$ QDs, a blueshift is also observed, but much larger, reaching up to 44 nm.

It is evident that significant changes must be occurring in the structure and local environment of the luminescent particles to explain these wavelength shifts, which this time are not only significant for the QDs but also for the phosphors.

6.1.2.3 Local Homogeneity of Emission

Another study is carried out with the aim of evaluating the local homogeneity of the emission spectrum and, consequently, the homogeneity of the aerogel's composition (at least at the surface level). To this end, two different ROIs of the same aerogel are analyzed, and the intensity is normalized according to Equation 4.2. Figure 6.9 shows the results obtained for all samples analyzed.

Figures 6.9a and 6.9c show the emission spectra of a silica and a CMC aerogel with 50%wt Y_2O_3:Eu^{3+} microparticles, respectively. The intensity of the spectra recorded in the silica aerogel is three orders of magnitude higher than that recorded in the CMC aerogel. This result is surprising, as in the RL experiments, the opposite is observed: the CMC aerogel emits a higher intensity than the silica aerogel. The emission spectra from the ROIs analyzed in both silica and CMC aerogels show intensity variations of up to one order of magnitude. This may suggest that aerogels containing Y_2O_3:Eu^{3+} microparticles, regardless of the host matrix, may not exhibit a homogenesous distribution. However, it is premature to draw definitive conclusions, more ROIs and several aerogels with the same compositions should be analyzed.

For the aerogels containing YVO_4:Eu^{3+} nanoparticles, the spectra from the silica aerogel (Figure 6.9b) show a prominent peak around 450 nm, which appears to correspond to the sodium citrate ligands. In the case of the ROI B, this peak is even more intense than the emission peak at 624 nm. In addition, it appears as a double peak, which could be due to a misalignment of the spectrometer. What is likely happening in this aerogel is that, since the spectrum is recorded in a region that has never previously been exposed to the electron beam, all the sodium citrate ligands are still present. As a result, the signal below 600 nm is very strong, making it difficult to clearly observe the 624 nm emission peak. It would be best to expose the region to the electron beam beforehand to reduce the number of ligands and allow for clearer observation of the main YVO_4:Eu^{3+} emission at 625 nm. The same occurs in the case of the CMC aerogel (Figure 6.9d), where ROI B seems to show less emission below 600 nm and thus reveals the peak more clearly, in this case located at 617 nm.

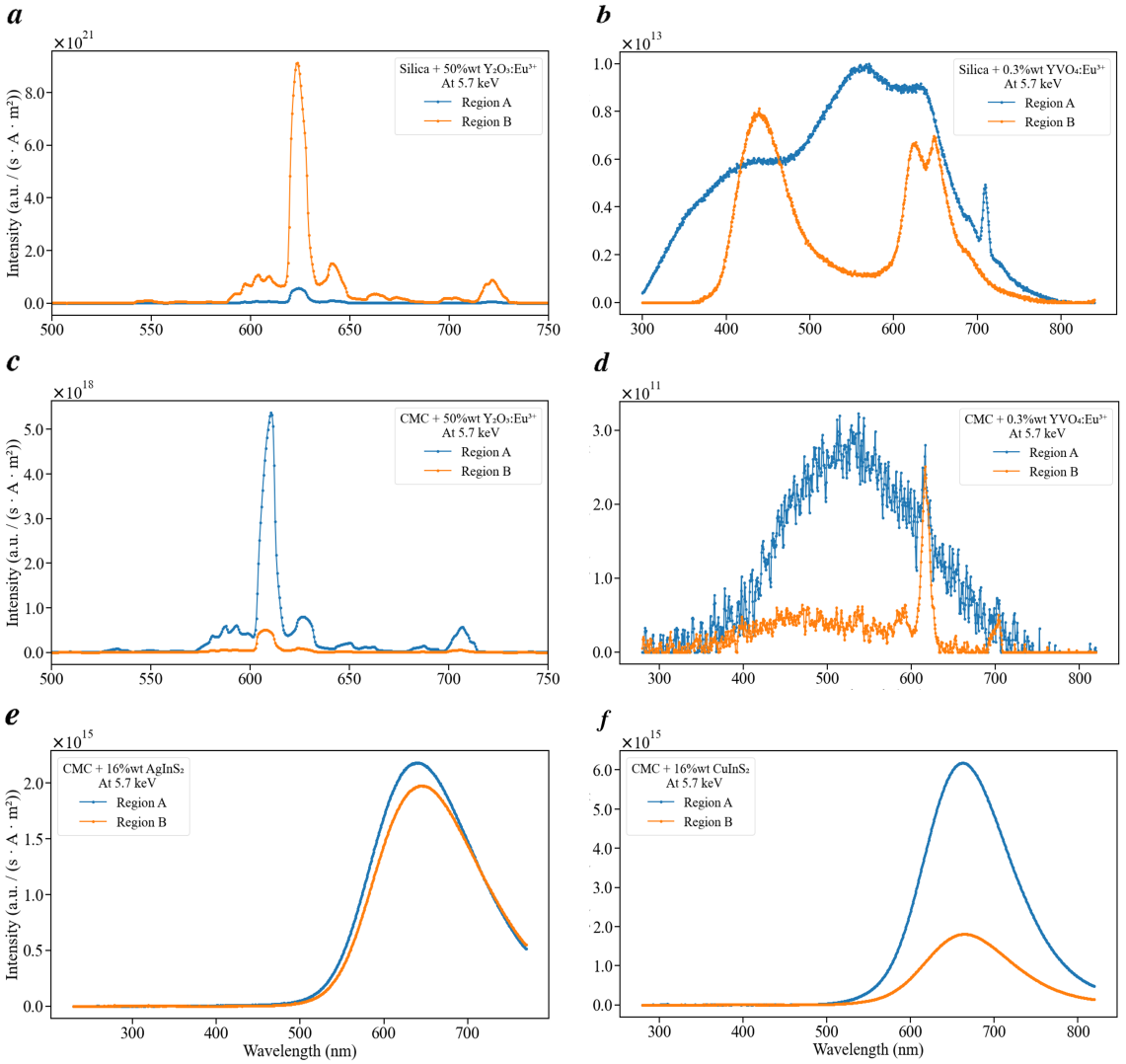

Figure 6.9: Emission spectra under exposure to a 5.7 keV electron beam for two different ROIs from: ***a)*** a silica aerogel loaded with 50%wt Y_2O_3:Eu^{3+}, ***b)*** a silica aerogel loaded with 0.3%wt YVO_4:Eu^{3+}, ***c)*** a CMC aerogel loaded with 50%wt Y_2O_3:Eu^{3+}, ***d)*** a CMC aerogel loaded with 0.3%wt YVO_4:Eu^{3+}, ***e)*** a CMC aerogel loaded with 16%wt $AgInS_2$, and ***f)*** a CMC aerogel loaded with 16%wt $CuInS_2$. The intensity is calculated using Equation 4.2.

The CMC aerogels loaded with 16%wt $AgInS_2$ and $CuInS_2$ are shown in Figures 6.9e and 6.9f, respectively. In the case of $AgInS_2$, the spectra from the two ROIs show slight differences in intensity, whereas the $CuInS_2$ spectrum shows a greater difference, though still less than an order of magnitude.

This is consistent, since the electron beam (whose diameter can reach several hundred nm) is larger than the size of the QDs. As a result, the beam sees a surface with a homogeneous distribution of particles. In contrast, in the case of microparticles, such as Y_2O_3:Eu^{3+},

the electron beam diameter is smaller than the particles, meaning the beam may strike a particle or fall into an empty region. This explains the greater heterogeneity in the recorded spectra. This situation is schematized in Figure 6.10.

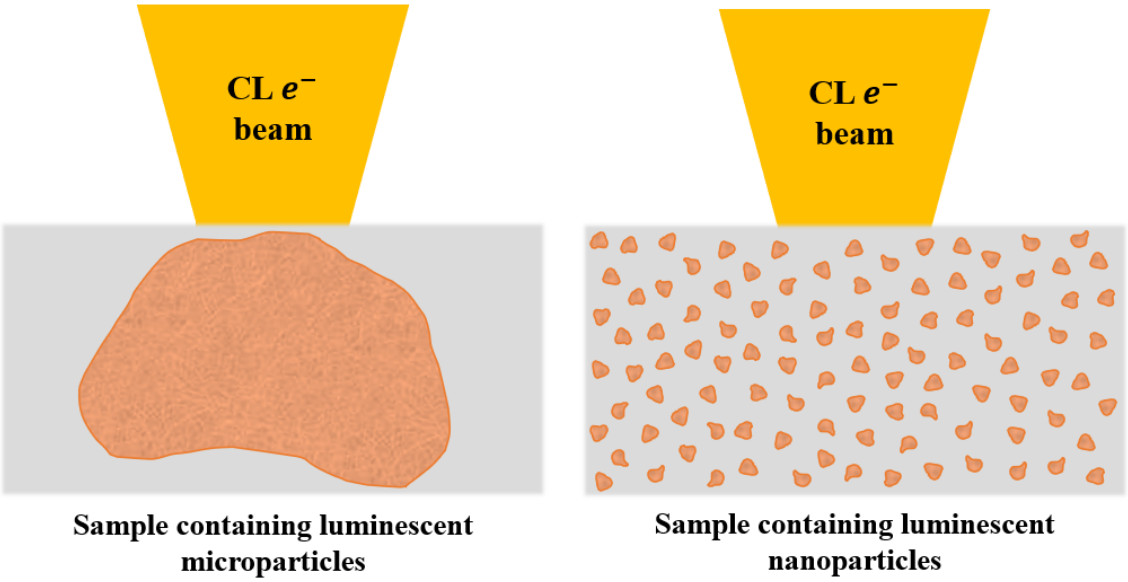

Figure 6.10: Schematic of what the electron beam in CL encounters when interacting with a sample containing microparticles and with another containing nanoparticles.

Finally, the intensity of the spectra obtained by CL can be compared with the radiance values obtained in RL. In RL, the highest to lowest radiance values are obtained with the CMC aerogel loaded with Y_2O_3:Eu^{3+} microparticles, followed by the silica aerogel with Y_2O_3:Eu^{3+} microparticles, very close to the CMC aerogels loaded with QDs (both $AgInS_2$ and $CuInS_2$), then the silica aerogel with YVO_4:Eu^{3+} nanoparticles, and finally, the CMC aerogel with YVO_4:Eu^{3+} nanoparticles. In CL, the ranking is similar, except for the silica aerogel with Y_2O_3:Eu^{3+} microparticles, which shows a more intense spectrum than the CMC aerogel loaded with the same luminescent particles.

The differences observed in emission intensity rankings between CL and RL may be explained by the difference in excitation volume and depth. In CL, the highly localized and monoenergetic electron beam at 5.7 keV excites only a shallow surface layer of the aerogel, limiting the penetration depth. In RL, beta particles emitted by tritium gas penetrate deeper and excite a larger volume of the aerogel, resulting in a globally and polyenergetic excitation that better integrates the bulk luminescent properties.

6.1.2.4 Energy Dependence of Emission Spectra

The dependence of the emission spectra on the energy of the electron beam is also investigated. To this end, two ROIs from the same aerogel are once again exposed to an electron beam but this time, with energies varying from 2 to 4, 6, 8, and 10 keV.

Figure 6.11 shows the spectra obtained for CMC aerogels containing Y_2O_3:Eu^{3+} at three different concentrations, thereby also allowing the study of the effect of luminescent material concentration.

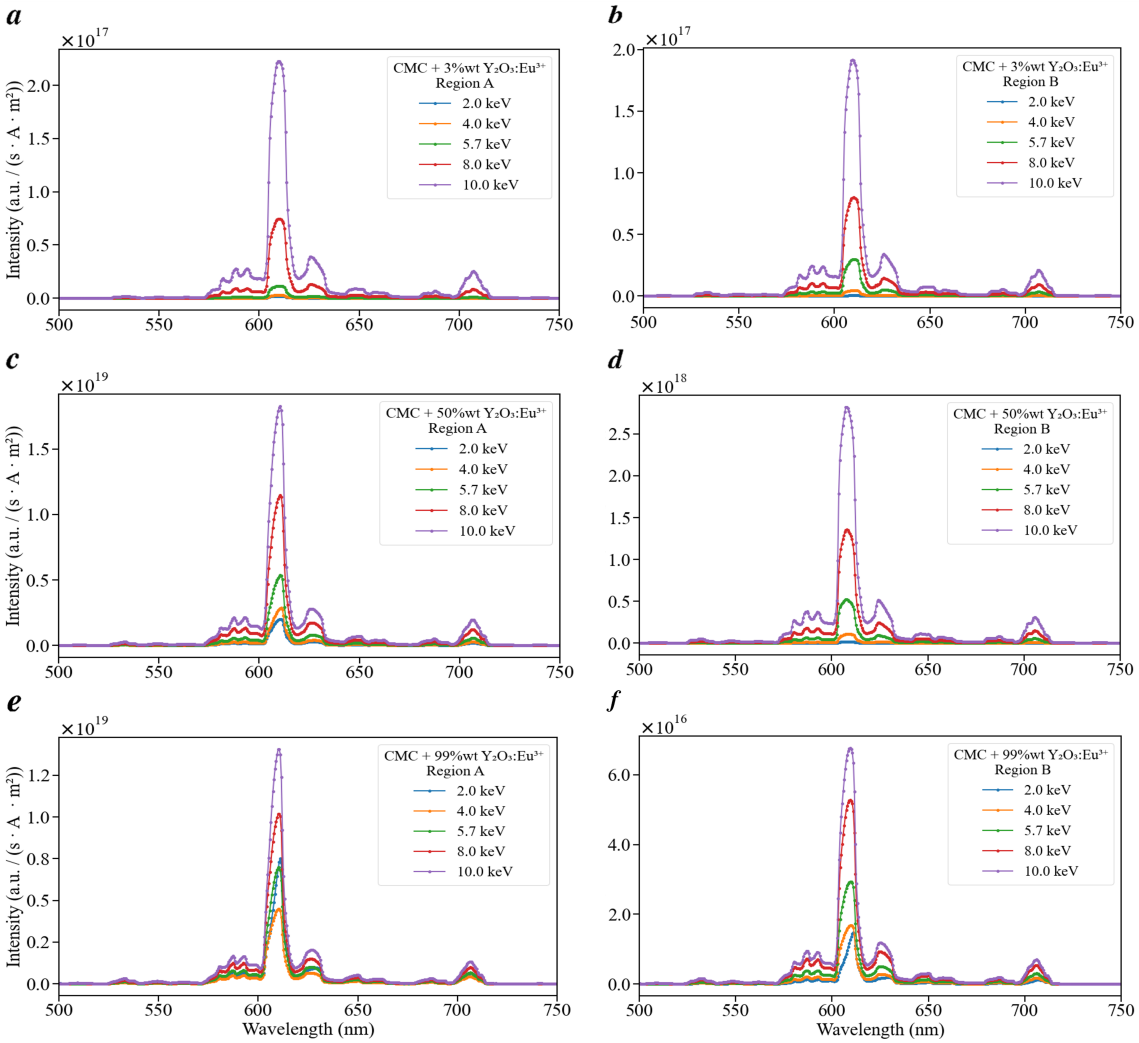

Figure 6.11: Emission spectra under exposure to electron beams at different energies (2, 4, 6, 8, and 10 keV) from CMC aerogels loaded with Y_2O_3:Eu^{3+} ***a)*** at a concentration of 3%wt in ROI A, ***b)*** at a concentration of 3%wt in ROI B, ***c)*** at a concentration of 50%wt in ROI A, ***d)*** at a concentration of 50%wt in ROI B, ***e)*** at a concentration of 99%wt in ROI A, and ***f)*** at a concentration of 99%wt in ROI B. The intensity is calculated using Equation 4.2.

Starting with the lowest concentration, 3%wt, Figures 6.11a and 6.11b show that the spectra from both ROIs have very similar intensities, which may indicate good dispersion of the luminescent particles throughout the volume of the aerogel.

As the concentration of luminescent particles increases, at 50%wt, shown in Figures 6.11c and 6.11d, the spectral intensity increases by one to two orders of magnitude compared to the previous concentration. Between the two ROIs, there is a difference of about one order of magnitude, which could suggest that the particles are not as uniformly distributed as in the previous case. Nevertheless, the overall optical emission is significantly higher.

Finally, in the sample containing 99%wt luminescent material, the intensities between the two ROIs (Figures 6.11e and 6.11f) vary substantially, with a difference of more than two orders of magnitude. At such high concentrations, the Y_2O_3:Eu^{3+} microparticles are so abundant that they tend to aggregate, forming clusters instead of being uniformly distributed. Two things could be occurring:

- Regions with denser Y_2O_3:Eu^{3+} clusters may produce a very strong signal, while regions containing voids or CMC residues may show weaker emission.
- The high density of luminescent material could lead to self-absorption, where photons emitted by one Y_2O_3:Eu^{3+} particle are absorbed by nearby particles before they can exit the aerogel. In this case, the denser regions would lose more photons due to self-absorption, resulting in a weaker signal, whereas regions with lower microparticle density might allow photons generated deeper below the surface to escape through the gaps between clusters.

To try to understand which of these two reasons explains the difference in intensity between the two ROIs, it is necessary to examine the secondary electron images of these regions, which are shown in Figure 6.12. These images qualitatively reveal that ROI B has a higher density of luminescent material than ROI A, which would suggest that the lower intensity recorded in ROI B could be due to the phenomenon of self-absorption.

Moreover, for all concentrations of luminescent materials and for both ROIs studied, the emission spectrum is observed to be proportional to the energy of the electron beam. This implies that, once the Y_2O_3:Eu^{3+} microparticles are integrated into the organic CMC matrix, the system shows no signs of saturation, which may lead to the following conclusions:

- The integration of Y_2O_3:Eu^{3+} into the CMC matrix does not hinder excitation or emission processes, indicating that the aerogel does not affect the optical and electronic properties of Y_2O_3:Eu^{3+}, as it does not introduce trap states or absorb

part of the excitation energy. The properties of Y_2O_3:Eu^{3+} are preserved despite being embedded in a CMC matrix.

- The crystal lattice of Y_2O_3 (the ordered cubic-C bixbyite phase, as mentioned in section 3.2 of chapter 3) provides a stable environment for Eu^{3+} ions, minimizing mechanisms that could lead to non-radiative effects.

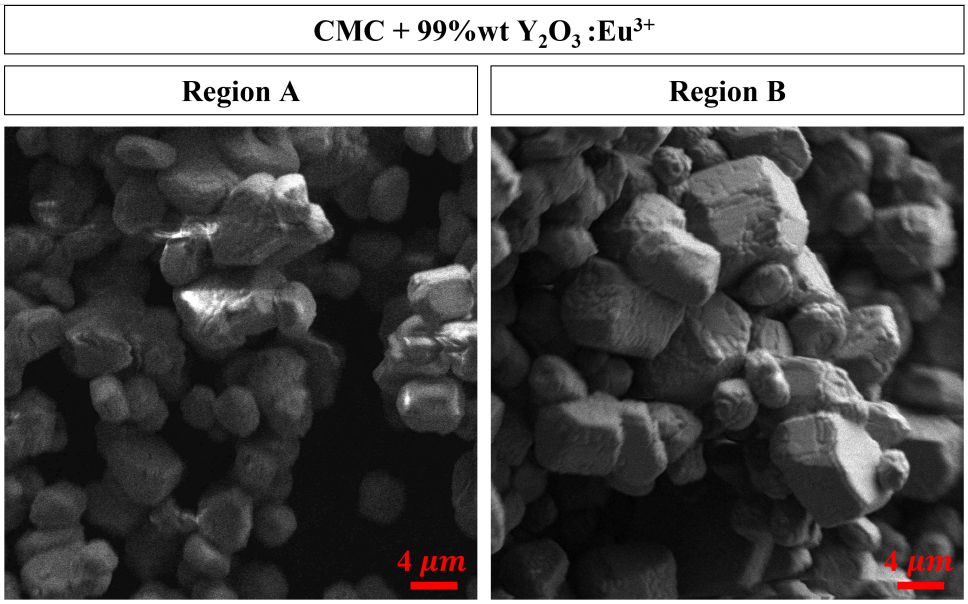

Figure 6.12: Electron microscope images of a CMC aerogel loaded with 99%wt Y_2O_3:Eu^{3+} in ***a)*** ROI A, and ***b)*** ROI B.

On the other hand, CMC aerogels with QDs, both $AgInS_2$ and $CuInS_2$, at a concentration of 16%wt, have also been studied. In both cases, the recorded intensity of the spectra in both regions is similar, as it is show in Figure 6.13, which could support the hypothesis that the nanoparticles are more uniformly distributed than the micrometric particles, as previously mentioned. Moreover, the spectral intensities are proportional to the energy of the electron beam, indicating that these luminescent materials also do not show signs of saturation.

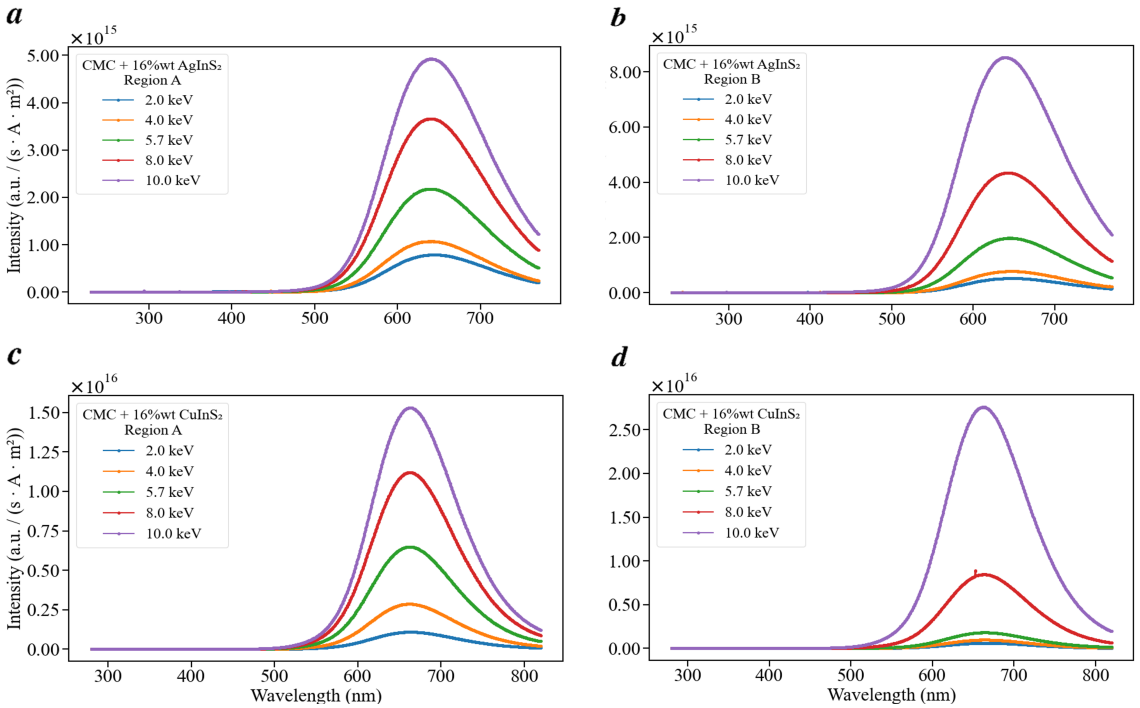

Figure 6.13: Emission spectra under exposure to electron beams at different energies (2, 4, 6, 8, and 10 keV) from: ***a)*** a CMC aerogel loaded with 16%wt $AgInS_2$ in ROI A, ***b)*** a CMC aerogel loaded with 16%wt $AgInS_2$ in ROI B, ***c)*** a CMC aerogel loaded with 16%wt $CuInS_2$ in ROI A, and ***d)*** a CMC aerogel loaded with 16%wt $CuInS_2$ in ROI B. The intensity is calculated using Equation 4.2.

6.1.2.5 Rapid Aging Effects under Electron Beam Exposure

To conclude these CL experiments, the effects of aerogel rapid aging under electron beam exposure are investigated. Rapid aging since CL allows rapid simulation of RL aging taking into account the electron density.

Spectra are recorded at different exposure times for the same ROI, at T_0, T_0 + 10 s, T_0 + 1 min, and T_0 + 3 min under electron beam at 5.7 keV. This procedure is repeated for three ROIs per sample analyzed.

Figure 6.14 shows the behavior of a silica aerogel loaded with 50%wt Y_2O_3:Eu^{3+}. The spectra from the three ROIs exhibit the dominant peak at 624 nm, as previously observed. However, in ROI A, at times T_0 + 1 min and T_0 + 3 min (green and red spectra in Figure 6.14a), the peak has slightly shifted to the right, to 630 nm. These shifts could be due to charge accumulation in that region, which may locally alter the potential and cause changes in the surroundings of the Y_2O_3:Eu^{3+} particles. This could be modifying their crystal structure and thereby shifting the emission peak.

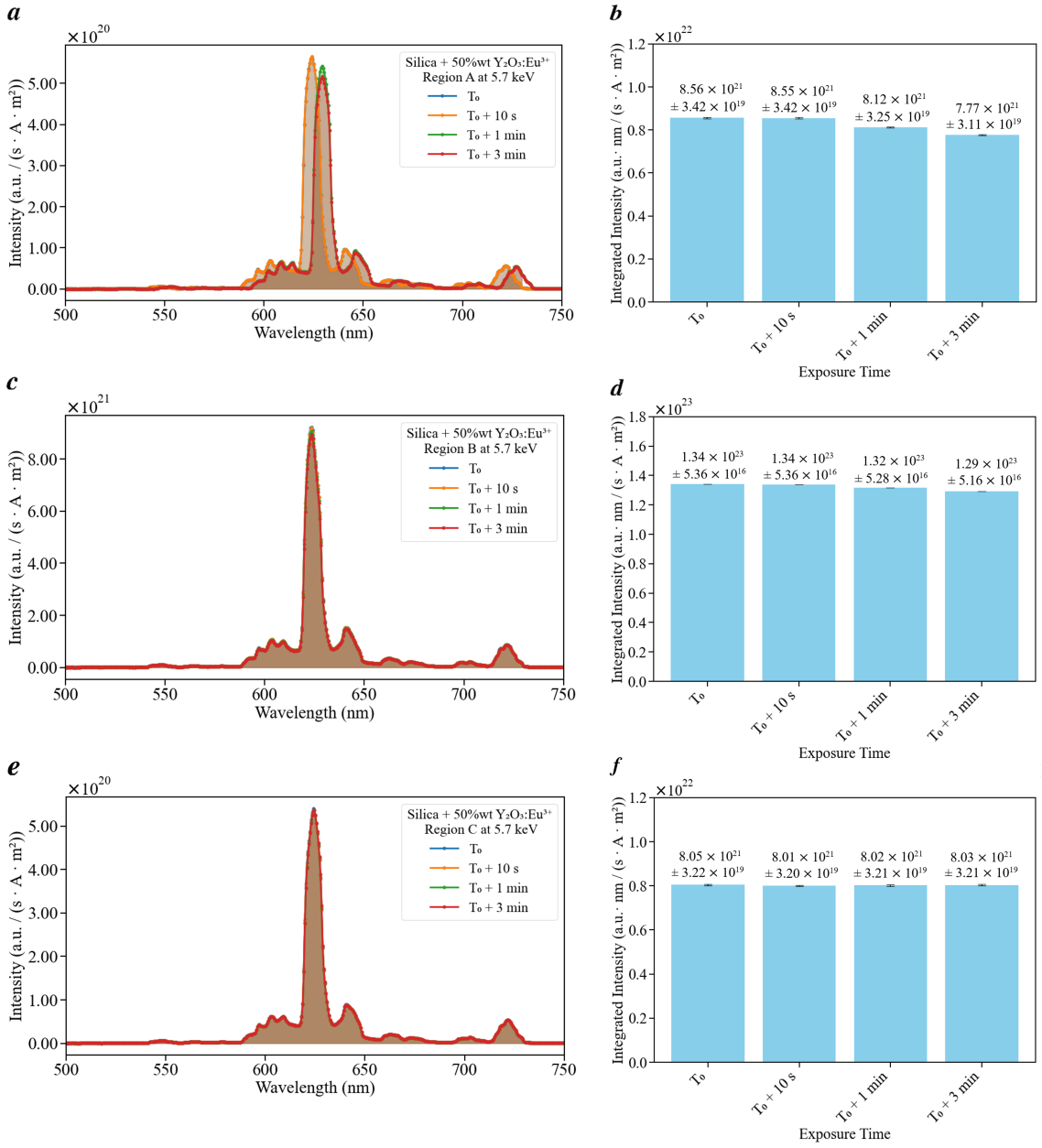

Figure 6.14: Emission behavior of a silica aerogel loaded with 50%wt Y_2O_3:Eu^{3+} under electron beam irradiation at 5.7 keV. ***a)*** Emission spectra in ROI A at different exposure times. ***b)*** Evolution of the integrated intensity over time in ROI A. ***c)*** Emission spectra in ROI B at different exposure times. ***d)*** Evolution of the integrated intensity over time in ROI B. ***e)*** Emission spectra in ROI C at different exposure times. ***f)*** Evolution of the integrated intensity over time in ROI C. The intensity is calculated using Equation 4.2.

By integrating the area under the curves of these spectra (integrated intensity), a slight decrease is observed in ROIs A and B (Figures 6.14b and 6.14d), which could indicate the aging of Y_2O_3:Eu^{3+} under the electron beam.

Figure 6.15 shows the results obtained for the CMC aerogel loaded with 50%wt Y_2O_3:Eu^{3+}.

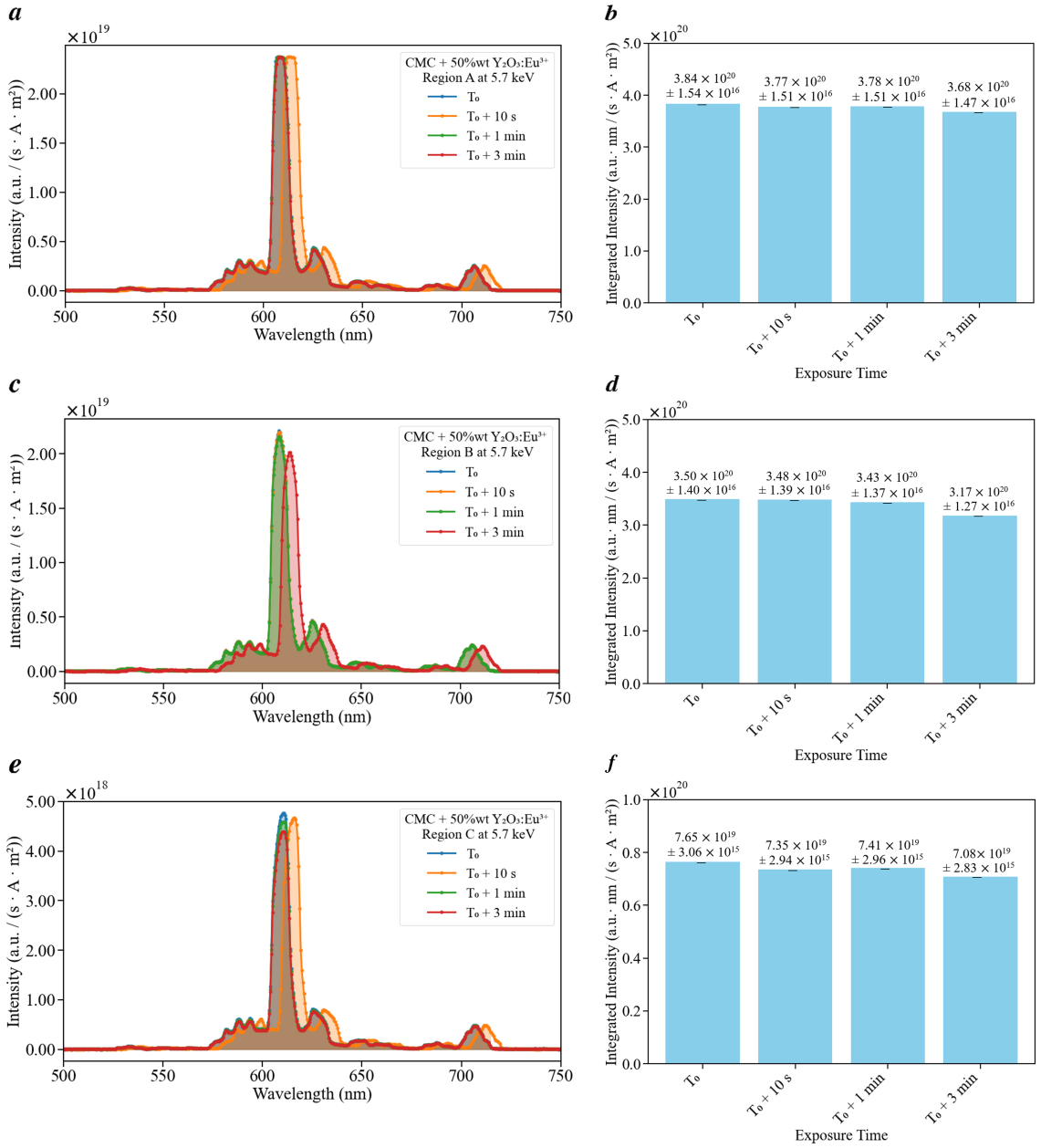

Figure 6.15: Emission behavior of a CMC aerogel loaded with 50%wt Y_2O_3:Eu^{3+} under electron beam irradiation at 5.7 keV. ***a)*** Emission spectra in ROI A at different exposure times. ***b)*** Evolution of the integrated intensity over time in ROI A. ***c)*** Emission spectra in ROI B at different exposure times. ***d)*** Evolution of the integrated intensity over time in ROI B. ***e)*** Emission spectra in ROI C at different exposure times. ***f)*** Evolution of the integrated intensity over time in ROI C. The intensity is calculated using Equation 4.2.

In all three ROIs, spectra are observed at certain exposure times showing a shift from 610

nm to 615 nm. This is particularly noticeable in ROI A at T_0 + 10 s (orange spectrum in Figure 6.15a), in ROI B at T_0 + 3 min (red spectrum in Figure 6.15c), and in ROI C at T_0 + 10 s (orange spectrum in Figure 6.15e). One might assume that the changes occurring in the structure of Y_2O_3:Eu^{3+} are irreversible and become noticeable after a certain exposure time, when sufficient charge accumulation has occurred and continues to increase. However, the fact that this shift appears, for example, at T_0 + 10 s, and then the peak shifts back to the left, potentially returning to its original position, is questionable. The magnitude of the redshift, 5 nm, is the same as that observed in the silica aerogel, which could suggest that it is an instrument-related error.

In all three ROIs analyzed, a slight decrease in spectral intensity is observed as exposure time to the electron beam increases, indicating aging of Y_2O_3:Eu^{3+}, as in silica aerogel.

In reality, the ROIs are not irradiated for 3 minutes continuously, since the electron beam performs a continuous raster scan so the beam only remains a few μs on each pixel. Taking this into account, let's try to determine the beta radiation dose received by this sample, CMC loaded with 50%wt of Y_2O_3:Eu^{3+}, which is the sample that shows the most interesting behavior in RL. To do this, let's begin by determining the number of incident electrons, N_e:

$$N_e = \frac{I_{beam}}{e} = \frac{103.00 \cdot 10^{-6}\ A}{1.602 \cdot 10^{-19}\ C} = 6.43 \cdot 10^{14}\ \text{electrons / s} \tag{6.1}$$

If the image is composed of 512×512 pixels and the time the electron beam spends on each pixel is 1 μs, the time, t_{scan}, that the electron beam takes to irradiate the entire region pixel by pixel is:

$$t_{scan} = N_{pix} \times t_{dwell} = (512)^2\ \text{pixels} \times 1 \cdot 10^{-6}\ s = 0.26\ s \tag{6.2}$$

Therefore, in 3 minutes (180 s), the electron beam scans the ROI n times, being:

$$n = \frac{180\ s}{0.26\ s} = 692 \tag{6.3}$$

Thus, the total accumulated exposure time per pixel, t_{pix}, is:

$$t_{pix} = t_{dwell} \times n = 1 \cdot 10^{-6}\ s \times 692 = 692\ \mu s \tag{6.4}$$

The number of incident electrons per pixel, $N_{e,pix}$, absorbed during these 3 minutes is:

$$N_{e,pix} = N_e \times t_{pix} = 6.43 \cdot 10^{14}\ \text{electrons / s} \times 692 \cdot 10^{-6}\ s = 4.45 \cdot 10^{11}\ \text{electrons} \tag{6.5}$$

Taking into account that the energy of each electron is $E_e = 5.7\ keV = 9.13 \cdot 10^{-16}$ J, it deposits an energy, E_{pix}, per pixel:

$$E_{pix} = N_{e,pix} \times E_e = 4.45 \cdot 10^{11}\ \text{electrons} \times 9.13 \cdot 10^{-16}\ J = 4.06 \cdot 10^{-4}\ J \tag{6.6}$$

Given that the ROI has a side length of 735 μm, the size of one pixel, l_{pix}, is given by:

$$l_{pix} = \frac{ROI}{N_{pix}} = \frac{735\ \mu m}{512\ pixels} = 1.44 \cdot 10^{-6}\ m \tag{6.7}$$

and considering that the penetration depth, d_{depth}, of the electron beam in a material with this composition is 1.8 μm (estimated via CASINO simulations), the irradiated volume per pixel, V_{pix}, can be estimated to (estimated since it is a pear-shaped interaction volume):

$$V_{pix} = (l_{pix})^2 \times d_{depth} = \left(1.44 \cdot 10^{-6}\ m\right)^2 \times 1.8 \cdot 10^{-6}\ m = 3.73 \cdot 10^{-18}\ m^3 \tag{6.8}$$

The virtual mass of a voxel, m_{pix}, corresponding to the irradiated volume can be calculated using the experimental density of the aerogel loaded with luminescent materials, ρ = 0.8 g/cm^3:

$$m_{pix} = V_{pix} \times \rho = 3.73 \cdot 10^{-18}\ m^3 \times 800\ kg/m^3 = 2.99 \cdot 10^{-15}\ kg \tag{6.9}$$

Thus, the absorbed dose deposited in a single pixel is:

$$Dose_{pix} = \frac{E_{pix}}{m_{pix}} = \frac{4.06 \cdot 10^{-4}\ J}{2.99 \cdot 10^{-15}\ kg} = 1.36 \cdot 10^{11}\ Gy \tag{6.10}$$

To calculate the absorbed dose deposited in the complete volume of the aerogel, it is first necessary to determine the total energy, E_{total}, deposited in that volume (but this is an approximation, as the electron beam does not penetrate the entire volume):

$$E_{total} = E_{pix} \times N_{pix} = 4.06 \cdot 10^{-4}\ J \times (512)^2\ pixels = 1.06 \cdot 10^{2}\ J \tag{6.11}$$

so that the total absorbed dose deposited in that mass, m_{vol}:

$$m_{vol} = m_{pix} \times N_{pix} = 2.99 \cdot 10^{-15}\ kg \times (512)^2 = 7.84 \cdot 10^{-10}\ kg \tag{6.12}$$

is:

$$Dose_{total} = \frac{E_{total}}{m_{vol}} = \frac{1.06 \cdot 10^{2}\ J}{7.84 \cdot 10^{-10}\ kg} = 1.35 \cdot 10^{11}\ Gy \tag{6.13}$$

It is possible to compare the absorbed dose in CL with the absorbed dose in RL, and to estimate what duration of exposure in RL would correspond to 3 minutes of exposure in CL. In this way, these CL-based aging simulations can be related to the behavior of the material after prolonged exposure to tritium.

From the absorbed dose, the dose rate in CL is:

$$Rate_{CL} = \frac{1.35 \cdot 10^{11}\ Gy}{180\ s} = 7.50 \cdot 10^{8}\ Gy\ /\ s \tag{6.14}$$

Now let us determine the dose rate in RL. To do so, note that the volumetric tritium activity is 2.55 $\mathrm{Ci}/(\mathrm{mL}\cdot\mathrm{bar})$, the isotopic purity of the source is 85%, and the volume of the aerogel is 0.07 mL but the interacting volume would be:

$$\begin{aligned}\left(S_{BET}\times d_{\text{depth}}\right)\times m_{\text{total}} &= \left(2.5\cdot 10^{-1}\,\mathrm{m^2/g}\times 1.8\cdot 10^{-6}\ \mathrm{m}\right)\times 5.8\cdot 10^{-5}\ \mathrm{kg}\\ &= 2.61\cdot 10^{-8}\ \mathrm{m^3} = 2.61\cdot 10^{-2}\ \mathrm{mL}\end{aligned} \tag{6.15}$$

where S_{BET} is the surface accesible to tritum gas (and thus to electrons), aproximated from the experimental value from gas adsorption and desorption measurements when exposing the sample to nitrogen gas (it will be explained in the next section, see Figure 6.25c); d_{depth} is the penetration depth of electrons in this material that has been previously estimated via CASINO simulations (already mentioned) and m_{total} is the total mass of the sample, which is equal to 58 mg.

Now, supposing that the dose rate is to be found for the aerogel exposed to a tritium atmosphere at a constant pressure of 400 mbar, the total tritium activity is given by:

$$\begin{aligned}\mathrm{A_{total}} &= 2.55\ \mathrm{Ci}/(\mathrm{mL}\cdot\mathrm{bar})\times 85\%\times 2.61\cdot 10^{-2}\ \mathrm{mL}\times 0.4\ \mathrm{bar} =\\ &= 2.23\cdot 10^{-2}\ \mathrm{Ci} = 8.37\cdot 10^{8}\ \mathrm{Bq}\end{aligned} \tag{6.16}$$

which is Equation 3.7, already shown in chapter 3. For tritium, each decay emits one electron, so $\mathrm{A_{total}}$ is also the number of electrons emitted per second. Since the mean energy of the electrons emitted by tritium is 5.7 keV ($9.13\cdot 10^{-16}$ J), the dose rate for this tritium atmosphere would be:

$$\mathrm{Rate_{RL}} = \frac{\mathrm{A_{total}}\times\langle \mathrm{E}\rangle}{\mathrm{m_{total}}} = \frac{8.37\cdot 10^{8}\ \text{electrons / s}\times 9.13\cdot 10^{-16}\ \mathrm{J}}{5.8\cdot 10^{-5}\ \mathrm{kg}} = 1.32\cdot 10^{-2}\ \mathrm{Gy\ /\ s} \tag{6.17}$$

If the equivalent dose is $1.35\cdot 10^{11}$Gy, the exposure time to this tritium atmosphere would be:

$$\mathrm{t_{RL}} = \frac{1.35\cdot 10^{11}\ \mathrm{Gy}}{1.32\cdot 10^{-2}\ \mathrm{Gy/s}} \approx 324\,000\ \text{years} \tag{6.18}$$

These CL experiments therefore make it possible to simulate the aging of an aerogel under a tritium gas atmosphere at a constant pressure of 400 mbar for a period equivalent to 324 000 years.

Caution must be taken with this estimation made in CL since:

- Excitation in CL occurs very locally and not throughout the entire volume of the aerogel as it does in RL.
- The interaction volume in CL has been approximated as a cube determined by: the surface area measured experimentally by exposing the aerogel to gaseous nitrogen

(which may have different affinity with the aerogel than tritium does); and by the penetration depth determined through CASINO simulations.

- The measurement of the number of incident electrons in CL is actually performed at the electron beam column, not at the sample level.

In the case of the CMC aerogel loaded with 50%wt Y_2O_3:Eu^{3+} (Figure 6.15), a decrease in light intensity of 4.2% in ROI A, 9.4% in ROI B, and 7.4% in ROI C is observed after what would correspond to a simulated exposure to tritium for over 324 000 years. In comparison, the silica aerogel loaded with 50%wt Y_2O_3:Eu^{3+} (Figure 6.14) showed a decrease of 9.2% in ROI A, 3.7% in ROI B, and 0.3% in ROI C.

Figure 6.16 shows the behavior of a silica aerogel with 0.3%wt YVO_4:Eu^{3+}, where it can be observed that in ROIs B and C (Figures 6.16c and 6.16e, respectively), the expected peak at 624 nm increases in intensity over time, while the peak at 450 nm, likely corresponding to sodium citrate ligands, decreases with increased exposure to the electron beam. This supports the hypothesis that it is the ligands that do not withstand radiation, whereas the YVO_4:Eu^{3+} nanoparticles do. It is true that this behavior is not observed in ROI A (Figures 6.16a); in fact, the opposite trend is seen there. Additional measurements would be needed to confirm these results.

As for the CMC aerogels with 0.3%wt YVO_4:Eu^{3+} (Figure 6.17), their behavior is quite different from that observed with the silica aerogel containing the same luminescent materials. In this case, the emission attributed to the ligands slightly increases over time in all three ROIs, along with the emission peak at 617 nm. However, the 617 nm peak slightly increases only in ROI A (Figure 6.17a).

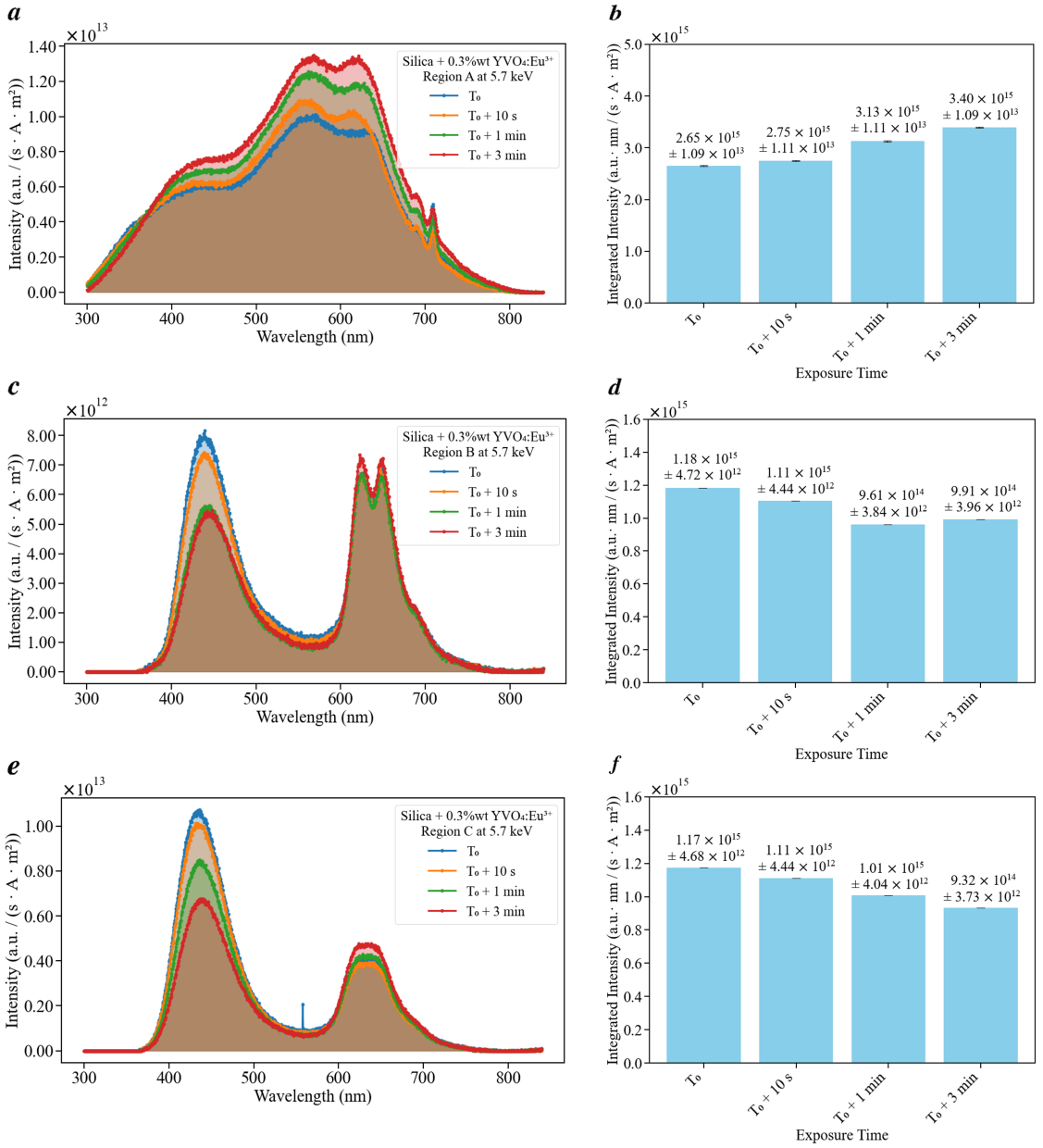

Figure 6.16: Emission behavior of a silica aerogel loaded with 0.3%wt $YVO_4:Eu^{3+}$ under electron beam irradiation at 5.7 keV. ***a)*** Emission spectra in ROI A at different exposure times. ***b)*** Evolution of the integrated intensity over time in ROI A. ***c)*** Emission spectra in ROI B at different exposure times. ***d)*** Evolution of the integrated intensity over time in ROI B. ***e)*** Emission spectra in ROI C at different exposure times. ***f)*** Evolution of the integrated intensity over time in ROI C. The intensity is calculated using Equation 4.2.

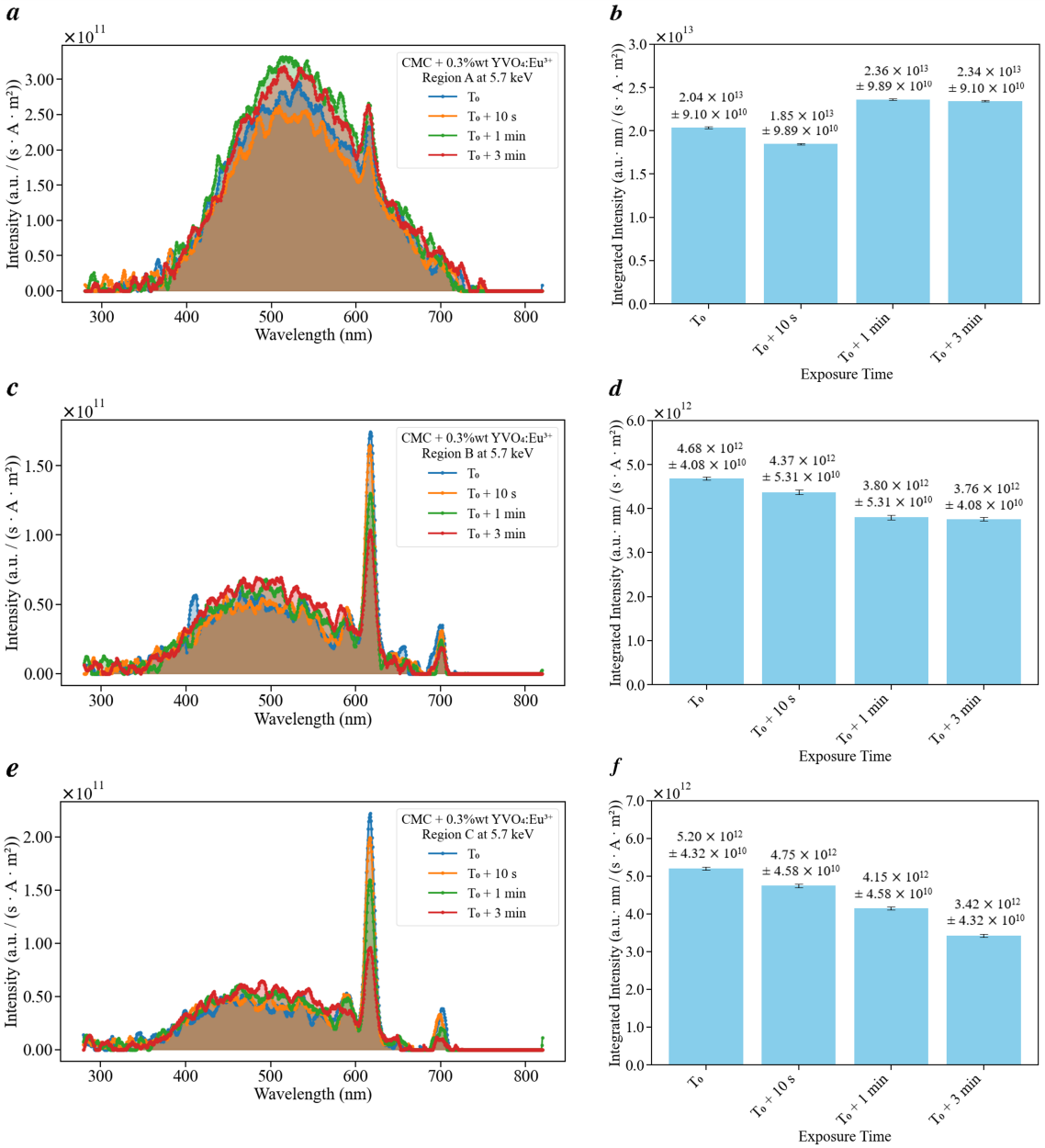

Figure 6.17: Emission behavior of a CMC aerogel loaded with 0.3%wt YVO_4:Eu^{3+} under electron beam irradiation at 5.7 keV. ***a)*** Emission spectra in ROI A at different exposure times. ***b)*** Evolution of the integrated intensity over time in ROI A. ***c)*** Emission spectra in ROI B at different exposure times. ***d)*** Evolution of the integrated intensity over time in ROI B. ***e)*** Emission spectra in ROI C at different exposure times. ***f)*** Evolution of the integrated intensity over time in ROI C. The intensity is calculated using Equation 4.2.

Finally, other samples are exposed for a longer duration to the electron beam, at T_0 + 1 h, in order to study aging over an even longer period, and under a more intense electron beam of 10 keV. Based on the previously carried out calculations, these conditions simulate the

aging that would occur in RL after 570 000 years.

Figure 6.18 shows images taken with the electron microscope before and after exposing a CMC aerogel loaded with 16%wt $AgInS_2$ to the electron beam for one hour.

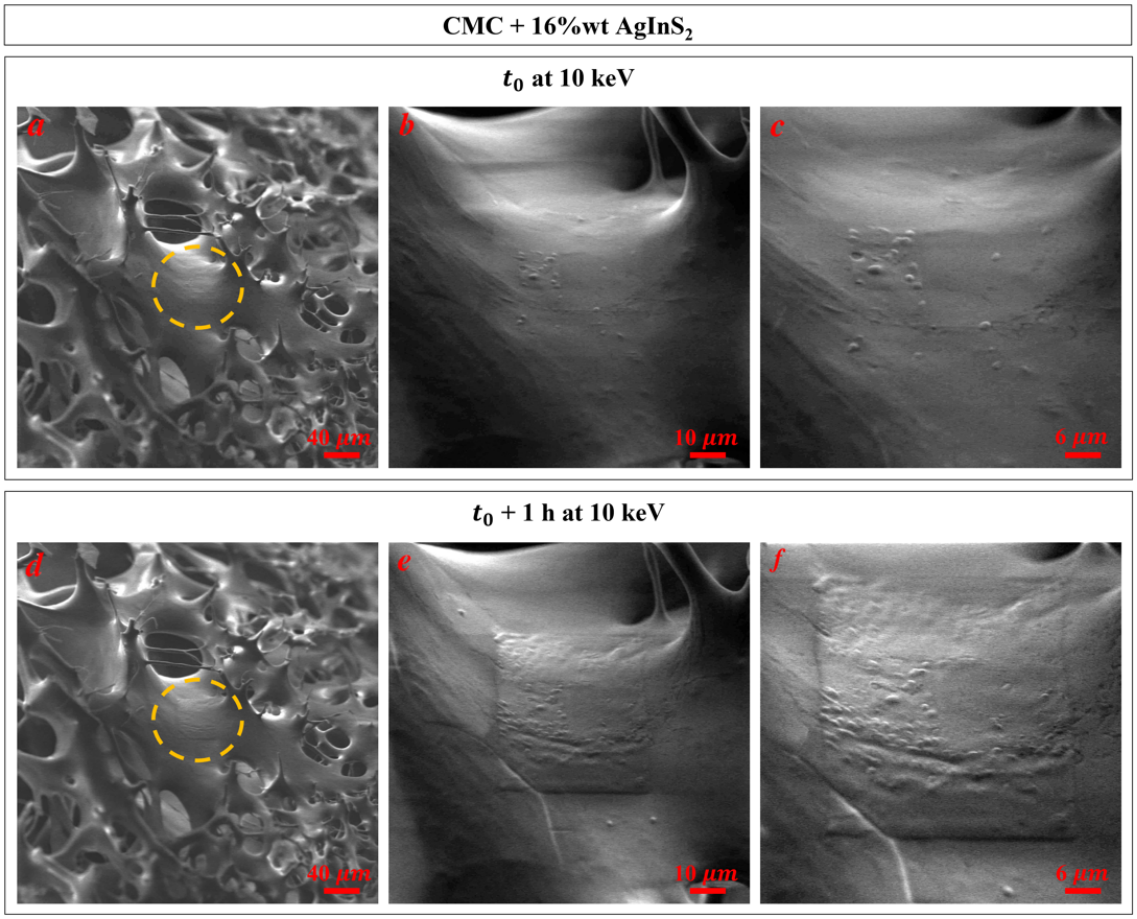

Figure 6.18: Electron microscope images of the same ROI of a CMC aerogel loaded with $AgInS_2$ at a concentration of 16%wt ***a)*** before irradiation, with a Reference Field of View (RFoV) of 400 μm; ***b)*** before irradiation, with a RFoV of 100 μm; ***c)*** before irradiation, with a RFoV of 60 μm; ***d)*** after 1 hour of irradiation, with a RFoV of 400 μm; ***e)*** after 1 hour of irradiation, with a RFoV of 100 μm; and ***f)*** after 1 hour of irradiation, with a RFoV of 60 μm.

It can be observed that the path of the electron beam, traced pixel by pixel, has been imprinted, and the radiation appears to have created bubble-like features on the surface of the aerogel. Some of the bubbles, already visible in the images taken before exposure, began to appear very quickly, within the few seconds it takes to configure the mapping and launch it. The appearance of bubbles in CL has already been reported in the literature, and it seems to be related to the effect of radiolysis [142]. In this case, it could be the radiolysis of residual water (since no other solvents have been used), which produces reactive radicals

that recombine to generate molecular hydrogen and oxygen gases, potentially responsible for the observed bubble formation.

This time, the same experiment is carried out using a CMC aerogel loaded with 50%wt Y_2O_3:Eu^{3+}. However, due to cartography configuration limitations, a single one-hour mapping cannot be performed, so three 25-minute mappings are conducted instead.

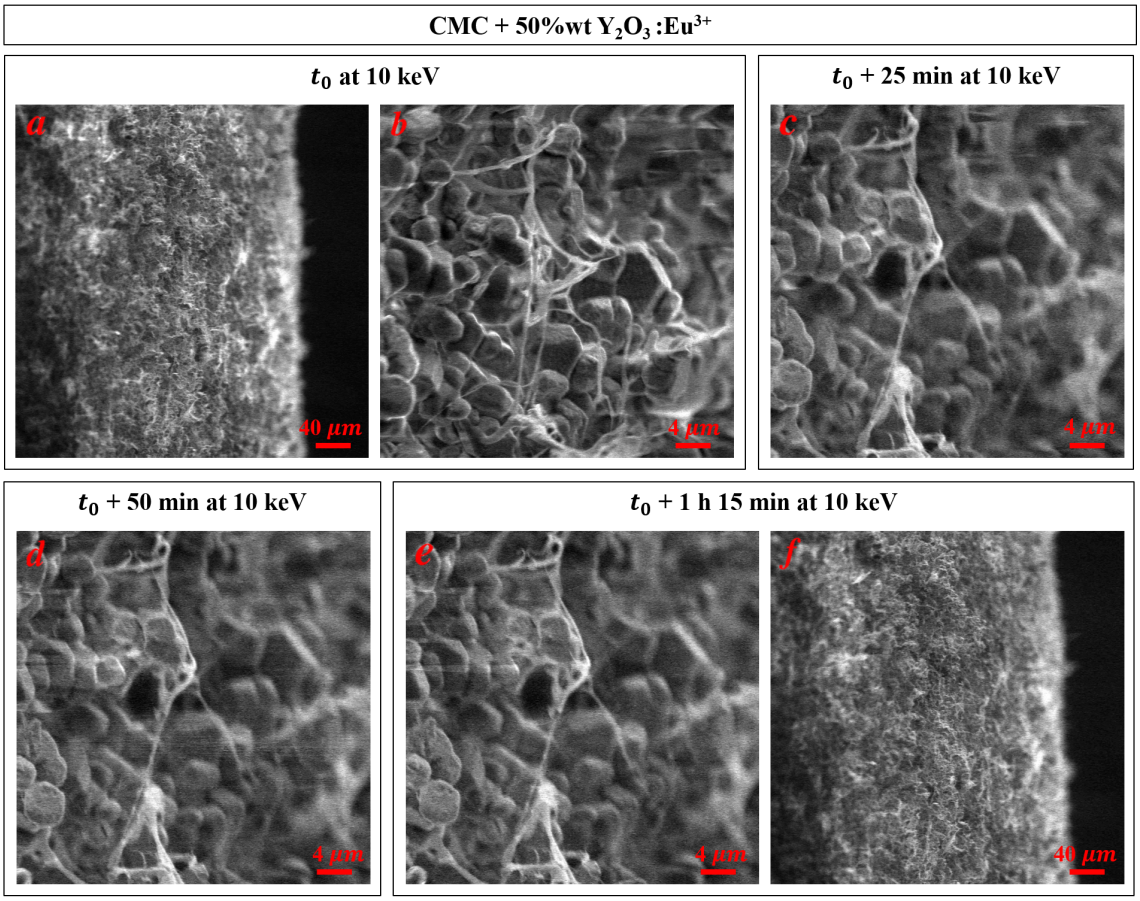

Figure 6.19: Electron microscope images of the same ROI of a CMC aerogel loaded with 50%wt Y_2O_3:Eu^{3+} ***a)*** before irradiation, with a RFoV of 400 μm; ***b)*** before irradiation, with a RFoV of 40 μm; ***c)*** after 25 minutes of irradiation, with a RFoV of 40 μm; ***d)*** after 50 minutes of irradiation, with a RFoV of 40 μm; ***e)*** after 1 hour and 15 minutes of irradiation, with a RFoV of 40 μm; and ***f)*** after 1 hour and 15 minutes of irradiation, with a RFoV of 400 μm.

In Figure 6.19, images taken with the scanning electron microscope are shown before exposure to the electron beam and after each mapping. In Figure 6.19b, before launching the first mapping, Y_2O_3:Eu^{3+} microparticles can be observed along with a web-like structure that likely corresponds to the CMC fibers. After the first 25-minute mapping (Figure 6.19c), the CMC fibers appear to have partially collapsed, forming a thin, sticky membrane-like structure covering the Y_2O_3:Eu^{3+} particles, likely as a result of polymer

network degradation. The luminescent particles do not appear to have undergone any changes, as the same distribution is still observed. After the second mapping, no further changes are observed, the CMC fibers appear the same as after the first mapping. Finally, after the third and last mapping, the region still shows the same appearance, meaning that degradation of the CMC structure occurred only during the first 25 minutes of irradiation, but the structure then seems to have remained stable. When zooming in at 400 μm (Figure 6.19f), no modifications are observed in the aerogel structure compared to the image taken initially (Figure 6.19a), before exposure to the electron beam.

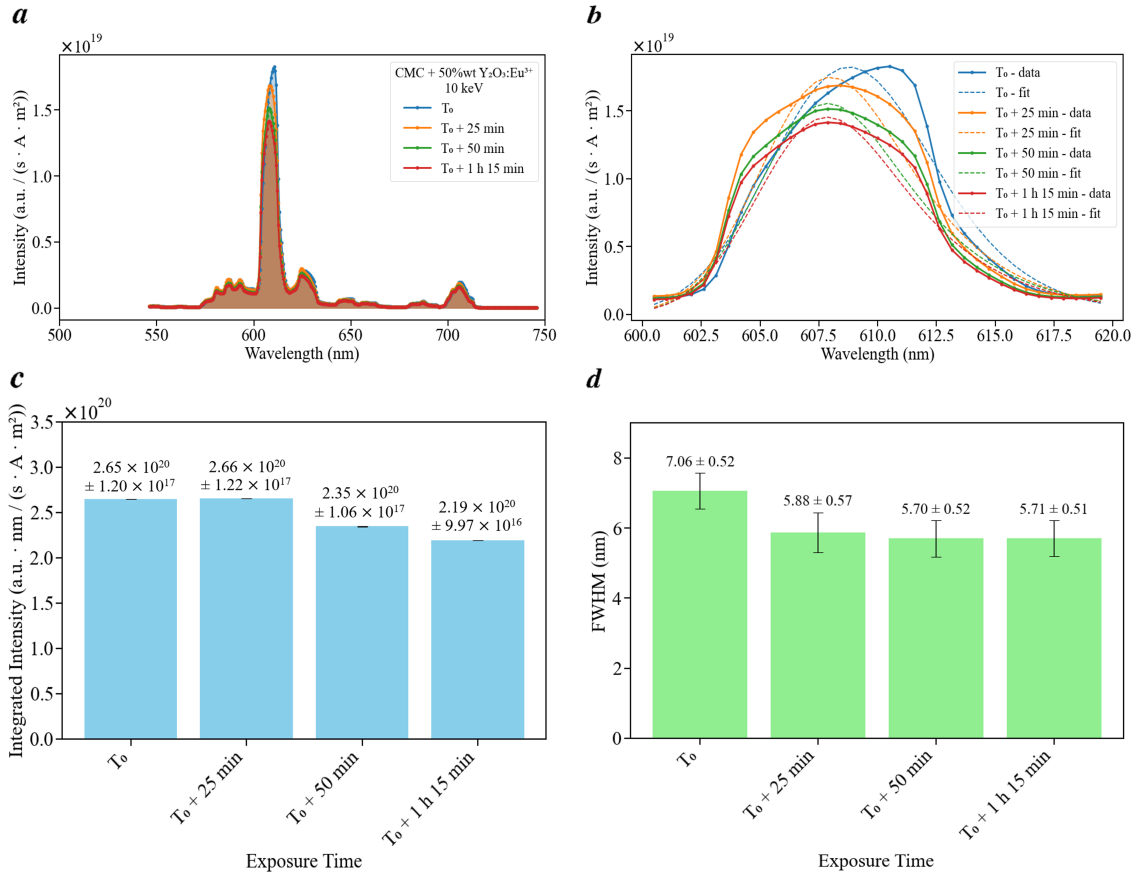

Figure 6.20: Emission behavior of a CMC aerogel loaded with 50%wt Y_2O_3:Eu^{3+} under electron beam irradiation at 10 keV. ***a)*** Emission spectra at different exposure times. ***b)*** Fit of the peaks at 610 nm using a skewed gaussian. ***c)*** Evolution of the integrated intensity over time. ***d)*** Evolution of the FWHM over time. The intensity is calculated using Equation 4.2.

At the end of each mapping, a spectrum is recorded to evaluate potential aging effects induced by electron beam irradiation. Figure 6.20a presents the superimposed spectra, showing that the dominant emission peak remains centered at 610 nm, with no observable redshift across the different mappings. The area under each curve is calculated to obtain the

integrated intensity, which is plotted as a function of exposure time in Figure 6.20c. The results indicate that the integrated intensity remains unchanged after the first 25-minute mapping, but decreases progressively after the second and third mappings. After a total irradiation time of 1 hour and 15 minutes, the integrated intensity shows a reduction of 17.4%.

To further analyze the emission peak, a fit is performed using skewed Gaussian functions (Figure 6.20b) to better account for the asymmetric peak shape, although the fit still shows noticeable deviations from the experimental data. The Full Width at Half Maximum (FWHM) is extracted to assess potential changes in the crystalline structure of Y_2O_3:Eu^{3+}. The FWHM values, presented in Figure 6.20d, show a slight decrease after the first exposure to the electron beam, although not significant enough to clearly indicate structural change. After the second and third mappings, no further variation is observed within the estimated error margin, suggesting that the crystalline structure of Y_2O_3:Eu^{3+} remains stable under continued electron beam exposure.

6.1.3 Three-Dimensional Characterization via Gas Adsorption and Desorption Measurements

Gas adsorption and desorption measurements provide insight into the porosity and surface properties of the aerogels. In this work, nitrogen adsorption and desorption measurements at 77 K are employed to evaluate the isotherm shapes, specific surface area, pore volume, and pore size distribution of the samples. The analyses are conducted using aerogel disks, which are used to fill approximately two-thirds of the volume of the sample cells, as described in section 3.5.1.3.4 of chapter 3.

6.1.3.1 Adsorption/Desorption Isotherms

Let us begin by analyzing the resulting isotherms, which are shown in Figure 6.21. At first glance, it can be observed that the aerogels containing YVO_4:Eu^{3+} nanoparticles have, regardless of the host matrix, adsorbed more gas than those aerogels whose composition includes micrometric Y_2O_3:Eu^{3+} particles. The silica aerogels with nanometric YVO_4:Eu^{3+} particles show the highest amount of absorbed nitrogen, followed by the silica aerogels with micrometric Y_2O_3:Eu^{3+} particles, then the CMC aerogels with nanometric YVO_4:Eu^{3+} particles, and finally, the CMC aerogels with micrometric Y_2O_3:Eu^{3+} particles.

For the silica aerogels, regardless of whether they contain micrometric Y_2O_3:Eu^{3+} particles or nanometric ones, the isotherms exhibit a type IV(a) shape with H1-type hysteresis

loops, according to the IUPAC classification illustrated in Figures 3.26 and 3.27, found in chapter 3. This behavior is typical of mesoporous materials with cylindrical, open-ended pores larger than 4 nm in diameter. The observed hysteresis loops arise from capillary condensation: nitrogen condenses in the pores at a higher relative pressure during adsorption than it evaporates during desorption, resulting in the characteristic delay of the desorption branch relative to adsorption. Such isotherms and hysteresis loops have already been reported in the literature for silica-based materials [143, 144].

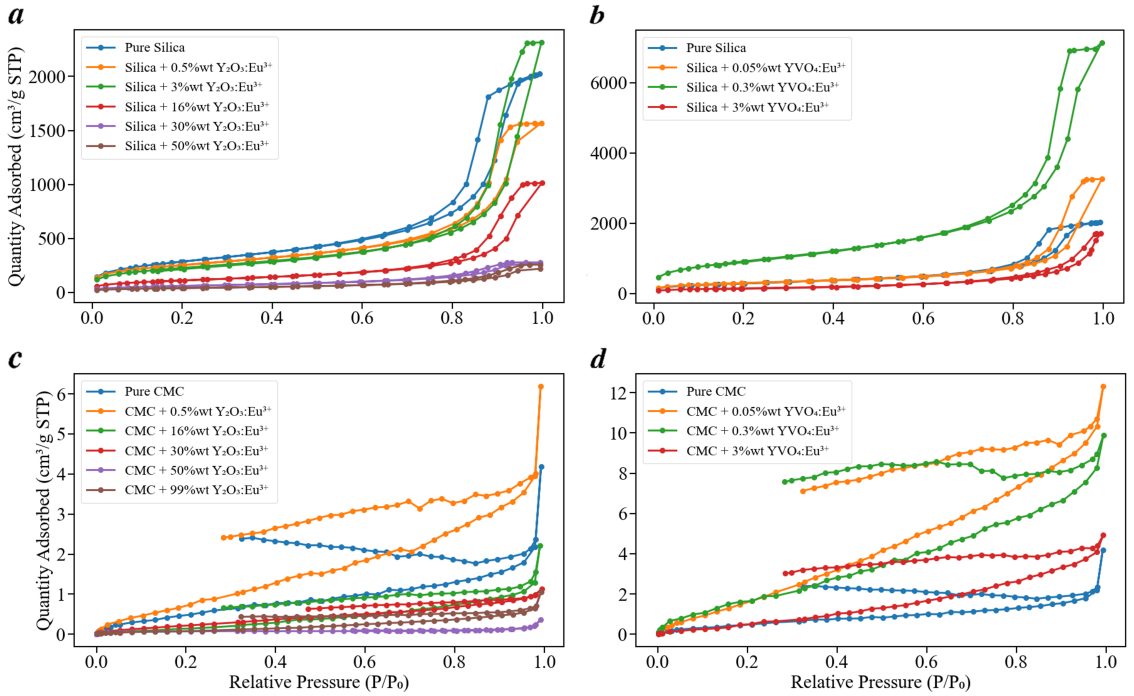

Figure 6.21: Adsorption and desorption isotherms for ***a)*** silica aerogels containing micrometric Y_2O_3:Eu^{3+} particles, ***b)*** silica aerogels containing nanometric YVO_4:Eu^{3+} particles, ***c)*** CMC aerogels containing micrometric Y_2O_3:Eu^{3+} particles, and ***d)*** CMC aerogels containing nanometric YVO_4:Eu^{3+} particles.

In contrast, the CMC-based aerogels display isotherms whose shapes do not correspond to any of the standard IUPAC isotherm types. Notably, the desorption branch does not overlap with the adsorption branch at low relative pressures; instead, the gap between the two branches widens, with the desorption curve diverging even further from the adsorption curve. This atypical, “open” hysteresis is indicative of different adsorption mechanisms and pore structures compared to silica host matrices.

Based on the reported literature, several hypotheses may account for this unusual behavior:

- Structural rearrangements of the CMC polymer chains could play a significant role.

While this mechanism has been clearly demonstrated for water sorption in cellulose-like materials, it is plausible that similar reorganization of the polymer network occurs during nitrogen adsorption and desorption in CMC, potentially leading to persistent metastable states and non-overlapping isotherm branches [145].

- Irregularities in pore geometry, such as corrugation (ridged surface), bottlenecks, or interconnected networks, can profoundly alter the mechanisms of capillary condensation and evaporation, resulting in significant changes to the hysteresis cycle. In such cases, desorption may be delayed (as experimentally observed for silica aerogels) or even blocked, preventing the desorption branch from rejoining the adsorption branch. Both modeling and experimental studies [144] have shown that even minor deviations from ideal pore shapes can significantly modify the hysteresis loop. It is important to note that the degree of pore irregularity can vary depending on the synthesis method followed.

- In flexible porous materials the interplay between adsorption and the mechanical deformation of the matrix may result in the trapping of nitrogen molecules within metastable domains during desorption. This coupling leads to unusually wide or even open hysteresis loops, a phenomenon that has been demonstrated both theoretically and experimentally for nitrogen and other gases in certain polymers [146, 147].

- Experimental evidence suggests that CMC-based aerogels are more likely to form layered, slit-shaped pores rather than the cylindrical pores assumed in the BET model, further contributing to the atypical hysteresis loops.

To better interpret these isotherms, the theoretical adsorption process described in the literature and illustrated in Figure 6.22 will be referenced. Although this representation has been obtained by exposing a sample to water vapor, the various steps involved in the exposure to different gases, such as nitrogen, are essentially the same.

For all samples analyzed, the low-pressure region ($P/P_0 < 0.05$, region E) shows a convex isotherm, which corresponds to the filling of the highest-energy adsorption sites on the surface. These are typically micropores and surface defects or corners, where nitrogen molecules can interact with several surface atoms simultaneously. In the subsequent region ($0.05 < P/P_0 < 0.3$, region D), monolayer adsorption dominates, associated with capillary condensation in the smallest mesopores or micropores. In our samples, this regime appears to end earlier, around $P/P_0 \approx 0.2$ for silica aerogels and even sooner for CMC-based aerogels. Region C ($0.3 < P/P_0 < 0.7$) corresponds to the multilayer adsorption region,

where the slope of the isotherm reflects the number of nitrogen layers formed, as described by the BET model.

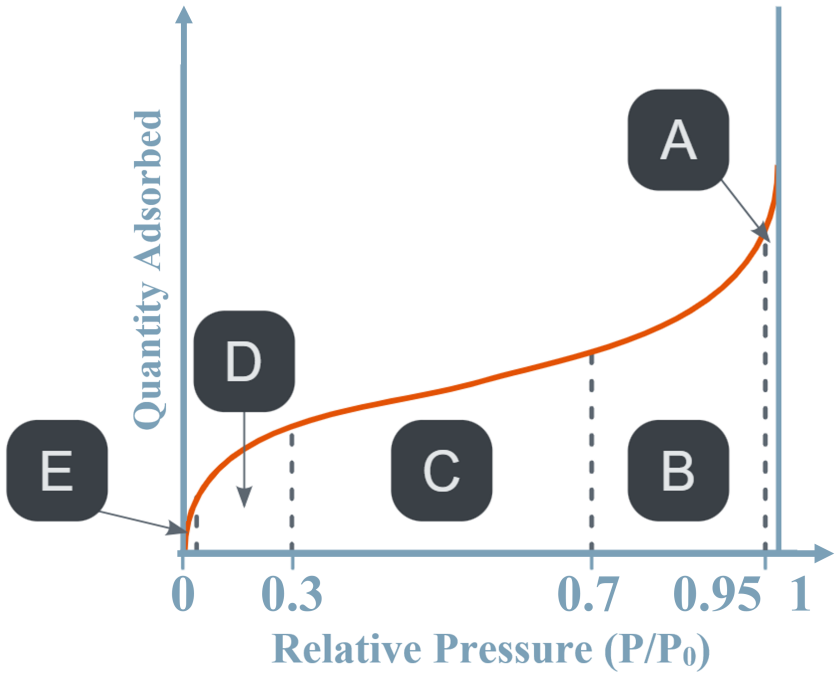

Figure 6.22: The different regions of an adsorption isotherm. Figure adapted from [148].

The influence of the luminescent particles and their concentration is particularly evident in this multilayer region:

- For silica aerogels with micrometric Y_2O_3:Eu^{3+}, the addition of particles generally decreases the amount of nitrogen adsorbed (i.e., the slope in the multilayer region drops).

- For silica aerogels with nanometric YVO_4:Eu^{3+}, the introduction of nanoparticles leads to a marked increase in multilayer adsorption, especially at 0.05% and 0.3% mass concentrations. At the highest concentration (3%wt), the amount of nitrogen adsorbed drops below that of pure silica, indicating possible pore blockage and/or aggregation of nanoparticles (because the surfaces of nanoparticles that are in contact with each other are no longer accessible to the gas).

- In CMC aerogels with micrometric Y_2O_3:Eu^{3+}, the highest multilayer adsorption occurs at the lowest particle loading (0.5%wt), then decreases with increasing concentration, eventually falling below the value for pure CMC.

- For CMC with nanometric YVO_4:Eu^{3+}, all concentrations yield higher nitrogen adsorption than pure CMC, with a maximum at 0.05%wt and a gradual decrease at higher concentrations, though still above the pure CMC matrix.

Region B ($0.7 < P/P_0 < 0.95$) is dominated by capillary condensation in mesopores, and some trends can be identified:

- In silica aerogels with micrometric Y_2O_3:Eu^{3+}, this region reveals a pronounced mesoporous character. The capillary condensation in mesopores decreases with the concentration of luminescent particles, except at a mass concentration of 3%, where an increase is observed, suggesting a pore structure that favors nitrogen uptake at this specific loading.

- For silica aerogels doped with YVO_4:Eu^{3+} nanoparticles, a dramatic increase in nitrogen uptake is observed at 0.05%wt and 0.3%wt, even surpassing pure silica, which points to enhanced mesoporosity. However, at the highest concentration (3%wt), the adsorption capacity drops below that of pure silica.

- CMC-based aerogels with Y_2O_3:Eu^{3+} microparticles show a moderate nitrogen uptake compared to silica aerogels. The addition of a small amount of microparticles (0.5%wt) increases nitrogen adsorption relative to pure CMC, suggesting the creation or preservation of mesopores.

- CMC-based aerogels doped with YVO_4:Eu^{3+} nanoparticles display all of them higher nitrogen uptake than pure CMC, with the 0.05%wt sample achieving the greatest capacity. As the nanoparticle concentration increases, the adsorption capacity gradually decreases.

The last region A ($0.95 < P/P_0 < 1$) corresponds to the filling of macropores. At P/P_0 approaching 1, all accessible pores are essentially filled with condensed nitrogen, and any further increase in adsorbed volume is mostly due to the condensation of nitrogen in the free space of the measurement cell, which is not related to the material's porosity. Therefore, data in this region are generally not used for quantitative analysis because they are affected by non-porous volume and experimental artifacts.

6.1.3.2 BET Surface Area Determination

Figure 6.23 shows the BET plots for all samples to verify the presence of a linear region before applying the model. For the silica aerogels, these plots display a clear and well-defined linear region, consistent with the presence of cylindrical mesopores as assumed in

the BET theory. This strong linearity confirms the suitability of the BET model for these samples. In contrast, the CMC-based aerogels exhibit a less pronounced linear region, with deviations. This may suggest that the pore structure in CMC aerogels deviates from the cylindrical geometry assumed by the BET model, likely tending toward slit-shaped pores as also observed experimentally by CL.

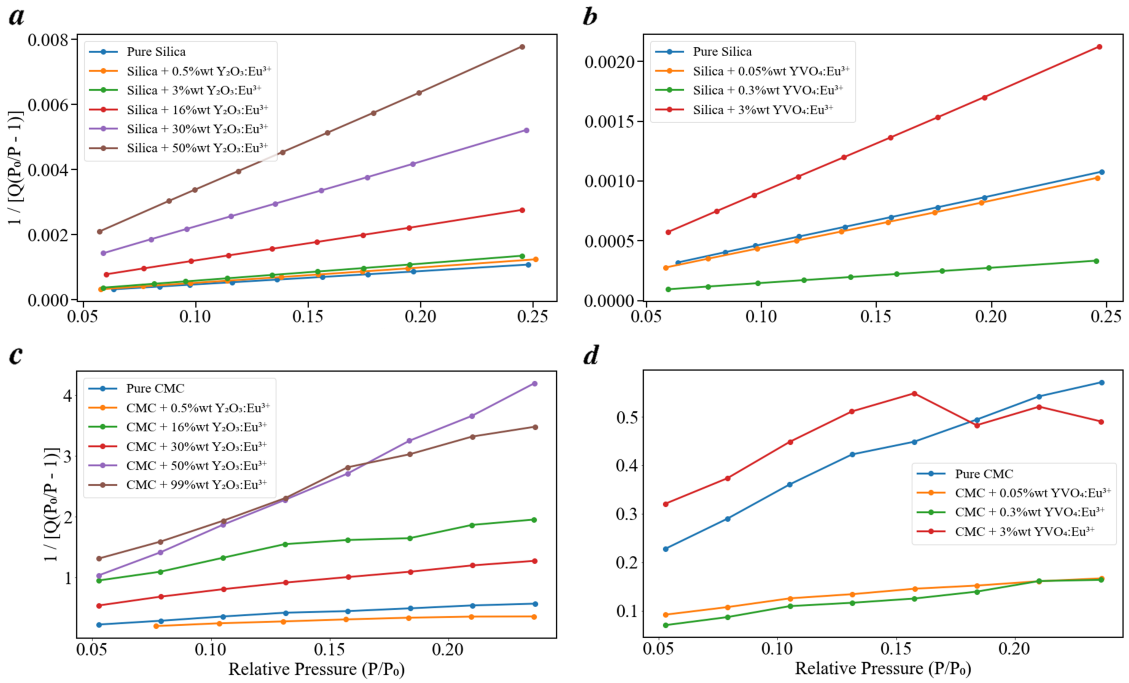

Figure 6.23: The variable $1/[Q(P_0/P-1)]$ as a function of the relative pressure in the range $0.05 < P/P_0 < 0.25$ for ***a)*** silica aerogels containing micrometric Y_2O_3:Eu^{3+} particles, ***b)*** silica aerogels containing nanometric YVO_4:Eu^{3+} particles, ***c)*** CMC aerogels containing micrometric Y_2O_3:Eu^{3+} particles, and ***d)*** CMC aerogels containing nanometric YVO_4:Eu^{3+} particles.

Another way to verify the validity of the results obtained from the adsorption and desorption measurements is by checking the value of the constant C. As shown in Figure 6.24, the values of the constant C for both the CMC and silica aerogels are positive, with those of the silica aerogels being higher than those of the CMC aerogels regardless of the luminescent materials present. The higher C constant in the silica aerogels indicates that the interactions between gaseous nitrogen and the aerogel are stronger than those in the CMC aerogels.

For silica aerogels, as previously mentioned, the isotherm corresponds to type IV(a) due to the presence of a hysteresis loop; however, the adsorption branch closely resembles that of a type II isotherm. For the CMC aerogels, the isotherm does not match any of the standard IUPAC types, but if it were to resemble any, it would be type III.

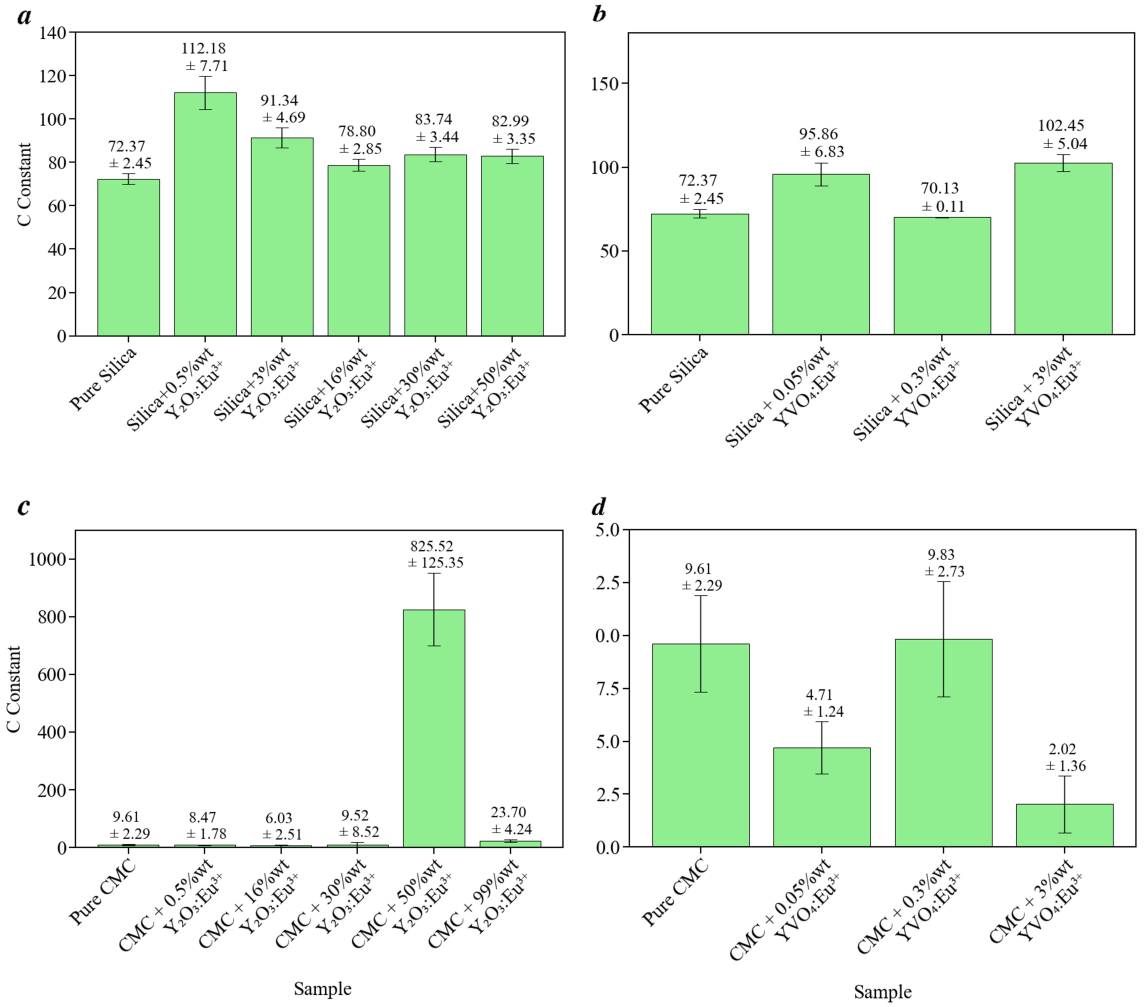

Figure 6.24: C constant value for ***a)*** silica aerogels containing micrometric Y_2O_3:Eu^{3+} particles, ***b)*** silica aerogels containing nanometric YVO_4:Eu^{3+} particles, ***c)*** CMC aerogels containing micrometric Y_2O_3:Eu^{3+} particles, and ***d)*** CMC aerogels containing nanometric YVO_4:Eu^{3+} particles.

The value of the constant C in the case of the CMC aerogel loaded with 50%wt Y_2O_3:Eu^{3+} is striking, showing a very high value of 825 compared to values between 2 and 23 for all other CMC aerogels, whether loaded with Y_2O_3:Eu^{3+} or YVO_4:Eu^{3+}.

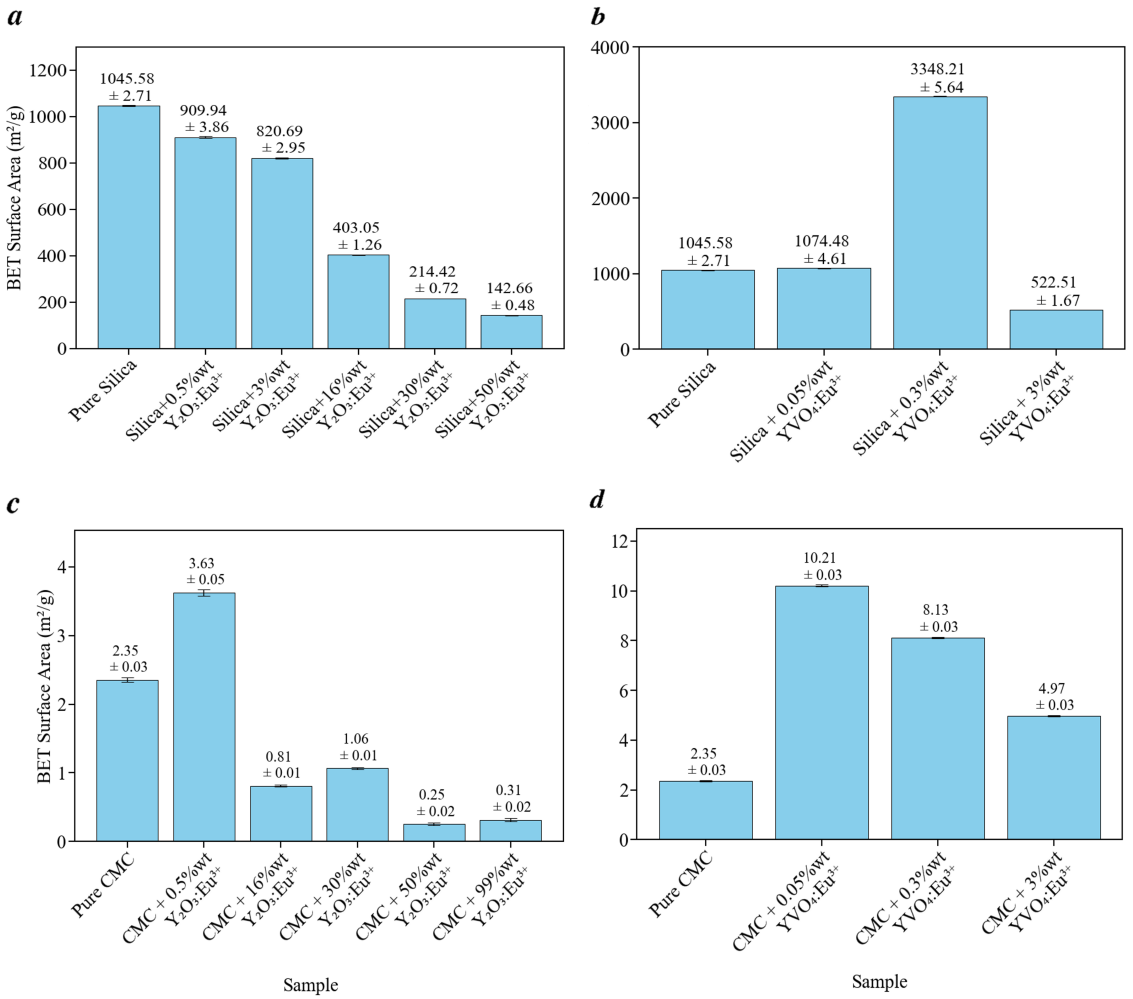

Figure 6.25: BET surface area values for ***a)*** silica aerogels containing micrometric Y_2O_3:Eu^{3+} particles, ***b)*** silica aerogels containing nanometric YVO_4:Eu^{3+} particles, ***c)*** CMC aerogels containing micrometric Y_2O_3:Eu^{3+} particles, and ***d)*** CMC aerogels containing nanometric YVO_4:Eu^{3+} particles.

As for the values obtained for the BET surface area, these are shown in Figure 6.25.

The results show that the BET surface area is greater in the aerogels that contain YVO_4:Eu^{3+} nanoparticles. In most cases, the BET surface area is proportional to the total quantity of nitrogen adsorbed, indicating that adsorption predominantly occurs in the monolayer region. This implies that the majority of the accessible surface area is effectively utilized for nitrogen adsorption, and that the pore structure is favorable for monolayer formation.

Interestingly, the silica sample with 3%wt Y_2O_3:Eu^{3+} does not display the highest surface area, even though its isotherm showed the largest amount of nitrogen adsorbed. This apparent discrepancy may arise because the BET surface area calculation is most sensitive to the monolayer adsorption region, whereas the total nitrogen uptake at higher pressures

reflects contributions from larger pores not fully captured by the model.

In the case of CMC aerogels with Y_2O_3:Eu^{3+} microparticles, the BET surface area for the 16%wt sample is slightly lower than that of the 30%wt sample, which is not entirely consistent with the isotherm trends. This could be due to experimental artifacts. For the highest concentrations (50%wt and 99%wt), the 99%wt sample shows a higher BET surface area than the 50%wt sample, which is also reflected in the isotherm data. However, the exact mechanism underlying this trend is not fully understood and would require further investigation.

6.1.3.3 Pore Volume Distribution

Adsorption and desorption measurements also provide information on the incremental and cumulative pore volumes. The incremental pore volume distribution plots provide detailed insight into the pore size distribution of the different aerogel samples. For silica aerogels containing Y_2O_3:Eu^{3+} microparticles (Figure 6.26a), a common peak is observed for all concentrations around 20 nm, except for pure silica, which shows a greater number of smaller mesopores, approximately 10 nm in diameter. The pore distribution of pure silica suggests a structure with a wider range of pore sizes, as it also contains a significant amount of macropores, while the aerogels containing luminescent microparticles are mostly composed of mesopores. This suggests that the addition of micrometric particles reduces the average pore size. Among these samples, the 3%wt Y_2O_3:Eu^{3+} concentration exhibits a greater presence of larger mesopores, explaining the discrepancy between its relatively lower BET surface area and high adsorbed gas quantity, since large pores contribute more to volume than to surface area.

In the case of silica aerogels with YVO_4:Eu^{3+} nanoparticles (Figure 6.26b), the pore size increases upon nanoparticle addition, with the maximum number of mesopores found at the 0.3%wt concentration. This result is consistent with the observations from the adsorption isotherms and BET surface area measurements.

Additionally, when comparing the 3%wt concentration of luminescent materials, the highest number of pores in silica aerogels with nanoparticles is centered around 50 nm, whereas in aerogels loaded with microparticles, the dominant pore size is closer to 20 nm.

For CMC aerogels containing Y_2O_3:Eu^{3+} microparticles (Figure 6.26c), the majority of pores fall within the micropore range or small mesopores below 5 nm. The 0.5%wt concentration shows greater porosity than pure CMC, which aligns with the results from the isotherms and BET surface area measurements. Beyond the 5%wt concentration, as the concentration of microparticles increases, the porosity decreases.

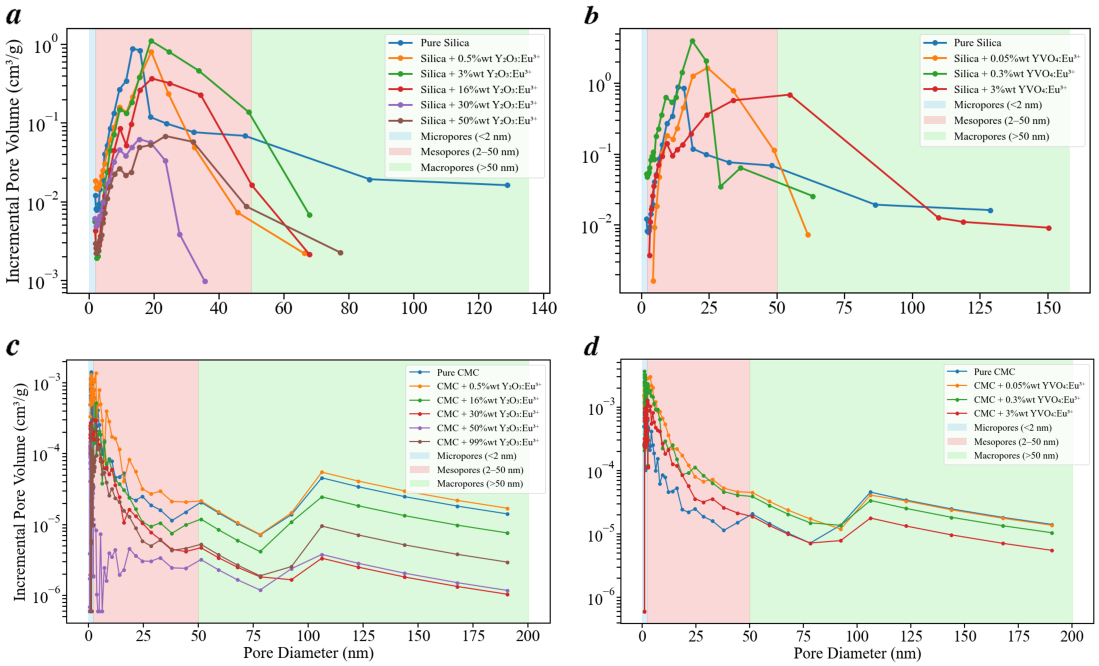

Figure 6.26: Incremental pore volume for ***a)*** silica aerogels containing micrometric Y_2O_3:Eu^{3+} particles, ***b)*** silica aerogels containing nanometric YVO_4:Eu^{3+} particles, ***c)*** CMC aerogels containing micrometric Y_2O_3:Eu^{3+} particles, and ***d)*** CMC aerogels containing nanometric YVO_4:Eu^{3+} particles.

As for CMC aerogels with YVO_4:Eu^{3+} nanoparticles (Figure 6.26d), the highest pore concentration is also found in the range of micropores and small mesopores (< 5 nm). Similarly to silica-based aerogels, CMC aerogels tend to be more porous when loaded with nanoparticles rather than microparticles.

For pure CMC aerogels, the wide variety of pore sizes that can reach up to 190 nm is maintained when the different luminescent materials are added, whereas in silica aerogels, the larger pores, between 80 and 130 nm, appear to disappear when the different luminescent materials are added.

Regarding the cumulative pore volume plots (Figure 6.27), they provide valuable insight into the total amount of gas adsorbed as a function of pore size. These distributions confirm the mesoporous nature of all aerogels, with silica-based systems generally showing larger mesopores, especially with nanoparticles, while CMC-based aerogels are richer in micropores and small mesopores.

The analysis of nitrogen gas adsorption/desorption measurements provided information about pores on the nanometer scale. However, electron microscope images reveal the presence of much larger pores on the order of several tens of micrometers, specially in the

case of CMC aerogels loaded with low concentrations of Y_2O_3:Eu^{3+} microparticles or QDs. This discrepancy may reveal two things: first, that surface pores are significantly larger than those located deeper within the aerogel volume, being the latter the ones that play a key role in trapping tritium atoms; and second, that the adsorption/desorption method is only useful for quantifying the internal porosity of the aerogel, but not the surface porosity. To investigate the impact of the larger surface pores, Mercury Intrusion Porosimetry (MIP) experiments would be necessary.

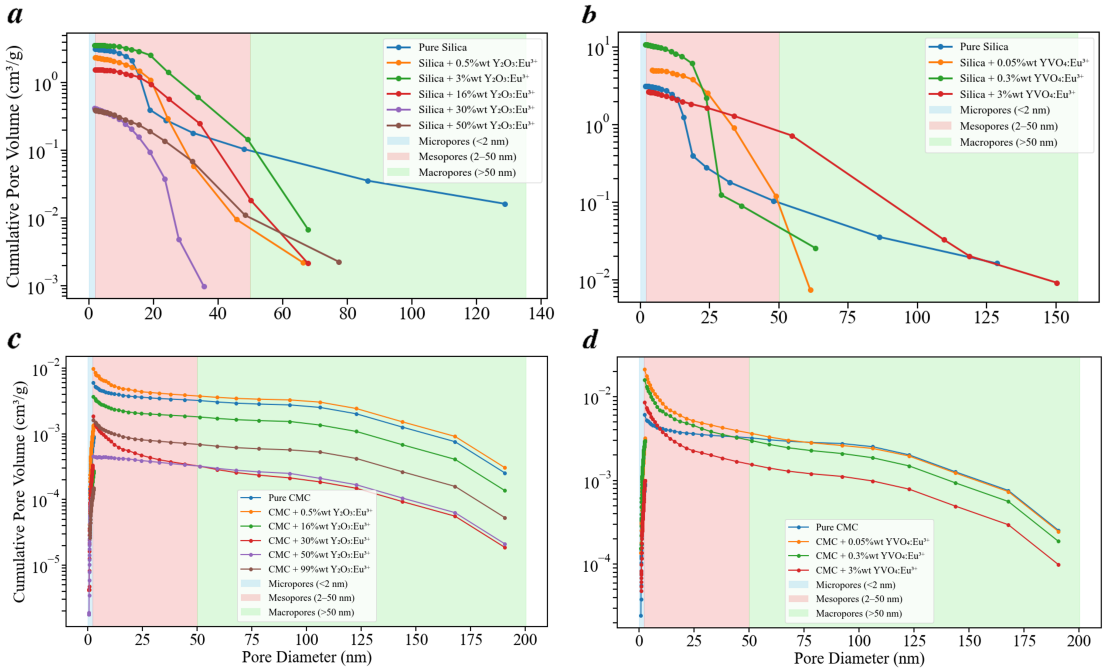

Figure 6.27: Cumulative pore volume for ***a)*** silica aerogels containing micrometric Y_2O_3:Eu^{3+} particles, ***b)*** silica aerogels containing nanometric YVO_4:Eu^{3+} particles, ***c)*** CMC aerogels containing micrometric Y_2O_3:Eu^{3+} particles, and ***d)*** CMC aerogels containing nanometric YVO_4:Eu^{3+} particles.

In the literature, no studies have been reported with gas adsorption and desorption measurements in aerogels loaded with luminescent materials, so this would be an exploratory work.

6.1.4 Three-Dimensional Characterization by X-Ray Tomography

X-ray tomography of aerogels enables the analysis of the spatial distribution of the luminescent materials, with the aim of verifying whether the experimentally observed concentration aligns with the theoretical concentration defined during sample preparation. Additionally,

it allows assessment of the homogeneity of this distribution throughout the entire volume of the aerogel.

6.1.4.1 Laboratory X-Ray Tomography

Preliminary X-ray tomography measurements are performed on a few samples using a laboratory setup, with the resulting images shown in Figure 6.28. However, the three-dimensional distribution and spatial arrangement of the luminescent materials could not be clearly resolved due to the limited resolution and sensitivity of laboratory-based X-ray tomography. Consequently, synchrotron radiation is employed to study the samples, as it provides significantly higher spatial resolution and improved image contrast.

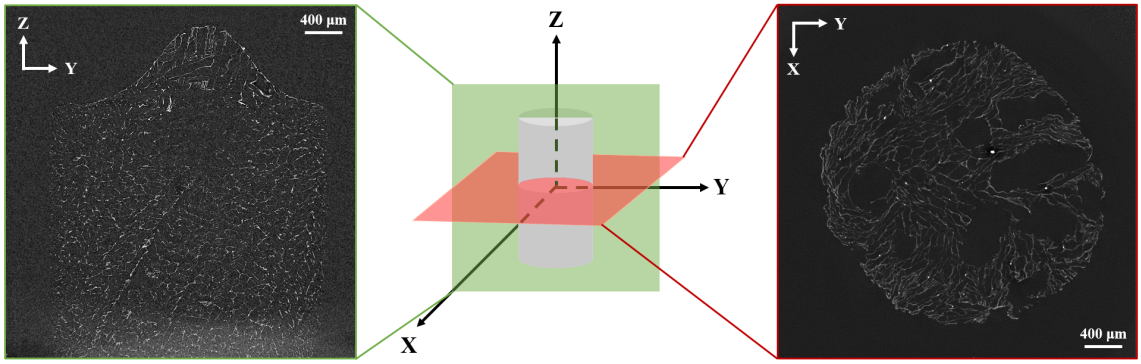

Figure 6.28: Laboratory X-ray tomography images of a CMC aerogel loaded with nanometric YVO_4:Eu^{3+} particles (left), and a CMC aerogel containing $AgInS_2$ QDs (right), respectively.

6.1.4.2 Synchrotron Radiation Tomography

Thus, we proceeded to analyze different samples, all containing the same concentration of luminescent materials (3%wt), using synchrotron radiation. To take advantage of the higher spatial resolution, smaller aerogels are analyzed, as previously mentioned in section 3.5.1.4.3 of chapter 3.

6.1.4.2.1 Y_2O_3:Eu^{3+} Embedded in CMC

First, a sample of CMC containing Y_2O_3:Eu^{3+} and prepared from the 1 mm-diameter aerogel is analyzed. Figure 6.29 shows the two regions analyzed using local tomography and the corresponding three-dimensional reconstructions, with dimensions of 450 μm $\times$ 450 μm $\times$ 287 μm. Both analysis regions are separated by a distance of 280 μm in the

z-axis (axial axis of the cylindrical sample). For each of the reconstructions, orthogonal views are shown.

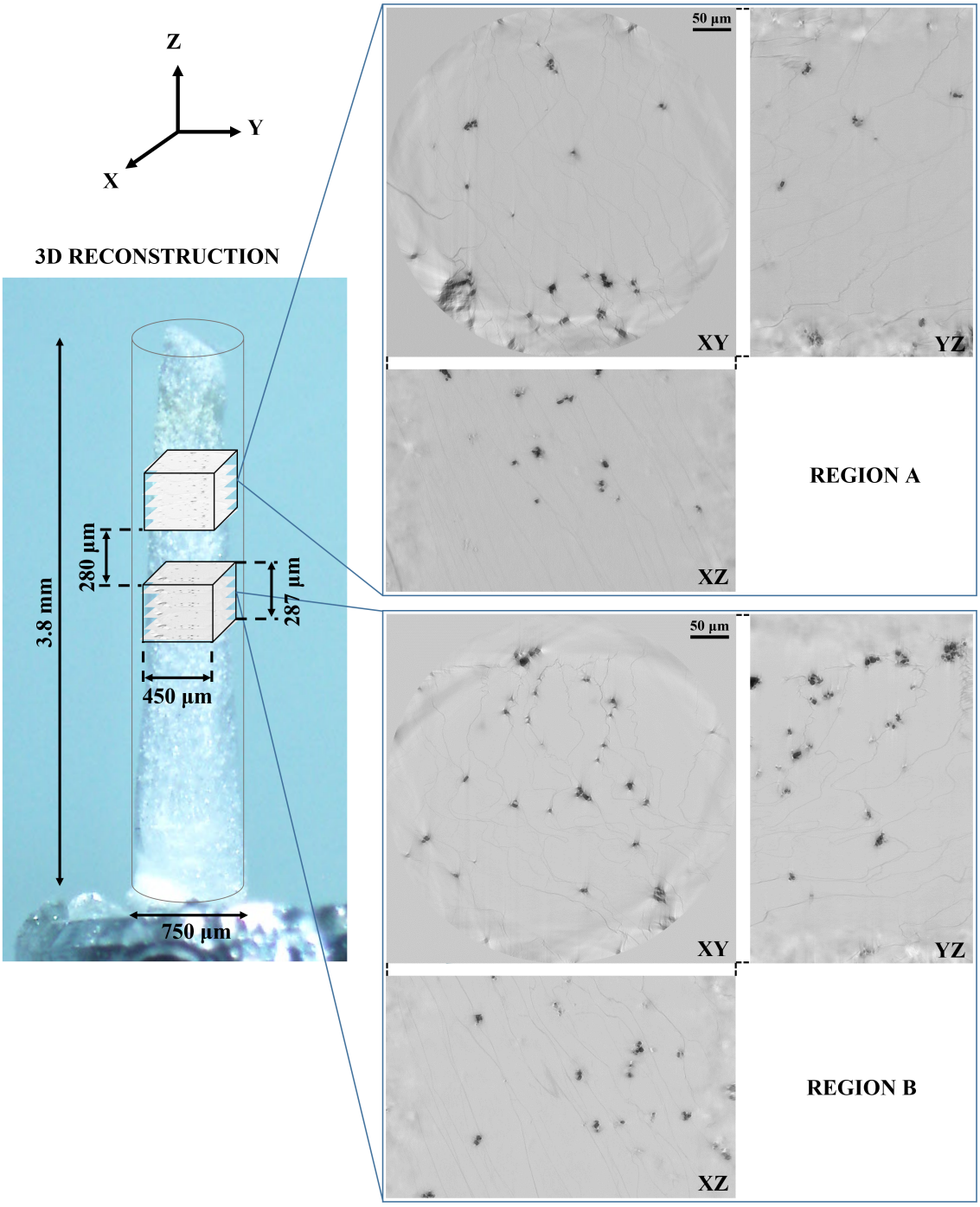

Figure 6.29: Orthogonal views of the three-dimensional reconstructions obtained by local tomography in regions A and B, of a sample of CMC containing 3%wt Y_2O_3:Eu^{3+}, and prepared from the 1 mm-diameter aerogel.

The sample structure exhibits a heterogeneous porous morphology with varying pore sizes

and distribution. The lighter gray regions distributed throughout the CMC matrix suggest the presence of both: macropores (visible as larger void spaces) and interconnected pore networks within the fibrous CMC structure. The porosity appears to be moderate to high, as evidenced by the significant volume fraction of void spaces relative to the solid matrix material.

Orthogonal views of the porous structure of the sample reveal a certain degree of anisotropy, as the CMC fibers (gray lines delineating the edges of pores) are oriented in different directions depending on the projection. For example, in both regions A and B, the XZ projections show fibers oriented from the upper left to the lower right corner, whereas in the YZ projections, the fibers are oriented from the lower left to the upper right corner. This observed anisotropy in fiber orientation, specifically, the closely vertical alignment of CMC fibers in the XZ and YZ projections, may be attributed to the incompatibility between the hydrophilic CMC and the hydrophobic PTFE mold. The CMC network, formed from a 2%wt aqueous solution, likely minimizes contact with the PTFE wall during gelation or drying, favoring fiber orientations parallel to the cylindrical axis. This effect is consistent with the general behavior of hydrophilic polymers in hydrophobic molds, as reported in the literature [149] and shown in Figure 6.30.

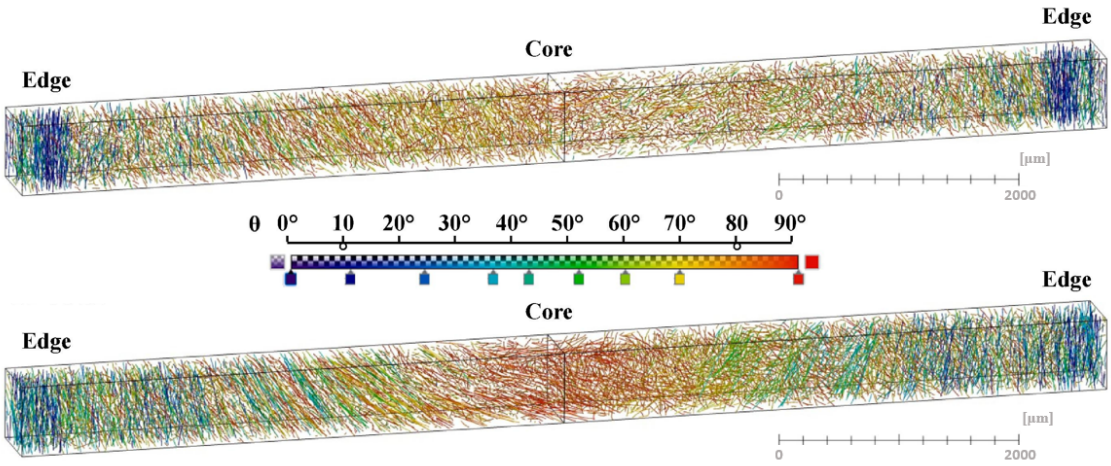

Figure 6.30: CMC fiber orientation developed during the gelation or drying process in a hydrophobic mold, such as PTFE. Adapted from [149].

The black spots correspond to the Y_2O_3:Eu^{3+} particles or aggregates. The orthogonal tomography views indicate that the luminescent particles, are predominantly located within the pore spaces of the CMC matrix. The consistent localization of the particles within these regions across all projections supports the conclusion that the particles are effectively trapped within the porous structure of the CMC matrix. Let us study in more detail the

distribution of these luminescent particles.

For this purpose, in each of the three-dimensional reconstructions, five ROIs are defined at two different heights, as illustrated in Figure 6.31a. These ROIs are cubic, with a side length of 140 μm. Once the ROIs are defined, segmentation is performed to determine the distribution of the micrometric luminescent particles within the CMC matrix. 6.31b and 6.31c show this distribution in the ROI defined in regions A and B, respectively.

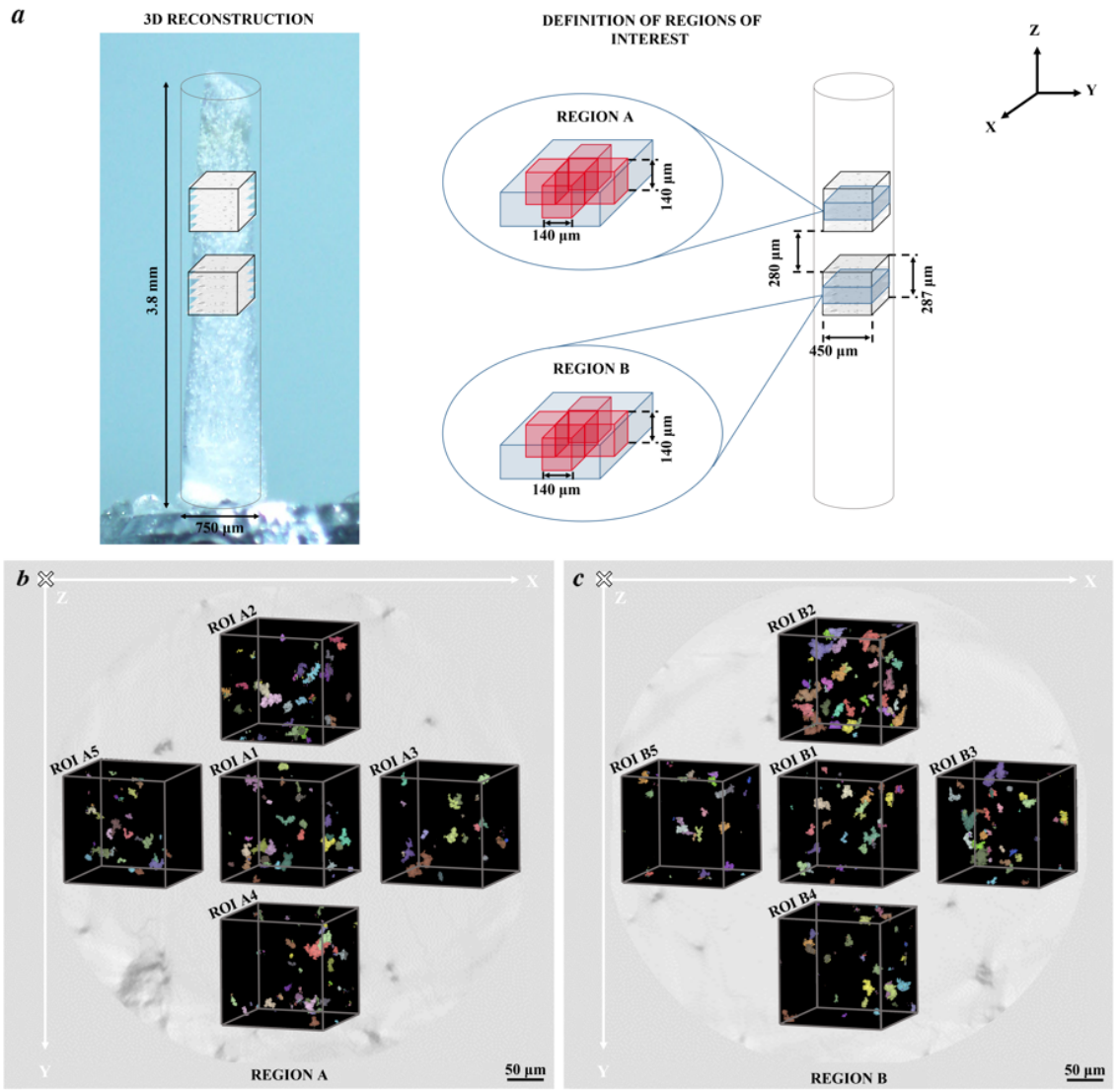

Figure 6.31: ***a)*** Definition of the ROIs in each of the three-dimensional reconstructions obtained by local tomography during the analysis of a CMC sample loaded with 3%wt Y_2O_3:Eu^{3+}, prepared from the 1 mm-diameter aerogel. Image not to scale. ***b)*** Distribution of Y_2O_3:Eu^{3+} particles in the three-dimensional reconstruction corresponding to region A. ***c)*** Distribution of Y_2O_3:Eu^{3+} particles in the three-dimensional reconstruction corresponding to region B.

Visually, the distribution of Y_2O_3:Eu^{3+} microparticles appears to be homogeneous in both regions, although in ROI B2 there appears to be a greater accumulation of particles. Let's make a more detailed analysis from the qualitative information that can be obtained from the segmentation. Tables 6.3 and 6.4 show all the information corresponding to regions A and B, respectively. Each parameter has been previously defined in section 3.5.1.4.4 of chapter 3.

Information obtained after segmentation	**ROI A1**	**ROI A2**	**ROI A3**	**ROI A4**	**ROI A5**
$N_{particles}$	86	246	90	307	139
$\bar{V}_{particle}(\mu m^3)$	163	60	89	41	47
$V_{particles}(\mu m^3)$	14 049	14 698	8 033	12 607	6 525
$V_{ROI}(\mu m^3)$	2 744 000				
$C_V(\%)$	0.51	0.54	0.29	0.46	0.24
$\bar{A}_{particle}(\mu m^2)$	155	63	92	45	58
$A_{particles}(\mu m^2)$	2 717	2 988	1 589	2 628	1 854
$A_{ROI}(\mu m^2)$	19 600				
$C_S(\%)$	14	15	8	13	9
$\bar{d}_{particle}(\mu m)$	3.71	1.75	2.16	1.54	1.89
$\bar{S}_{particle}$	0.33	0.34	0.33	0.33	0.34
$C_M(\%)$	1.90	1.98	1.08	1.70	0.88
$\bar{C}_M(\%)$	1.51 ± 0.44				

Table 6.3: Information obtained after segmentation of the three-dimensional reconstruction performed in region A (shown in Figure 6.31b), for the sample of CMC loaded with 3%wt Y_2O_3:Eu^{3+}, prepared from the 1 mm-diameter aerogel.

Information obtained after segmentation	**ROI B1**	**ROI B2**	**ROI B3**	**ROI B4**	**ROI B5**
$N_{particles}$	68	265	145	229	110
$\bar{V}_{particle}(\mu m^3)$	152	128	94	45	66
$V_{particles}(\mu m^3)$	10 362	33 798	13 692	10 287	7 272
$V_{ROI}(\mu m^3)$	2 744 000				
$C_V(\%)$	0.38	1.23	0.50	0.37	0.27

$\bar{A}_{particle}(\mu m^2)$	158	121	99	50	74
$A_{particles}(\mu m^2)$	2 245	5 411	2 705	2 160	1 860
$A_{ROI}(\mu m^2)$	19 600				
$C_S(\%)$	11	28	14	11	9
$\bar{d}_{particle}(\mu m)$	3.84	2.23	2.38	1.56	2.39
$\bar{S}_{particle}$	0.29	0.35	0.34	0.37	0.33
$C_M(\%)$	1.40	4.56	1.85	1.39	0.98
$\bar{C}_M(\%)$	2.04 ± 1.29				

Table 6.4: Information obtained after segmentation of the three-dimensional reconstruction performed in region B (shown in Figure 6.31c), for the sample of CMC loaded with 3%wt Y_2O_3:Eu^{3+}, prepared from the 1 mm-diameter aerogel.

The experimental average particle's diameter is 2.35 μm while the reported mean size by PhosphorTechnology is 8 μm. Moreover, the sphericity values obtained are between 0.29 and 0.37, which are very low values that indicate that the identified particles have very irregular and non-spherical shapes. There could be two reasons to try to justify this. On the one hand, the process of particle segmentation and identification has its limitations and particles are partially but not completely identified. The particles would not be identified as spherical bodies, which would explain the low values of sphericity and then, when determining the mean particle diameter from the particle volume, an underestimated value is obtained. On the other hand, it could happen that the particles have been fragmented during the sample preparation, when preparing the liquid solution of CMC and luminescent materials, so that the particles would have lost their sphericity. In any case, as can be seen in the orthogonal views of both three-dimensional reconstructions shown in Figure 6.29, the particles and particle aggregates show quite irregular shapes.

The mass concentration, $\bar{C}_M(\%)$, has been obtained from equation (3.10) with:

- $\rho_{particles}$ = 5.03 g/cm^3, which is the density of pure Y_2O_3 in its bulk cubic phase [150]. The density of pure Y_2O_3 is used as an approximation for the density of Y_2O_3:Eu^{3+}.

- $\rho_{solution}$ = 1.36 g/cm^3, the density of the liquid solution containing CMC and Y_2O_3:Eu^{3+} at a mass concentration of 3%wt, that has been experimentally measured.

Therefore, in the segmentation of region A, a mass concentration value of $(1.51 \pm 0.44)\%$ is obtained, and $(2.04 \pm 1.29)\%$ in the case of region B. These values are consistent with

the theoretical mass concentration of 3% defined during sample preparation, indicating that the preparation procedure is reliable.

6.1.4.2.2 $YVO_4:Eu^{3+}$ Embedded in CMC

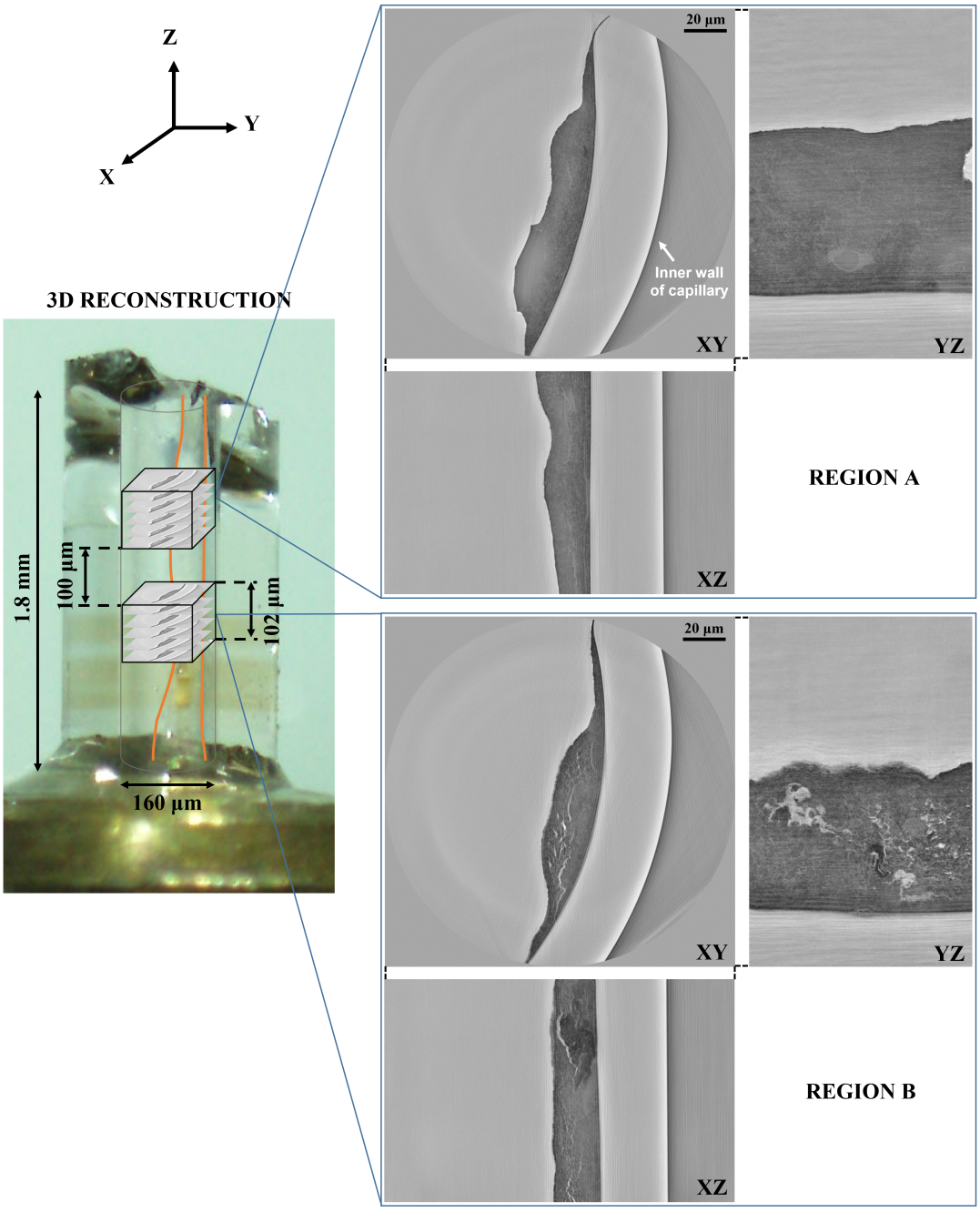

Figure 6.32: Orthogonal views of the three-dimensional reconstructions obtained by holotomography in regions A and B, of a sample of CMC containing 3%wt $YVO_4:Eu^{3+}$, and prepared by microcapillary filling.

The second sample to be analyzed is a sample of CMC containing $YVO_4:Eu^{3+}$ prepared by microcapillary filling. In this case it is a much smaller sample than the previous one, the diameter is around 80–120 μm, and that is why it has been possible to perform a global scan by holotomography. Figure 6.32 shows the orthogonal views of the two regions analyzed.

This sample does not appear to be as porous as the previous one. There are no macropores, but the textured structure could indicate meso- or micropores. In any case, these pores cannot be clearly distinguished in any of the orthogonal views.

There is no evidence of CMC fibers. Centric rings are present in the XY projections, horizontal lines in the YZ projections, and vertical lines in the XZ projections, but these are merely image artefacts and do not represent real structures within the sample.

Due to the lack of contrast between the CMC matrix and the $YVO_4:Eu^{3+}$ particles, a quantitative analysis cannot be performed from the three-dimensional reconstructions. The sample preparation was complex due to the short notice before the experiment.

Finally, some irregular white shapes can be observed, mainly in the projections obtained from region B. These features may be related to specific interactions between the CMC polymer matrix and the sodium citrate ligands on the $YVO_4:Eu^{3+}$ nanoparticles. Previous research [151] on sodium citrate and methylcellulose (MC) hydrogels has shown that citrate ions directly interact with cellulose chains, inducing structural changes in the polymer network. In MC hydrogels, citrate ions attract water molecules away from the cellulose chains, suppressing intermolecular hydrogen bonding between water and the hydroxyl groups of the polymer. This interaction leads to a "salt-out effect", which can create localized stress concentrations and structural heterogeneities within the matrix. By extrapolation to the CMC-based system, the irregular white features may represent dehydration zones where sodium citrate ligands have locally altered the hydration state of CMC, resulting in regions with different mechanical properties and potential weak points for crack initiation. Future work could aim to validate this hypothesis using complementary techniques, such as Fourier Transform Infrared spectroscopy (FTIR) or Raman spectroscopy and high-resolution imaging methods like Atomic Force Microscopy (AFM) or Transmission Electron Microscopy (TEM).

The clear observation of cracks by holotomography, along with the sample's wet visual appearance, suggests that it is more likely a hydrogel rather than an aerogel. In aerogels, which are predominantly porous, distinguishing between inherent porosity and actual cracks or fractures would be much more challenging. A better sample preparation could lead to different results; therefore this conclusion still has to be confirmed.

6.1.4.2.3 $AgInS_2$ Embedded in CMC

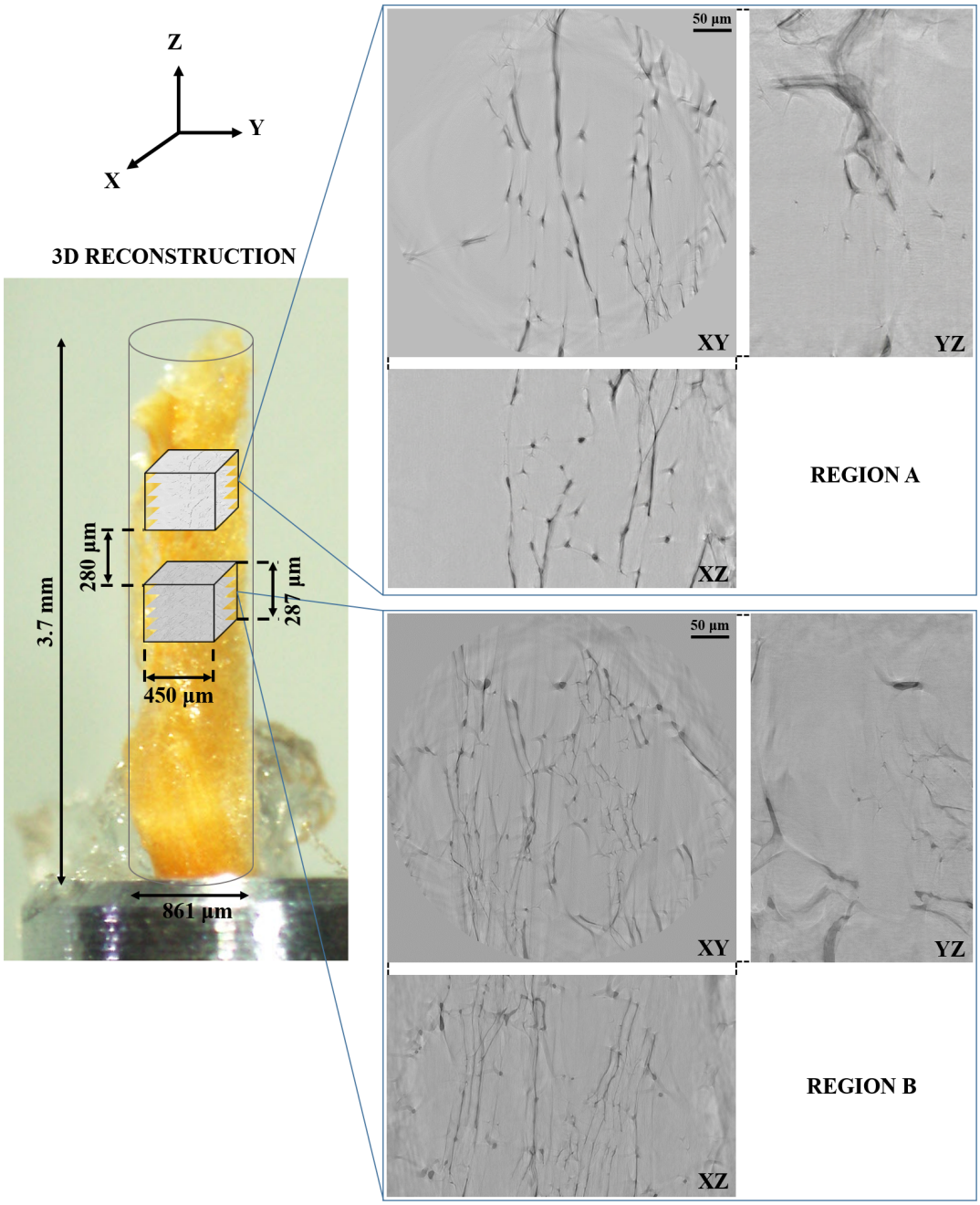

Figure 6.33: Orthogonal views of the three-dimensional reconstructions obtained by local tomography in regions A and B, of a sample of CMC containing 3%wt $AgInS_2$, and prepared from the 1 mm-diameter aerogel.

The third sample to be analysed contains the CMC matrix and $AgInS_2$ QDs as luminescent materials. This sample's preparation follows the second procedure described in section

3.5.1.4.3 so the sample's diameter is about 861 μm. Therefore, the three-dimensional reconstructions shown in Figure 6.33 are obtained by local tomography.

Regarding the porosity of the sample, macropores and an interconnected network of fibers are observed, as with the Y_2O_3:Eu^{3+} microparticles embedded in CMC. Different orientations of these fibers are observed, particularly in the XZ projections, where the fibers are vertically oriented. This continues to support the hypothesis that the CMC fibers have been oriented to minimise contact with the PTFE surface of the mold.

In the images obtained, some contrast can be observed. However, it differs from the case of CMC with Y_2O_3:Eu^{3+}, where light gray areas appear to correspond to pores, darker gray regions to CMC fibers, and black particles to Y_2O_3:Eu^{3+} particles. In the present case, both the presumed CMC fibers and the $AgInS_2$ QDs produce similar contrast. While some clusters of QDs are visible (given that the spatial resolution of 140 nm does not allow us to distinguish the individual 2.5 nm $AgInS_2$ particles), it is possible that the luminescent particles are so well distributed within the CMC that the generated fibers already incorporate the QDs internally. This hypothesis could be validated using TEM.

Thus, it could be that the clusters of $AgInS_2$ particles are trapped in the pores of the porous structure, similar to what is observed with the micrometric Y_2O_3:Eu^{3+} particles, while other $AgInS_2$ nanoparticles may be directly embedded within the CMC-derived fibers.

The images obtained for this sample are less well-defined than those obtained in previous cases, making it difficult to study the distribution of luminescent materials quantitatively.

6.1.4.2.4 $CuInS_2$ Embedded in CMC

The fourth and final sample to be analyzed is a CMC aerogel loaded with $CuInS_2$, prepared by microcapillary filling. Its diameter ranges from 60 to 130 μm, and therefore, a global scan can be performed using holotomography. Orthogonal views of the two analyzed three-dimensional reconstructions are shown in Figure 6.34.

As in the CMC and YVO_4:Eu^{3+} sample, this sample does not show porosity. There does not appear to be any macropores, and the granular appearance could indicate the presence of meso- or micropores, but they are not distinguishable in the images. CMC fibers are also not observed.

Regarding the distribution of the $CuInS_2$ nanoparticles, there is good contrast between what would be the CMC polymeric matrix in gray and the $CuInS_2$ particles in black. The spatial resolution of these images is 50 nm, so it is not possible to identify the individual nanoparticles, as their diameters are around 3 nm. The black particles observed must

therefore correspond to clusters of nanoparticles.

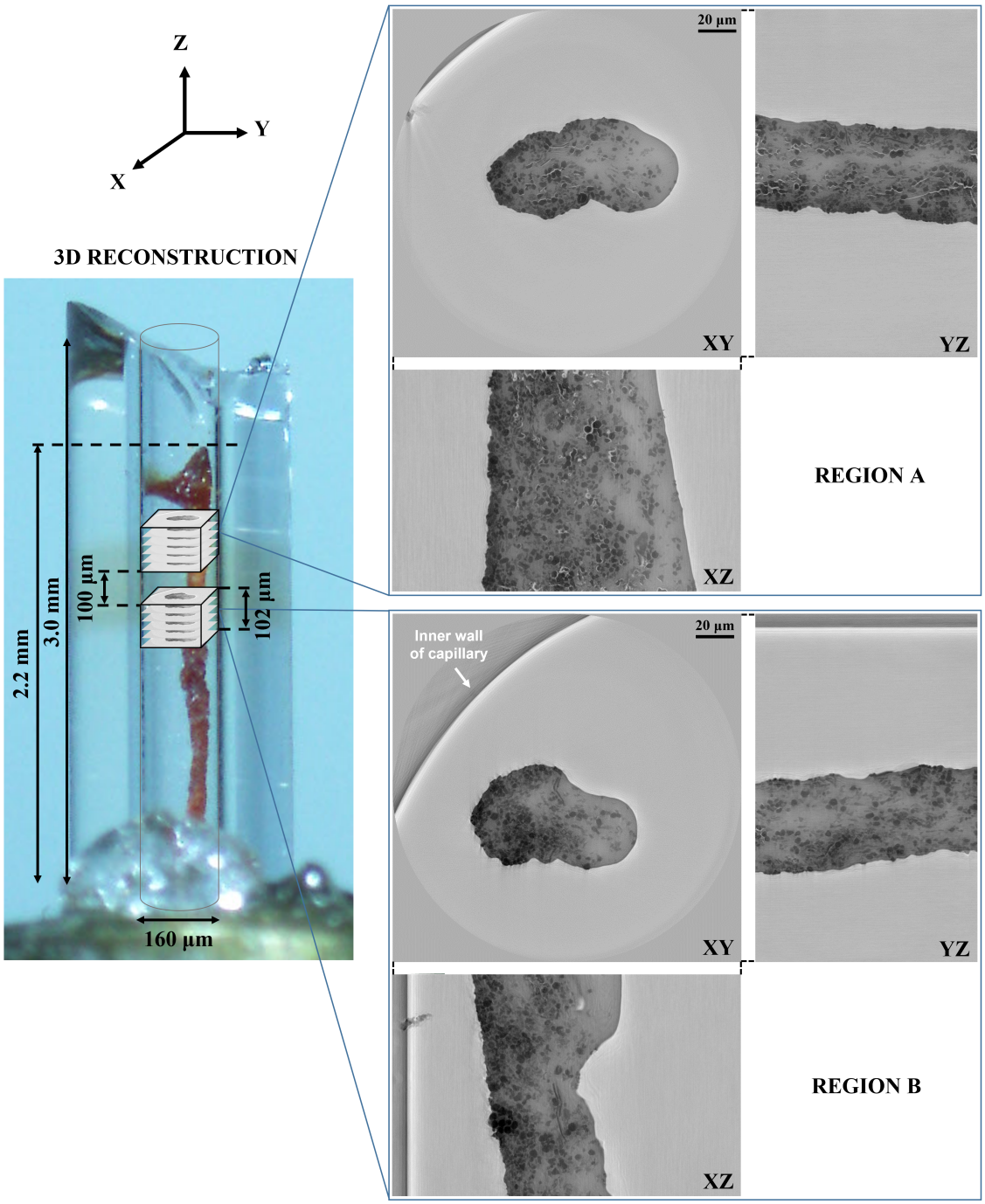

Figure 6.34: Orthogonal views of the three-dimensional reconstructions obtained by local tomography in regions A and B, of a sample of CMC containing 3%wt $CuInS_2$, and prepared from the 1 mm-diameter aerogel.

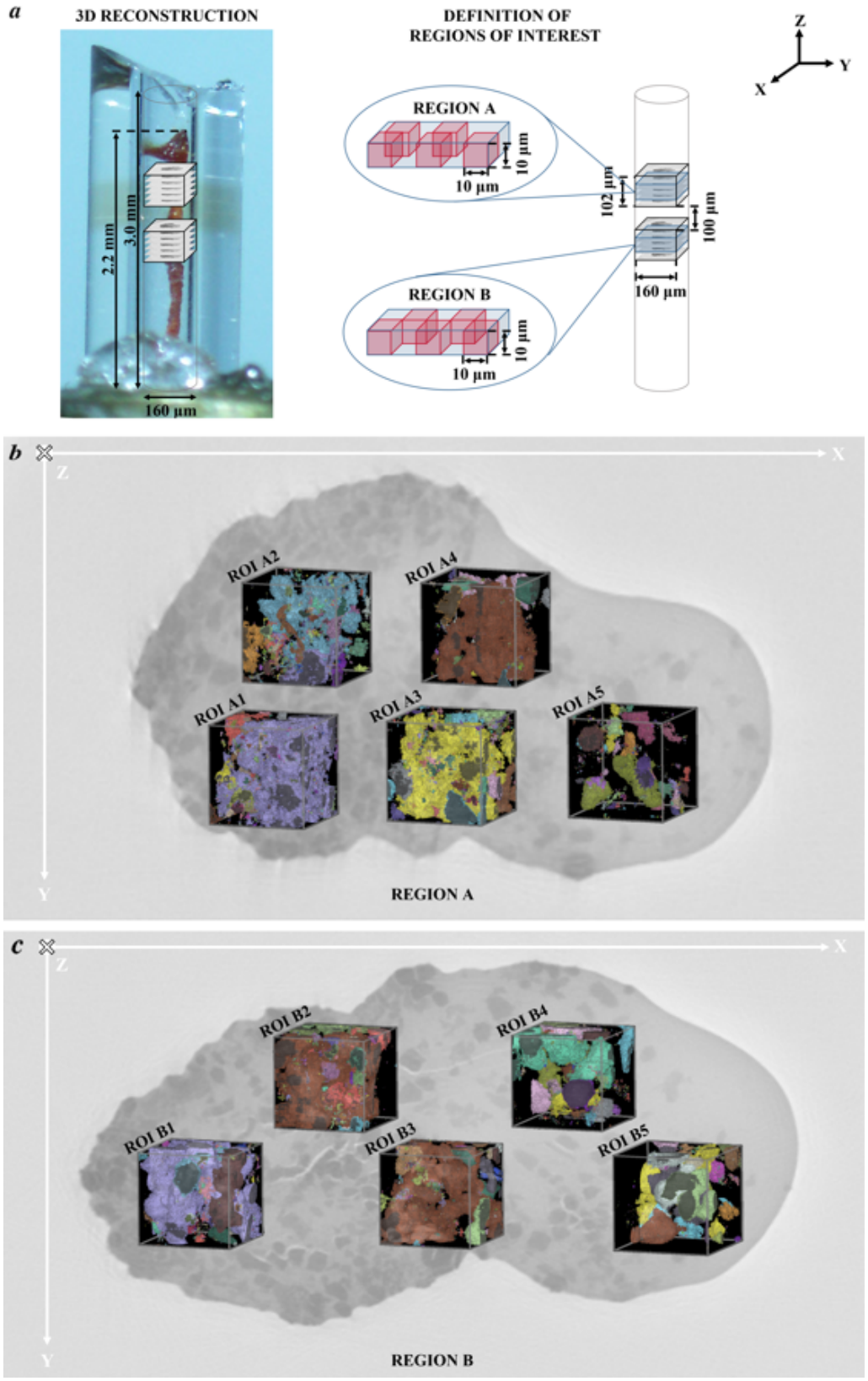

Figure 6.35: ***a)*** Definition of the ROIs in each of the three-dimensional reconstructions obtained by holotomography during the analysis of a CMC sample loaded with $CuInS_2$, prepared by microcapillary filling. Image not to scale. ***b)*** Distribution of $CuInS_2$ particles in the three-dimensional reconstruction corresponding to region A. ***c)*** Distribution of $CuInS_2$ particles in the three-dimensional reconstruction corresponding to region B.

Additionally, irregular white regions are observed at the interface between the $CuInS_2$ nanoparticles and the CMC matrix. These features may be attributed to the GSH ligands on the $CuInS_2$ nanoparticles, which can induce the formation of hydration shells, where structured layers of water molecules surround the hydrophilic GSH ligands and create local low-density zones [152]. Alternatively, steric effects caused by the bulky GSH ligands may physically displace CMC chains, generating microvoids at the interface [153].

Let's analyze in more detail the distribution of these particles. Figure 6.35 shows the 5 ROIs used during the segmentation of the three-dimensional reconstructions of regions A and B. It can be observed that these ROIs contain large clusters of particles. Tables 6.5 and 6.6 show all the data obtained from this segmentation in regions A and B, respectively.

Information obtained after segmentation	**ROI A1**	**ROI A2**	**ROI A3**	**ROI A4**	**ROI A5**
$N_{particles}$	1 794	1 902	1 652	1 108	1 002
$\bar{V}_{particle}(\mu m^3)$	0.12	0.06	0.13	0.12	0.04
$V_{particles}(\mu m^3)$	209.94	113.24	212.31	135.57	43.88
$V_{ROI}(\mu m^3)$	1 000.02				
$C_V(\%)$	20.99	11.32	21.23	13.56	4.39
$\bar{A}_{particle}(\mu m^2)$	0.78	0.47	0.78	0.83	0.37
$A_{particles}(\mu m^2)$	94.24	81.38	95.07	71.80	51.24
$A_{ROI}(\mu m^2)$	100.00				
$C_S(\%)$	94.24	81.38	95.07	71.80	51.24
$\bar{d}_{particle}(\mu m)$	0.12	0.12	0.13	0.12	0.13
$\bar{S}_{particle}$	0.50	0.49	0.48	0.49	0.49
$C_M(\%)$	99.72	39.60	74.25	47.41	15.35
$\bar{C}_M(\%)$	55.27 ± 29.11				

Table 6.5: Information obtained after segmentation of the three-dimensional reconstruction performed in region A (shown in Figure 6.35b), for the sample of CMC and $CuInS_2$ at a mass concentration of 3%wt, prepared by microcapillary filling.

Information obtained after segmentation	ROI B1	ROI B2	ROI B3	ROI B4	ROI B5
$N_{particles}$	977	1 318	1 191	1 188	561
$\bar{V}_{particle}(\mu m^3)$	0.30	0.16	0.15	0.12	0.26
$V_{particles}(\mu m^3)$	288.59	215.96	183.27	147.06	144.22
$V_{ROI}(\mu m^3)$	1 000.02				
$C_V(\%)$	28.86	21.60	18.33	14.71	14.42
$\bar{A}_{particle}(\mu m^2)$	1.24	0.96	0.85	0.62	1.22
$A_{particles}(\mu m^2)$	95.12	95.01	80.83	79.48	69.55
$A_{ROI}(\mu m^2)$	100.00				
$C_S(\%)$	95.12	95.01	80.83	79.48	69.55
$\bar{d}_{particle}(\mu m)$	0.13	0.13	0.13	0.13	0.17
$\bar{S}_{particle}$	0.49	0.50	0.49	0.48	0.48
$C_M(\%)$	137.08	75.53	64.09	51.43	50.44
$\bar{C}_M(\%)$	75.71 $\pm$ 32.03				

Table 6.6: Information obtained after segmentation of the three-dimensional reconstruction performed in region B (shown in Figure 6.35c), for the sample of CMC and $CuInS_2$ at a mass concentration of 3%wt, prepared by microcapillary filling.

The observed average particle's diameter is approximately 130 nm, reflecting large aggregates composed of many primary 3 nm particles. For instance, a 130 nm sphere cluster would be made up of $\left(\frac{130}{3}\right)^3 = 8 \cdot 10^4$ nanoparticles. The sphericity values are between 0.48 and 0.50, indicating that the particle clusters are irregular in shape, and suggesting uncontrolled aggregation.

The particle clusters are not uniformly distributed across the polymeric matrix. Some ROIs, such as A2, are almost completely filled with $CuInS_2$ particles, while other ROIs, such as A5, are more sparsely populated.

The mass concentration, $\bar{C}_M(\%)$, has been obtained from equation (3.10) with:

- $\rho_{particles} = 4.75$ g/cm^3, which is the density of pure $CuInS_2$ in its bulk cubic phase [150].
- $\rho_{solution} = 1.013$ g/cm^3, the density of the liquid solution containing CMC and $CuInS_2$ at a mass concentration of 3%wt that has been experimentally measured.

The unexpectedly high and variable mass concentrations of nanoparticles observed after segmentation, ranging from 15.35% to even more than 100%, likely result from a combination of segmentation artifacts, inhomogeneous nanoparticle distribution during sample preparation, and the use of bulk density values for nanoparticles in equation (3.10). Limited contrast between $CuInS_2$ and the CMC matrix may have led to overestimation of nanoparticle volume in some regions, while aggregation during freezing and drying could cause local concentration "hot spots". Indeed, even with rapid freezing using liquid nitrogen, the literature shows that nanoparticles are excluded from the growing ice crystals and become concentrated in the remaining pockets of unfrozen solution [154]. Lyophilization does not dissolve these aggregates; instead, the regions of high nanoparticle concentration formed during freezing are preserved in the final structure. Additionally, the use of bulk density for nanoparticles does not account for the presence of surface ligands, which may further inflate the calculated mass fractions. Taken together, these factors may explain the observed discrepancies. Improvements in imaging contrast and sample preparation may help achieve more accurate quantification in future experiments.

6.2 Characterization of Radioluminescent Aerogels After Tritium Exposure

6.2.1 Spectral Properties of Radioluminescence

Besides being able to determine the instantaneous radiance emitted by the aerogel exposed to the tritium atmosphere with the setup described in section 3.4.1 of chapter 3, it is also possible to capture the emission spectrum of the studied aerogel. To do this, instead of connecting the output of the optical fiber to the detector, it is connected to a spectrometer (commercially available from Thorlabs, ref. CCS200). However, acquiring a good emission spectrum is quite complicated, likely due to the optical losses occurring along the setup, which should be optimized in the future. Therefore, only the emission spectra of the CMC aerogels loaded with Y_2O_3:Eu^{3+}, which emit higher radiance, could be acquired.

Figure 6.36 shows the spectrum of a CMC aerogel loaded with 50%wt of Y_2O_3:Eu^{3+} during its exposure to gaseous tritium atmosphere at 1200 mbar. The predominant peak is located at 612 nm, while the secondary peaks blend into the noise of the signal.

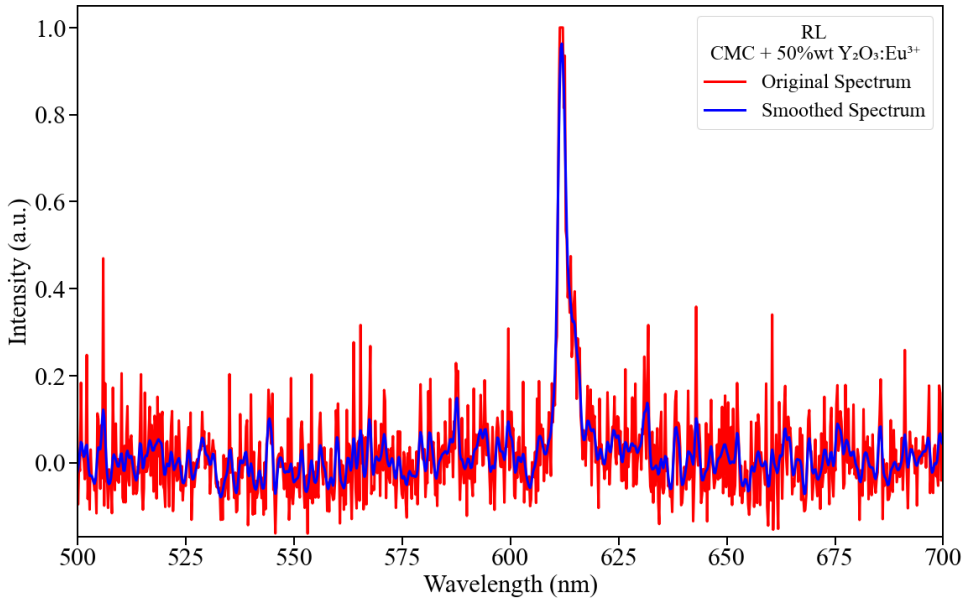

Figure 6.36: Emission spectrum of a CMC aerogel loaded with 50%wt of Y_2O_3:Eu^{3+} during its exposure to gaseous tritium atmosphere at 1200 mbar.

6.2.1.1 Comparison of Spectral Properties under Different Excitation Mechanisms

It is possible to compare the emission spectrum of the CMC aerogels loaded with Y_2O_3:Eu^{3+} when excited by different sources: PL with UV light at 280 nm (section 6.1.1 of this chapter), CL with an electron beam at 5.7 keV (section 6.1.2.2 of this chapter), and RL in contact with the tritium atmosphere (previous section). It should be noted that spectral characterization under RL has only been possible for CMC aerogels loaded with Y_2O_3:Eu^{3+} due to optical losses in the setup. Additionally, these results can be compared with the characteristic wavelengths of the luminescent Y_2O_3:Eu^{3+} coating studied under PL (section 4.1 of chapter 4) and CL (section 4.2 of chapter 4). Therefore, Table 6.7 shows the characteristic emission wavelengths of the Y_2O_3:Eu^{3+} coating spectrum and when these phosphors are integrated into the CMC aerogel.

Sample	λ_{PL} (nm)	λ_{CL} (nm)	λ_{RL} (nm)
Y_2O_3:Eu^{3+} coating	611	608	/
CMC + Y_2O_3:Eu^{3+}	609	610	612

Table 6.7: Summary of characteristic emission wavelengths for the Y_2O_3:Eu^{3+} coating and for CMC aerogels loaded with Y_2O_3:Eu^{3+} under PL, CL, and RL.

Slight shifts of 2-3 nm are observed for both the coating and the phosphor-loaded aerogel, for each type of excitation. It is unclear whether these shifts are due to the measurement instrumentation in each case or to a real change in the intrinsic emission of the sample depending on the excitation mechanism. In any case, it is demonstrated that the emission spectrum can be studied with the proposed setup for the RL experiments.

6.2.2 Optical Efficiency Characterization via Quantum Yield Measurements

The aerogels have already been characterized prior to tritium exposure, and the RL experiments have been completed. The next step is to study and compare the optical efficiency of these radioluminescent devices under the different light-producing mechanisms: PL, CL, and RL. For this purpose, the quantum yield will be analyzed.

6.2.2.1 Photoluminescence (PL) Quantum Yield Measured Using a Commercial System

The results obtained from the absolute PL quantum yield measurements with the dedicated instrumentation, whose operation has already been explained in section 3.5.1.5 of chapter 3, are shown below in Figure 6.37.

The graph reveals several key points. First, the absolute PL quantum yield appears to be independent of the aerogel's host matrix, as CMC and silica aerogels loaded with Y_2O_3:Eu^{3+} display similar curves, as do the CMC and silica aerogels loaded with YVO_4:Eu^{3+}. The highest quantum yields are obtained with aerogels containing Y_2O_3:Eu^{3+}, reaching 94% for the silica aerogel and 91% for the CMC aerogel when excited at 260 nm. The CMC aerogel loaded with $AgInS_2$ QDs follows, exhibiting excitation over a broad wavelength range (from 270 nm to 550 nm) while maintaining a quantum yield between 50% and 60%. The CMC aerogel loaded with $CuInS_2$ QDs shows a lower quantum yield but is also excited over a wide range of wavelengths, with slightly higher values around 600 nm, reaching approximately 30%. Finally, the CMC and silica aerogels loaded with YVO_4:Eu^{3+} present maximum quantum yields of 14% and 10%, respectively, when excited at 250 nm.

The broad excitation spectra observed in aerogels containing QDs indicate the presence of self-absorption, caused by the overlap of their absorption and emission spectra. In contrast, aerogels containing phosphor materials do not exhibit this effect, as their maximum quantum yield occurs at UV excitation wavelengths far from their emission peaks.

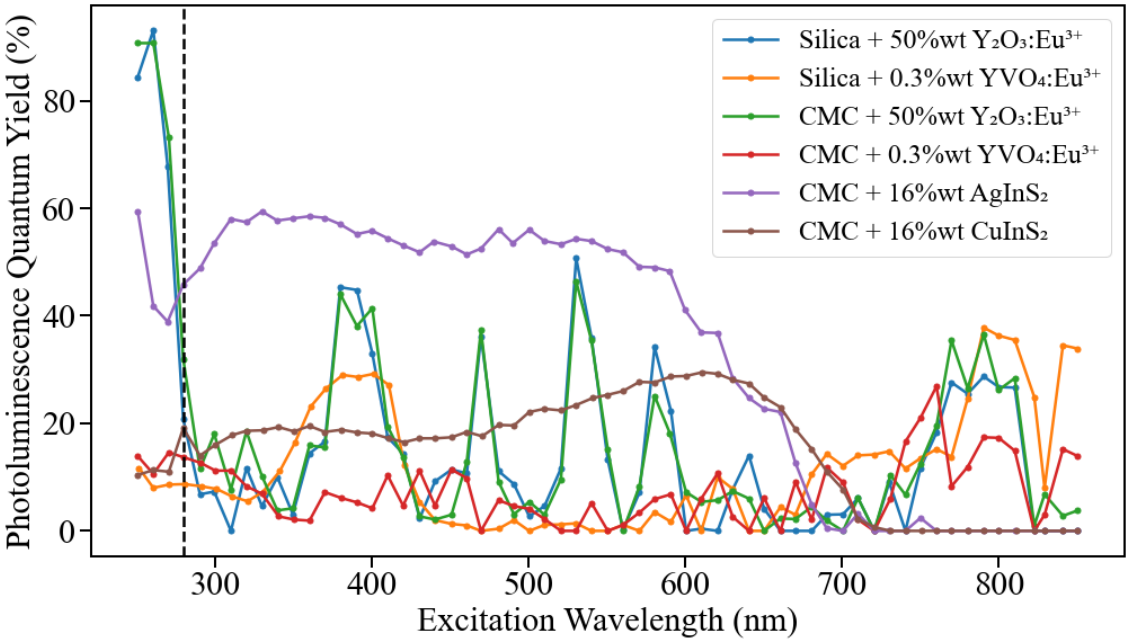

Figure 6.37: Absolute PL quantum yield of CMC and silica aerogels loaded with different luminescent materials as a function of the excitation wavelength. The black dashed vertical line indicates the quantum yield values for an excitation wavelength of 280 nm.

As the UV lamp integrated into the custom system emits at a wavelength, $\lambda_{ex,\,PL}$, of 280 nm, only the quantum yield values corresponding to this excitation wavelength are taken into account.

Thus, the following results are obtained:

Sample	η_{PL}^{ref} (%)
Silica + 50%wt Y_2O_3:Eu^{3+}	21.03
Silica + 0.3%wt YVO_4:Eu^{3+}	8.62
CMC + 50%wt Y_2O_3:Eu^{3+}	31.31
CMC + 0.3%wt YVO_4:Eu^{3+}	13.53
CMC + 16%wt $AgInS_2$	46.03
CMC + 16%wt $CuInS_2$	18.81

Table 6.8: Summary of absolute PL quantum yields, measured using the commercial system, for CMC and silica aerogels loaded with different luminescent materials under 280 nm excitation.

Comparing these values with those obtained from the analysis of luminescent material coatings (see Figure 4.5 in chapter 4), it is observed that the Y_2O_3:Eu^{3+} microphosphor exhibits the greatest loss in PL quantum yield when incorporated into aerogels compared

to the other luminescent materials.

6.2.2.2 Radioluminescence (RL) Quantum Yield

Regarding the RL quauntum yield, the one that can be directly measured experimentally with the setup used for the radiance measurements (described in section 3.4.1 of chapter 3) is the energetic quantum yield, which can be expressed as:

$$\eta_{\mathrm{RL,\,E}} = \frac{N_{h\nu\ \mathrm{em,\,RL}}}{N_{e^-\ \mathrm{abs,\,RL}}} \times \frac{E_{h\nu\ \mathrm{em,\,RL}}}{E_{e^-\ \mathrm{ex,\,RL}}} = \frac{P_{\mathrm{det,\,RL}}}{P_{\mathrm{abs,\,RL}}} \tag{6.19}$$

where:

- The number of photons emitted per second, $N_{h\nu\ \mathrm{em,\,RL}}$, multiplied by the energy of each photon $E_{h\nu\ \mathrm{em,\,RL}}$ is equal to the directly detected optical power, P_{det}.
- The energy absorbed by the sample per second, $N_{e^-\ \mathrm{abs,\,RL}} \times E_{e^-\ \mathrm{ex,\,RL}}$, can be estimated from the energy generated per second by a 22.65 Ci atmosphere of gaseous tritium (at 1200 mbar), assuming a mean electron energy of 5.7 keV.

Accordingly, the following quantum yield values for RL are obtained:

Sample	$P_{\mathrm{det,RL}}\,(\mu\mathrm{W})$	$P_{\mathrm{abs,RL}}\,(\mu\mathrm{W})$	$\eta_{\mathrm{RL,E}}\,(\%)$
Silica + 50%wt Y_2O_3:Eu^{3+}	5.11	764	$6.69 \cdot 10^{-1}$
Silica + 0.3%wt YVO_4:Eu^{3+}	$3.46 \cdot 10^{-2}$		$4.53 \cdot 10^{-3}$
CMC + 50%wt Y_2O_3:Eu^{3+}	$1.03 \cdot 10$		1.35
CMC + 0.3%wt YVO_4:Eu^{3+}	$4.70 \cdot 10^{-2}$		$6.15 \cdot 10^{-3}$
CMC + 16%wt $AgInS_2$	2.40		$3.14 \cdot 10^{-1}$
CMC + 16%wt $CuInS_2$	2.21		$2.89 \cdot 10^{-1}$

Table 6.9: Summary of RL quantum yields for CMC and silica aerogels loaded with different luminescent materials, under exposure to a tritium gas atmosphere at 1200 mbar.

The CMC aerogel with Y_2O_3:Eu^{3+} shows the highest quantum yield in RL, followed by the silica aerogel with Y_2O_3:Eu^{3+}. Next are the CMC aerogels with QDs, with the $AgInS_2$ one on top, and lastly, the CMC aerogel loaded with YVO_4:Eu^{3+}, followed by the silica aerogel with the same luminescent materials.

Theses values, $\eta_{\mathrm{RL,E}}$, could then be compared with the theoretical quantum yields, $\eta^{\mathrm{max}}_{\mathrm{RL,E}}$, representing the upper limit. It would be calculated as follows: assuming a scintillation

yield of 50 photons emitted per 1 keV of absorbed electrons (which is already considered a very good scintillation yield) and that these photons are emitted, for example, in the CMC aerogel loaded with 50%wt Y_2O_3:Eu^{3+}, at 610 nm, this corresponds to 101.64 eV of emitted light per keV of electrons, giving a maximum energy efficiency of 10.16%. The corresponding values for the other samples are shown in Table 6.10. It should be noted that the emission wavelength is taken from the CL spectra (section 6.1.2.2), since it was not possible to measure the emission spectra for all samples under RL.

Sample	$\lambda_{em,CL}$ (nm)	$E_{h\nu\ em,max}$eV	$\eta^{max}_{RL,E}$ (%)
Silica + 50%wt Y_2O_3:Eu^{3+}	624	99.20	9.92
Silica + 0.3%wt YVO_4:Eu^{3+}	624	99.20	9.92
CMC + 50%wt Y_2O_3:Eu^{3+}	610	101.64	10.16
CMC + 0.3%wt YVO_4:Eu^{3+}	617	100.49	10.05
CMC + 16%wt $AgInS_2$	641	96.88	9.69
CMC + 16%wt $CuInS_2$	662	93.94	9.39

Table 6.10: Summary of upper limits for RL quantum yields for CMC and silica aerogels loaded with different luminescent materials, under exposure to a tritium gas atmosphere at 1.2 bar.

All experimental quantum yield values are below these upper limits, indicating that the methodology used appears to be consistent. However, there is still room for improvement to approach the theoretical upper limit.

6.2.2.3 Determination of Cathodoluminescence (CL) Quantum Yield

The motivation for the following approach is to enable a future meaningful comparison of light emission processes under different excitation mechanisms (photonic, electronic, and radiative), determining the quantum efficiency for each process.

To attempt to determine the quantum yield in CL, the setup already shown in section 3.5.1.2.1 of chapter 3 is to be used. The limitation is that the intensity recorded in the emission spectra is given in arbitrary units. This necessitates comparing the measurements made with this setup to another reference instrument.

Therefore, a possible solution would be to carry out quantum yield measurements in PL using the customized PL instrument, by exciting the sample with the UV lamp that has already been installed in the CL equipment (as previously described in section 3.5.1.1.1 of chapter 3, which is the same setup that has been used to measure the spectral properties of

the samples in PL). For this, it would simply be necessary to record an emission spectrum of the sample under PL excitation.

From this spectrum, the PL quantum yield, η_{PL}^{cust}, could be determined with the customized setup as follows:

$$\eta_{PL}^{cust} = \frac{N_{h\nu\ em,\ PL}^{cust}}{N_{h\nu\ abs,\ PL}^{cust}} \propto \frac{I_{em,\ PL}^{int}}{N_{h\nu\ inc,\ PL}^{cust} \times (1 - 10^{-A})} \tag{6.20}$$

where:

- $I_{em,\ PL}^{int}$ is the spectrally integrated emission intensity in arbitrary units, which is proportional, but not equal, to the absolute number of emitted photons, $N_{h\nu\ em,\ PL}^{cust}$.
- $N_{h\nu\ inc,\ PL}^{cust}$ is the number of incident photons, estimated from the optical power of the UV lamp divided by the photon energy at the excitation wavelength (280 nm), taking into account the fiber attenuation at the excitation wavelength (0.19 dB/m).
- A is the absorbance of the sample at 280 nm, obtained from measurements with the commercial quantum yield setup which also provides this value.

This quantum yield could be compared with that obtained from the commercial instrument, η_{PL}^{ref}, so that the factor K accounting for all the instrumental differences between both systems can be established:

$$\eta_{PL}^{custom} = K \times \eta_{PL}^{ref} \tag{6.21}$$

Finally, the quantum yield under CL excitation would be estimated as:

$$\eta_{CL} = K \times \left(\frac{N_{h\nu\ em,\ CL}}{N_{e^-\ abs,\ CL}} \right) \propto K \times \frac{I_{em,\ CL}^{int}}{N_{e^-\ inc,\ CL}} \quad = K \times \frac{I_{em,\ CL}^{int}}{I_{beam} \ / \ e} \tag{6.22}$$

where:

- The same calibration factor, K, is applied to convert arbitrary unit intensities and normalize efficiency across the PL and CL measurements, since the detection system and spectrometer response remain unchanged between custom PL and CL setups.
- The number of emitted photons, $N_{h\nu\ em,\ CL}$, is derived from the integrated emission spectra, $I_{em,\ CL}^{int}$. Again, this integrated emission intensity in arbitrary units is proportional, but not equal, to the absolute photon number.
- The number of absorbed electrons, $N_{e^-\ abs,\ CL}$, is approximated by the number of incident electrons, $N_{e^-\ inc,\ CL}$, since accurately measuring the number of absorbed electrons in the CL setup is not implemented and is too complex.

This complex method has been attempted to determine the CL quantum yield, but no consistent results have been obtained.

6.2.3 Radiochemical Characterization via Tritium Quantification

The radiance cycles presented in the results of chapter 5 (Figure 5.1), raise the question of where the tritium gas is retained after exposure of the sample to a tritium gas atmosphere. This phenomenon has only been observed in silica and CMC aerogels containing micrometric Y_2O_3:Eu^{3+} phosphors. Four hypotheses are currently under consideration to explain the possible mechanisms of tritium atom incorporation in the aerogels:

1. Trapping of tritium atoms in the aerogel pores.
2. Trapping of tritium atoms in the pores of the luminescent microparticles.
3. HIE on the aerogel surface.
4. HIE on the surface of the luminescent microparticles.

6.2.3.1 Liquid Scintillation Counting (LSC)

LSC experiments quantify only the tritium content resulting from HIE, as tritium gas trapped in the porous structure is released during aerogel dissolution[1]. In order to perform these experiments, a first sample composed of pure CMC is exposed overnight to tritium gas at 1.2 bar and subsequently dissolved under acidic conditions. Results show that only 0.48% of the total initial activity in the sample is detected. This preliminary result may point to two hypotheses: (i) HIE on the aerogel surface plays an insignificant role, and (ii) the undetected fraction of tritium is likely retained as gas within the aerogel pores.

Additional LSC measurements are carried out on some of the aerogels used during the RL experiments, both silica and CMC aerogels loaded with different luminescent materials. The amounts of tritium estimated in the volume of the aerogel, when possible, after its exposure to tritium, together with the amounts of tritium measured by LSC, are shown in Table 6.11.

[1]The LSC measurements are carried out by Pierre Colonna, a postdoctoral colleague funded by the Programmes Exploratoire et Transversaux de Compétences (PE-PTC), in the CEA/DRF/JOLIOT laboratories at the CEA Saclay site.

Sample	Estimated Radioactivity (mCi)	Measured Radioactivity (mCi)	Detected Fraction (%)	Completely Dissolved?
Silica + 16%wt Y_2O_3:Eu^{3+}	38	4.04	$1.06 \cdot 10^{1}$	No
Silica + 30%wt Y_2O_3:Eu^{3+}	Not Estimated	3.72	/	No
Silica + 50%wt Y_2O_3:Eu^{3+} *	1 934	30.62	1.58	No
Silica + 0.05%wt YVO_4:Eu^{3+}	Not Estimated	3.33	/	Yes
Silica + 1.7%wt YVO_4:Eu^{3+}	Not Estimated	0.41	/	Yes
Silica + 3%wt YVO_4:Eu^{3+}	Not Estimated	0.22	/	No
CMC + 3%wt Y_2O_3:Eu^{3+}	38	0.11	$2.95 \cdot 10^{-1}$	Yes
CMC + 30%wt Y_2O_3:Eu^{3+}	Not Estimated	0.21	/	No
CMC + 50%wt Y_2O_3:Eu^{3+} *	1 435	0.94	$6.55 \cdot 10^{-2}$	No
CMC + 3%wt YVO_4:Eu^{3+}	19	0.39	2.05	Yes

Table 6.11: Estimated, measured, and detected fraction of radioactivity obtained from LSC measurements for CMC and silica aerogels containing different luminescent materials, along with the dissolution condition. All samples are exposed for 30 minutes to the tritium atmosphere, except for those marked with an *, which are exposed overnight.

Quite disparate results are obtained, and it is believed that, although preliminary, the luminescent particles may produce a "quenching" effect that limits the detection of photons generated by the scintillation solution used for the LSC measurements, potentially distorting the results. As described in section 3.5.2.1 of chapter 3, the photons emitted by the scintillation cocktail Ultima Gold have a wavelength of 420 nm, and, as indicated by the PL quantum yield measurements (Figure 6.37), aerogels loaded with luminescent materials absorb a significant fraction of these photons. This absorption reduces the

counting efficiency, causing the measured radioactivity values to be lower than the actual values. Therefore, only LSC measurements carried out with pure or unloaded matrices may provide the true amount of tritium stored in the sample.

Moreover, many of the samples do not dissolve completely. In some cases, particularly in aerogels containing a concentration of luminescent materials (especially Y_2O_3:Eu^{3+} microparticles) above 3%wt, they remain undissolved, leaving a kind of white pellet. Consequently, part of the tritium may remain trapped in these pellets, and the total amount of tritium bound to the aerogel chemical structure after HIE could be underestimated.

To investigate the mechanism based on HIE on the surface of luminescent microparticles, LSC measurements of Y_2O_3:Eu^{3+} particles are needed.

Regarding the hypotheses involving the trapping of tritium atoms in aerogel pores and in the pores of luminescent Y_2O_3:Eu^{3+} microparticles, thermodesorption measurements are required to confirm it.

6.2.3.2 Thermodesorption Measurements

A first thermodesorption measurement is therefore carried out with a pure CMC aerogel in order to study both tritium present as molecular gas (HT) physically trapped in the aerogel porous structure and tritium bound to the aerogel's chemical structure (incorporated as HTO after HIE), as long as heating induces their release[2].

The aerogel is exposed to a tritium atmosphere for 30 minutes at 1.2 bar . The evolution of the released radioactivity measured by thermodesorption, as a function of time and temperature, is shown in Figure 6.38.

Based on these results, two observations can be made. First, 91% of the total activity (HT + HTO) is released at room temperature within 2 hours at 20 °C.

Second, tritium is found predominantly, 99.6%, in the form of HTO (which would indicate that a large fraction of tritium has been incorporated into the aerogel's chemical structure following HIE), and only 0.4% in the form of HT (which would indicate the fraction of tritium trapped as gas within the aerogel's porous structure).

Based on these preliminary results, some hypotheses to explain where the tritium is stored would include:

- An aerogel containing luminescent materials would store more tritium than a pure

[2]The thermodesorption measurements are carried out by Pierre Colonna, a postdoctoral colleague funded by the Programmes Exploratoire et Transversaux de Compétences (PE-PTC), in the CEA/DRF/JOLIOT laboratories at the CEA Saclay site.

host matrix aerogel.

- In a pure host matrix aerogel, most of the tritium is bound to the chemical structure via HIE, with only a small percentage trapped in the form of gas.
- In an aerogel composed of the host matrix with incorporated luminescent materials, most of the tritium would be trapped due to the luminescent particles, either via HIE or by retention in the porosity.
- Considering that only aerogels loaded with micrometric luminescent particles show the loop cycle during radiance experiments, it is likely that tritium retention through porosity is more important than incorporation via HIE.

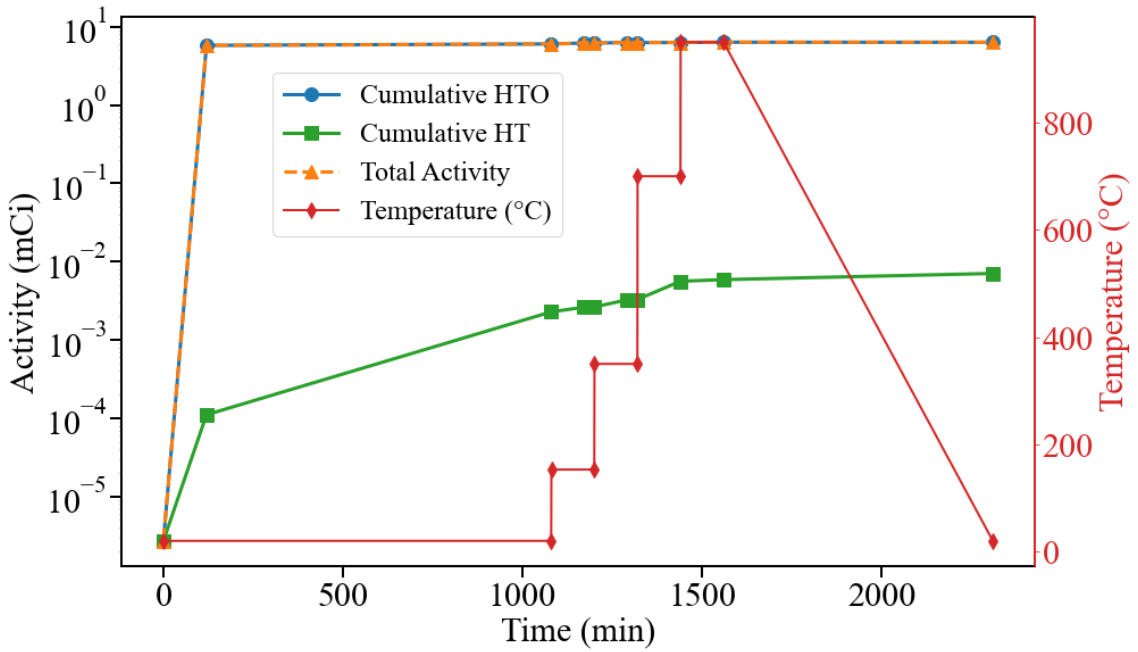

Figure 6.38: On the left y-axis: evolution of cumulative released activity of tritiated water (HTO), molecular tritium gas (HT), and total activity measured by thermodesorption for a CMC aerogel after tritium exposure, as a function of time. On the right y-axis: evolution of the temperature as a function of time.

To confirm these hypotheses, thermodesorption measurements of aerogels containing luminescent materials are needed, since LSC measurements may present basically two problems: the need to find other conditions that allow complete dissolution of the samples, and, more critically and irresolvable, the fact that the measurements may be distorted by the "quenching" effect of the luminescent particles, as already noted.

Nuclear Magnetic Resonance (NMR) analyses could also be performed in order to investigate the molecular structure of the sample, specifically to identify the types and arrangements of atoms within the material and to assess how exposure to tritium affects its chemical environment.

6.3 Radioluminescent Implant vs. Electroluminescent Implant

Once the characterization of the radioluminescent devices has been completed, the goal is to compare the future radioluminescent implant with the electroluminescent implant used in the current clinical trial. Given that the radioluminescent device emits continuous light and the current clinical device emits pulsed light, the most appropriate approach is to compare the energy emitted over a given time interval.

The current device uses a battery supplied by Boston Scientific, the same model employed in DBS systems. This battery produces double pulses of 250 μs separated by 110 μs, repeated at a frequency of 150 Hz. All of this results in a duty cycle of 7.5%. These pulses reach a maximum peak power of 15 mW/cm^2. In addition, the battery operates for 1 minute and then switches off for 4 minutes, meaning it operates 20% of the time. When the energy emitted over the course of a day is calculated, the result is:

$$E_{\text{NIR, day}} = \left(15\frac{\text{mW}}{\text{cm}^2} \times 7.5\% \times 20\%\right) \times 24\ \text{h} \times 3600\ \text{s} = 1.94 \cdot 10^{1}\ \text{J / cm}^2 \tag{6.23}$$

For the radioluminescent device, the sample used for the long-term radiance evolution study is considered (see section 5.5 in chapter 5): the CMC aerogel loaded with 50%wt Y_2O_3:Eu^{3+} and sealed at 600 mbar. The stabilized radiance value is 7.58 mW/(sr·m^2) (see Figure 5.7), equivalent to 2.4 μW/cm^2. The daily emitted energy is then calculated as:

$$E_{\text{RL, day}} = 2.4\frac{\mu\text{W}}{\text{cm}^2} \times 24\ \text{h} \times 3600\ \text{s} = 2.07 \cdot 10^{-1}\ \text{J / cm}^2 \tag{6.24}$$

There are two orders of magnitude difference between the daily energy emitted by the two devices. However, the clinical trial device energy is measured at the fiber optic output. Since the fiber optic is positioned 7.5 mm from both SNpc, photon losses are estimated at up to four orders of magnitude by the time they reach the SNpc. Thus, the actual energy delivered to the SNpc over one day would be 1.94×10^{-3} J/cm^2 for the clinical trial device, so two orders of magnitude lower than that emitted by the radioluminescent device. Moreover, the radioluminescent device could be implanted closer to the target.

6.4 Conclusion

This chapter has presented the results obtained from various characterization techniques used to analyze the different aerogels, both before and after exposure to a tritium gas atmosphere. The aim was to gain insight into the distinct behaviors exhibited by each type of aerogel under tritium exposure.

Finally, the radioluminescent device has been compared with the one currently used in the clinical trial in terms of energy emitted over a certain period of time.

Techniques de Caractérisation et Analyses Complémentaires

Résumé du Chapitre

Ce chapitre a présenté les résultats obtenus à partir de différentes techniques de caractérisation utilisées pour analyser les divers aérogels, à la fois avant et après exposition à une atmosphère de tritium gazeux. L'objectif était de mieux comprendre les comportements distincts présentés par chaque type d'aérogel lors de l'exposition au tritium.

Enfin, le dispositif radioluminescent a été comparé à celui actuellement utilisé dans l'essai clinique en termes d'énergie émise sur une certaine période de temps.

General Conclusion & Perspectives

The goal of this thesis was to develop a radioluminescent light source for the treatment of neurodegenerative diseases, particularly PD, by PBM.

This work has identified key radioluminescent device strategies from the literature and established an aerogel synthesis protocol loaded with luminescent materials and its further exposure to tritium gas. A custom optical bench has enabled real-time characterization of aerogel radiance under tritium atmosphere, facilitating comparative studies that have identified the best candidate as the CMC aerogel loaded with 50%wt Y_2O_3:Eu^{3+} microphosphors, emitting red light at 612 nm.

Various characterization techniques have been employed to study both the spectral and optical efficiency of aerogels under different excitation mechanisms, such as PL and CL, and their morphology in two and three dimensions. These results complement the RL experiments, enhancing understanding of tritium integration mechanisms within the porous structure, though further investigations remain necessary. Future work should extend the radiochemical characterizations with LSC and thermodesorption measurements initiated in this thesis to a larger sample set and include NMR analysis. Complementary experiments such as gas adsorption and desorption measurements in radioactive atmosphere and X-ray diffraction would also prove valuable.

The scintillating aerogel has been successfully encapsulated in a borosilicate glass capsule at 600 mbar, providing a first proof-of-concept and enabling temporal tracking of radiance evolution over several months. Initiated at the end of January 2025, this ongoing experiment has shown very interesting results, including up to a 30% increase in the initial radiance value over seven months without any intervention. This behavior is unexpected, as one would typically anticipate a decline due to beta decay (although slight) and aging of the luminescent materials. Such behavior has not been observed before since luminescent materials are usually studied by PL, where this exotic behaviour has never been observed. These findings open the door for the development of tritium-based radioluminescent medical devices that could be charged in a controlled tritium atmosphere at constant

pressure and then continue increasing in luminous intensity on their own after encapsulation during their initial months of operation, prior to potential future medical implantation.

Perspectives

The results obtained during this doctoral work contributed substantially to securing Agence Nationale de la Recherche (ANR) funding for the "Radiolight" project, which will enable continued development of these radioluminescent devices. This project may involve multiple research directions:

- In this new phase, alongside collaborators already involved from various CEA laboratories in Grenoble and Saclay, researchers from the École Normale Supérieure (ENS) Lyon and Université Claude Bernard Lyon 1 (UCBL1) will join the project to study aerogels based solely on luminescent materials [155, 156]. These aerogels will be exposed to the tritium gas atmosphere, analogous to the approach followed in this thesis but without a host matrix; here, the luminescent materials will serve as the host matrix.

- Exploring polystyrene as an alternative host matrix instead of aerogels, as the Saclay team has extensive experience incorporating tritium via HIE [157].

- Investigating a novel concept derived from Aggregation-Induced Emission (AIE) materials, which have recently revolutionized solid-state fluorescence by overcoming the limitations of aggregation-caused quenching [158]. These small or polymeric organic molecules typically exhibit strong electronic-vibrational coupling in dispersed states, leading to non-radiative transitions and fluorescent quenching. However, aggregation causes restriction of intramolecular motion, reducing electronic-vibrational coupling, suppressing non-radiative processes, and greatly enhancing fluorescence emission.

- Studying luminescent materials emitting near 800 nm, corresponding to absorption by copper centers of the CcO enzyme, already described in section 1.4.5 of chapter 1. This would allow investigate the effect of PBM compared to emissions in the 600–700 nm range.

- Optimizing radioluminescent devices via simulations of tritium and luminescent particle interactions to better understand light production and maximize RL quantum yield.

Beyond these exploratory studies, the first preclinical trial of these radioluminescent devices in rodents is scheduled within the next four years, which will provide in vivo proof-of-concept regarding the device's safety.

If the preclinical study proceeds favorably, it may enable subsequent preclinical trials using other animal models, notably non-human primates.

Regarding the potential for clinical trials, the radioluminescent device could be used for de novo PD patients, i.e., those recently diagnosed, to slow dopaminergic neuron cell death through PBM. To facilitate this, the radioluminescent device could be attached to an implantable probe (with explantation capability if needed), following the same neurosurgical trajectory currently used for DBS probe implantation.

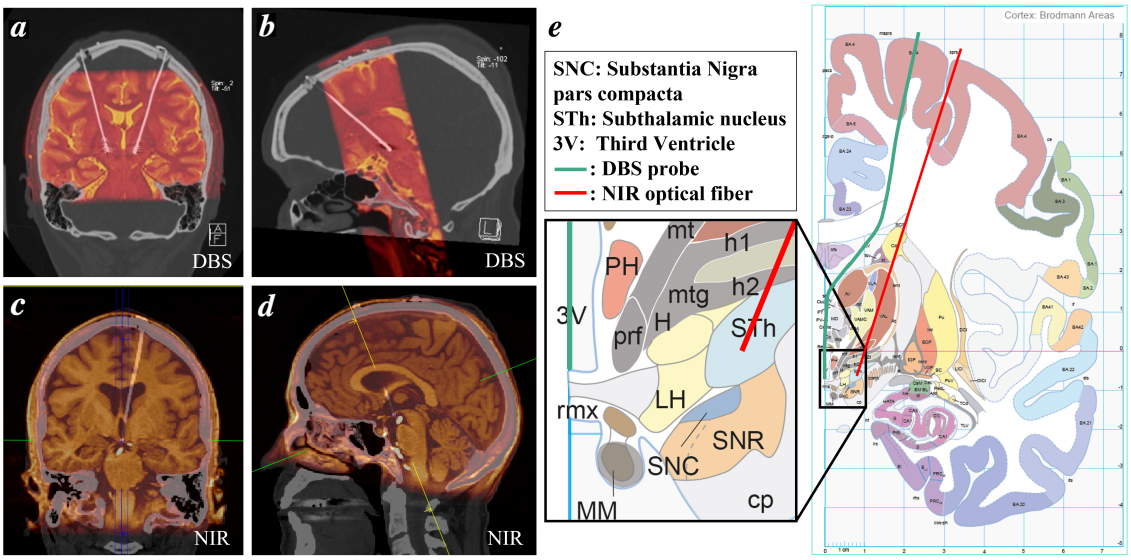

Figure 7.1: MRI images of a patient implanted with a DBS probe: ***a)*** coronal view and ***b)*** sagittal view. MRI images of a patient implanted with the photobiomodulation device from the clinical trial at Clinatec: ***c)*** coronal view and ***d)*** sagittal view. The MRI contrast settings differ between the two patients, which is why the images of one appear as the negative of the other. ***e)*** Coronal section (adapted from [3]) showing the approximate trajectories of the DBS probe (in red) and the optical fiber of the clinical trial device (in greenish-blue).

This trajectory is shown in Figures 7.1a and 7.1b, which present MRI images of a patient implanted with a DBS probe for the mitigation of motor symptoms of PD. In Figure 7.1e, the approximate trajectory of the probe is indicated in red, showing that it runs directly to the subthalamic nucleus and lies almost in contact with the SNpc. This configuration would position the radioluminescent device much closer than the optical fiber tip of the implant currently used in the clinical trial. The trajectory of this current implant is shown

in Figures 7.1c and 7.1d, which display MRI images of a clinical trial patient, with the implant trajectory indicated in greenish-blue in the brain schematic. In this case, the optical fiber tip is located at the bottom of the third ventricle, approximately 7.5 mm from the SNpc.

Moreover, for patients with more advanced PD, the radioluminescent device could even be integrated at the tip of the DBS probe, as illustrated in Figure 7.2, enabling immediate mitigation of motor symptoms through DBS while simultaneously providing neuroprotection via PBM.

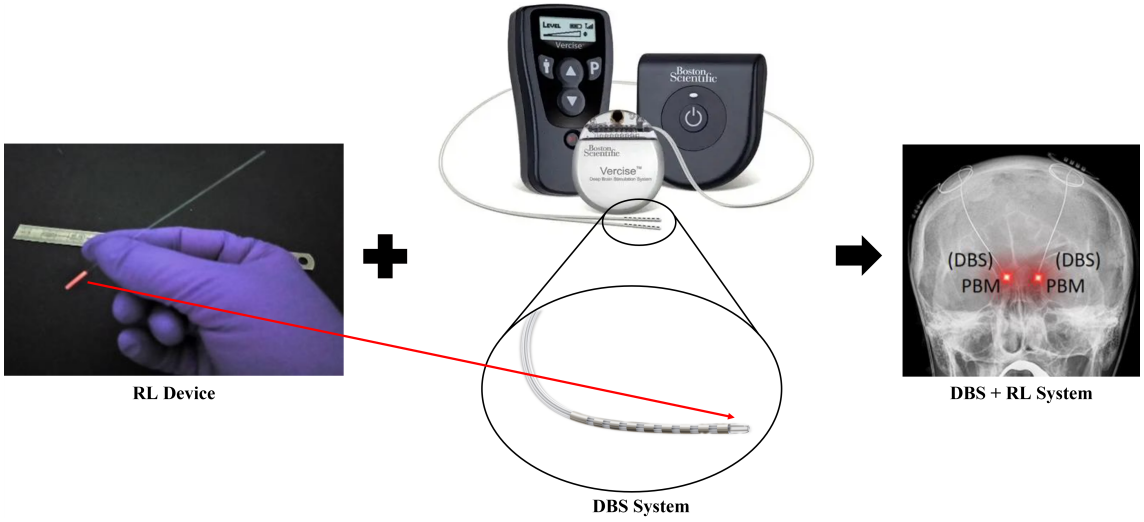

Figure 7.2: The radioluminescent device could be implemented at the tip of the DBS probe.

Additionally, it would be ideal to develop a characterization framework that allows, on one hand, the diagnosis of PD and assessment of disease progression, for example using PET imaging to quantify the number of remaining dopaminergic neurons in the SNpc, and, on the other hand, to determine the optical power necessary to treat the disease. The optical power emitted by the radioluminescent device would then depend on its composition, such as the concentration of luminescent materials.

Finally, it may also be possible to extend this medical device to other neurodegenerative diseases such as AD, where the cortex and hippocampus would be illuminated, or HD, with illumination focused on the striatum, adapting the size and shape of the aerogels.

Therefore, in a broader perspective, the results obtained over these three years represent only the beginning of the development of new radioluminescent devices for treatment, not only of neurodegenerative diseases, as this work has mainly focused on PD, but also potentially applicable to other pathologies treatable by PBM.

Conclusion Générale et Perspectives

L'objectif de cette thèse était de développer une source lumineuse radioluminescente pour le traitement des maladies neurodégénératives, en particulier la PD, par PBM.

Ce travail a identifié les principales stratégies de développement de dispositifs radioluminescents dans la littérature et a établi un protocole de synthèse d'aérogels chargés de matériaux luminescents et exposés ultérieurement au gaz de tritium. Un banc optique dédié a permis la caractérisation en temps réel de la radiance des aérogels sous atmosphère de tritium, facilitant des études comparatives qui ont identifié le meilleur candidat: l'aérogel de CMC chargé à 50%wt de microphosphores Y_2O_3:Eu^{3+}, émettant une lumière rouge à 612 nm.

Diverses techniques de caractérisation ont été employées pour étudier les propriétés spectrales et l'efficacité optique des aérogels sous différents mécanismes d'excitation, notamment en PL et CL, ainsi que leur morphologie en deux et trois dimensions. Ces résultats complètent les expériences de RL, améliorant la compréhension des mécanismes d'intégration du tritium dans la structure poreuse, bien que des investigations supplémentaires restent nécessaires. Les travaux futurs devront étendre les caractérisations radiochimiques avec des mesures de LSC et thermodesorption initiées dans cette thèse à un ensemble plus large d'échantillons et inclure des analyses NMR. Des expériences complémentaires comme des mesures d'adsorption et désorption de gaz en atmosphère radioactive et des expériences de diffraction des rayons X seraient également précieuses.

L'aérogel scintillant a été encapsulé avec succès dans une capsule de verre borosilicaté à 600 mbar, apportant une première preuve de concept et permettant le suivi temporel de l'évolution de la radiance sur plusieurs mois. Lancée fin janvier 2025, cette expérience en cours a montré des résultats très intéressants, notamment une augmentation de la radiance initiale allant jusqu'à 30% sur sept mois, sans aucune intervention. Ce comportement est

inattendu, car on s'attendrait typiquement à une décroissance due à la désintégration bêta (bien que légère) et au vieillissement des matériaux luminescents. Un tel comportement n'a jamais été observé auparavant, car les matériaux luminescents sont habituellement étudiés par PL, où ce phénomène exotique n'a jamais été rapporté. Ces résultats ouvrent la voie au développement de dispositifs médicaux radioluminescents à base de tritium, qui pourraient être chargés dans une atmosphère contrôlée de tritium à pression constante, puis continuer d'augmenter en intensité lumineuse de manière autonome après encapsulation durant leurs premiers mois de fonctionnement, avant un éventuel futur implant médical.

Perspectives

Les résultats obtenus durant cette thèse doctorale ont largement contribué à l'obtention d'un financement de l'ANR pour le projet "Radiolight", qui permettra la poursuite du développement de ces dispositifs radioluminescents. Ce projet pourrait inclure plusieurs axes de recherche :

- Dans cette nouvelle phase, aux côtés des collaborateurs déjà impliqués venus de plusieurs laboratoires CEA à Grenoble et Saclay, des chercheurs de l'École Normale Supérieure (ENS) Lyon et de l'Université Claude Bernard Lyon 1 (UCBL1) rejoindront le projet pour étudier des aérogels constitués uniquement de matériaux luminescents [155, 156]. Ces aérogels seront exposés à une atmosphère de gaz tritium, de manière analogue à l'approche suivie dans cette thèse mais sans matrice hôte; ici, les matériaux luminescents constitueront la matrice hôte.

- L'exploration du polystyrène comme matrice hôte alternative aux aérogels, l'équipe de Saclay ayant une vaste expérience dans l'incorporation de tritium via HIE [157].

- L'étude d'un concept novateur dérivé des matériaux à émission induite par agrégation (AIE), qui ont récemment révolutionné la fluorescence à l'état solide en dépassant les limitations liées à la désactivation par agrégation [158]. Ces petites molécules organiques ou polymériques présentent généralement un couplage électronique-vibrationnel fort en phase dispersée, entraînant des transitions non radiatives et une désactivation fluorescente. Cependant, l'agrégation provoque une restriction des mouvements intramoléculaires, réduisant ce couplage électronique-vibrationnel, supprimant les processus non radiatifs et améliorant considérablement l'émission fluorescente.

- L'étude de matériaux luminescents émettant aux alentours de 800 nm, correspondant à l'absorption par les centres de cuivre de l'enzyme CcO, déjà décrite en section 1.4.5 du chapitre 1. Cela permettra d'étudier l'effet de la PBM par rapport aux émissions dans la gamme 600–700 nm.

- L'optimisation des dispositifs radioluminescents par des simulations des interactions entre le tritium et les particules luminescentes afin de mieux comprendre la production lumineuse et maximiser le rendement quantique en RL.

Au-delà de ces études exploratoires, le premier essai préclinique de ces dispositifs radioluminescents chez des rongeurs est prévu dans les quatre prochaines années, ce qui fournira une preuve de concept in vivo concernant la sécurité du dispositif.

Si l'étude préclinique est favorable, elle pourrait permettre des essais précliniques ultérieurs avec d'autres modèles animaux, notamment des primates non humains.

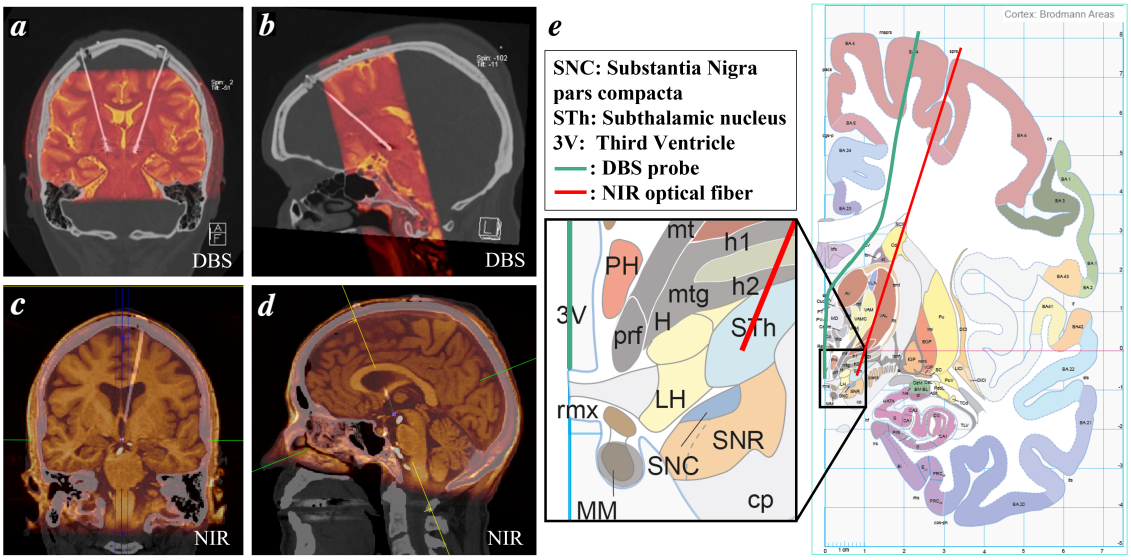

Figure 8.1: Images d'IRM d'un patient implanté avec une sonde de DBS: ***a)*** vue coronale et ***b)*** vue sagittale. Images d'IRM d'un patient implanté avec le dispositif de PBM de l'essai clinique à Clinatec: ***c)*** vue coronale et ***d)*** vue sagittale. Les réglages de contraste de l'IRM diffèrent entre les deux patients, ce qui explique que les images de l'un apparaissent comme le négatif de l'autre. ***e)*** Coupe coronale (adaptée de [3]) montrant les trajectoires approximatives de la sonde DBS (en rouge) et de la fibre optique du dispositif de l'essai clinique (en vert-bleu).

Concernant le potentiel pour les essais cliniques, le dispositif radioluminescent pourrait être utilisé chez les patients atteints de PD de novo, c'est-à-dire récemment diagnostiqués, afin de ralentir la mort cellulaire des neurones dopaminergiques par PBM. Pour faciliter cela,

le dispositif radioluminescent pourrait être fixé à une sonde implantable (avec possibilité d'explantation si nécessaire), suivant la même trajectoire neuroschirurgicale actuellement utilisée pour l'implantation d'une sonde DBS.

Cette trajectoire est présentée dans les figures 8.1a et 8.1b, qui montrent des images d'IRM d'un patient implanté avec une sonde de DBS pour atténuer les symptômes moteurs de PD. Dans la figure 8.1e, la trajectoire approximative de la sonde est indiquée en rouge, montrant qu'elle se dirige directement vers le noyau sous-thalamique et se trouve quasiment en contact avec la SNpc. Cette configuration positionnerait le dispositif radioluminescent beaucoup plus près que la pointe de la fibre optique de l'implant actuellement utilisé dans l'essai clinique. La trajectoire de cet implant actuel est montrée dans les figures 8.1c et 8.1d, qui présentent des images d'IRM d'un patient de l'essai clinique, la trajectoire de l'implant étant indiquée en vert-bleu sur le schéma du cerveau. Dans ce cas, la pointe de la fibre optique se situe au fond du troisième ventricule, à environ 7.5 mm de la SNpc.

De plus, pour les patients atteints de PD à un stade plus avancé, le dispositif radioluminescent pourrait même être intégré à l'extrémité de la sonde DBS, comme illustré à la Figure 8.2, permettant une atténuation immédiate des symptômes moteurs par DBS tout en fournissant simultanément une neuroprotection via PBM.

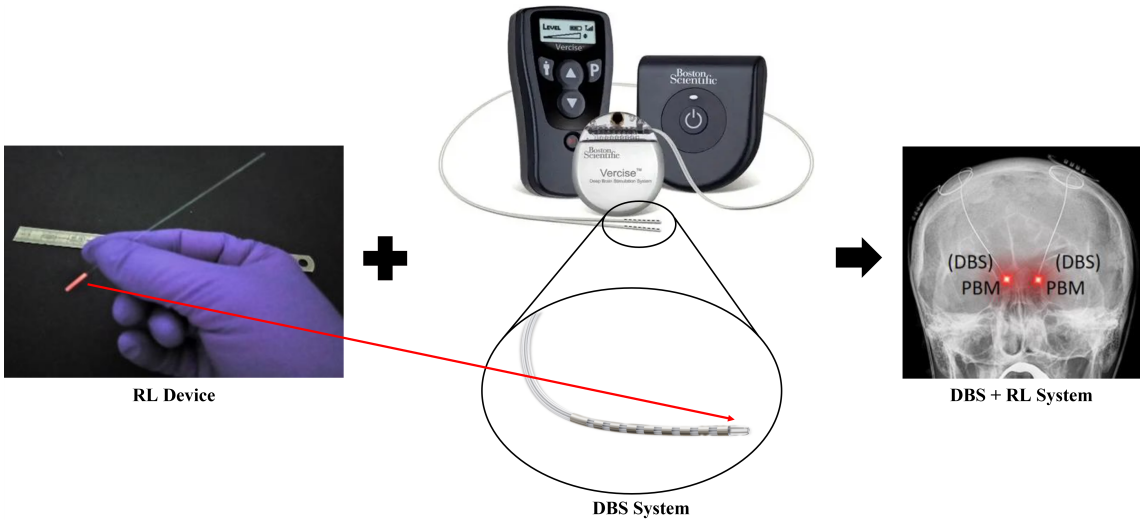

Figure 8.2: Le dispositif radioluminescent pourrait être implanté à l'extrémité de la sonde de DBS.

Par ailleurs, il serait idéal de développer un cadre de caractérisation permettant, d'une part, le diagnostic de PD et l'évaluation de la progression de la maladie, par exemple grâce à l'imagerie PET pour quantifier le nombre de neurones dopaminergiques restants dans la SNpc, et, d'autre part, de déterminer la puissance optique nécessaire pour traiter la maladie. La puissance optique émise par le dispositif radioluminescent dépendrait alors de

sa composition, telle que la concentration en matériaux luminescents.

Enfin, il pourrait également être possible d'étendre ce dispositif médical à d'autres maladies neurodégénératives telles que la AD, où le cortex et l'hippocampe seraient illuminés, ou la HD, avec une illumination focalisée sur le striatum, en adaptant la taille et la forme des aérogels.

Ainsi, dans une perspective plus large, les résultats obtenus au cours de ces trois années ne représentent que le début du développement de nouveaux dispositifs radioluminescents pour le traitement, non seulement des maladies neurodégénératives, puisque ce travail s'est principalement concentré sur PD, mais également potentiellement applicables à d'autres pathologies traitables par PBM.

Bibliography

[1] O. M. de la Santé (OMS), "Principaux repères de l'oms sur la démence." https://www.who.int/fr/news-room/fact-sheets/detail/dementia, 2025. Accessed on 16th September, 2025.

[2] Inserm, "Maladie d'alzheimer. une maladie neurodégénérative complexe mais de mieux en mieux comprise." https://www.inserm.fr/dossier/alzheimer-maladie/, 2019. Accessed on March 19th, 2025.

[3] J. K. Mai, M. Majtanik, and G. Paxinos, *Atlas of the Human Brain*. Amsterdam, Netherlands: Elsevier, 1997.

[4] Elivie, "Journée mondiale de parkinson 2025." https://www.elivie.fr/journee-mondiale-parkinson-2025/, 2025. Accessed on 16th September, 2025.

[5] Inserm, "Maladie de parkinson. deuxième maladie neurodégénérative la plus fréquente." https://www.inserm.fr/dossier/parkinson-maladie/, 2022. Accessed on March 19th, 2025.

[6] C. Wolfson, D. Gauvin, F. Ishola, and M. Oskoui, "Global Prevalence and Incidence of Amyotrophic Lateral Sclerosis: A Systematic Review," *Neurology*, vol. 101, June 2023.

[7] Inserm, "Sclérose latérale amyotrophique (SLA) / maladie de Charcot. Une dégénérescence des motoneurones encore incurable." https://www.inserm.fr/dossier/sclerose-laterale-amyotrophique-sla-maladie-charcot/, 2017. Accessed on March 19th, 2025.

[8] Inserm, "Maladie de Huntington. Vers des solutions thérapeutiques?." https://www.inserm.fr/dossier/huntington-maladie/, 2022. Accessed on March 19th, 2025.

[9] E. Dorsey, T. Sherer, M. Okun, and B. Bloem, "The Emerging Evidence of the Parkinson Pandemic," *Journal of Parkinson's Disease*, vol. Aug., pp. S3–S8, Dec. 2018.

[10] J. Parkinson, "An Essay on the Shaking Palsy," *The Journal of Neuropsychiatry and Clinical Neurosciences*, vol. 14, pp. 223–236, May. 2002. PMID: 11983801.

[11] J. M. Charcot and A. Vulpian, *De la paralysie agitante*. Paris: Victor Masson et fils, Extrait de la gazelle hebdomadaire de Médecin et Chirurgie, 1862.

[12] J. M. Charcot, *Leçons du mardi à la Salpêtrière, professeur Charcot : policlinique 1887-1888 / notes de cours de MM. Blin, Charcot et H. Colin [avec une préface de J. Babinski]*. Bureaux du Progrès Médical, 1892.

[13] E. Brissaud, *Leçons sur les maladies nerveuses à la Salpêtrière, 1893-1894*. Paris: G. Masson, 1895.

[14] C. Trétiakoff, *Contribution a l'étude de l'anatomie pathologique du Locus Niger de Soemmering: avec quelques déductions relatives à la pathogénie des troubles du tonus musculaire et de la maladie de Parkinson*. Jouve, 1919.

[15] M. Lima, E. Fachin-Martins, A. Delattre, M. Proença, M. Mori, B. Carabelli, and A. Ferraz, "Motor and Non-Motor Features of Parkinson's Disease – A Review of Clinical and Experimental Studies," *CNS & Neurological Disorders - Drug Targets*, vol. 11, pp. 439–449, Apr. 2012.

[16] W. Poewe, K. Seppi, C. Tanner, G. Halliday, P. Brundin, J. Volkmann, A. E. Schrag, and A. Lang, "Parkinson disease," *Nature Reviews Disease Primers*, vol. 3, Mar. 2017.

[17] F. Lewy, "Paralysis agitans. I. Pathologische Anatomie," *Lewandowsky M, ed. Handbuch der Neurologie. Berlin: Springer*, pp. 920–933, 1912.

[18] M. Shadrina and P. Slominsky, "Modeling Parkinson's Disease: Not Only Rodents?," *Frontiers in Aging Neuroscience*, vol. 13, p. 695718, Aug. 2021.

[19] C. von Economo, "Grippe-encephalitis und Encephalitis lethargic," *Wiener klinishe Wochenschrift*, vol. 32, pp. 393–396, 1919.

[20] R. S. Schwab, A. C. England Jr, D. C. Poskanzer, and R. R. Young, "Amantadine in the treatment of Parkinson's disease," *JAMA*, vol. 208, no. 7, pp. 1168–1170, 1969.

[21] P. A. Ballard, J. W. Tetrud, and J. W. Langston, "Permanent human parkinsonism due to 1-methyl-4-phenyl-1,2,3,6-tetrahydropyridine (MPTP): seven cases," *Neurology*, vol. 35, no. 7, p. 949–956, 1985.

[22] A. Carlsson, M. Lindqvist, T. Magnusson, and B. Waldeck, "On the Presence of 3-Hydroxytyramine in Brain," *American Association for the Advancement of Science*, vol. 127, no. 3296, p. 471, 1958.

[23] A. Carlsson, M. Lindqvist, and T. Magnusson, "3,4-Dihydroxyphenylalanine and 5-Hydroxytryptophan as Reserpine Antagonists," *Nature*, vol. 180, no. 4596, p. 1200, 1957.

[24] A. Carlsson, "A Half-Century of Neurotransmitter Research: Impact on Neurology and Psychiatry." Nobel Lecture, December 8, 2000. Accessed on 16th September, 2025.

[25] G. C. Cotzias, P. S. Papavasiliou, and R. Gellene, "L-Dopa for Parkinsonism," *New England Journal of Medicine*, vol. 278, no. 11, pp. 630–630, 1968.

[26] P. Pollak, V. Fraix, P. Krack, E. Moro, A. Mendes, S. Chabardès, A. Koudsie, and A. L. Benabid, "Treatment results: Parkinson's disease," *Movement Disorders*, vol. 17, pp. S75–S83, Mar. 2002.

[27] A. L. Benabid, P. Pollak, A. Louveau, S. Henry, and J. de Rougemont, "Combined (Thalamotomy and Stimulation) Stereotactic Surgery of the VIM Thalamic Nucleus for Bilateral Parkinson Disease," *Applied Neurophysiology*, vol. 50, pp. 344–346, Jan. 1988.

[28] A. L. Benabid, S. Chabardès, J. Mitrofanis, and P. Pollak, "Deep brain stimulation of the subthalamic nucleus for the treatment of Parkinson's disease," *The Lancet Neurology*, vol. 8, pp. 67–81, Jan. 2009.

[29] V. D. Sharma, M. Patel, and S. Miocinovic, "Surgical Treatment of Parkinson's Disease: Devices and Lesion Approaches," *Neurotherapeutics*, vol. 17, pp. 1525–1538, Oct. 2020.

[30] A. Braccia, N. Golfrè Andreasi, F. Ghielmetti, D. Aquino, A. P. Savoldi, R. Cilia, R. Telese, F. Colucci, G. Gaudiano, L. M. Romito, A. E. Elia, V. Leta, V. Levi, N. Castelli, G. Devigili, S. Rinaldo, M. Stanziano, V. Caldiera, M. Grisoli, E. F. M. Ciceri, and R. Eleopra, "Magnetic Resonance–Guided Focused Ultrasound Thalamotomy in a Prospective Cohort of 52 Patients with Parkinson's Disease: A Possible

Critical Role of Age and Lesion Volume for Predicting Tremor Relapse," *Movement Disorders*, vol. 40, no. 3, pp. 478–489, 2025.

[31] P. Tambe, V. Undale, A. Sanap, R. Bhonde, and N. Mante, "The prospective role of mesenchymal stem cells in Parkinson's disease," *Parkinsonism & Related Disorders*, vol. 127, p. 107087, Oct. 2024.

[32] O. Dumbhare and S. Gaurkar, "A Review of Genetic and Gene Therapy for Parkinson's Disease," *Cureus*, vol. 15, Feb. 2023.

[33] A. Kouli, K. Torsney, and W. Kuan, *Parkinson's Disease: Pathogenesis and Clinical Aspects*, ch. 1: Parkinson's Disease: Etiology, Neuropathology, and Pathogenesis. Codon Publications, 2018.

[34] R. Barker, A. Björklund, D. Gash, A. Whone, A. Van Laar, J. Kordower, K. Bankiewicz, K. Kieburtz, M. Saarma, S. Booms, H. Huttunen, A. Kells, M. Fiandaca, A. J. Stoessl, D. Eidelberg, H. Federoff, M. Voutilainen, D. Dexter, J. Eberling, and A. Lang, "GDNF and Parkinson's Disease: Where Next? A Summary from a Recent Workshop," *Journal of Parkinson's Disease*, vol. 10, pp. 875–891, July 2020.

[35] Y. Meng, L. Kalia, S. Kalia, C. Hamani, Y. Huang, K. Hynynen, N. Lipsman, and B. Davidson, "Current Progress in Magnetic Resonance-Guided Focused Ultrasound to Facilitate Drug Delivery across the Blood-Brain Barrier," *Pharmaceutics*, vol. 16, p. 719, May. 2024.

[36] F. Fregni and A. Pascual-Leone, "Technology Insight: Noninvasive brain stimulation in neurology - Perspectives on the therapeutic potential of rTMS and tDCS," *Nature clinical practice. Neurology*, vol. 3, pp. 383–93, Aug. 2007.

[37] A. Bruggeman, C. Vandendriessche, H. Hamerlinck, D. De Looze, D. J. Tate, M. Vuylsteke, L. De Commer, L. Devolder, J. Raes, B. Verhasselt, D. Laukens, R. E. Vandenbroucke, and P. Santens, "Safety and efficacy of faecal microbiota transplantation in patients with mild to moderate Parkinson's disease (GUT-PARFECT): a double-blind, placebo-controlled, randomised, phase 2 trial," *eClinicalMedicine*, vol. 71, p. 102563, May. 2024.

[38] W. G. Meissner, P. Remy, C. Giordana, D. Maltête, P. Derkinderen, J.-L. Houéto, M. Anheim, I. Benatru, T. Boraud, C. Brefel-Courbon, N. Carrière, H. Catala,

O. Colin, J.-C. Corvol, P. Damier, E. Dellapina, D. Devos, S. Drapier, M. Fabbri, V. Ferrier, A. Foubert-Samier, S. Frismand-Kryloff, A. Georget, C. Germain, S. Grimaldi, C. Hardy, L. Hopes, P. Krystkowiak, B. Laurens, R. Lefaucheur, L.-L. Mariani, A. Marques, C. Marse, F. Ory-Magne, V. Rigalleau, H. Salhi, A. Saubion, S. R. W. Stott, C. Thalamas, C. Thiriez, M. Tir, R. K. Wyse, A. Benard, and O. Rascol, "Trial of Lixisenatide in Early Parkinson's Disease," *New England Journal of Medicine*, vol. 390, pp. 1176–1185, Apr. 2024.

[39] F. Colucci, M. Avenali, R. Micco, M. Poli, S. Cerri, M. Stanziano, A. Bacila, G. Cuconato, V. Franco, D. Franciotta, C. Ghezzi, M. Gastaldi, A. Elia, L. Romito, G. Devigili, V. Leta, B. Garavaglia, N. Golfrè Andreasi, F. Cazzaniga, and R. Cilia, "Ambroxol as a disease-modifying treatment to reduce the risk of cognitive impairment in GBA-associated Parkinson's disease: a multicentre, randomised, double-blind, placebo-controlled, phase II trial. The AMBITIOUS study protocol," *BMJ Neurology Open*, vol. 5, Nov. 2023.

[40] C. Moreau, P. Odou, J. Labreuche, A. Demailly, G. Touzet, N. Reyns, B. Gouges, A. Duhamel, C. Barthelemy, D. Lannoy, N. Carta, B. Palas, M. Vasseur, F. Marchand, T. Ollivier, C. Leclercq, C. Potey, T. Ouk, S. Baigne, K. Dujardin, L. Carton, A. S. Rolland, J. C. Devedjian, V. Foutel, D. Deplanque, M. Fisichella, and D. Devos, "Intracerebroventricular anaerobic dopamine in Parkinson's disease with l-dopa-related complications: a phase 1/2 randomized-controlled trial," *Nature Medicine*, vol. 31, pp. 819–828, Jan. 2025.

[41] N. R. Finsen, *La lutte contre le lupus vulgaire*. Copenhague, Denmark: Gyldendalske Boghandels Forlag, 1902. Rapport présenté à la conférence d'automne du Bureau central international pour la lutte contre la tuberculose, Berlin, 1902.

[42] M. Endre, S. Béla, and G. P., "The effect of laser beams on the growth of hair in mice," *Radiobiologia, radiotherapia*, vol. 9, pp. 621–626, 1968.

[43] P. McGuff, R. Deterling, L. Gottlieb, H. Fahimi, D. Bushnell, and F. Roeber, "The Laser Treatment of Experimental Malignant Tumours," *Canadian Medical Association journal*, vol. 91, pp. 1089–95, Dec. 1964.

[44] E. Mester, T. Spiry, B. Szende, and J. G. Tota, "Effect of laser rays on wound healing," *The American Journal of Surgery*, vol. 122, pp. 532–535, Oct. 1971.

[45] T. L. I. Roberts, J. T. Lettieri, and L. B. Ellis, "CO2 Laser Resurfacing: Recognizing and Minimizing Complications," *Aesthetic Surgery Journal*, vol. 16, pp. 142–148, June 1996.

[46] H. Whelan, E. Buchmannla, N. Whelan, S. Turner, V. Cevenini, H. Stinson, R. Ignatius, T. Martin, J. Cwiklinski, G. Meyer, B. Hodgson, and L. Gould, "NASA light emitting diode medical applications from deep space to deep sea," *AIP Conference Proceedings*, vol. 552, pp. 35–45, Feb. 2001.

[47] M. Mason, P. Nicholls, and C. Cooper, "Re-evaluation of the Near Infrared spectra of mitochondrial cytochrome c oxidase: implications for non invasive in vivo monitoring of tissues.," *Biochimica et biophysica acta*, vol. 1837, Aug. 2014.

[48] L. Freitas and M. Hamblin, "Proposed Mechanisms of Photobiomodulation or Low Level Light Therapy," *IEEE Journal of Selected Topics in Quantum Electronics*, vol. 22, pp. 1–1, May 2016.

[49] M. R. Hamblin, "Mechanisms and Mitochondrial Redox Signaling in Photobiomodulation," *Photochemistry and Photobiology*, vol. 94, no. 2, pp. 199–212, 2018.

[50] D. M. Johnstone, C. Hamilton, L. C. Gordon, C. Moro, N. Torres, F. Nicklason, J. Stone, A. L. Benabid, and J. Mitrofanis, "Exploring the Use of Intracranial and Extracranial (Remote) Photobiomodulation Devices in Parkinson's Disease: A Comparison of Direct and Indirect Systemic Stimulations," *Journal of Alzheimer's Disease*, vol. 83, pp. 1399–1413, Apr. 2021.

[51] P. L. Lima, C. V. Pereira, N. Nissanka, T. Arguello, G. Gavini, C. M. da Costa Maranduba, F. Diaz, and C. T. Moraes, "Photobiomodulation enhancement of cell proliferation at 660 nm does not require cytochrome c oxidase," *Journal of Photochemistry and Photobiology B: Biology*, vol. 194, pp. 71–75, May. 2019.

[52] A. P. Sommer, "Mitochondrial cytochrome c oxidase is not the primary acceptor for near infrared light—it is mitochondrial bound water: the principles of low-level light therapy," *Annals of Translational Medicine*, vol. 7, Mar. 2019.

[53] C. Xu, J. Zhang, D. M. Mihai, and I. Washington, "Light-harvesting chlorophyll pigments enable mammalian mitochondria to capture photonic energy and produce ATP," *Journal of Cell Science*, vol. 127, pp. 388–399, Jan. 2014.

[54] V. Heiskanen and M. Hamblin, "Photobiomodulation: Lasers vs Light Emitting Diodes?," *Photochemical & Photobiological Sciences*, vol. 17, July 2018.

[55] G. B. Altshuler and I. Yaroslavsky, "Absorption Characteristics of Tissues as a Basis for the Optimal Wavelength Choice in Photodermatology," 2018. Palomar Medical Technologies, Burlington, MA.

[56] R. Zein, W. Selting, and M. R. Hamblin, "Review of light parameters and photobiomodulation efficacy: dive into complexity," *Journal of Biomedical Optics*, vol. 23, pp. 1–17, Dec. 2018.

[57] Y.-Y. Huang, A. C.-H. Chen, J. D. Carroll, and M. R. Hamblin, "Biphasic Dose Response in Low Level Light Therapy," *Dose-Response*, vol. 7, no. 4, 2009. PMID: 20011653.

[58] V. Heiskanen, "Photobiomodulation (pbm) research - a comprehensive database." https://docs.google.com/spreadsheets/d/1ZKl5Me4XwPj4YgJCBes3VSCJjiVO4XI0tIR0rbMBj08/edit?gid=0#gid=0, 2025. Accessed on March 25th, 2025.

[59] F. Salehpour and M. R. Hamblin, "Photobiomodulation for Parkinson's Disease in Animal Models: A Systematic Review," *Biomolecules*, vol. 10, Apr. 2020.

[60] F. Salehpour, J. Mahmoudi, F. Kamari, S. Sadigh-Eteghad, S. Hossein Rasta, and M. R. Hamblin, "Brain Photobiomodulation Therapy: a Narrative Review," *Molecular Neurobiology*, vol. 55, pp. 6601–6636, Jan. 2018.

[61] M. Vos, B. Lovisa, A. Geens, V. A. Morais, G. Wagnières, H. van den Bergh, A. Ginggen, B. De Strooper, Y. Tardy, and P. Verstreken, "Near-Infrared 808 nm Light Boosts Complex IV-Dependent Respiration and Rescues a Parkinson-Related pink1 Model," *PLOS ONE*, vol. 8, pp. 1–9, Nov. 2013.

[62] V. E. Shaw, S. Spana, K. Ashkan, A. L. Benabid, J. Stone, G. E. Baker, and J. Mitrofanis, "Neuroprotection of midbrain dopaminergic cells in MPTP-treated mice after near-infrared light treatment," *Journal of Comparative Neurology*, vol. 518, pp. 25–40, Sep. 2010.

[63] C. Peoples, V. E. Shaw, J. Stone, G. Jeffery, G. E. Baker, and J. Mitrofanis, "Survival of Dopaminergic Amacrine Cells after Near-Infrared Light Treatment in MPTP-Treated Mice," *International Scholarly Research Notices*, vol. 2012, p. 850150, May 2012.

[64] C. Moro, N. Torres, N. El Massri, D. Ratel, D. Johnstone, J. Stone, J. Mitrofanis, and A. L. Benabid, "Photobiomodulation preserves behaviour and midbrain

dopaminergic cells from MPTP toxicity: Evidence from two mouse strains," *BMC neuroscience*, vol. 14, p. 40, Mar. 2013.

[65] D. Johnstone, N. El Massri, C. Moro, S. Spana, X. S. Wang, N. Torres, C. Chabrol, X. De Jaeger, F. Reinhart, S. Purushothuman, A. L. Benabid, J. Stone, and J. Mitrofanis, "Indirect application of near infrared light induces neuroprotection in a mouse model of parkinsonism - An abscopal neuroprotective effect," *Neuroscience*, vol. 274, pp. 93–101, May 2014.

[66] F. Reinhart, N. El Massri, D. M. Johnstone, J. Stone, J. Mitrofanis, A. L. Benabid, and C. Moro, "Near-infrared light (670 nm) reduces MPTP-induced parkinsonism within a broad therapeutic time window," *Experimental Brain Research*, vol. 234, p. 1787–1794, Jul. 2016.

[67] N. El Massri, D. M. Johnstone, C. L. Peoples, C. Moro, F. Reinhart, N. Torres, J. Stone, A. L. Benabid, and J. Mitrofanis, "The effect of different doses of near infrared light on dopaminergic cell survival and gliosis in MPTP-treated mice," *International Journal of Neuroscience*, vol. 126, no. 1, pp. 76–87, 2016.

[68] M. San Miguel, K. L. Martin, J. Stone, and D. M. Johnstone, "Photobiomodulation Mitigates Cerebrovascular Leakage Induced by the Parkinsonian Neurotoxin MPTP," *Biomolecules*, vol. 9, Oct. 2019.

[69] F. Reinhart, N. El Massri, F. Darlot, N. Torres, D. M. Johnstone, C. Chabrol, T. Costecalde, J. Stone, J. Mitrofanis, A. L. Benabid, and C. Moro, "810nm near-infrared light offers neuroprotection and improves locomotor activity in MPTP-treated mice," *Neuroscience Research*, vol. 92, pp. 86–90, Mar. 2015.

[70] F. Reinhart, N. El Massri, N. Torres, C. Chabrol, J. Molet, D. M. Johnstone, J. Stone, A. L. Benabid, J. Mitrofanis, and C. Moro, "The behavioural and neuroprotective outcomes when 670nm and 810nm near infrared light are applied together in MPTP-treated mice," *Neuroscience Research*, vol. 117, pp. 42–47, Apr. 2017.

[71] A. Oueslati, B. Lovisa, J. Perrin, G. Wagnières, H. van den Bergh, Y. Tardy, and H. A. Lashuel, "Photobiomodulation Suppresses Alpha-Synuclein-Induced Toxicity in an AAV-Based Rat Genetic Model of Parkinson's Disease," *PLOS ONE*, vol. 10, pp. 1–13, Oct. 2015.

[72] A. Salgado and E. Carraro, "Effects of Light Emitting Diode and Low-intensity Light on the immunological process in a model of Parkinson's disease," *Medical Research Archives*, vol. 4, Jan. 2016.

[73] J. A. O'Brien and P. J. Austin, "Effect of Photobiomodulation in Rescuing Lipopolysaccharide-Induced Dopaminergic Cell Loss in the Male Sprague–Dawley Rat," *Biomolecules*, vol. 9, Aug. 2019.

[74] S. Purushothuman, C. Nandasena, D. M. Johnstone, J. Stone, and J. Mitrofanis, "The impact of near-infrared light on dopaminergic cell survival in a transgenic mouse model of parkinsonism," *Brain Research*, vol. 1535, pp. 61–70, Oct. 2013.

[75] A. R. Guillen, D. Q. Truong, P. C. Faria, B. Pryor, L. de Taboada, and A. Datta, "High-resolution computational modeling of Transcranial Photobiomodulation: Light propagation and thermal effects," *medRxiv*, Jan. 2025.

[76] C. Moro, N. El Massri, N. Torres, D. Ratel, X. De Jaeger, C. Chabrol, F. Perraut, A. Bourgerette, M. Berger, S. Purushothuman, D. Johnstone, J. Stone, J. Mitrofanis, and A. L. Benabid, "Photobiomodulation inside the brain: a novel method of applying near-infrared light intracranially and its impact on dopaminergic cell survival in MPTP-treated mice," *Journal of Neurosurgery*, vol. 120, pp. 670 – 683, Mar. 2014.

[77] N. El Massri, A. Lemgruber, I. Rowe, C. Moro, N. Torres, F. Reinhart, C. Chabrol, A. L. Benabid, and J. Mitrofanis, "Photobiomodulation-induced changes in a monkey model of Parkinson's disease: changes in tyrosine hydroxylase cells and GDNF expression in the striatum," *Experimental Brain Research*, vol. 235, p. 1861–1874, Mar. 2017.

[78] F. Reinhart, N. E. Massri, C. Chabrol, C. Cretallaz, D. M. Johnstone, N. Torres, F. Darlot, T. Costecalde, J. Stone, J. Mitrofanis, A. L. Benabid, and C. Moro, "Intracranial application of near-infrared light in a hemi-parkinsonian rat model: the impact on behavior and cell survival," *Journal of Neurosurgery*, vol. 124, p. 1829–1841, June 2016.

[79] F. Darlot, C. Moro, N. El Massri, C. Chabrol, D. Johnstone, F. Reinhart, D. Agay, N. Torres, D. Bekha, V. Auboiroux, T. Costecalde, C. Peoples, H. Anastascio, V. Shaw, J. Stone, J. Mitrofanis, and A. L. Benabid, "Near-infrared light is neuroprotective in a monkey model of Parkinson disease," *Annals of neurology*, vol. 79, pp. 59–75, Jan. 2016.

[80] C. Moro, N. El Massri, F. Darlot, N. Torres, C. Chabrol, D. Agay, V. Auboiroux, D. M. Johnstone, J. Stone, J. Mitrofanis, and A. L. Benabid, "Effects of a higher

dose of near-infrared light on clinical signs and neuroprotection in a monkey model of Parkinson's disease," *Brain Research*, vol. 1648, pp. 19–26, Oct. 2016.

[81] C. Moro, N. Torres, K. Arvanitakis, K. Cullen, C. Chabrol, D. Agay, F. Darlot, A. L. Benabid, and J. Mitrofanis, "No evidence for toxicity after long-term photobiomodulation in normal non-human primates," *Experimental Brain Research*, vol. 235, p. 3081–3092, Jul. 2017.

[82] N. El Massri, K. M. Cullen, S. Stefani, C. Moro, N. Torres, A. L. Benabid, and J. Mitrofanis, "Evidence for encephalopsin immunoreactivity in interneurones and striosomes of the monkey striatum," *Experimental Brain Research*, vol. 236, p. 955–961, Jan. 2018.

[83] C.-L. Clinatec and U. H. of Grenoble, "Clinical Trial for Near Infrared Endoventricular Illumination for Neuroprotection in Very Early Cases of Parkinson's Disease (Ev-NIRT)," 2020-2028. Identifier: NCT04261569.

[84] S. Chabardès, S. Thobois, J. Mitrofanis, M. Beaudoin-Gobert, D. Anglade, N. Aubert, V. Auboiroux, P. Bleuet, T. Costecalde, E. De Schlichting, O. Faivre, M. Mastrosimone, J. Molet, A. Poizat, S. Renault, N. Torres, C. Chabrol, C. Moro, and A. L. Benabid, "Intracranial Photobiomodulation In De Novo Parkinson's Patients: preliminary data of an ongoing randomized controlled trial," *medRxiv*, Jan. 2025.

[85] S. L. Jacques, "Optical properties of biological tissues: a review," *Physics in Medicine & Biology*, vol. 58, p. R37, May 2013.

[86] B.-A. Jönsson, "Henri Becquerel's discovery of radioactivity – 125 years later," *Physica Medica*, vol. 87, pp. 144–146, 2021.

[87] J. Welsh, "Beta Decay in Science and Medicine," *American journal of clinical oncology*, vol. 30, pp. 437–9, Sep. 2007.

[88] PhysicsOpenLab, "Bremsstrahlung radiation." https://physicsopenlab.org/2017/08/02/bremsstrahlung-radiation/, 2017. Accessed on 19th May, 2025.

[89] IonActive, "Distance travelled by beta particles in air and other materials." https://ionactive.co.uk/resource-hub/guidance/distance-travelled-by-beta-particles-in-air-and-other-materials, Sept. 2021. Accessed on 19th May, 2025.

[90] B. Coursey, "The National Bureau of Standards and the Radium Dial Painters," *Journal of Research of the National Institute of Standards and Technology*, vol. 126, Jan. 2021.

[91] J. Klein, C. Sun, and G. Pratx, "Radioluminescence in biomedicine: physics, applications, and models," *Physics in Medicine and Biology*, vol. 64, Feb. 2019.

[92] P. Laurens, "Nuclear-Powered Pacemakers: An Eight-Year Clinical Experience," *Pacing and Clinical Electrophysiology*, vol. 2, pp. 356–360, May 1979.

[93] Laboratoire National Henri Becquerel (LNHB), "Nuclear Data Table." http://www.lnhb.fr/home/nuclear-data/nuclear-data-table/, 2024. Accessed on March 4th, 2025.

[94] B. Henke, E. Gullikson, and J. Davis, "Henke X-Ray Attenuation Length Calculator." Center for X-Ray Optics and Advanced Light Source, Lawrence Berkeley National Laboratory, 1993. Accessed on 8th September, 2025.

[95] A. C. Thompson, D. T. Attwood, E. M. Gullikson, M. R. Howells, J. B. Kortright, A. L. Robinson, J. H. Underwood, K.-J. Kim, J. Kirz, I. Lindau, P. Pianetta, H. Winick, G. P. Williams, and J. H. Scofield, *X-Ray Data Booklet*. Berkeley, California: Lawrence Berkeley National Laboratory, University of California, second ed., 2001. Accessed on 8th September, 2025.

[96] Autorité de Sûreté Nucléaire (ASN), *"Impact sur l'homme" in "Livre blanc du Tritium"*, ch. 5, p. 258. France: ASN, 2022. Accessed on: September 19th, 2024.

[97] J. G. MacHutchin, D. L. Prosser, and C. H. Wright, "Self-luminous light sources," 1957. United States Patent.

[98] A. Korin, M. Givon, and D. Wolf, "Parameters affecting the intensity of light sources powered by tritium," *Nuclear Instruments and Methods*, vol. 130, pp. 231–237, Dec. 1975.

[99] R. J. Traub and G. A. Jensen, *Tritium Radioluminescent Devices Health and Safety Manual*. International Nuclear Information System - INIS, International Atomic Energy Agency - IAEA, Washington, U.S., 1995. INIS Collection, Report No. INIS-2012-xxxx.

[100] Organisation for Economic Co-operation and Development (OECD), "Radiation Protection Standards for Gaseous Tritium Light Devices." https://legalinstruments.oecd.org/public/doc/452/452.en.pdf, 2025. Accessed on 12th September, 2025.

[101] K. Kim, K. Kim, S. Son, and W.-S. Kim, "Manufacturing process of self-luminous glass tube (SLGT) utilizing tritium gas: Design of tritium handling facilities," *Korean Journal of Chemical Engineering*, vol. 21, pp. 562–566, May 2004.

[102] C. A. Cook, "Phototherapeutic Devices for the Treatment of Diabetic Retinopathy," 2019.

[103] M. Hara, H. Sakaguchi, M. Nakayama, S. Abe, M. Matsuyama, T. Abe, and T. Aso, "Tritium Counting Using a Europium Coordination Complex," *Fusion Science and Technology*, vol. 71, pp. 496–500, May 2017.

[104] H. Cahuzac, A. Sallustrau, C. Malgorn, F. Beau, P. Barbe, V. Babin, S. Dubois, A. Palazzolo, R. Thai, I. Correia, K. B. Lee, S. Garcia-Argote, O. Lequin, M. Keck, H. Nozach, S. Feuillastre, X. Ge, G. Pieters, D. Audisio, and L. Devel, "Monitoring In Vivo Performances of Protein–Drug Conjugates Using Site-Selective Dual Radiolabeling and Ex Vivo Digital Imaging," *Journal of Medicinal Chemistry*, vol. 65, pp. 6953–6968, May 2022.

[105] C. L. Renschler, R. L. Clough, and T. J. Shepodd, "Demonstration of completely organic, optically clear radioluminescent light," *Journal of Applied Physics*, vol. 66, pp. 4542–4544, Nov. 1989.

[106] C. Renschler, J. Gill, R. Walko, C. Ashley, T. Shepodd, S. Reed, G. Malone, L. Leonard, R. Ellefson, and R. Clough, "Solid state radioluminescent lighting," *Radiation Physics and Chemistry*, vol. 44, pp. 629–644, Dec. 1994.

[107] J. T. Gill, D. B. Hawkins, and C. L. Renschler, "Solid State Radioluminescent Sources Using Tritium-Loaded Zeolites, and Their Proposed Use as Process Monitors," *Fusion Technology*, vol. 21, pp. 325–329, Mar. 1992.

[108] E. Zelenina, V. Bakhmetyev, E. Pechertseva, and M. Sychov, "A modified sol–gel technique of phosphor screens preparation for tritium solid-state radioluminescent light sources (SRLS)," *Journal of Sol-Gel Science and Technology*, vol. 92, pp. 467–473, Nov. 2019.

[109] O. Payanda Konuk, A. Alsuhïle, H. Yousefzadeh, Z. Ülker, S. Bozbağ, C. García-González, I. Smirnova, and C. Erkey, "The effect of synthesis conditions and process parameters on aerogel properties," *Frontiers in Chemistry*, vol. 11, Oct. 2023.

[110] O. Dorofeev and A. Lobanov, "Beta decay in the field of electromagnetic wave and neutrino mass search," *Physics Letters B - PHYS LETT B*, vol. 590, pp. 35–38, June 2004.

[111] R. Gaboriaud, F. Paumier, and B. Lacroix, "Disorder–order phase transformation in a fluorite-related oxide thin film: In-situ X-ray diffraction and modelling of the residual stress effects," *Thin Solid Films*, vol. 601, pp. 84–88, 2016. European Materials Research Society (EMRS) Spring Meeting 2015 Symposium N: "Synthesis, Processing and Characterization of Nanoscale Multi-Functional Oxide Films V".

[112] CASIX Optical Components, "Yttrium vanadate (yvo4) crystal properties and applications." https://web.archive.org/web/20080517130732/http://www.casix.com/product/prod_cry_yvo4.html, 2008. Accessed on 18th September, 2025.

[113] P. Reiss, M. Carriere, C. Lincheneau, L. Vaure, and S. Tamang, "Synthesis of Semiconductor Nanocrystals, Focusing on Nontoxic and Earth-Abundant Materials," *Chemical reviews*, vol. 116, July 2016.

[114] F.-A. Kauffer, *Synthèse, stabilité et toxicité de quantum dots à coeur CdSe*. PhD thesis, Université de Lorraine, Jan. 2014.

[115] C. Rivaux, T. Akdas, R. Yadav, O. El-Dahshan, D. Moodelly, W. L. Ling, D. Aldakov, and P. Reiss, "Continuous Flow Aqueous Synthesis of Highly Luminescent $AgInS_2$ and $AgInS_2$/ZnS Quantum Dots," *Journal of Physical Chemistry C*, vol. 126, p. 20524-34, July 2022.

[116] X.-Y. Xiao, B. Yan, and X. Lian, "Wearable glove sensor for non-invasive organophosphorus pesticides detection based on double-signal fluorescence strategy," *Nanoscale*, vol. 10, June 2018.

[117] R. J. Pearson, A. B. Antoniazzi, and W. J. Nuttall, "Tritium supply and use: a key issue for the development of nuclear fusion energy," *Fusion Engineering and Design*, vol. 136, pp. 1140–1148, 2018. Special Issue: Proceedings of the 13th International Symposium on Fusion Nuclear Technology (ISFNT-13).

[118] Department of Physics and Astronomy, Georgia State University, "Brightness and Night/Day Sensitivity." http://hyperphysics.phy-astr.gsu.edu/hbase/vision/bright.html. Accessed on 8th September, 2025.

[119] W. Commons, "Electron interaction with matter." https://commons.wikimedia.org/wiki/File:Electron_Interaction_with_Matter.svg. Accessed on 21st August, 2025.

[120] Attolight, "Feg source." https://www.attolight.com/products-options/feg-source. Accessed on 21st August, 2025.

[121] M. Thommes, K. Kaneko, A. V. Neimark, J. P. Olivier, F. Rodriguez-Reinoso, J. Rouquerol, and K. S. Sing, "Physisorption of gases, with special reference to the evaluation of surface area and pore size distribution (IUPAC Technical Report)," *Pure and Applied Chemistry*, vol. 87, pp. 1051–1069, Jul. 2015.

[122] Micromeritics Instrument Corporation, "Adsorption des gaz - Micromeritics," 2025. Accessed on 25th June, 2025.

[123] "Annexe G. Caractérisation de la porosité par adsorption de gaz." Accessed on 25th June, 2025.

[124] F. Rouquerol, J. Rouquerol, I. Beurroies, P. LLewellyn, and R. Denoyel, "Texture des matériaux divisés - aire spécifique des matériaux pulvérulents ou nanoporeux," Rapport technique P1050V4, Techniques de l'Ingénieur, France, Oct. 2020.

[125] Micromeritics Instrument Corporation, *ASAP 2420 Operator Manual*. Micromeritics Instrument Corporation, Jan. 2012.

[126] ESRF, "The European Synchrotron Radiation Facility (ESRF)," 2025. Accessed on 8th June, 2025.

[127] M. Grabski, "Overview and Challenges of the Vacuum Systems of Diffraction Limited Storage Rings," in *67th ICFA Advanced Beam Dynamics Workshop on Future Light Sources (FLS 2023)*, (Luzerne, Switzerland), ICFA, Aug. 2023.

[128] S.-A. Zhou and A. Brahme, "Development of phase-contrast X-ray imaging techniques and potential medical applications," *Physica Medica*, vol. 24, no. 3, pp. 129–148, 2008.

[129] P. Cloetens, "Status of the nano-imaging beamline ID16A," Imaging I/Full field microscopy, (Bari, Italy), International Union of Crystallography (IUCr), 2018.

[130] European Synchrotron Radiation Facility (ESRF), "Sample mounting." Internal document, 2024. Unpublished internal document.

[131] Hamamatsu, "Quantaurus-QY Absolute PL quantum yield spectrometer." https://www.hamamatsu.com/jp/en/product/photometry-systems/luminescence-efficiency-measurement-system/quantaurus-qy/C11347series.html. Accessed on 29th August, 2025.

[132] J. Bi, L. Sun, Q. Wei, K. Zhang, L. Zhu, S. Wei, D. Liao, and J. Sun, "Rapid ultrasonic-microwave assisted synthesis of Eu^{3+} doped Y_2O_3 nanophosphors with enhanced luminescence properties," *Journal of Materials Research and Technology*, vol. 9, no. 5, pp. 9523–9530, 2020.

[133] M. Saltarelli, M. Matos, E. De Faria, K. Ciuffi, L. Rocha, and E. Nassar, "Preparation of YV_4:Eu^{3+} at low temperature by the hydrolytic sol–gel methodology," *Journal of Sol-Gel Science and Technology*, vol. 73, Sept. 2014.

[134] X. Hu, T. Chen, Y. Xu, M. Wang, W. Jiang, and W. Jiang, "Hydrothermal synthesis of bright and stable $AgInS_2$ quantum dots with tunable visible emission," *Journal of Luminescence*, vol. 200, pp. 189–195, 2018.

[135] N. A. Vitshima, B. Silwana, N. Tsolekile, and M. C. Matoetoe, "Effect of ZnS coating on the optoelectronic properties of aqueous glutathione capped AgInS quantum dots," *Journal of Alloys and Compounds*, vol. 900, p. 163386, 2022.

[136] D. Selmarten, M. Jones, G. Rumbles, P. Yu, J. Nedeljkovic, and S. Shaheen, "Quenching of Semiconductor Quantum Dot Photoluminescence by a π-Conjugated Polymer," *The Journal of Physical Chemistry B*, vol. 109, no. 33, pp. 15927–15932, 2005.

[137] B. Lacroix, *Influence des défauts cristallins sur les changements de phase induits par faisceaux d'ions dans les films minces d'oxyde d'yttrium Y_2O_3*. PhD thesis, Dec. 2009.

[138] M. Tang, J. A. Valdez, K. E. Sickafus, and P. Lu, "Order-disorder phase transformation in ion-irradiated rare earth sesquioxides," *Applied Physics Letters*, vol. 90, p. 151907, Apr. 2007.

[139] S. Gupta, J. Zuniga, M. Abdou, P. Ghosh, and Y. Mao, "Optical properties of undoped, Eu^{3+} doped and Li^+ co-doped $Y_2Hf_2O_7$ nanoparticles and polymer nanocomposite films," *Inorganic Chemistry Frontiers*, vol. 7, Nov. 2019.

[140] P. Jegadeesan, *Radiation effects in oxides used in nuclear applications*. PhD thesis, Aug.. 2019.

[141] H. Wang, H. Qian, Z. Luo, K. Zhang, X. Shen, Y. Zhang, M. Zhang, and F. Liebner, "ZCIS/ZnS QDs fluorescent aerogels with tunable emission prepared from porous 3D nanofibrillar bacterial cellulose," *Carbohydrate Polymers*, vol. 224, p. 115173, 2019.

[142] W. Massover, "Electron Beam-Induced Radiation Damage: The Bubbling Response in Amorphous Dried Sodium Phosphate Buffer," *Microscopy and microanalysis : the official journal of Microscopy Society of America, Microbeam Analysis Society, Microscopical Society of Canada*, vol. 16, pp. 346–57, Apr. 2010.

[143] G. W. Scherer, S. Calas, and R. Sempéré, "Adsorption in Sparse Networks: II. Silica Aerogels," *Journal of Colloid and Interface Science*, vol. 202, no. 2, pp. 411–416, 1998.

[144] K. Morishige, "Revisiting the Nature of Adsorption and Desorption Branches: Temperature Dependence of Adsorption Hysteresis in Ordered Mesoporous Silica," *ACS Omega*, vol. 6, p. 15964–15974, Jun. 2021.

[145] M. Chen, B. Coasne, R. Guyer, D. Derome, and J. Carmeliet, "Role of hydrogen bonding in hysteresis observed in sorption-induced swelling of soft nanoporous polymers," *Nature Communications*, vol. 9, Aug. 2018.

[146] J. T. Culp, M. R. Smith, E. Bittner, and B. Bockrath, "Hysteresis in the Physisorption of CO_2 and N_2 in a Flexible Pillared Layer Nickel Cyanide," *Journal of the American Chemical Society*, vol. 130, pp. 12427–12434, Aug. 2008.

[147] Y. Zou, B. Maillet, P. Coussot, and L. Brochard, "Sorption hysteresis in nanoporous swelling adsorbents," *Phys. Rev. Res.*, vol. 7, p. 013205, Feb. 2025.

[148] IMT Mines Albi, Sciences et Technologies des Poudres, "Le déroulement théorique d'une isotherme d'adsorption." https://nte.mines-albi.fr/STP/fr/co/uc_IsothermeAdsorption.html. Accessed on 8th July, 2025.

[149] J. Zarges, P. Sälzer, and H. Heim, "Correlation of fiber orientation and fiber-matrix-interaction of injection-molded polypropylene cellulose fiber composites," *Composites Part A: Applied Science and Manufacturing*, vol. 139, pp. 106–112, 2020.

[150] IUPAC, *Compendium of Chemical Terminology, 2nd ed. (the "Gold Book")*. Oxford: Blackwell Scientific Publications, 1997. Accessed on June 7th, 2025.

[151] O. Demir and D. Ege, "Effect of Concentration of Citric Acid on The Rheological Properties of Methylcellulose Hydrogels," *Journal of Ankara University Faculty of Medicine*, vol. 71, pp. 172–176, Dec. 2018.

[152] H. Kishimoto, Y. Shinohara, M. Naito, A. Takeuchi, K. Uesugi, Y. Suzuki, and Y. Amemiya, "Visualization of nanoscale deformation in polymer composites with

zernike-type phase-contrast X-ray microscopy and the finite element method," *Polymer Journal*, vol. 45, pp. 64–69, Nov. 2012.

[153] L. Xu, Z. Chu, J. Zhang, T. Cai, X. Zhang, Y. Li, H. Wang, X. Shen, R. Cai, H. Shi, C. Zhu, J. Pan, and D. Pan, "Steric Effects in the Deposition Mode and Drug-Delivering Efficiency of Nanocapsule-Based Multilayer Films," *ACS Omega*, vol. 7, pp. 30321–30332, Aug. 2022.

[154] L. Niu and J. Panyam, "Freeze concentration-induced PLGA and polystyrene nanoparticle aggregation: Imaging and rational design of lyoprotection," *Journal of Controlled Release*, vol. 248, pp. 125–132, 2017.

[155] M. Odziomek, F. Chaput, F. Lerouge, C. Dujardin, M. Sitarz, S. Karpati, and S. Parola, "From Nanoparticle Assembly to Monolithic Aerogels of YAG, Rare Earth Fluorides and Composites," *Chemistry of Materials*, vol. 30, Jul. 2018.

[156] C. Dujardin, M. Luce, P. Mai, F. Lerouge, Y. Cheref, S. Pierre, B. Sabot, and F. Chaput, "Real-Time Detection and Discrimination of Radioactive Gas Mixtures Using Nanoporous Inorganic Scintillators," Mar. 2024.

[157] M. Lepron, M. Daniel-Bertrand, G. Mencia Berlinches, B. Chaudret, S. Feuillastre, and G. Pieters, "Nanocatalyzed Hydrogen Isotope Exchange," *Accounts of Chemical Research*, vol. 54, Feb. 2021.

[158] J. Ma, Y. Gu, D. Ma, W. Lu, and J. Qiu, "Insights into AIE materials: A focus on biomedical applications of fluorescence," *Frontiers in Chemistry*, vol. 10, p. 985578, Sept. 2022.

Scientific Contributions

Participation in International Conferences

I. Muñoz Velasco, S. Sousa Nobre, O. Renard, S. Garcia-Argote, P. Colonna, C. Rivaux, S. Feuillastre, P. Reiss, M. Jay, G. Pieters, P. Bleuet, Potential of a Radioluminescent Light Source for Photobiomodulation in the Treatment of Parkinson's Disease, **oral presentation**, *21st Congress of the European Society for Photobiology (ESP 2025)*, August 2025, Bari, Italy.

I. Muñoz Velasco, S. Sousa Nobre, O. Renard, S. Garcia-Argote, P. Colonna, S. Feuillastre, P. Reiss, G. Pieters, P. Bleuet, Potential of Radioluminescence for Phototherapy in the Treatment of Parkinson's Disease, **keynote oral presentation**, *17th International Conference on Scintillating Materials and their Applications (SCINT 2024)*, July 2024, Milan, Italy.

Publications in Peer-Reviewed Journals

I. Muñoz Velasco, P. Colonna, S. Sousa Nobre, O. Renard, S. Garcia-Argote, C. Rivaux, S. Feuillastre, P. Reiss, G. Pieters, P. Bleuet, **Exploring the Potential of a Radioluminescent Light Source for Photobiomodulation**, IEEE Transactions on Nuclear Science, vol. 72, no. 7, pp. 2089-2096, July 2025, doi: 10.1109/TNS.2025.3541916.

Patents

I. Muñoz Velasco, P. Bleuet, S. Sousa Nobre, O. Renard, **Procédé et Dispositif pour Electrodéposer un Revêtement à la Surface d'une Electrode**, patent application submitted (DD23810), April 2024.

Other Contributions

PhD Student Day 2025 of the CEA Department, **oral presentation**, June 2025, Grenoble, France. **Prize for best oral presentation (3rd year PhD category).**

Participation in the "PhD Generation" video series from CEA/DRT/LETI, 2025 edition, **science divulgation**, June 2025. [Link: https://www.youtube.com/shorts/Rh9NlPHFQkg]

Séminaire scientifique et technologique CEA annuel des programmes exploratoire (PE-BU) et transversaux de compétences (PTC), Study and Development of a Radioluminescent Implant - Applications to Neurodegenerative Diseases (PTC 22ID14 BETA4NIR), **oral presentation**, November 2024, Grenoble, France.

Parvis des Sciences 2024, **science divulgation** of the Clinatec stand to primary school children, October 2024, Grenoble, France.

PhD Student Day 2024 of the CEA Department, **poster**, September 2024, Grenoble, France. **Prize for best poster (2nd year PhD category).**

Internal seminar at CEA/DES/LITEN, **oral presentation**, August 2024, Grenoble, France.

Internal seminar at CEA/DRT/LETI, Potential of Radioluminescence for Phototherapy in the Treatment of Parkinson's Disease, **oral presentation**, June 2024, Grenoble, France.

PhD Student Day 2023 of the CEA Department, **oral presentation and poster**, May 2023, Grenoble, France.

Abstract

Photobiomodulation is a promising approach to slow neurodegeneration by illuminating specific brain regions. Clinatec is currently conducting the world's first clinical trial with seven Parkinson's disease patients implanted with an intracerebral optical fiber operating at 670 nm. In this context, a radioluminescent device based on materials excited by tritium beta decay is of high interest. Such an approach could be less invasive, provide more efficient light delivery due to compactness and diffuse illumination, and offer extended energy autonomy, all contributing to improved patient comfort and treatment efficacy. This thesis aims to develop millimetric-scale aerogels used as host matrices serving simultaneously as reservoirs for tritium and luminescent materials. Silica- and cellulose-based aerogels loaded with phosphors or quantum dots are synthesized and exposed to a tritium gas atmosphere. Radiance is analyzed as a function of tritium pressure (and thus, tritium activity) and aerogel size, revealing distinct behaviors depending on material composition. The most promising scintillating aerogel is identified and encapsulated in borosilicate glass to study the evolution of radiance over a long timescale, yielding novel results not previously documented. This work highlights the potential of self-powered luminescent devices with prospects for optimizing photobiomodulation in clinical applications.

Key words: Parkinson's disease, photobiomodulation, radioluminescence, scintillation, tritium, aerogel, phosphor, quantum dots.

Résumé

La photobiomodulation constitue une approche prometteuse pour ralentir la neurodégénérescence par illumination de régions cérébrales spécifiques. Clinatec mène actuellement le premier essai clinique mondial avec sept patients atteints de la maladie de Parkinson implantés d'une fibre optique intracérébrale fonctionnant à 670 nm. Dans ce contexte, un dispositif radioluminescent basé sur des matériaux excités par la désintégration bêta du tritium présente un intérêt majeur. Une telle approche pourrait être moins invasive, offrir une délivrance lumineuse plus efficace grâce à sa compacité et à son illumination diffuse, ainsi qu'une autonomie énergétique prolongée, contribuant à améliorer le confort des patients et l'efficacité du traitement. Cette thèse a pour objectif de développer des aérogels de l'échelle millimétrique utilisés comme matrices hôtes servant simultanément de réservoir pour le tritium et les matériaux luminescents. Des aérogels à base de silice et de cellulose, dopés en luminophores ou en boîtes quantiques, sont synthétisés et exposés à une atmosphère de tritium gazeux. La radiance est analysée en fonction de la pression de tritium (et donc, de son activité) et de la taille des aérogels, révélant des comportements distincts selon la composition des matériaux. L'aérogel scintillant le plus prometteur est identifié et encapsulé dans du verre borosilicate afin d'étudier l'évolution de la radiance sur de longues périodes, produisant des résultats inédits jamais documentés auparavant. Ce travail met en évidence le potentiel de dispositifs luminescents autoalimentés, avec des perspectives d'optimisation de la photobiomodulation pour des applications cliniques.

Mots-clés : maladie de Parkinson, photobiomodulation, radioluminescence, scintillation, tritium, aérogel, luminophore, boîtes quantiques.